



HAL
open science

Synthesis and Catalytic Applications of the Transition Elements Nanoparticles

Fangyu Fu

► **To cite this version:**

Fangyu Fu. Synthesis and Catalytic Applications of the Transition Elements Nanoparticles. Micro and nanotechnologies/Microelectronics. Université de Bordeaux, 2019. English. NNT : 2019BORD0195 . tel-02409177v1

HAL Id: tel-02409177

<https://theses.hal.science/tel-02409177v1>

Submitted on 13 Dec 2019 (v1), last revised 19 Dec 2019 (v2)

HAL is a multi-disciplinary open access archive for the deposit and dissemination of scientific research documents, whether they are published or not. The documents may come from teaching and research institutions in France or abroad, or from public or private research centers.

L'archive ouverte pluridisciplinaire **HAL**, est destinée au dépôt et à la diffusion de documents scientifiques de niveau recherche, publiés ou non, émanant des établissements d'enseignement et de recherche français ou étrangers, des laboratoires publics ou privés.

THÈSE PRÉSENTÉE
POUR OBTENIR LE GRADE DE
**DOCTEUR DE
L'UNIVERSITÉ DE BORDEAUX**

ÉCOLE DOCTORALE
SPÉCIALITÉ : POLYMÈRE

Par Fangyu FU

**SYNTHÈSES ET APPLICATIONS CATALYTIQUES
DE NANOPARTICULES D'ÉLÉMENTS DE TRANSITION**

Sous la direction de : Eric FOUQUET
(co-directeur : Didier ASTRUC)

Soutenue le 13 November 2019

Membres du jury :

M. Jean-Marie BASSET	Professeur à KAUST, Thuwal, Arabie Saoudite	Rapporteur
M. Jean-Yves SAILLARD	Professeur émérite, Université de Rennes 1	Rapporteur
M. Jean-René HAMON	Directeur de recherche au CNRS	Examineur
M. Daniel TATON	Professeur à l'Université de Bordeaux	Examineur
M. Eric FOUQUET	Professeur à l'Université de Bordeaux	Directeur de thèse
M. Didier ASTRUC	Professeur émérite, Université de Bordeaux	Co-directeur de thèse

Acknowledgement

This thesis was completed at the Institut des Sciences Moléculaires (ISM), UMR CNRS N°5255, Université de Bordeaux. I thank the ISM director, Professor Eric Fouquet, for having accepted to serve as my official PhD director with care and attention and for kind discussions during the overall PhD period.

I would like to thank my supervisor Prof. Didier Astruc for his inspiring, patient instructions, insightful criticisms and expert guidance on my thesis. His profound knowledge of chemistry triggers my love for this area, his earnest attitude teaches me how a good chemist is done. I appreciate the excellent example he has provided as successful chemist and professor, and I am also deeply grateful to him for his kind help in daily life.

I am greatly indebted to the PhD reviewers, Prof. Jean-Marie Basset, founder and director of the prestigious Catalysis Institute of KAUST and Prof. Jean-Yves Saillard, member of the Institut Universitaire de France, for providing the analysis, support and scientific blessing to this PhD work.

I am also indebted to Dr Jean-René Hamon and Prof. Daniel Taton for having accepted to come and participate to the PhD defense and for their time and constructive remarks as reknown experts.

I am deeply grateful to Dr. Jaime Ruiz for his patient guidance on experiment operation. I also would like to thank the permanent members of the CSH group of ISM, and in particular Dr. Muriel Berlande, for her frequent kind help in the lab.

High tribute shall be paid to Drs Sergio Moya, Lionel Salmon, Angel Martinez, Ane Escobar from CIC bioMAGUNE, San Sebastian, and my friends Hanbao Chong, Xin Wang, Yongbo Song, Tao Chen for their excellent physico-chemical analyses of numerous nanoparticle samples.

My sincere gratitude also go to my former and current laboratory companions, including Dr Changlong Wang, Dr Xiang Liu, Dr Roberto Ciganda, Qi Wang, Dr Rodrigue Djeda, Naixin Kang, Wenjuan Wang and all the CSH students including Alexis Tabey, Julien Gicquiaud, Nicolas Fantozzi, Laura Bourmeyster, Thifanie Christine, Kalyan Dhara, Obinna Osuji, who kindly gave me invaluable advices and help to solve various problems in both study and everyday laboratory life.

I would like to warmly thank my good friends in Bordeaux: Qian Li, Jinhua Wang, Yue He, Zheng Cao, Yongxiang Zheng, Hongwei Li, Wenzhi Wang, Yun Wang, Shuang Peng, Tong Wu, Hongtao Ji, Bin Liu and Chen Ling for the wonderful time spent with them.

I gratefully acknowledge the funding support from the China Scholarship Council for my 4 years of Ph.D. The Universities of Bordeaux, Toulouse III and Anhui, the CICbiomaGUNE Institute, and the CNRS are gratefully acknowledged for research facilities and contributions to research funding.

I would especially like to thank my grandmother, parents, brother, my girl friend Xiaolu Cai and her parents who provided to me continuous support and encouragements during my 4 years of oversea life.

Table of Content

Résumé de la thèse en Français	004
General Introduction	010
Part I: Synthesis of late transition-metal nanoparticles by Na naphthalenide reduction of salts and their catalytic applications.....	015
Chapter 1. Exposure to air boosts CuAAC reactions catalyzed by PEG-stabilized Cu nanoparticles.....	016
Chapter 2. Synthesis of late transition-metal nanoparticles by Na naphthalenide reduction of salts and catalytic efficiency.....	042
Part II: Electron- and Hydride-Reservoir Organometallics as Precursors of Catalytically Efficient Transition Metal Nanoparticles and reduced neutral gold clusters to robust nanocomposite with 18-electron sandwich complexes as counter cations.....	074
Chapter 3. Electron- and Hydride-Reservoir Organometallics as Precursors of Catalytically Efficient Transition Metal Nanoparticles in Water.....	075
Chapter 4. Cobaltocene Reduction of Cu and Ag Salts and Catalytic Behavior of the Nanoparticles Formed.....	117
Chapter 5. Synthesis of New Gold Nanoparticle Salts with Organometallic Counter Cations	155
Part III: Metal-organic frameworks (MOFs) supported heterogeneous catalyst.....	172
Chapter 6. Highly Selective and Sharp Volcano-type Synergistic Ni ₂ Pt@ZIF-8-Catalyzed Hydrogen Evolution from Ammonia Borane Hydrolysis.....	173
Conclusion and Perspectives	207
Publications	212

Résumé de la thèse en Français

Pendant la décennie précédent le début de cette thèse, le groupe du professeur Astruc a développé l'utilisation des arbres moléculaires ou dendrimères de connectivité 3, préalablement synthétisés par le groupe au début des années 2000,¹ en catalyse, dans le domaine des capteurs et en électronique moléculaire. Le travail de cette thèse s'est situé consécutif aux applications de ces dendrimères, particulièrement à l'étude des dendrimères "click",² en catalyse nanoparticulaires. L'intérêt de ces dendrimères "click" de connectivité 3, dont le coeur est construit à partir du mésitylène, réside dans leur aptitude à la fois de coordonner de façon douce les cations des éléments de transition grâce à leur ligands 1,2,3-triazolyle intra dendritiques et d'être solubles dans l'eau grâce à la fonctionnalisation de leurs branches par le tétra éthylène glycol. Ce comportement micellaire leur permet d'ailleurs d'encapsuler les cations, les catalyseurs moléculaires et les nanoparticules (NPs) générées par réduction des cations coordonnés et les activités catalytiques obtenues sont remarquables dans ces trois domaines de la catalyse. Il a ainsi été possible de composer des systèmes actifs en milieu aqueux à partir de quantités ultra-faibles de catalyseurs, allant de l'ordre du ppm à parfois jusqu'à des quantités inférieures au ppm.³⁻⁵ Le défi, pour cette thèse, consistait alors à dessiner d'autres voies d'accès à des nanoparticules très actives en catalyse.

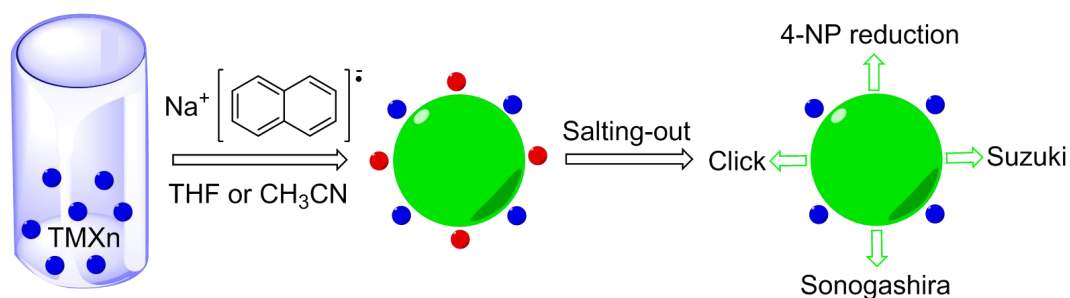
En conséquence, nous avons déterminé et examiné dans ce travail une nouvelle voie en catalyse homogène et l'autre voie en catalyse hétérogène.

En catalyse homogène, nous avons choisi d'utiliser des composés réservoirs d'électron,⁶ c'est-à-dire possédant à la fois un potentiel redox très négatif afin que la forme réduite agisse comme puissant réducteur vis-à-vis des cations métalliques et en même temps des formes réduite et oxydée stables de façon à contrôler le comportement moléculaire aussi bien que nano particulaire des entités catalytiques formées. Une grande force motrice de réduction des cations est en effet habituellement associée à la formation de NPs de faibles tailles.⁷ Trois types de réservoirs d'électron moléculaires ont été utilisés: un réservoir d'électron organique, le système naphthyle sodium/naphtalène, les réservoirs d'électron organométalliques classiques, c'est-à-dire les complexes métal-sandwich à 19 électrons de valence du métal avec les systèmes redox $[\text{FeCp}(\eta^6\text{-C}_6\text{R}_6)]^{0/+}$ et $[\text{Co}(\eta^5\text{-C}_5\text{R}_5)]^{+0}$, $\text{Cp} = \eta^5\text{-C}_5\text{R}_5$, $\text{R} = \text{H}$ ou Me , et enfin les réservoirs d'hydrures de structures dérivées de ces derniers.⁸

En catalyse hétérogène, nous avons souhaité aborder la thématique de la production d'hydrogène⁹ à partir de l'hydrolyse d'hydrures inorganiques tels que l'ammonia borane catalysée par des nanoparticules métalliques. Pour cela, nous avons choisi, dans la continuité de la thèse de Chanlong Wang,¹⁰ les réseaux zéolitiques imidazolates (ZIF), plus particulièrement ZIF-8. Parallèlement, cette thématique a

également été examinée avec succès en catalyse homogène avec la thèse de Qi Wang à l'aide des dendrimères "click" comme stabilisants.¹¹

Ce manuscrit de thèse comprend ainsi trois parties. La première partie, incluant deux chapitres, procure des méthodes de synthèse des NPs des éléments de transition par réduction de sels métallique par le réservoir d'électron naphthyle sodium en utilisant le polyéthylène glycol comme ligand soluble dans l'eau.

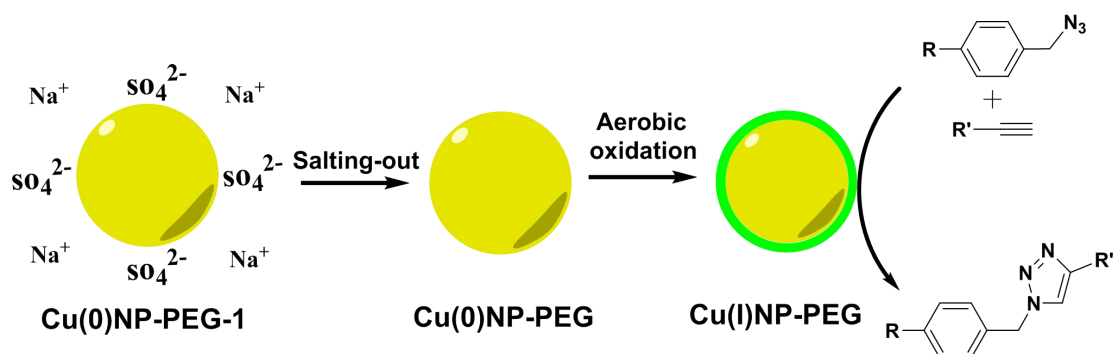


TMXn=HAuCl₄ • 3H₂O, AgPF₆, PdCl₂, CuSO₄ • 5H₂O

● = PEG-2000

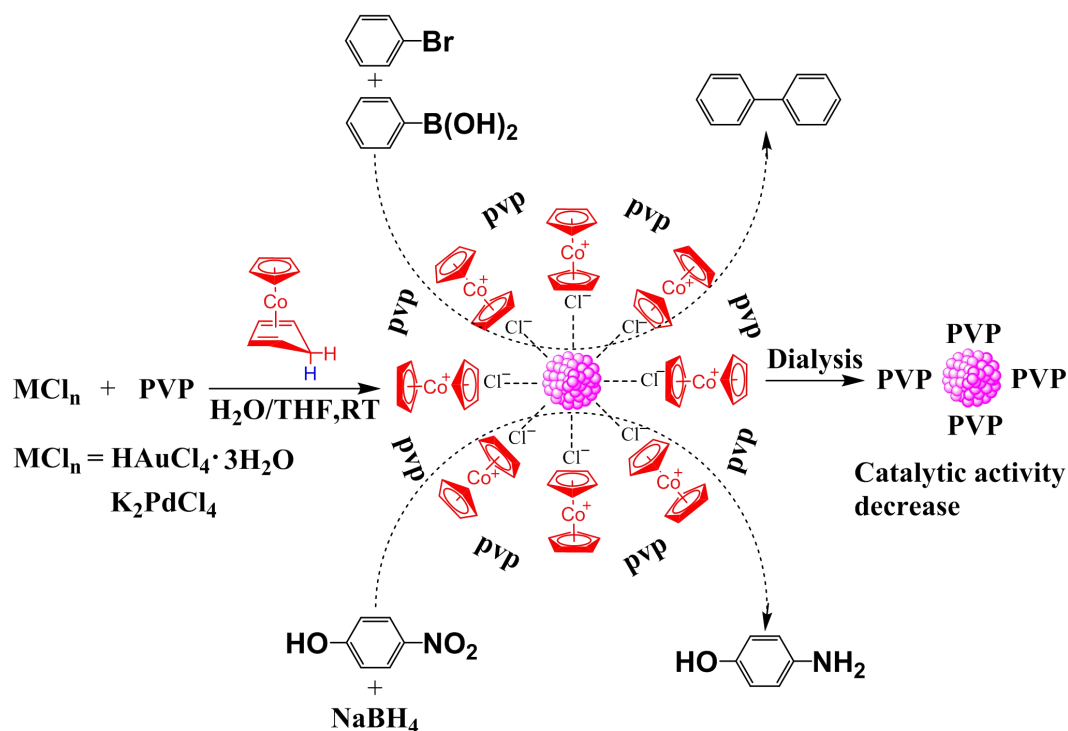
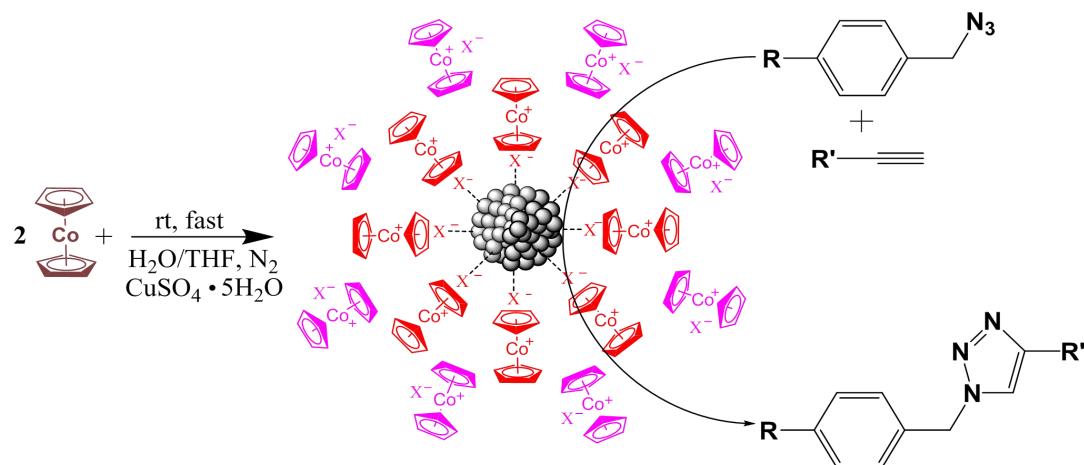
● = Na salt

La synthèse des catalyseurs, leur purification par effet de sel (schémas ci-dessus et ci-dessous), leur recyclage (avec SBA-15 comme support) et leurs applications en catalyse de plusieurs réactions organiques essentielles sont examinées (par exemple, la réduction du p-nitrophénol, les réaction de couplage carbone-carbone de Suzuki et Sonogashira et la réaction "click" d'un alcyne terminal avec un azoture schématisée ci-dessous).^{12,13}



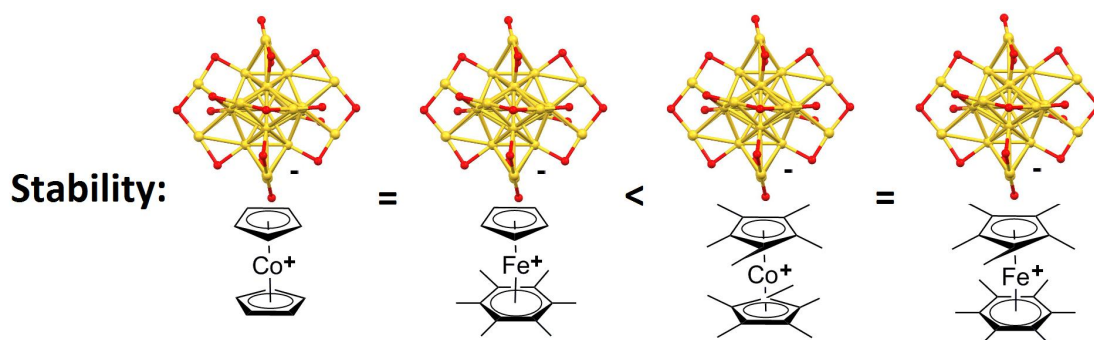
Dans la seconde partie, ce sont les complexes réservoirs d'électron organométalliques de structure sandwich à 19 électrons de valence du métal central (fer ou cobalt) ou leur analogues structuraux réservoirs d'hydrure qui sont utilisés. De cette façon, les formes oxydées cationiques de ces complexes métal-sandwich se retrouvent autour de la NP formée, assurant une protection stérique sans contact direct avec la NP, tandis que le contre-anion du cation précurseur (souvent le chlorure) ligand faiblement la NP en tant que ligand anionique à deux électrons. Ce ligandage a pu être démontré par la grande sensibilité à la couleur et à la localisation de la bande plasmon dans le domaine visible dans le cas des NP d'argent. Ces système nano particulières

présentent une activité catalytique assez remarquable pour la réduction du p-nitrophénol (4-NP) en p-aminophénol (4-AP) avec les AuNPs, la réaction de Suzuki-Miyaura avec les PdNPs et la réaction “click” entre les alcynes terminaux et les azotures avec les CuNPs (schémas ci-dessous), ces réactions étant avantageusement comparées à celles utilisant les catalyseurs habituels.^{14,15}

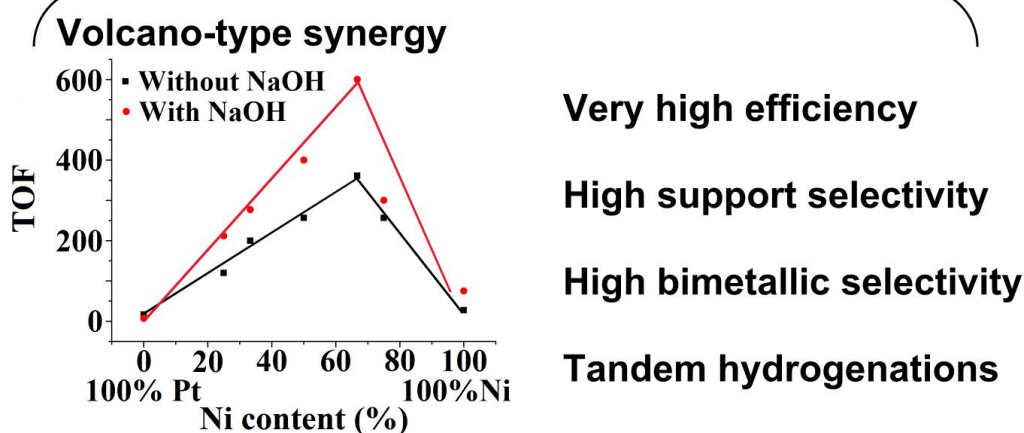


Ce nouveau concept de stabilisation des NPs par encombrement stérique par les formes oxydées cationiques des complexes organométalliques sandwich à 19 électrons de valence du fer et du cobalt, servant de réservoir d'électron lors de la réduction de précurseur, a été étendu à la réduction d'un cluster métallique neutre (au lieu de cation précurseur) produisant alors un cluster mono anionique. Nous avons

ainsi démontré que la stabilité cinétique (en particulier à l'air) de l'anion cluster d'or ainsi formé, $[\text{Au}_{25}(\text{SR})_{18}]^-$ ($\text{R} = \text{CH}_2\text{CH}_2\text{Ph}$) dépend fortement de l'encombrement stérique du cation. Par exemple, la stabilité à l'air de ces systèmes est largement supérieure avec les deux cycles du complexe métal-sandwich perméthylés à ce qu'elle est avec un seul des deux cycles perméthylé, car avec deux cycles perméthylés, la surface de la NP subit obligatoirement l'encombrement maximum (schéma ci-dessous). Ce concept est certainement généralisable à la stabilisation à l'air d'autres clusters et NPs anioniques. Il peut aussi être utilisé à partir de réservoirs d'hydrure dérivant des structures de réservoirs d'électron qui peuvent fournir un électron au cluster (comme dans le cas présent)¹⁶ ou éventuellement un hydrure dans d'autres cas.



La troisième partie du manuscrit de thèse utilise le support hétérogène stabilisant et encapsulant ZIF-8 pour proposer la synthèse et les caractérisations physiques d'une série d'alliages bimétalliques nano particulaires des éléments de transition de droite. L'optimisation de la nature des éléments de transition et de leur pourcentage dans l'alliage nous a permis de mettre au point un catalyseur extrêmement efficace, $\text{Ni}_2\text{Pt}_1@\text{ZIF-8}$, pour l'hydrolyse de l'ammonia borane en hydrogène. La synergie entre les deux métaux accroît de façon remarquable l'activité catalytique, de même que la présence de soude, probablement pour cette dernière par accroissement de la densité électronique due à la coordination de l'anion OH^- à la surface de la NP. Par exemple, ce catalyseur est 87 fois plus efficace que le catalyseur monométallique $\text{Pt}@\text{ZIF-8}$ malgré la toute puissance habituelle du platine pour cette réaction. Ceci met en exergue l'utilisation judicieuse d'un élément courant (Ni), d'autant que celui-ci est majoritaire dans la forme la plus active de l'alliage. Nous avons montré que le support ZIF-8 est plus actif que d'autres supports classiquement utilisés. Finalement ce catalyseur permet des réactions tandem utilisant en hydrogénation de substrat oléfinique l'hydrogène formé (schéma ci-dessous).¹⁷



Références

- 1 Ruiz, J.; Lafuente, G.; Marcen, S.; Ornelas, C.; Lazare, S.; Cloutet, E.; Blais, J.-C.; Astruc, D. Construction of Giant Dendrimers Using a Tripodal Building Block. *J. Am. Chem. Soc.* **2003**, *125*, 7250-7257.
- 2 Ornelas, C.; Ruiz, J.; Cloutet, E.; Alves, S.; Astruc, D. Click Assembly of 1,2,3-Triazole-Linked Dendrimers Including Ferrocenyl Dendrimers that Sense Both Oxo-anions and Metal Cations. *Angew. Chem. Int. Ed.* **2007**, *46*, 872-877.
- 3 Diallo, A. K.; Ornelas, C.; Salmon, L.; Ruiz, J.; Astruc, D. Homeopathic Catalytic Activity and Atom-Leaching Mechanism in the Miyaura-Suzuki Reactions under Ambient Conditions Using Precise "Click" Dendrimer-Stabilized Pd Nanoparticles. *Angew. Chem. Int. Ed. Engl.* **2007**, *46*, 8644-8648.
- 4 Deraedt, C.; Pinaud, N.; Astruc, D. Recyclable catalytic dendrimer nanoreactor for part-per-million Cu^I Catalysis of "click" chemistry in water. *J. Am. Chem. Soc.* **2014**, *136*, 12092-12098.
- 5 Liu, X.; Gregurec, D.; Irigoyen, J.; Martinez, A.; Moya, S.; Ciganda, R.; Hermange, P.; Ruiz, J.; Astruc, D. Precise Localization of Metal Nanoparticles in Dendrimer Nanosnakes or Inner Periphery and Consequences in Catalysis. *Nat. Commun.* **2016**, *7*, 13152.
- 6 Astruc, D.; Hamon, J.-R.; Althoff, G.; Román, E.; Batail, P.; Michaud, P.; Mariot, J.-P.; Varret, F.; Cozak, D. Design, Stabilization and Efficiency of Organometallic "Electron Reservoirs". 19-Electron Sandwiches $\eta^5\text{-C}_5\text{R}_5\text{Fe}(\text{I})\eta^6\text{-C}_6\text{R}_6$, a Key Class Active in Redox Catalysis. *J. Am. Chem. Soc.* **1979**, *101*, 5445-5447.
- 7 Nanoparticles and Catalysis, Astruc, D. Ed., Wiley-VCH, Weinheim, **2008**, 600 pp
- 8 Michaud, P.; Astruc, D.; Ammeter, J. H. Electron-Transfer Pathways in the Reduction of d⁶ and d⁷ Organo-Iron Cations by LiAlH₄ and NaBH₄. *J. Am. Chem. Soc.* **1982**, *104*, 3755-3757.
- 9 Wang, Q.; Astruc, D. State of the Art and Prospects in Metal-Organic Framework

- (MOF)-Based and MOF-Derived Nanocatalysis. *Chem. Rev.* **2020**
doi :10.1021/acs.chemrev.9b00223 (Numéro thématique sur les nanoparticules en catalyse, rédacteur invité: D. Astruc, voir *Chem. Rev.* ASAP).
- 10 Wang, C.; Tuminetti, J.; Wang, Z.; Zhang, C.; Ciganda, R.; Moya, S.; Ruiz, J. Astruc, D. Hydrolysis of Ammonia-Borane over Ni/ZIF-8 Nanocatalyst: High Efficiency, Mechanism, and Controlled Hydrogen Release. *J. Am. Chem. Soc.* **2017**, *139*, 11610-11615.
- 11 Wang, Q.; Fu, F.; Yang, S.; Martinez Moro, M. ; Ramirez, M. ; Moya, S.; Salmon, L.; Ruiz, J.; Astruc, D. *ACS Catal.* **2019**, *9*, 1110-1119.
- 12 Fu, F.; Martinez-Villacorta, A. M.; Escobar, A.; Irigoyen, J.; Moya, S.; Fouquet, E.; Ruiz, J.; Astruc, D. Synthesis of late transition-metal nanoparticles by Na naphthalenide reduction of salts and their catalytic efficiency. *Inorg. Chem. Front.* **2017**, *4*, 2037-2044.
- 13 Fu, F.; Martinez, A.; Wang, C.; Ciganda, R.; Yate, L.; Escobar, A.; Moya, S.; Fouquet, E.; Ruiz, J.; Astruc, D. Exposure to air boosts CuAAC reactions catalyzed by PEG-stabilized Cu nanoparticles. *Chem. Commun.* **2017**, *53*, 5384-5387.
- 14 Fu, F.; Wang, Q.; Ciganda, R.; Martinez-Villacorta, A. M.; Escobar, A.; Moya, S.; Fouquet, E.; Ruiz, J.; Astruc, D. Electron- and Hydride- Reservoir Organometallics as Precursors of Catalytically Efficient Transition Metal Nanoparticles in Water. *Chem. Eur. J.* **2018**, *24*, 6645-6653.
- 15 Fu, F.; Ciganda, R.; Wang, Q.; Tabey, A.; Wang, C.; Escobar, A.; Martinez-Villacorta, A. M.; Hernández, R.; Moya, S.; Fouquet, E.; Ruiz, J.; Astruc, D. Cobaltocene Reduction of Cu and Ag Salts and Catalytic Behavior of the Nanoparticles Formed. *ACS Catal.* **2018**, *8*, 8100-8106.
- 16 Fu, F.; Dedieu, A.; Wang, W.; Chen, T.; Song, Y.; Fouquet, E.; Hamon, J. -R.; Zhu, M.; Astruc, D.; Stabilization of a New Nanocomposite Family by Reduction of Gold Nanoclusters with Electron-reservoir Complexes. *Chem. Commun.* **2019**, *55*, 10277-10280.
- 17 Fu, F.; Wang, C.; Wang, Q.; Martinez-Villacorta, A. M.; Escobar, A.; Chong, H.; Wang, X.; Moya, S.; Salmon, L.; Fouquet, E.; Ruiz, Jaime.; Astruc, D. Highly Selective and Sharp Volcano-type Synergistic Ni₂Pt@ZIF-8- Catalyzed Hydrogen Evolution from Ammonia Borane Hydrolysis. *J. Am. Chem. Soc.* **2018**, *140*, 10034-10042.

General Introduction

Late transition-metal nanomaterials, especially late transition-metal nanoparticles (TMNPs), are an essential part of nanoscience because of their fundamental aspects and multiple applications in biomedicine, sensing, optoelectronics and catalysis.¹ Taking advantage of these properties, the present PhD has been devoted to nanocatalysis. In this concern, due to the unique physical and chemical properties (surface-to-volume effect, quantum size effect, etc.) of the nanoscale materials, nanocatalysts display better catalytic activity and selectivity compared with traditional catalysts,²⁻⁶ Our group has exemplified these concepts in former (for recent examples, see^{7,8}) and present⁹ PhDs.

Problems generally encountered with TMNPs involve their agglomeration resulting from insufficient stabilization by ligands, surfactants or other macromolecules leading to the formation of larger-size TMNPs and sharp decrease of their catalytic activity. Various stabilizers such as *N,N*-dimethylformamide, cetyltrimethylammonium bromide, alkylthiolates, phosphines are toxic; therefore it is necessary to disclose a protective template to avoid the agglomeration, oxidation, stabilized mono-dispersed TMNPs and ultimately optimize their specific physical and chemical properties. Among stabilizers, dendrimers have a place of choice due to their molecular design and precision for the preparation of small, catalytically active TMNPs.^{10,11}

Since “click” chemistry¹² opened the possibility to synthesize the first family of click metallodendrimers by our research group¹³ in 2007 including applications in sensing and catalysis, our group had also further investigated “click” dendrimers for the stabilization of catalytically efficient TMNPs towards a large variety of catalytic reactions using molecular, ionic and nanoparticle catalysts.¹⁴⁻¹⁷ For instance in 2014, our group published “Recyclable catalytic dendrimer nanoreactor for part-per-million Cu(I) catalysis of click chemistry in water”.¹⁴ Liu et al also showed a correlation between the catalytic activities of the TMNPs and their localization inside or outside the dendrimer.¹⁵ Furthermore, such “click” dendrimers were shown to stabilize bimetallic alloy systems for H₂ evolution from ammonia borane hydrolysis.¹⁶ “Click” dendrimers not only provide nanocatalysts, but also several key applications have been developed involving the dendrimer-nanoparticle interfaces such as nanowires, sensors, molecular electronics and redox responsive polymers.¹⁷⁻¹⁹

Along the design of stable and catalytically active TMNPs, our research group has also considered heterogeneous catalysts, because they appear much more practical and efficient than homogeneous systems, although usually not so well defined. Among heterogeneous catalysts, MOFs are a recent intriguing and important class of molecularly-well defined inorganic-organic hybrids with intrinsic porous structures that are used as versatile precursors or sacrificial templates for the preparation of

numerous functional nanomaterials.²⁰⁻²³ Indeed abundant works employing MOFs as precursors to access metal/MOF nanostructures have been reported. Our group has used zeolitic imidazolate framework (ZIF-8)²⁴ as a MOF template to prepare and compare the catalytically efficient ligand-free first-row late transition-metal nanoparticles for H₂ evolution from ammonia borane hydrolysis, a great challenge of the 21st century. The reaction mechanism was studied and H₂ release was efficiently controlled.⁸

As a part of our current studies on the development of new functional TMNPs, we have addressed a number of approaches involving both homogeneous and heterogeneous nanoparticle catalysts mentioned above. We have investigated the optimization of the synthesis of late transition metal nanoparticles using various reducing agents and stabilizers. In particular we have employed electron-reservoir- and hydride reservoir complexes²⁵ for these syntheses for the fabrication of M(0) nanoparticles with various supports. This thesis is thus devoted to the synthesis and functionalization of TMNPs and bimetallic NPs with catalytic applications to “click” (CuAAC) reactions, 4-NP reduction, Suzuki coupling and ammonia borane hydrolysis.

This thesis manuscript is divided into 3 parts. **The first part**, including 2 chapters, provides a method to synthesize the TMNPs by reduction of late transition metal salts using Na naphthalenide with water-soluble PEG as ligand. Catalyst synthesis, purification (by salting-out effect), recycling (with SBA-15 support) and applications in several important organic reactions are examined.

In part II, 19-electron Fe and Co sandwich electron-reservoir and 18-electron hydride reservoir sandwich complexes are introduced to synthesize the TMNPs. In this concept, sandwich complexes not only stabilize small nanoparticles by electrostatic pattern, but also contribute to their excellent catalytic activity. The catalytic activities of the TMNPs obtained by reduction of late transition metal salts by various sandwich complexes towards catalytic reduction of 4-nitrophenol (4-NP) to 4-aminophenol (4-AP) with AuNPs, Suzuki with PdNPs and click reaction with CuNPs are compared. At last, static bulk electron-reservoir such as decamethylcobaltocene, Co(II)Cp*₂, (Cp* = η⁵-C₅Me₅), and [Fe(I)Cp*(η⁶-C₆Me₆)] are used to reduce the nanocluster Au₂₅(SR)₁₈ (R = CH₂CH₂Ph) leading to a largely increased kinetic stabilization of the anionic nanocluster due to the protecting bulk of the electron reservoir cation compared to previous salts of this anionic cluster.

Part III describes the synthesis and characterization of a series of nearly monodispersed alloyed bimetallic nanoparticle catalysts, optimized among late transition metals, and found to be extremely efficient and highly selective with sharp positive synergy between 2/3 Ni and 1/3 Pt embedded inside a zeolitic imidazolate framework (ZIF-8) support. The presence of NaOH boosts H₂ evolution catalyzed by

Ni₂Pt₁@ZIF-8 that becomes 87 times faster than the noble metal-only-based nanocatalyst Pt@ZIF-8. This catalyst Ni₂Pt₁@ZIF-8 shows the best selectivity compared to related catalysts with other supports and metal alloys. At last, kinetic studies and tandem reactions were conducted using this excellent heterogeneous catalyst.⁹

References

- 1 Daniel, M. -C.; Astruc, D. Gold Nanoparticles: Assembly, Supramolecular Chemistry, Quantum-Size-Related Properties, and Applications toward Biology, Catalysis, and Nanotechnology. *Chem. Rev.* **2004**, *104*, 293-346.
- 2 Pelletier, J. D. A.; Basset, J.-M. Catalysis by Design: Well-Defined Single-Site Heterogeneous Catalysts. *Acc. Chem. Res.* **2016**, *49*, 4664-677.
- 3 Samantarav, M. K.; Pump, E.; Bendjeriou-Sedjerari, A.; D'Elia, V.; Pelletier, J. D. A.; Guidotti, M.; Psaro, R.; Basset, J.-M. Surface organometallic chemistry in heterogeneous catalysis. *Chem. Soc. Rev.* **2018**, *47*, 8403-8437.
- 4 Corma, A.; Leyva-Perez, A.; Maria Sabater, J. Gold-Catalyzed Carbon-Heteroatom Bond-Forming Reactions. *Chem. Rev.* **2011**, *111*, 1657-1712.
- 5 Sankar, M.; Dimitratos, N.; Miedziak, P. J.; Wells, P. P.; Kiely, C. J.; Hutchings, G. J. Designing Bimetallic Catalysts for a Green and Sustainable Future. *Chem. Sci.* **2012**, *3*, 20-44.
- 6 Haruta, M. Chance and Necessity: My Encounter with Gold Catalysts. *Angew. Chem., Int. Ed.* **2014**, *53*, 52-56.
- 7 Wang, C.; Ciganda, R.; Salmon, L.; Gregurec, D.; Irigoyen, J.; Moya, S.; Ruiz, J.; Astruc, D. Highly efficient transition metal nanoparticle catalysts in aqueous solutions. *Angew. Chem. Int. Ed.* **2016**, *55*, 3091-3095.
- 8 Wang, C.; Tuninetti, J.; Wang, Z.; Zhang, C.; Ciganda, R.; Salmon, L.; Moya, S.; Ruiz, J.; Astruc, D. Hydrolysis of Ammonia-Borane over Ni/ZIF-8 Nanocatalyst: High Efficiency, Mechanism, and Controlled Hydrogen Release. *J. Am. Chem. Soc.* **2017**, *139*, 11610-11615.
- 9 Fu, F.; Wang, C.; Wang, Q.; Martinez-Villacorta, A. M.; Escobar, A.; Chong, H.; Wang, X.; Moya, S.; Salmon, L.; Fouquet, E.; Ruiz, J.; Astruc, D. Highly Selective and Sharp Volcano-type Synergistic Ni₂Pt@ZIF-8-Catalyzed Hydrogen Evolution from Ammonia Borane Hydrolysis. *J. Am. Chem. Soc.* **2018**, *140*, 10034-10042.
- 10 Meyers, V. S.; Weier, M. G.; Carino, E. V.; Yancey, D. F.; Pande, S.; Crooks, R. M. Dendrimer-encapsulated Nanoparticles: New Synthetic and Characterization Methods and Catalytic Applications. *Chem. Sci.* **2011**, *2*, 1632-1646.

- 11 Bronstein, L. M.; Shifrina, Z. B. Dendrimers as Encapsulating, Stabilizing, or Directing Agents for Inorganic Nanoparticles. *Chem. Rev.* **2011**, *111*, 5301-5344.
- 12 Kolb, H. C.; Finn, M. G.; Sharpless, K. B. Click Chemistry: Diverse Chemical Function from a Few Good Reactions, *Angew. Chem. Int. Ed.* **2001**, *40*, 2004-2021.
- 13 Ornelas, C.; Ruiz, J.; Cloutet, E.; Alves, S.; Astruc, D. Click Assembly of 1,2,3-Triazole-Linked Dendrimers Including Ferrocenyl Dendrimers that Sense Both Oxo-anions and Metal Cations. *Angew. Chem. Int. Ed.* **2007**, *46*, 872-877.
- 14 Deraedt, C.; Pinaud, N.; Astruc, D. Recyclable catalytic dendrimer nanoreactor for part-per-million Cu^I Catalysis of “click” chemistry in water. *J. Am. Chem. Soc.* **2014**, *136*, 12092-12098.
- 15 Liu, X.; Gregurec, D.; Irigoyen, J.; Martinez, A.; Moya, S.; Ciganda, R.; Hermange, P.; Ruiz, J.; Astruc, D. Precise Localization of Metal Nanoparticles in Dendrimer Nanosnakes or Inner Periphery and Consequences in Catalysis. *Nature Commun.* **2016**, *7*, 13152.
- 16 Wang, Q.; Fu, F.; Yang, S.; Martinez Moro, M. ; Ramirez, M. ; Moya, S.; Salmon, L.; Ruiz, J.; Astruc, D. Dramatic Synergy in CoPt Nanocatalysts Stabilized by “Click” Dendrimers for Hydrogen Evolution from Hydrolysis of Ammonia Borane. *ACS Catal.* **2019**, *9*, 1110-1119.
- 17 C. Rapakousiou, Deraedt, C.; Salmon, L.; Ruiz, J.; Astruc, D. Mixed-Valent Intertwined Polymer Units Containing Biferrocenium Side Chains Form Nanosnakes that Encapsulate Gold Nanoparticles. *J Am. Chem. Soc.* **2014**, *136*, 13995-13998.
- 18 Deraedt, C.; Rapakousiou, A.; Wang, Y.; Salmon, L.; Bousquet, M.; Astruc, D. Multi-function Redox Polymers. *Angew. Chem., Int. Ed.* **2014**, *53*, 8445-8449.
- 19 Wang, Y.; Salmon, L.; Ruiz, J.; Astruc, D. Metallodendrimers in Three Oxidation States with Electronically Interacting Metals and Stabilization of Size-Selected Gold Nanoparticles. *Nature Commun.* **2014**, *5*, 3489.
- 20 Lee, J. Y.; Farha, O. K.; Roberts, J.; Scheidt, K. A.; Nguyen, S. T.; Hupp, J. T. Metal–organic framework materials as catalysts. *Chem. Soc. Rev.* **2009**, *38*, 1450-1459.
- 21 Dhakshinamoorthy, A.; Garcia, H. Catalysis by metal nanoparticles embedded on metal–organic frameworks. *Chem. Soc. Rev.* **2012**, *41*, 5262-5284.
- 22 Liu, J.; Chen, L.; Cui, H.; Zhang, J.; Zhang, L.; Su, C. -Y. Applications of metal–organic frameworks in heterogeneous supramolecular catalysis. *Chem. Soc. Rev.* **2014**, *43*, 6011-6061.
- 23 Chughtai, A. H.; Ahmad, N.; Younus, H. A.; Laypkov, A.; Verpoort, F. Metal–organic frameworks: versatile heterogeneous catalysts for efficient catalytic organic transformations. *Chem. Soc. Rev.* **2015**, *44*, 6804-6849.

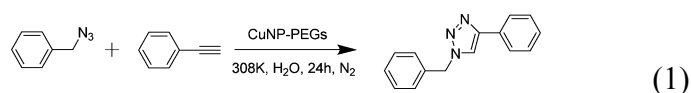
- 24 Park, K. S.; Ni, Z.; Côté, A. P.; Choi, J. Y.; Huang R., Uribe-Romo, F. J.; Chae, H. K.; O’Keeffe, M.; Yaghi, O. M. Exceptional Chemical and Thermal Stability of Zeolitic Imidazolate Frameworks. *Proc. Nat. Acad. Sci. USA* **2006**, *103*, 10186-10191.
- 25 Astruc, D.; Hamon, J.-R.; Althoff, G.; Román, E.; Batail, P.; Michaud, P.; Mariot, J.-P.; Varret, F.; Cozak, D. *J. Am. Chem. Soc.* **1979**, *101*, 5445-5447.

Part I: Synthesis of late transition-metal nanoparticles by Na naphthalenide reduction of salts and their catalytic applications.

Chapter 1. Exposure to air boosts CuAAC reactions catalyzed by PEG-stabilized Cu nanoparticles.

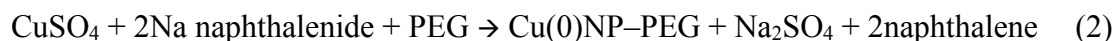
Introduction

Among the various “click” reactions,¹ Cu-catalyzed azide alkyne cycloaddition (CuAAC)² (eqn (1)) undisputedly dominates with applications spanning organic,³ polymer,⁴ biomedical⁵ and materials⁶ chemistry.



Since the early report on the use of CuSO₄ + Na ascorbate,⁷ a large variety of metal catalysts have been reported with the aim of decreasing the amount of toxic Cu sources and improving the greenness of the reaction medium and conditions.^{2–8} Transition metal nanoparticles (NPs), in particular those of noble metals, are excellent ligand-free catalysts in green solvents for many reactions.⁹ Among these nanocatalysts, biometal NPs of the first-row late transition metals are attracting increasing attention, although they are traditionally believed to be inferior catalysts compared to noble transition metal NP catalysts. Along this line, the finding by a number of research groups that CuNPs and Cu nanomaterials are active catalysts for the CuAAC reaction is of particular interest, because these catalysts avoid the use of costly and eventually toxic ligands.⁹ CuNPs are usually formed by reduction of a Cu salt by a reductant such as NaBH₄ in the presence of a stabilizer, and the resulting CuNPs are supposed to contain zero-valent Cu,^{10,11} although Cu nanomaterials under both Cu(I)¹² and Cu(II)¹³ oxidation states have also been reported with catalytic activity for this reaction.^{10–13} Molecular CuAAC catalysts have clearly been shown to be active as Cu(I) derivatives,^{2,10,12} but the oxidation state that is actually most active in nanomaterials is often not so well defined. Cu(0) nanomaterials might be active in the Cu(0) state^{10,11} or, as they are easily oxidized, in particular, in air, their catalytic activity can be due to Cu(I)^{10,12} or Cu(II).^{10,13} Cu(II) catalysts have been proposed for click reactions, but the possibility of their in situ reduction to Cu(I), in particular by azido derivatives or other substrates, cannot be underestimated.

Here, we report new PEG-stabilized, recyclable, homogeneous and heterogeneous CuNP catalysts for the CuAAC reactions including their applications to various biomolecule functionalizations with low Cu amounts. At the same time we also wish to shed light on the problem of the optimized Cu oxidation state in CuNPs for “click” catalysis by comparing the catalytic activity in CuAAC reactions of these new Cu(0)NPs with those obtained upon exposure to air. In particular, we have now examined the catalytic activity of Cu(0)NPs synthesized by reduction of CuSO₄·5H₂O by the strong reductant sodium naphthalenide and stabilized by polyethylene glycol (PEG-2000, eqn (2)).



Sodium naphthalenide, with a redox potential $E^\circ_{\text{NaNaph}/\text{NaNaph}^-}$ of -3.1V vs. NHE in THF¹⁴ has recently been used successfully for the reduction of early transition metal salts to the corresponding zero-valent NPs.¹⁵ We show herein that the catalytic activity of CuNPs synthesized using this method is boosted upon exposure to air.

Whereas various stabilizers such as *N,N*-dimethylformamide, cetyltrimethylammonium bromide, alkylthiolates, phosphines are toxic, poly(ethylene glycol) (PEG) has emerged as one of the most promising nanocomponents in bio-materials and green chemistry.¹⁶ Indeed, PEGs are currently used as carriers of anticancer drugs, with efficiency related to the enhanced permeability and retention effect.¹⁷

Results and discussion

Thus we have used PEG-2000 to stabilize Cu(0)NP prepared by reduction of CuSO₄·5H₂O sodium-naphthalenide in CH₃CN. These Cu(0)NPs (noted Cu(0)NP-PEG-1 before purification) have been purified by simple extraction with a mixture of CH₂Cl₂ and degassed H₂O under N₂. In this first extraction, the Cu(0)NPs are soluble in the organic phase, due to the salting-out effect of Na⁺₂SO₄²⁻ in the aqueous phase. This allowed removing the colorless aqueous solution containing Na⁺₂SO₄²⁻ formed during the synthesis of the CuNPs. In a second extraction of the organic phase by degassed water, the CuNPs were transferred to the aqueous phase, leaving naphthalene in the organic phase that was also well separated in this way (Figure 1).

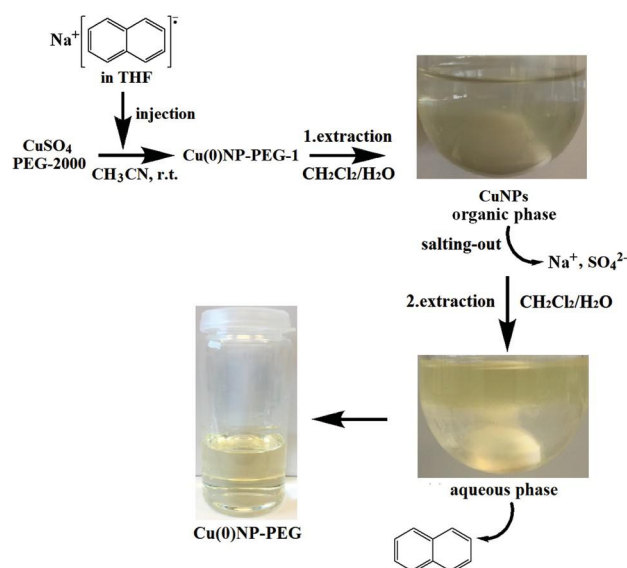


Figure 1. Synthesis and purification of Cu(0)NP-PEG NPs by salting-out under N₂.

The absence of the absorption band in the UV-*vis.* spectra (Figure 3, Experimental Section) showed that these purified CuNPs were zero-valent Cu species (denoted Cu(0)NP-PEG). On the other hand, upon exposure to air for several minutes these CuNPs were characterized by the appearance of an UV-*vis.* band at 360 nm for Cu₂O and are denoted as Cu(I)NP-PEG.¹⁸ Indeed UV-*vis* spectroscopy was very useful in monitoring this oxidation in air (Figure 4, Experimental Section). These changes appeared to be complete after 30 min, and no further change was observed after one day or one week (Figure 5, Experimental Section).

The XPS spectra showed an absorption for Cu(0) or Cu(I); however, in contrast to UV-*vis.* spectroscopy, it was not possible to distinguish between Cu(0) and Cu(I) using XPS. On the other hand, it allows distinguishing Cu(0/I) from Cu(II). Only tiny traces of Cu(II) due to CuO are observed after one week. The Cu 2p spectrum showed the Cu 2p_{3/2} and 2p_{1/2} peaks (Figure 6, Experimental Section). The fitting of the Cu 2p_{3/2} part of the spectrum revealed the presence of Cu(I) or Cu(0) at around 932.1 eV, and a small component at around 934.5 eV was attributed to Cu(II).¹⁹

The TEM of Cu(I)NP-PEG (Figure 2a, histogram in Figure 7, Experimental Section) shows that the average NP size is 3.2 nm, with a maximum distribution around 2.5-3 nm and a few NPs around 4-5 nm. Because the crystallinity of large NPs is better than that of the small ones, two NPs of 4 nm (Figure 10, Experimental Section) and 4.8 nm (Figure 2b), respectively, were selected in the HRTEM image, both showing the clear lattice fringes. The lattice spacing is about 2.4 Å, assuming that the crystallographic plane of the Cu₂O nanocrystal is {111}. This indicates that the Cu(0)NP-PEG surface was oxidized by O₂ to form Cu₂O NPs. The fast Fourier transformation of the HRTEM image (Figure 8, Experimental Section) further shows that good crystallinity was achieved in this case.

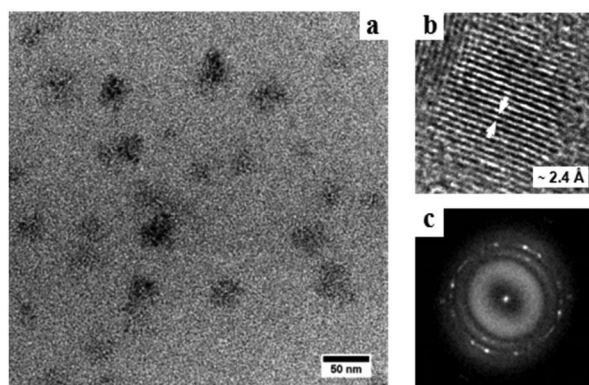


Figure 2. (a) TEM of the Cu(I)NP-PEG catalyst. (b) Details of a 4.8 nm NP observed in Figure 8 (Experimental Section) and (c) the corresponding fast Fourier transformation of the HRTEM image shown in Figure 8 (Experimental Section).

The CuNPs were examined for their catalytic activity in the CuAAC reaction in neat water. There were dramatic differences between the catalytic activities of raw Cu(0)NP-PEG-1, purified Cu(0)NP-PEG and air oxidized Cu(I)NP-PEG. For instance, with 50 ppm Cu, the isolated yields of the click reactions between PhCCH and PhCH₂N₃ for these 3 types of CuNP-PEGs were, respectively, traces (<1%), 21% and 72% (Table 1). The first conclusion is that pure aqueous Cu(0)NP-PEG performs better in this catalytic application than the Cu(0)NP-PEG-1 dissolved in water before these purification steps, because these side products inhibit the surface of non-purified Cu(0)NP-PEG-1. The second conclusion is that aerobically oxidized Cu(I)NP-PEG is a much better catalyst than before oxidation in air, and the conversion increased from 80% with 50 ppm to 100% (95% yield) with 100 ppm Cu (TON = 9500; TOF = 396 h⁻¹).

Table 1. CuAAC reaction (eqn (1)) catalyzed by CuNP-PEGs^a

Catalysts	Amount ^b	Conversion (%) ^c	Yield (%) ^d	TON	TOF (h ⁻¹)
Cu(I)NP-PEG ^e	100 ppm	100	95	9500	396
Cu(0)NP-PEG	100 ppm	74	65	6500	271
Cu(0)NP-PEG-1	100 ppm	50	40	4000	167
Cu(I)NP-PEG ^e	50 ppm	80	72	14400	600
Cu(0)NP-PEG	50 ppm	32	21	4200	175
Cu(0)NP-PEG-1	50 ppm	trace	trace	-	-
Cu(I)NP-PEG ^f	100 ppm	100	97	9700	404
Cu(I)NP-PEG ^f	50 ppm	84	75	15000	625

^a Reaction conditions: 0.5 mmol of benzyl azide, 0.505 mmol of phenylacetylene, and 2 mL of degassed H₂O, 35 °C, 24 h, under N₂. ^b Amount of catalysts used in the CuAAC reduction. ^c ¹H NMR conversion. ^d Isolated yield. ^e Cu(I)NP-PEG (exposed to air for 30 min before catalysis) work-up in deionized H₂O. ^f Cu(I)NP-PEG (exposed to air for 1 day before catalysis) work-up in deionized H₂O.

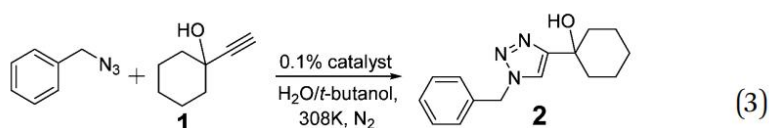
The scope of the applicability of this low level amount of the Cu(I)NP-PEG catalyst

was explored with CuAAC reactions between various alkynes and organic azides in water. Good yields were achieved in the CuAAC of a wide variety of alkynes with organic azides (Table 2, Experimental Section). In addition, after the reactions the “click” products were obtained by simple extraction-washing-filtration without silica chromatography, because they are water-insoluble solids, and the excess alkyne was removed by simple washing with a solvent.

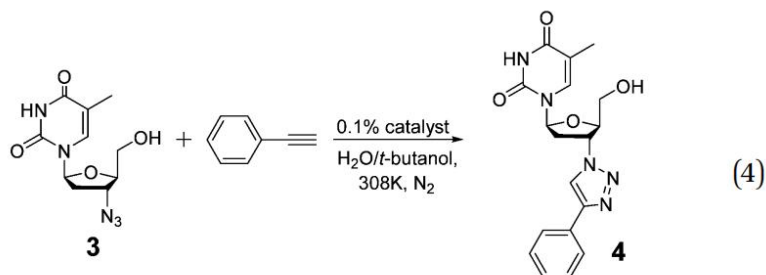
The Cu(I)NP-PEG catalyst was supported and immobilized onto SBA-15 using the sol-immobilization method, and this material was dried at 50 °C (ICP content: 0.06 wt%). The evaluation of the NP size distributions of the Cu(I)NP-PEG after immobilization on the support is shown in Figure 11 (Experimental Section) and reveals that the average particle size of the supported catalyst Cu(I)NP-PEG@SBA-15 is 2.5 nm, i.e., smaller than that of the unsupported Cu(I)NP-PEG. This indicates that the SBA-15 support prevents Cu(I)NP-PEG aggregation and better stabilizes very small Cu(I)NP-PEG@SBA-15 than unsupported Cu(I)NP-PEG. Recycling experiments using 300 ppm of Cu(I)NP-PEG@SBA-15 provided isolated yields greater than 85% for at least five successive cycles (Table 3, Experimental Section), showing the good stability of the catalyst Cu(I)NP-PEG@SBA-15. Following the catalytic reaction, the residual solution after centrifugation was used to test the CuAAC reaction. Traces of the final 1,2,3-triazole product were observed by thin-layer chromatography only after the first catalytic run, and the residual solution from other catalytic runs did not provide any more traces of this reaction product, indicating that catalyst leaching did not occur after the first use of the supported catalyst.

The Cu(I)NP-PEG@SBA-15 catalyst was also successfully used to prepare functional biomedical materials. The “click” reaction between 1-ethynylcyclohexanol (**1**), the precursor of ethinamate, a depressant drug that is an active metabolite of the central nervous system,²⁰ and benzyl azide provided **2** in good isolated yield (87.8%) with only 0.1% Cu in 50% aq. *t*-butanol at 35 °C for 24 h (eqn (3)). Another key natural product, 3'-deoxy-3-azidothymidine (AZT, zidovudine, **3**), is a nucleoside analogue reverse transcriptase inhibitor, and it was the first approved antiviral product for the treatment of human immunodeficiency virus (HIV) infection.²¹ The 3'-azido group of AZT has provided potential application for HIV RT binding.²² Its “click” functionalization has been shown to be a convenient tool for the synthesis of new nucleoside inhibitors with low to submicromolar potencies against HIV-1,^{23,24} new fluorescent markers, and cytostatic agents.^{25,26} Here, the “click” reaction between zidovudine **3** and phenylacetylene using 0.1% Cu from Cu(I)NP-PEG@SBA-15 in 50% *t*-butanol at 35 °C for 24 h provided **4** in 91.8% isolated yield (eqn (4)). Cu(I)NP-PEG@SBA-15 was also applied to synthesize “click”-triazole functionalized 7-(propargyloxy)- coumarin **6** from **5** in H₂O/*tert*-butanol. Coumarin

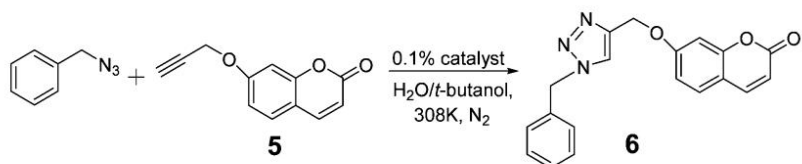
derivatives are often used in the perfume industry. Moreover, they are fluorophores and have recently been employed as fluorescent probes to visualize the metabolism of cysteine in living cells.²⁷ In this case (eqn (5)), a 92.7% isolated yield was achieved with 0.1% Cu from the Cu(I)NP-PEG@SBA-15 catalyst. Moreover, note that these three functional “click” reactions catalyzed by the supported catalyst Cu(I)NP-PEG@SBA-15 afford compounds **2**, **4** and **6** in higher yields with less reaction time than with the unsupported catalyst Cu(I)NP-PEG. The interfacial effect within the supported catalyst plays an important role in the “click” functionalization of biomedical products.



- (1) Catalyst: Cu(I)NP-PEG, 48h, isolated yield: 81.5%;
 (2) Catalyst: Cu(I)NP-PEG@SBA-15, 24h, isolated yield: 87.8%



- (1) Catalyst: Cu(I)NP-PEG, 48h, isolated yield: 87.4%;
 (2) Catalyst: Cu(I)NP-PEG@SBA-15, 24h, isolated yield: 91.8%



- (1) Catalyst: Cu(I)NP-PEG, 48h, isolated yield: 88%;
 (2) Catalyst: Cu(I)NP-PEG@SBA-15, 24h, isolated yield: 92.7%

Conclusion

In conclusion, the synthesis and purification of new PEG- stabilized homogeneous and heterogeneous nano-catalysts CuNP-PEG for “CuAAC” reactions has been achieved. The purified aqueous catalyst Cu(0)NP-PEG performs better than the crude catalyst Cu(0)NP-PEG-1 dissolved in water before the salting-out process, because these steps help purifying the side-products on the CuNP surface and expose more catalytically active sites for “click” substrates. Aerobic oxidation of Cu(0)NP-PEG to Cu(I)NP-PEG further largely improves the catalytic activity, indicating that Cu₂O NPs are the real “CuAAC” catalyst. This shows that among CuNPs and Cu-oxide NPs, the highest activity is by far exhibited by Cu₂O NPs,

resulting from the rapid aerobic oxidation of Cu(0)NPs. Both Cu(0) NPs and Cu₂O NPs are active, but this study highlights the superiority of the latter. The Cu(I)NP-PEG catalyst was heterogenized on SBA-15 for efficient recycling and was successfully applied in “CuAAC” reactions between various azides and alkynes, including functionalization of compounds of biomedical interest. These principles of biometal nanocatalyst design could be extended to various other catalysts in the near future.

Experimental Section

1. General data

All solvents and chemicals were used as purchased, unless otherwise noted.

- UV-vis. absorption spectra were measured with a Perkin-Elmer Lambda 19 UV-vis. spectrometer.

- NMR spectra were recorded at 25 °C with a Bruker AC 400, or 300 (400 or 300 MHz). All the chemical shifts are reported in parts per million (δ , ppm) with reference to Me₄Si for the ¹H NMR spectra.

- Transmission Electron Microscopy (TEM) images and High-resolution TEM (HRTEM) images were recorded with the JEOL JEM-2100F.

- X-ray photoelectron spectra (XPS):

System: SPECS SAGE HR, X-Ray source: Mg K α non-monochromatic, operated at 12.5 kV and 250 W. Take off angle 90°, at $\sim 10^{-8}$ Torr. Pass energy for survey spectra 30 eV, 15 eV for narrow scans. Analysis: spectra are calibrated to CC carbon 285 eV. Analysis consisted of Shirley background subtraction. Peaks are fitted with symmetrical Gaussian-Lorentzian (GL) line shapes. Sample is dispersed on silica substrate and evaporated prior to measurement.

- Flash column chromatography was performed using silica gel (300-400 mesh).

- Elemental analyses were recorded on a PAR 273 potentiostat under nitrogen atmosphere.

2. Details of the synthesis

Tetrahydrofuran (THF), acetonitrile (CH₃CN) and dichloromethane (CH₂Cl₂) were refluxed and freshly distilled, Milli-Q water was degassed by N₂ for 10 min to remove O₂ before use.

2.1 Sodium naphthalenide

Sodium naphthalenide was synthesized according to previous report.^{15a} Sodium metal (1.1 equiv) was dissolved in a solution of naphthalene (100 mg, 0.78 mmol) in THF (20 mL), the mixture was stirred for 12 h under N₂ atmosphere in a standard Schlenk flask, providing sodium-naphthalenide with green colour.

2.2 Cu(0)NP-PEG, Cu(0)NP-PEG-1 and Cu(I)NP-PEG nanoparticles.

CuSO₄·5H₂O (2 mg, 8×10^{-3} mmol) were dissolved in 20 mL CH₃CN under nitrogen in

a standard Schlenk flask and stirred for 3h at 80°C. The mixture was cooled down to room temperature, and PEG-2000 (43 mg, 2.15×10^{-2} mmol) was added. Thereafter, the fresh sodium-naphthalenide solution was injected in excess into the Schlenk flask, the color of the solution changed from colorless to grey. Crude Cu nanoparticles were dried under vacuum, then extracted using CH_2Cl_2 and degassed H_2O under N_2 . The aqueous phase was removed, and the CH_2Cl_2 phase was dried under vacuum. Extraction using degassed H_2O was continued, and CH_2Cl_2 was added under N_2 . This operation was repeated 3 times. Then pure aqueous Cu nanoparticles are acquired (denoted as Cu(0)NP-PEG). Crude Cu nanoparticles without purification were dissolved in degassed water (equal volume ratio) to destroy the excess of sodium-naphthalenide). The resulting CuNPs are denoted Cu(0)NP-PEG-1 and the fresh Cu(0)NP-PEG exposed to air 30 min are denoted Cu(I)NP-PEG.

2.3 Preparation of the supported catalyst Cu(I)NP-PEG@SBA-15

The Cu(I)NP-PEG and SBA-15 (pore size 8 nm) with mol ratio 1:300 were dispersed in degassed H_2O and ultra-sonic processed for 1 h, and stirring was conducted for 3 h. The system was kept overnight without stirring under N_2 . Thereafter, the CuNPs were centrifugated with washing by deionized water 3 times and dried at 50°C. The ICP content is 0.06 wt%.

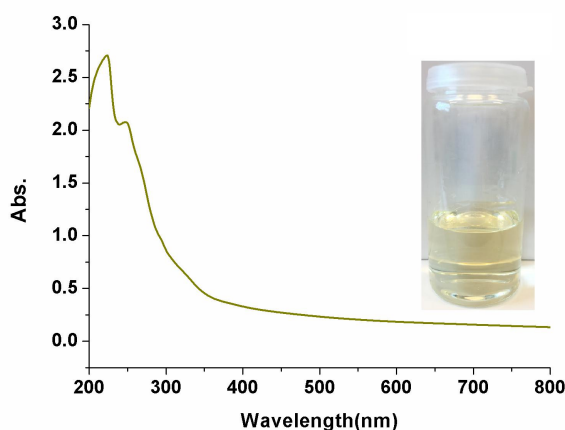


Figure 3. UV-vis. spectrum of pure Cu(0)NP-PEG nanoparticles.

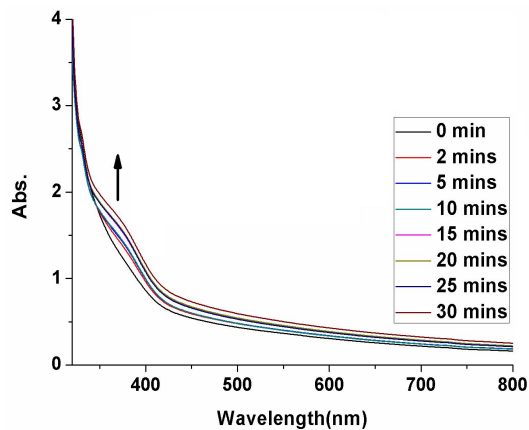


Figure 4. UV-vis. spectrum of the conversion from Cu(0)NP-PEG to Cu(I)NP-PEG in air.

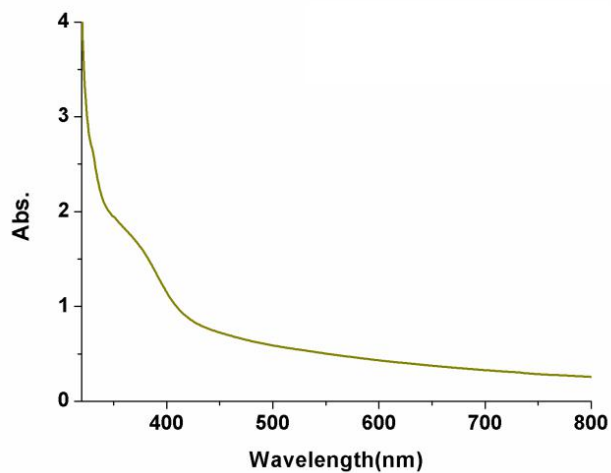


Figure 5. UV-vis. spectrum of Cu(0)NP-PEG exposed in air for 1 day leading to Cu(I)NP-PEG.

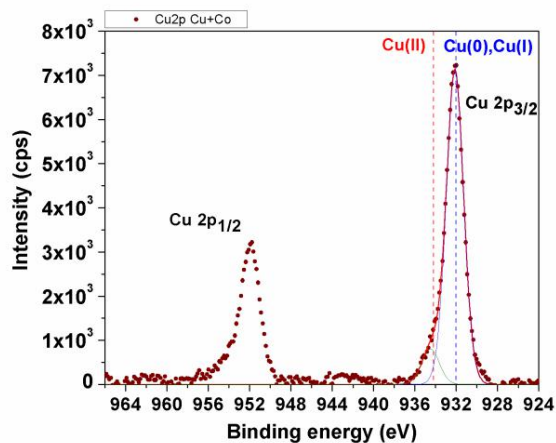


Figure 6. X-ray photoelectron spectroscopy of Cu(I)NP-PEG.

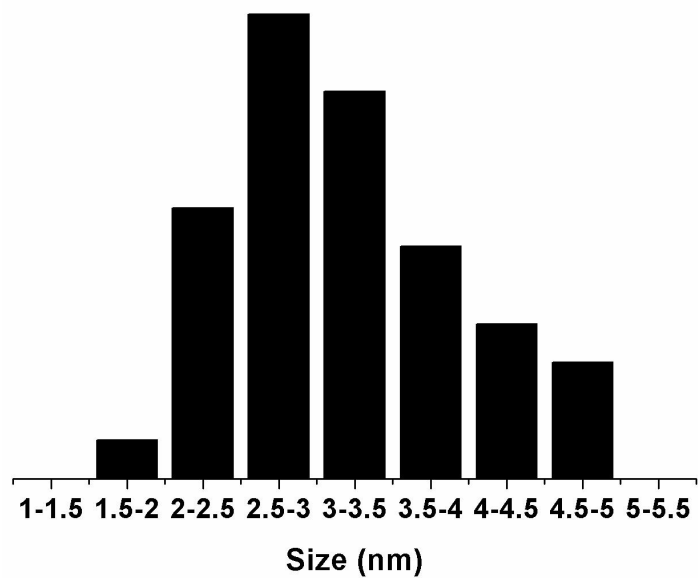


Figure 7. Histogram of Cu(I)NP-PEG nanoparticles.

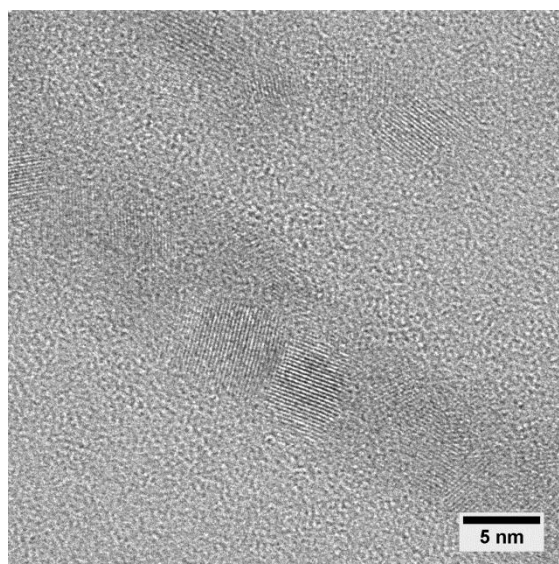


Figure 8. HRTEM of the Cu(I)NP-PEG catalyst.

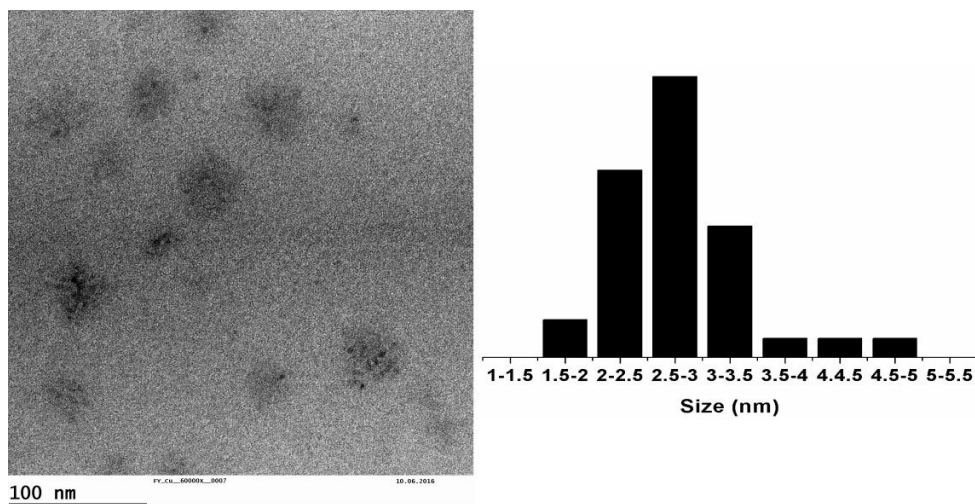


Figure 9. TEM image (left) and histogram (right) of Cu(I)NP-PEG-1 nanoparticles (without purification).

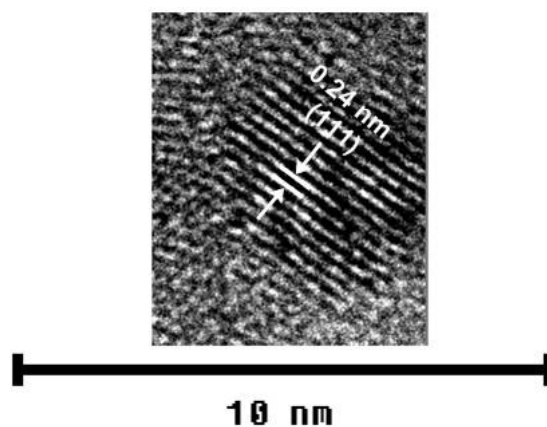


Figure 10. HRTEM of Cu(I)NP-PEG nanoparticle (4 nm)

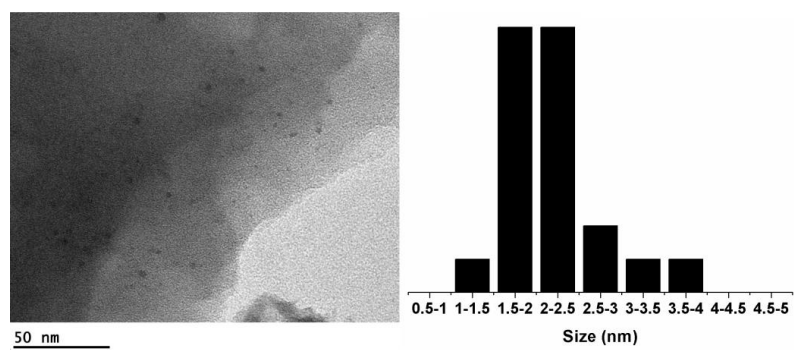
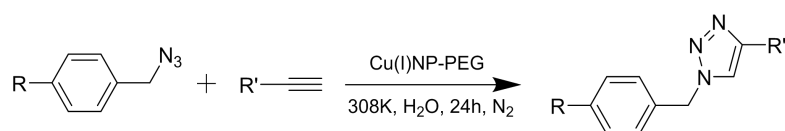


Figure 11. TEM image (left) and histogram (right) of the catalyst Cu(I)NP-PEG@SBA-15.

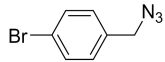
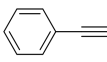
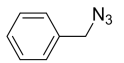
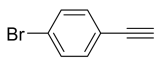
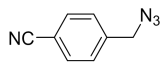
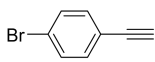
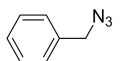
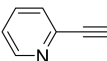
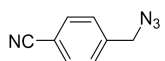
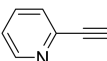
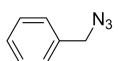
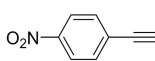
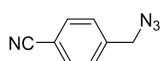
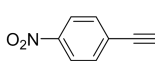
3. General procedure for the azide-alkyne cycloaddition reaction catalyzed by Cu(I)NP-PEG.

A glass vessel equipped with a magnetic stir bar was charged with 0.5 mmol of benzyl azide and 0.505 mmol of phenylacetylene under N₂. The catalyst was added into the vessel under N₂, and deionized water was added in order to obtain a given volume of aqueous solution (2 mL). The reaction mixture was then stirred for 24 h at 35 °C under N₂. After the reaction, the final product was extracted from water with CH₂Cl₂ (3 x 15 mL). The organic layer was dried over Na₂SO₄ and filtered, and the solvent was removed under vacuum to give the 1-benzyl-4-phenyl-1H-[1,2,3] triazole. The purity of the crude product was checked by ¹H NMR to calculate the conversion. In parallel, the reaction was checked using TLC. The product was then purified by silica chromatography when necessary.

Table 2. Substrates for the CuAAC reactions between various azides and alkynes using the catalyst Cu(I)NP-PEG.^a



Entry	Amount (ppm) ^b	Azide	Alkyne	Yield(%) ^c
1	100 (in air)			95 (80)
2	200			92
3	200			93
4	200			82
5	200			90
6	200			85
7	200			95
8	200			75
9	200			86

10	200			92
11	200			81
12	200			90
13	200			84
14	200			95
15	200			87
16	200			93

^a Reaction conditions: 0.5 mmol of azide, 0.505 mmol of alkyne, 2 mL H₂O, 35°C, 24 h, under N₂. ^b Amount of catalyst used in the catalyzed CuAAC reduction. ^c Isolated yield.

4. Procedure for the “click” functionalization of biomedical compounds

Taking the synthesis of (1-benzyl-1H-[1,2,3]triazol-4-yl)- cyclohexylmethanol (compound 2) as the example:

A glass vessel equipped with a magnetic stirring bar was charged with 1-ethynylcyclohexanol (0.505 mmol,) and 0.5 mmol of benzyl azide under N₂ atmosphere. The Cu(I)NP-PEG@SBA-15 catalyst (1000 ppm) was added into the vessel under N₂, and deionized water and *tert*-butanol (1:1) were added in order to obtain 2 mL as the total volume. The reaction mixture was stirred during 24 h at 35 °C, the white solid formed. After the reaction, *tert*-butanol was removed under vacuum and the final product was extracted from water with CH₂Cl₂ (3 x 15 mL). The organic layer was dried over Na₂SO₄ and filtrated, the solvent was removed in vacuo and washed twice with Et₂O to yield the pure product.

5. Recycling of the Cu(I)NP-PEG@SBA-15 catalyst

The catalyst Cu(I)NP-PEG@SBA-15 was well dispersed in water and insoluble in CH₂Cl₂. After the CuAAC reaction, extraction of the “click” products by water and CH₂Cl₂ was conducted several times, then the aqueous solution was centrifugated with washing by deionized water 3 times, and the white solid was directly used for the next catalytic run.

Table 3. Recycling results of CuAAC reactions between benzyl azide and phenylacetylene using 300 ppm of Cu(I)NP-PEG@SBA-15 (ICP content: 0.06 wt%).

Catalytic runs	1 st	2 nd	3 rd	4 th	5 th
Yield (%)	97	95	90	92	89

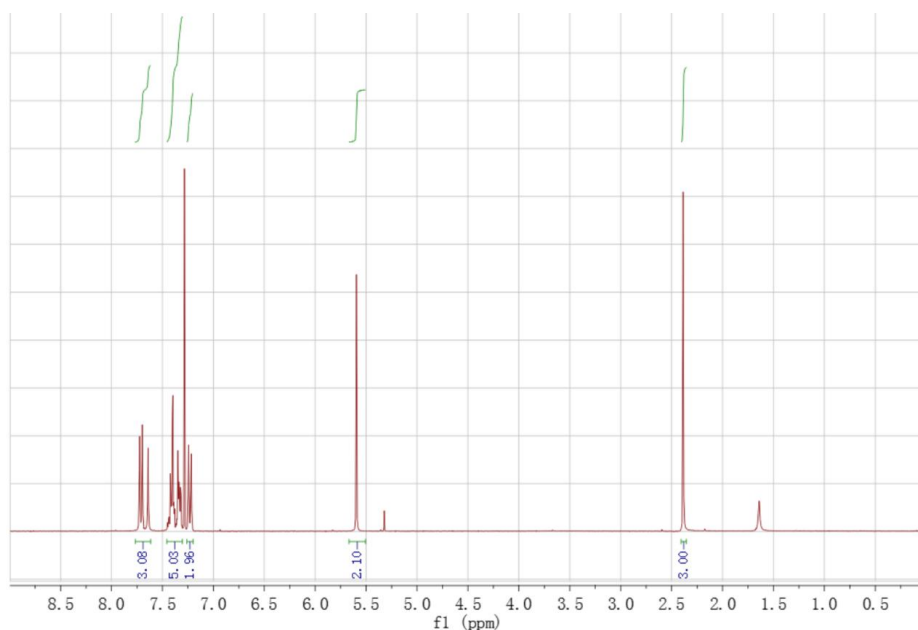


Figure 14. ^1H NMR spectrum of 1-benzyl-4-(p-tolyl)-1H-1,2,3-triazole.²⁹
 ^1H NMR (300 MHz, CDCl_3) δ 7.76 – 7.62 (m, 3H), 7.46 – 7.30 (m, 5H), 7.23 (d, J = 7.9 Hz, 2H), 5.60 (s, 2H), 2.39 (s, 3H).

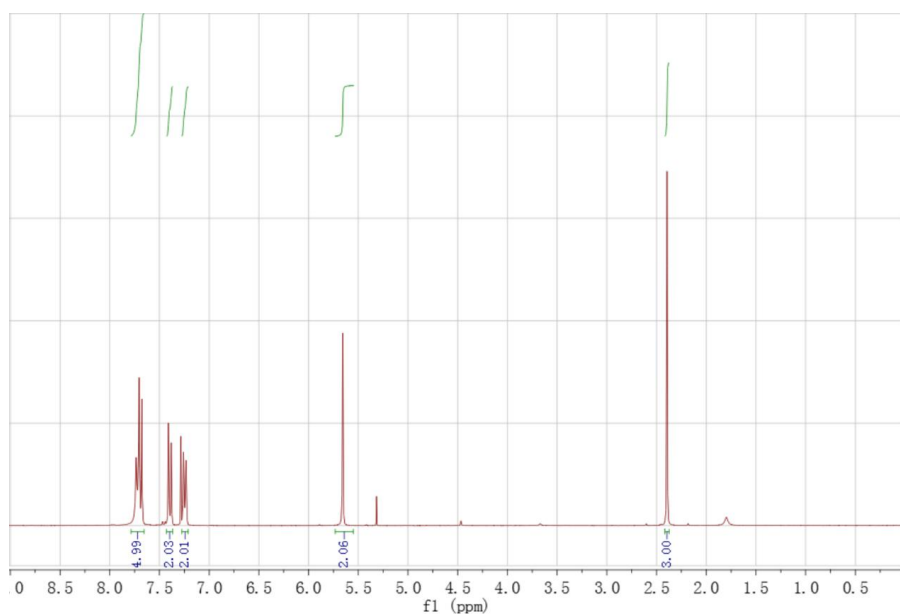


Figure 15. ^1H NMR spectrum of 4-((4-(p-tolyl)-1H-1,2,3-triazol-1-yl) methyl) benzonitrile.³⁰
 ^1H NMR (300 MHz, CDCl_3) δ 7.70 (dd, J = 12.0, 5.4 Hz, 5H), 7.40 (d, J = 8.4 Hz, 2H), 7.25 (d, J = 7.7 Hz, 2H), 5.66 (s, 2H), 2.39 (s, 3H).

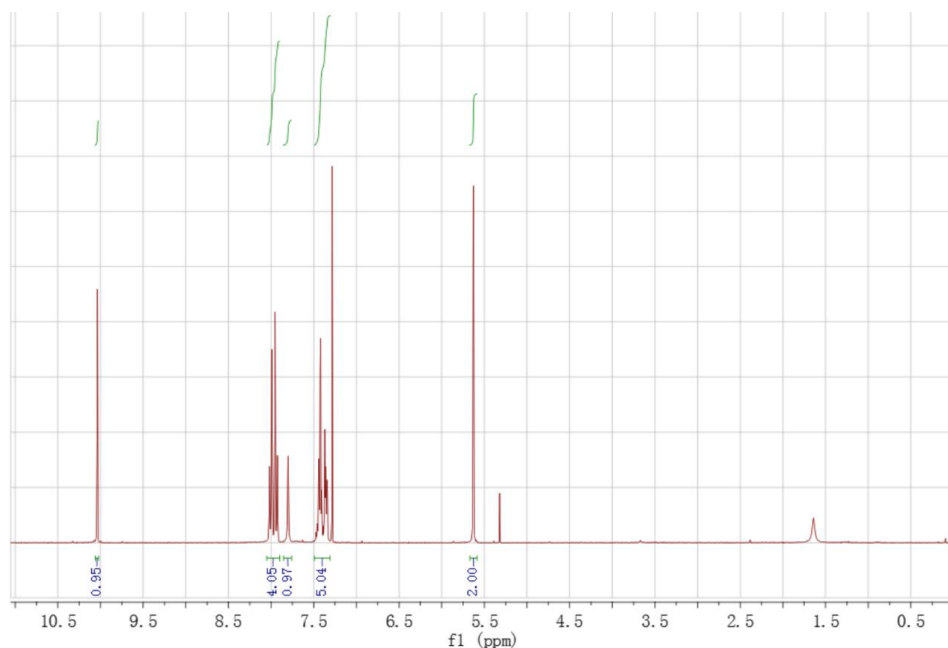


Figure 16. ^1H NMR spectrum of 4-(1-benzyl-1H-1,2,3-triazol-4-yl) benzaldehyde.²⁸
 ^1H NMR (300 MHz, CDCl_3) δ 10.04 (s, 1H), 7.97 (q, $J = 8.4$ Hz, 4H), 7.80 (s, 1H), 7.49 – 7.31 (m, 5H), 5.63 (s, 2H).

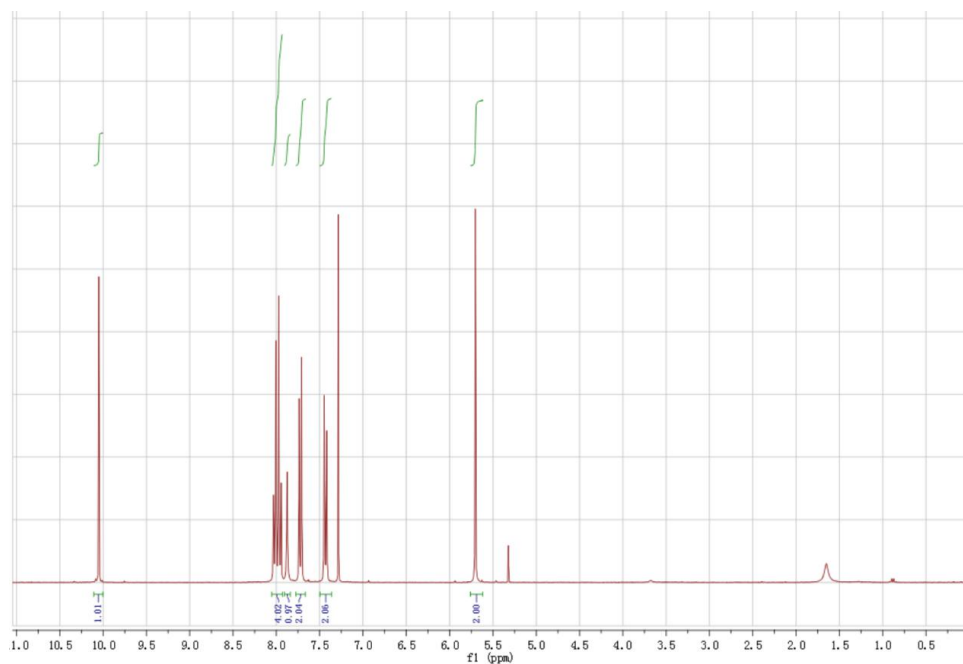


Figure 17. ^1H NMR spectrum of 4-((4-(4-formylphenyl)-1H-1,2,3-triazol-1-yl) methyl) benzonitrile.
 ^1H NMR (300 MHz, CDCl_3) δ 10.05 (s, 1H), 7.99 (q, $J = 8.4$ Hz, 4H), 7.88 (s, 1H), 7.78 – 7.66 (m, 2H), 7.43 (d, $J = 8.5$ Hz, 2H), 5.70 (s, 2H).

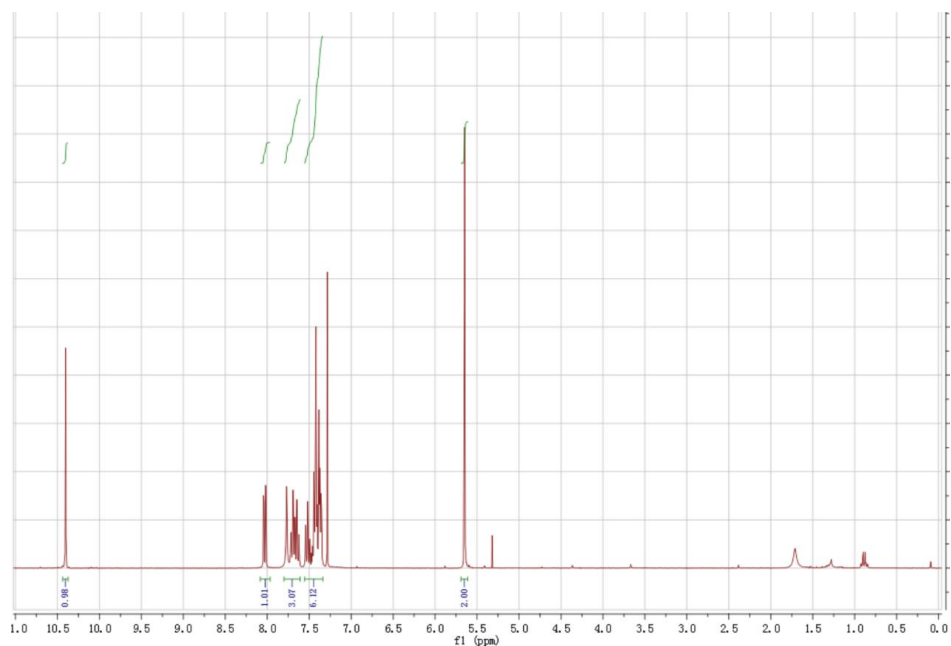


Figure 18. ^1H NMR spectrum of 2-(1-benzyl-1H-1,2,3-triazol-4-yl) benzaldehyde.³¹
 ^1H NMR (300 MHz, CDCl_3) δ 10.40 (d, $J = 0.6$ Hz, 1H), 8.03 (dd, $J = 7.7, 1.3$ Hz, 1H), 7.80 – 7.61 (m, 3H), 7.56 – 7.34 (m, 6H), 5.65 (s, 2H).

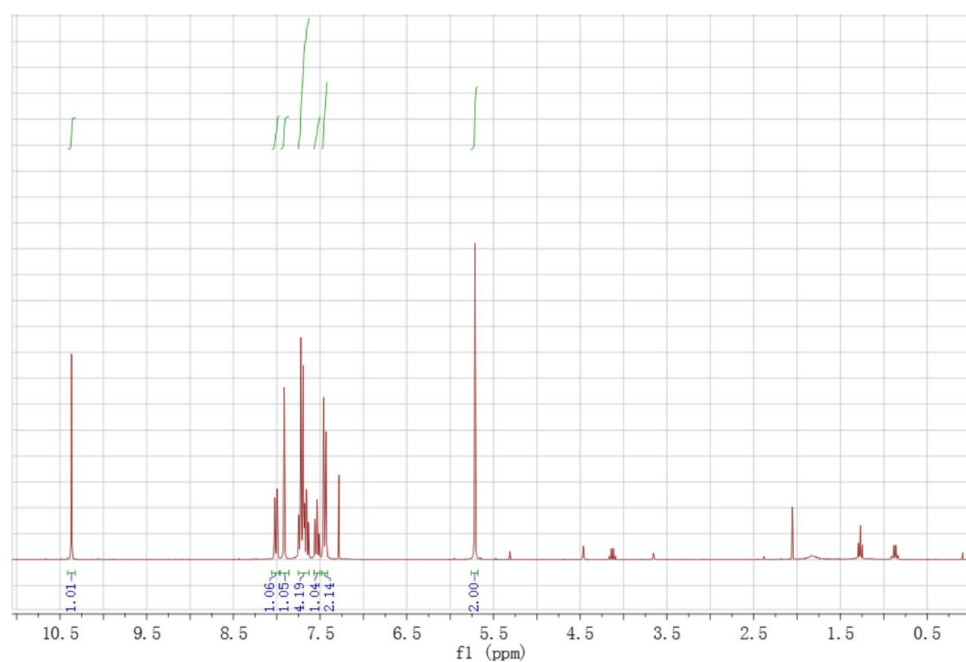


Figure 19. ^1H NMR spectrum of 4-((4-(2-formylphenyl)-1H-1,2,3-triazol-1-yl) methyl) benzonitrile.
 ^1H NMR (300 MHz, CDCl_3) δ 10.37 (d, $J = 0.5$ Hz, 1H), 8.00 (dt, $J = 7.7, 3.8$ Hz, 1H), 7.91 (s, 1H), 7.75 – 7.63 (m, 4H), 7.57 – 7.50 (m, 1H), 7.45 (d, $J = 8.5$ Hz, 2H), 5.71 (s, 2H).

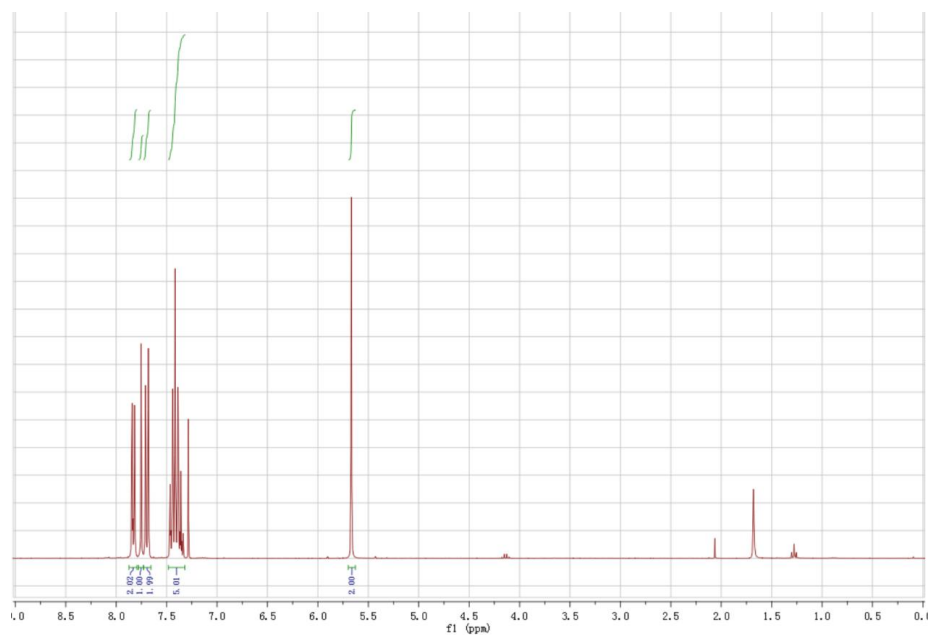


Figure 20. ^1H NMR spectrum of 4-((4-phenyl-1H-1,2,3-triazol-1-yl) methyl) benzonitrile.²⁸

^1H NMR (300 MHz, CDCl_3) δ 7.87 – 7.79 (m, 2H), 7.75 (s, 1H), 7.73 – 7.66 (m, 2H), 7.48 – 7.32 (m, 5H), 5.67 (s, 2H).

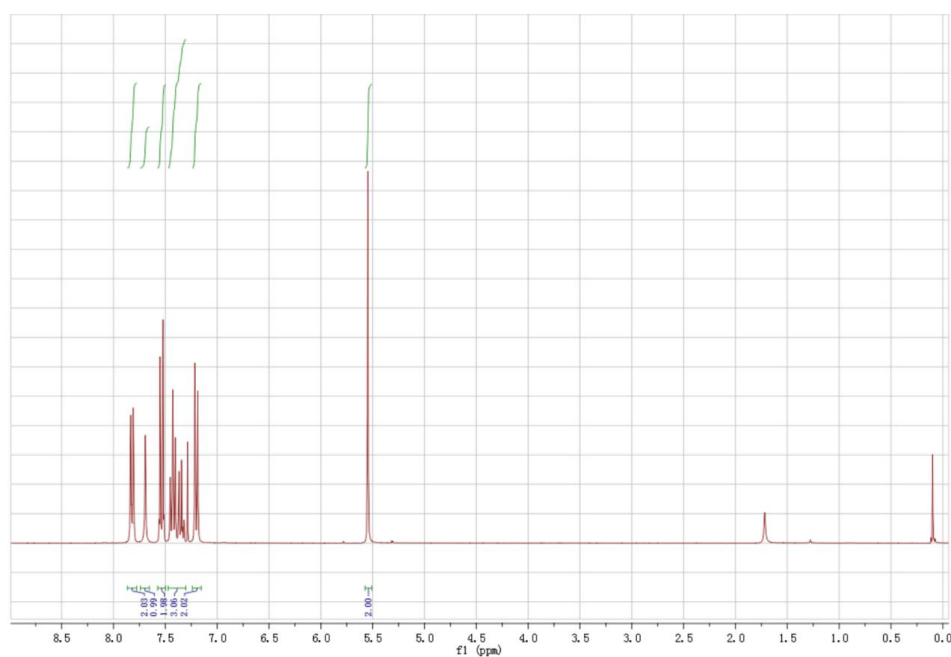


Figure 21. ^1H NMR spectrum of 1-(4-bromobenzyl)-4-phenyl-1H-1,2,3-triazole.²⁸

^1H NMR (300 MHz, CDCl_3) δ 7.86 – 7.77 (m, 2H), 7.69 (s, 1H), 7.57 – 7.50 (m, 2H), 7.47 – 7.30 (m, 3H), 7.24 – 7.15 (m, 2H), 5.55 (s, 2H).

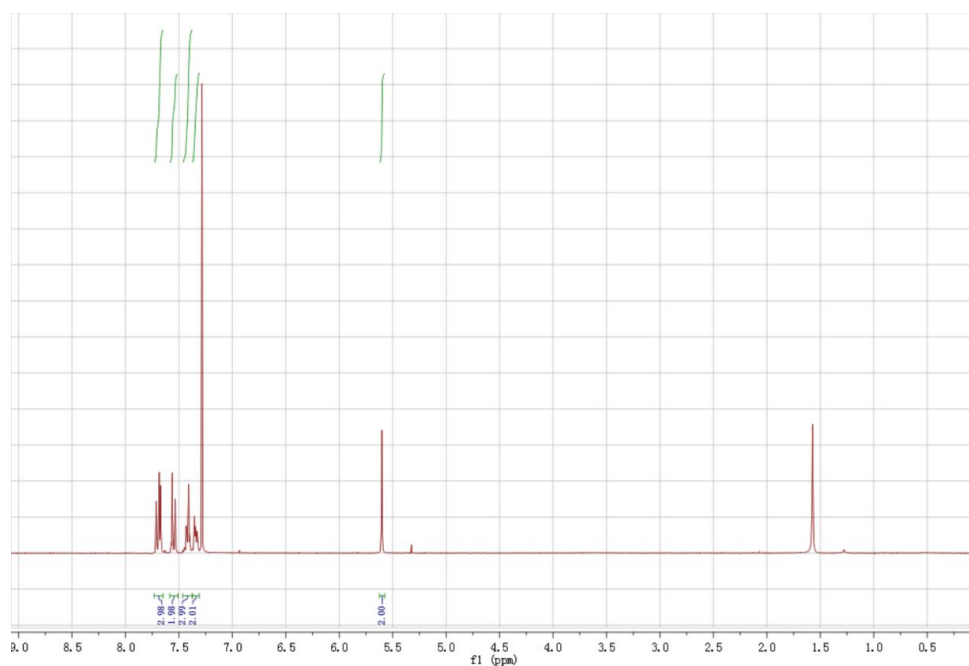


Figure 22. ^1H NMR spectrum of 1-benzyl-4-(4-bromophenyl)-1H-1,2,3-triazole.²⁹
 ^1H NMR (300 MHz, CDCl_3) δ 7.70 (dt, $J = 10.4, 3.0$ Hz, 3H), 7.58 – 7.51 (m, 2H), 7.46 – 7.38 (m, 3H), 7.37 – 7.31 (m, 2H), 5.60 (s, 2H).

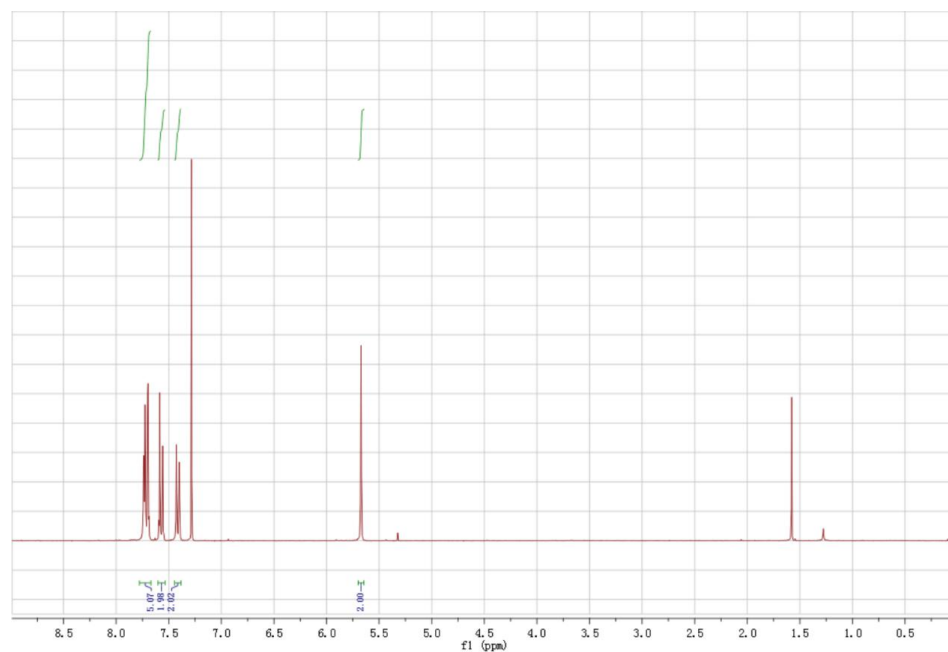


Figure 23. ^1H NMR spectrum of 4-((4-(4-bromophenyl)-1H-1,2,3-triazol-1-yl)methyl) benzonitrile.
 ^1H NMR (300 MHz, CDCl_3) δ 7.78 – 7.67 (m, 5H), 7.60 – 7.53 (m, 2H), 7.41 (d, $J = 8.6$ Hz, 2H), 5.67 (s, 2H).

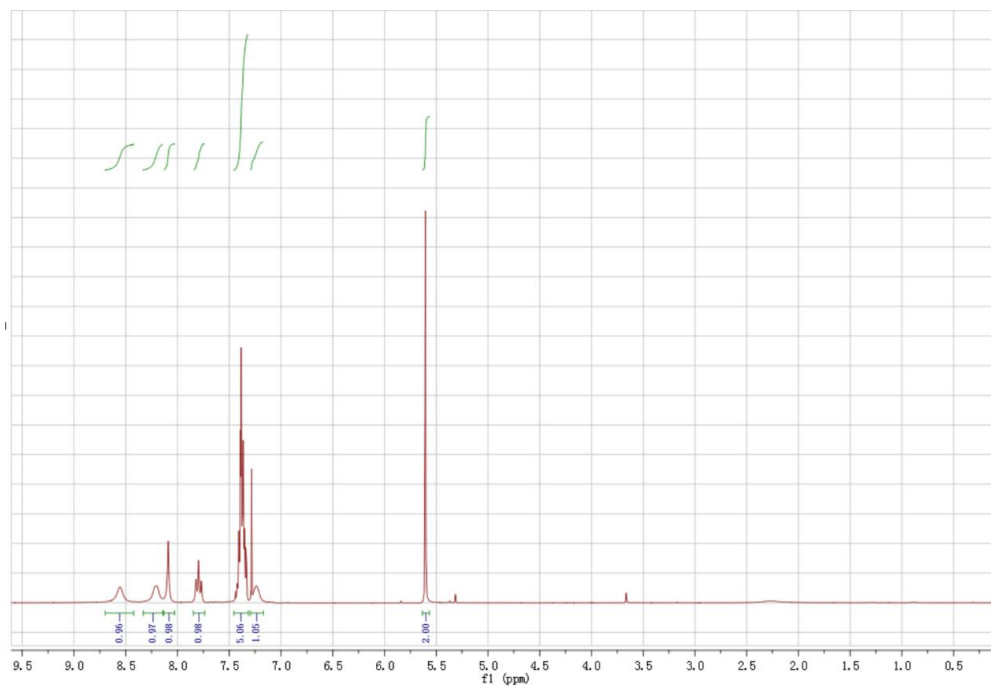


Figure 24. ^1H NMR spectrum of 2-(1-benzyl-1H-1,2,3-triazol-4-yl) pyridine.²⁸
 ^1H NMR (300 MHz, CDCl_3) δ 8.56 (s, 1H), 8.20 (s, 1H), 8.09 (s, 1H), 7.80 (t, $J = 7.7$ Hz, 1H), 7.46 – 7.31 (m, 5H), 7.26 (d, $J = 13.1$ Hz, 1H), 5.60 (s, 2H).

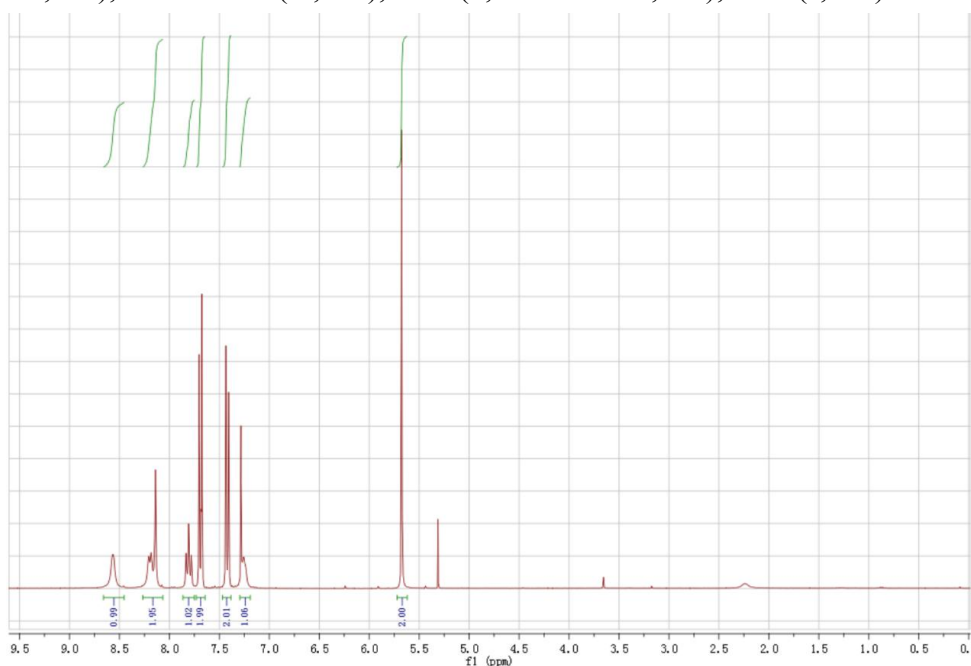


Figure 25. ^1H NMR spectrum of 4-((4-(pyridin-2-yl)-1H-1,2,3-triazol-1-yl) methyl) benzonitrile.³²
 ^1H NMR (300 MHz, CDCl_3) δ 8.51 (d, $J = 32.5$ Hz, 1H), 8.27 – 8.06 (m, 2H), 7.81 (t, $J = 7.7$ Hz, 1H), 7.73 – 7.64 (m, 2H), 7.42 (d, $J = 8.5$ Hz, 2H), 7.27 (d, $J = 7.7$ Hz, 1H), 5.68 (s, 2H).

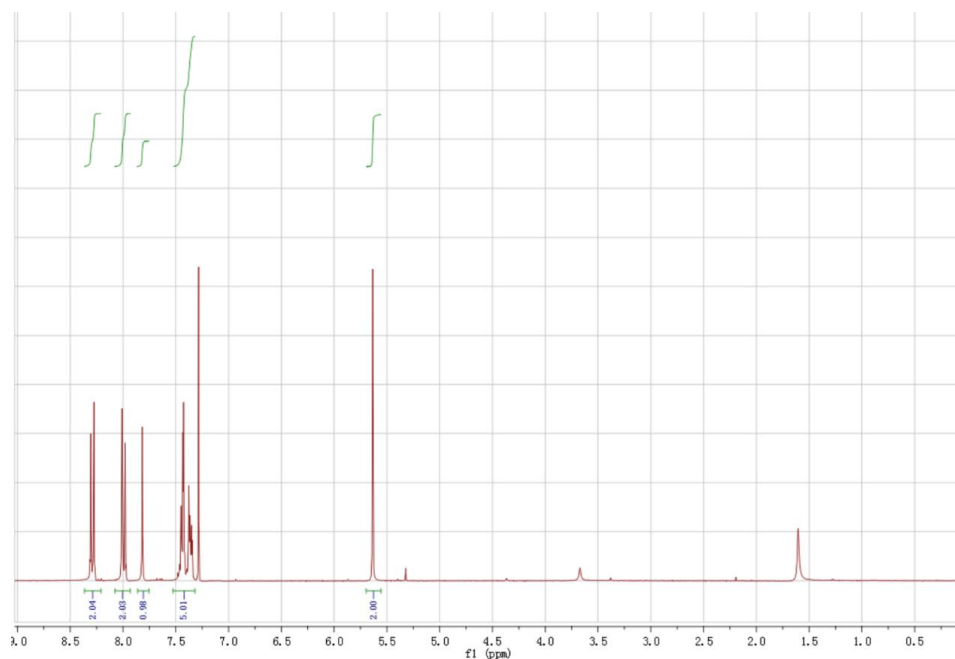


Figure 26. ^1H NMR spectrum of 1-benzyl-4-(4-nitrophenyl)-1H-1,2,3- triazole.³³
 ^1H NMR (300 MHz, CDCl_3) δ 8.37 – 8.21 (m, 2H), 8.08 – 7.93 (m, 2H), 7.82 (s, 1H), 7.52 – 7.32 (m, 5H), 5.63 (s, 2H).

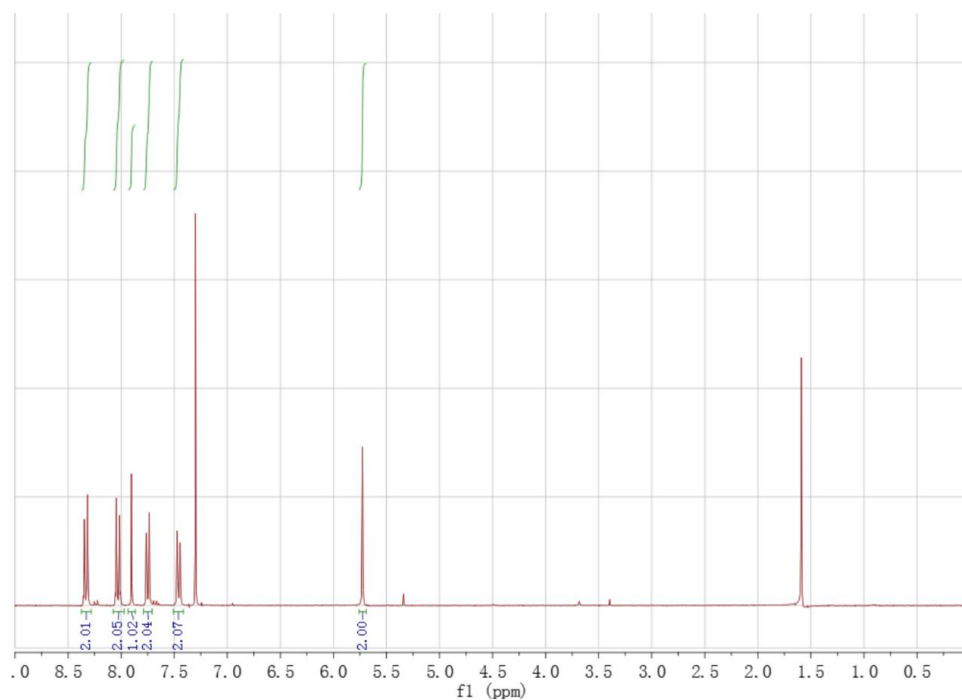


Figure 27. ^1H NMR spectrum of 4-((4-(4-nitrophenyl)-1H-1,2,3- triazol-1-yl) methyl) benzonitrile.³³
 ^1H NMR (300 MHz, CDCl_3) δ 8.37 – 8.28 (m, 2H), 8.07 – 7.97 (m, 2H), 7.90 (s, 1H), 7.79 – 7.71 (m, 2H), 7.46 (d, $J = 8.5$ Hz, 2H), 5.73 (s, 2H).

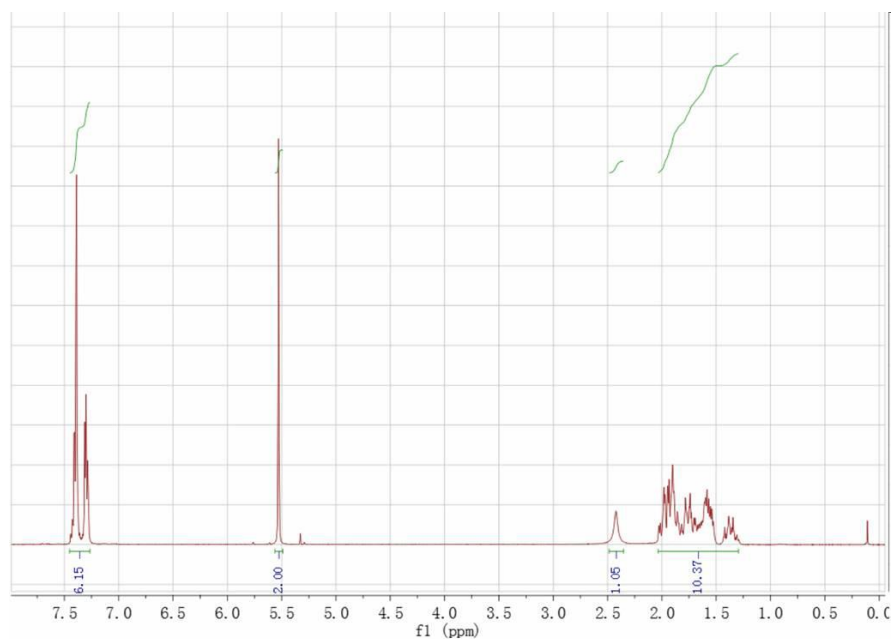


Figure 28. ^1H NMR spectrum of (1-benzyl-1H-[1,2,3]triazol-4-yl)-cyclohexylmethanol.²⁸

^1H NMR (300 MHz, CDCl_3) δ 7.45 – 7.26 (m, 6H), 5.53 (s, 2H), 2.42 (s, 1H), 2.03 – 1.30 (m, 10H).

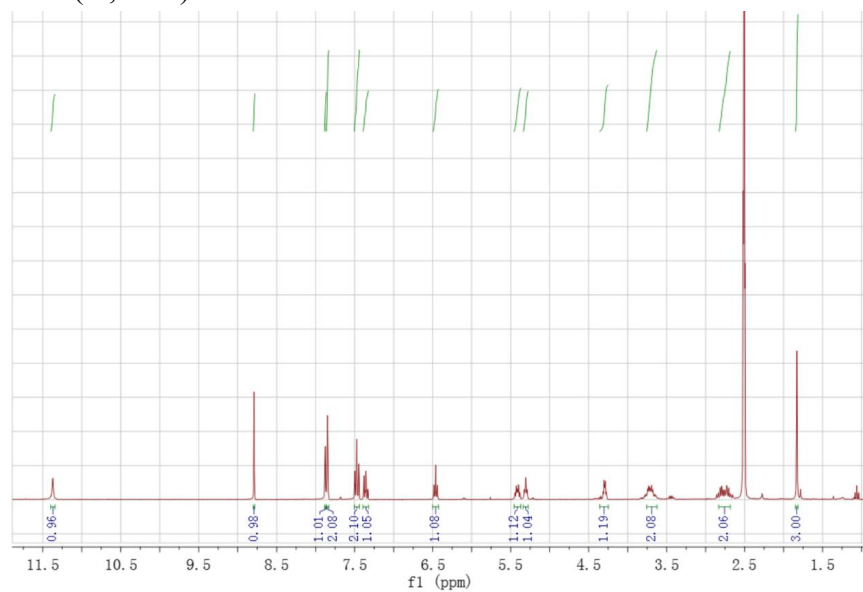


Figure 29. ^1H NMR spectrum of compound 4.³⁴

^1H NMR (300 MHz, DMSO) δ 11.37 (s, 1H), 8.79 (s, 1H), 7.86 (dt, $J = 7.4, 1.3$ Hz, 3H), 7.54 – 7.42 (m, 2H), 7.42 – 7.29 (m, 1H), 6.46 (t, $J = 6.6$ Hz, 1H), 5.41 (dt, $J = 8.7, 5.6$ Hz, 1H), 5.35 – 5.19 (m, 1H), 4.29 (dd, $J = 9.0, 3.5$ Hz, 1H), 3.79 – 3.61 (m, 2H), 2.75 (tdd, $J = 14.1, 11.3, 6.7$ Hz, 2H), 1.83 (d, $J = 1.1$ Hz, 3H).

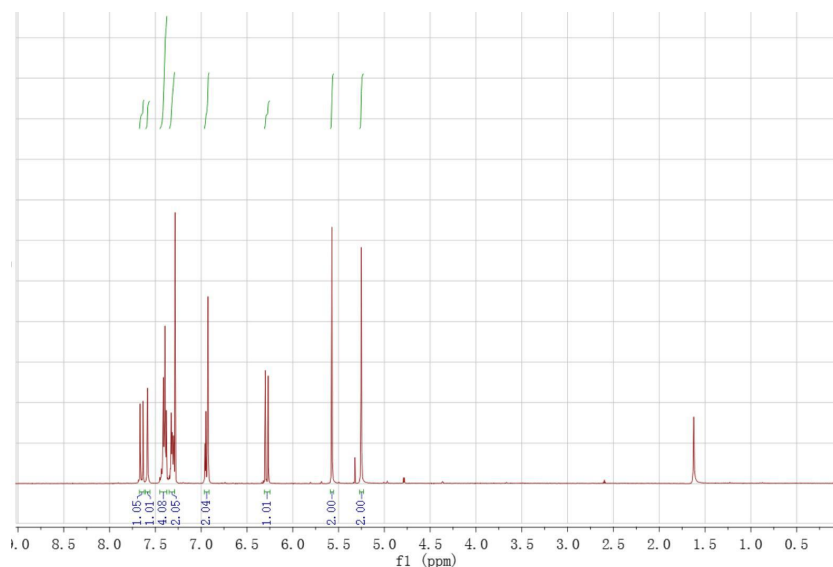


Figure 30. ^1H NMR spectrum of compound **6**.²⁸

^1H NMR (300 MHz, CDCl_3) δ 7.67 – 7.62 (m, 1H), 7.58 (s, 1H), 7.41 (dtd, $J = 6.5$, 4.7, 1.9 Hz, 4H), 7.35 – 7.29 (m, 2H), 6.94 (dd, $J = 7.5$, 2.1 Hz, 2H), 6.31 – 6.25 (m, 1H), 5.57 (s, 2H), 5.25 (s, 2H).

References

- 1 H. C. Kolb, M. G. Finn and K. B. Sharpless, *Angew. Chem. Int. Ed.*, **2001**, 40, 2004.
- 2 (a) M. Meldal and C. W. Tornøe, *Chem. Rev.*, **2008**, 108, 2952; (b) J. E. Hein and V. V. Fokin, *Chem. Soc. Rev.*, **2010**, 39, 1302; (c) A. Mandoli, *Molecules*, **2016**, 21, 1174; (d) C. Wang, D. Ikhlef, S. Kahlal, J.Y. Saillard and D. Astruc, *Coord. Chem. Rev.*, **2016**, 316, 1.
- 3 (a) H. C. Kolb and K. B. Sharpless, *Drug Disc. Today*, **2003**, 8, 1128; (b) F. Amblard, J. H. Cho and R. F. Schinazi, *Chem. Rev.*, **2009**, 109, 4207; (c) W. Tang and M. L. Becker, *Chem. Sc. Rev.*, **2014**, 43, 7013; (d) V. K. Tiwari, K. B. Mishra, N. Misra, A. S. Singh and X. Chen, *Chem. Rev.*, **2016**, 116, 3086.
- 4 (a) W. H. Binder and R. Sachsenhofer, *Macromol. Rapid Commun.*, **2007**, 28, 15; (b) D. Fournier, R. Hoogenboom and U. S. Schubert, *Chem. Soc. Rev.*, **2007**, 36, 1369; (c) M. Meldal, *Macromol. Rapid Commun.*, **2008**, 29, 1016; (d) P. L. Golas and K. Matyjaszewski, *Chem. Soc. Rev.*, **2010**, 39, 1338; (e) K. Kempe, A. Krieg and C. M. Berce, *Chem. Soc. Rev.*, **2012**, 41, 176; (f) G. Delaittre, N. K. Guimard and C. Barner-Kowollik, *Acc. Chem. Res.*, **2015**, 48, 1296.
- 5 (a) A. H. El-Sagheer and T. Brown, *Chem. Soc. Rev.*, **2010**, 39, 1388; (b) P. Thimurugan, D. Matosiuk and K. Jozwiak, *Chem. Rev.*, **2013**, 113, 4905; (c) S. Svenson, *Chem. Soc. Rev.*, **2015**, 44, 5131; (d) X. Wang, B. Huang and X. Liu, *Drug. Discov. Today*, **2016**, 21, 118.

- 6 (a) J. F. Lutz, *Angew. Chem. Int. Ed.*, **2007**, 46, 1018; (b) V. Castro, H. Rodrigue and F. Abeico, *ACS Combin. Sci.*, **2016**, 18, 1.
- 7 V. V. Rostovtsev, L. G. Geen, V. V. Fokin and K. B. Sharpless, *Angew. Chem. Int. Ed.*, **2002**, 41, 2596.
- 8 C. W. Tornøe, C. Christensen and M. Meldal, *J. Org. Chem.*, **2002**, 67, 3057.
- 9 (a) M. T. Reetz and J. G. de Vries, *Chem. Commun.*, **2004**, 1559; (b) D. Astruc, F. Lu and J. Ruiz, *Angew. Chem. Int. Ed.*, **2005**, 44, 7852; (c) V. Polshettiwar and R. S. Varma, *Green Chemistry*, **2010**, 12, 743; (d) V. S. Meyers, M. G. Weier, E. V. Carino, D. F. Yancey, S. Pande and R. M. Crooks, *Chem. Sci.*, **2011**, 2, 1632; (e) A. Balanta, C. Godard and C. Claver, *Chem. Soc. Rev.*, **2011**, 40, 4973; (f) A. Corma, A. Leyva-Perez and M. Sabater, *J. Chem. Rev.*, **2011**, 111, 1657; (g) L. M. Bronstein and Z. B. Shifrina, *Chem. Rev.* **2011**, 111, 5301; (h) E. Gross, J. H. C. Liu, F. D. Toste and G. A. Somorjai, *Nat. Chem.*, **2012**, 4, 947; (i) M. Sankar, N. Dimitratos, P. J. Miedziak, P. P. Wells, C. J. Kiely and G. J. Hutchings, *Chem. Sci.* **2012**, 3, 20; (j) M. Haruta, *Angew. Chem. Int. Ed.*, **2014**, 53, 52; (k) C. Amiens, D. Ciuculescu-Pradines and K. Philippot, *Coord. Chem. Rev.* **2016**, 308, 409; (l) D. Wang and D. Astruc, *Chem. Soc. Rev.*, **2017**, 46, 816.
- 10 (a) F. Alonso, Y. Moglie and G. Radivoy, *Acc. Chem. Res.*, **2015**, 48, 2516; (b) M. B. Gawande, A. Goswami, F.X. Felpin, T. Asefa, X. X. Huang, R. Silva, X. X. Zou, R. Zboril and R. S. Varma, *Chem. Rev.*, **2016**, 116, 3722.
- 11 a) T. N. Jin, M. Yan and Y. Yamamoto, *Chemcatchem*, **2012**, 4, 1217; (b) T. M. Vishwanatha and V. V. Sureshbabu, *J. Heterocyclic Chem.*, **2015**, 52, 1823; (c) M. d'Halluin, T. Mabit, N. Fairley, V. Fernandez, M. B. Gawande, E. Le Grogneec and F. X. Felpin, *Carbon*, **2015**, 93, 974; (d) M. N. S. Rad, S. Behrouz, S. J. Hoseini, H. Nasrabadi and M. S. Zare, *Helv. Chim. Acta*, **2015**, 98, 1210.
- 12 (a) Z. F. Zhang, C. M. Dong, C. H. Yang, D. Hu, J. Long, L. Wang, H. Li, Y. Chen and D. L. Kong, *Adv. Syn. Catal.*, **2010**, 352, 1600; (b) K. Wang, X. H. Bi, S. X. Xing, P. Q. Liao, Z. X. Fang, X. Y. Meng, Q. A. Zhang, Q. Liu and Y. Ji, *Green Chem.*, **2011**, 13, 562; (c) A. C. Cardiel, M. C. Benson, L. M. Bishop, K. M. Louis, J. C. Yeager, Y. Z. Tan and R. J. Hamers, *ACS Nano*, **2012**, 6, 310; (d) F. Alonso, Y. Moglie, G. Radivoy and M. Yus, *Synlett*, **2012**, 15, 2179; (e) A. S. Nia, S. Rana, D. Dohler, X. Noirfalise, A. Belfiore and W. H. Binder, *Chem. Commun.*, **2014**, 50, 15374; (f) A. S. Nia, S. Rana, D. Dohler, F. Jirsa, A. Meister, L. Guadagno, E. Koslowski, M. Bron and W. H. Binder, *Chem. Eur. J.*, **2015**, 21, 10763; (g) F. Masoud, A. Mojtaba and A. Alireza Pourvahabi, *Catal. Commun.*, **2016**, 76, 72; (h) B. W. Wang, J. Durantini, J. Nie, A.E. Lanterna and J. C. Scaiano, *J. Am. Chem. Soc.*, **2016**, 138, 13127.
- 13 (a) V. H. Reddy, Y. V. R. Reddy, B. Sridhar and B. V. S. Reddy, *Adv. Syn. Catal.*,

- 2016, 358, 1088; (b) S. Jang, Y. J. Sa, S. H. Joo and K. H. Park, *Catal. Commun.*, **2016**, 81, 24.
- 14 N. G. Connelly and W. E. Geiger, *Chem. Rev.*, **1996**, 96, 877.
- 15 (a) C. Schöttle, P. Bockstaller, R. Popescu, D. Gerthsen and C. Feldmann, *Angew. Chem. Int Ed.*, **2015**, 54, 9866; (b) C. Schöttle, D. E. Doronkin, R. Popescu, D. Gerthsen, J. D. Grünwald and C. Feldmann, *Chem. Commun.*, **2016**, 52, 6316.
- 16 E. Seo, J. Kim, Y. Hong, Y. S. Kim, D. Lee and B. S. Kim, *J. Phys. Chem. C*, **2013**, 117, 11686.
- 17 H. Maeda, *Adv. Enzyme Regul.*, **2001**, 41, 187.
- 18 (a) M. Salavati-Niasari and F. Davar, *Mater. Lett.*, **2009**, 63, 441; (b) X. Liu, D. Gregurec, J. Irigoyen, A. Martinez, S. Moya, R. Ciganda, P. Hermange, J. Ruiz and D. Astruc, *Nat. Commun.*, **2016**, 7, 13152.
- 19 J. F. Moulder, W. F. Stickle, P. E. Sobol and K. D. Bomben, Handbook of X-ray Photoelectron Spectroscopy, *Physical Electronics* **1995**.
- 20 H. Langecker, H. J. Schumann and K. Junkmann, *Arch. Exptl. Pathol. Pharmacol.*, **1953**, 219, 130.
- 21 W. Nickel, G. Bialek and F. Grosse, *J. Biol. Chem.*, **1992**, 267, 848.
- 22 P. Thirumurugan, D. Matosiuk and K. Jozwiak, *Chem. Rev.*, **2013**, 113, 4905.
- 23 L. Zhou, A. Amer, M. Korn, R. Burda, J. Balzarini, E. D. Clercq, E. R. Kern and P. F. Torrence, *Antiviral Chem. Chemother*, **2005**, 16, 375.
- 24 V. R. Sirivolu, S. K. V. Vernekar, T. Ilina, N. S. Myshakina, M. A. Parniak and Z. Wang, *J. Med. Chem.*, **2013**, 56, 8765.
- 25 D. Baraniak, K. Kacprzak and L. Celewicz, *Bioorg. Med. Chem. Lett.*, **2011**, 21, 723.
- 26 P. W. Szafranski, P. Kasza, M. Kępczyński and M. T. Cegła, *Heterocycl. Commun.*, **2015**, 21, 263.
- 27 Y. Yue, F. Huo, P. Ning, Y. Zhang, J. Chao, X. Meng and C. Yin. *J. Am. Chem. Soc.*, **2017**, 139, 3181.
- 28 C. Wang, D. Wang, S. L. Yu, T. Cornilleau, J. Ruiz, L. Salmon and D. Astruc, *ACS Catal.*, **2016**, 6, 5424.
- 29 S. Jang, Y. J. Sa, S. H. Joo and K. H. Park, *Catal. Commu.*, **2016**, 81, 24.
- 30 W. L. Wang, J. L. Wu, C. G. Xia and F. W. Li, *Green Chem.*, **2011**, 13, 3440.
- 31 S. Saha, M. Kaur and J. K. Bera. *Organometallics*, **2015**, 34, 3047.
- 32 X. Liu, N. Novoa, C. Manzur, D. Carrillo and J. R. Hamon, *New J. Chem.*, **2016**, 40, 3308.
- 33 R. Jahanshahi and B. Akhlaghinia, *RSC Adv.*, **2016**, 6, 29210.
- 34 V. R. Sirivolu, S. K. V. Vernekar, T. Ilina, N. S. Myshakina, M. A. Parniak, and Z. J. Wang, *Med. Chem.*, **2013**, 56, 8765.

Chapter 2. Synthesis of late transition-metal nanoparticles by Na naphthalenide reduction of salts and catalytic efficiency.

Introduction

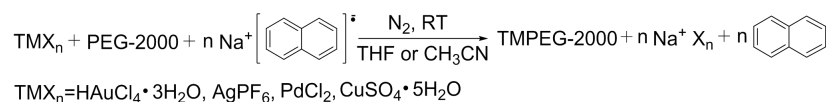
The synthesis of transition metal (TM) nanoparticles (NP) has attracted the attention of chemists for several decades viewing their applications in various areas including nanomaterials,¹⁻³ optoelectronic,^{1,4} biomedicine⁴ and catalysis.⁵⁻¹⁹ The most general synthetic route involve decomposition of low-valent metal precursor TM complexes or reduction of TM salts using various reductants such as H₂, NaBH₄, (SiMe₂)₆, Mg, Li or Na in liquid NH₃ in the presence of a stabilizer.²⁰⁻²⁸

Na naphthalenide is a well-known very strong reducing agent ($E^0([\text{NaNaph}]/\text{THF}) = -3.1 \text{ V vs. SCE}$)²⁹ that is easily prepared by reduction of naphthalene by sodium metal in THF and has been used at room temperature for the synthesis of low-valent main-group and TM NPs.³⁰⁻⁴⁰ Although this reagent has proved useful for the reduction of early TMs, no attention has been paid to the synthesis of late TMNPs, presumably because easy-to-handle reductants such as NaBH₄ are almost systematically used for the reduction of late TM salts to TMNPs.^{41,42} Ill-defined polyboron derivatives resulting from these reactions may partly inhibit catalysis by the surfaces of the TMNPs synthesized in this way, however.^{41,42} Therefore we have envisaged the synthesis of late TMNPs synthesized by reduction of late TM salts using sodium naphthalenide as a reductant in order to examine the efficiency of these late TMNPs as catalysts for several reactions. CuNPs synthesized by reduction of Cu sulfate have already been shown to be accessible using Na naphthalenide as a reductant in THF, and the catalytic activity of the CuNPs has been scrutinized for the Cu-catalyzed azide alkyne cycloaddition (CuAAC), the main “click” reaction. It was shown, however, that these CuNPs were less active than when they were oxidized in air, producing Cu₂O NPs.⁴³

In the present article, the synthesis and catalytic activities of most late TMNPs (noted TMPEG-2000 NPs) synthesized by Na naphthalenide reduction of TM salts are reported including salt-effect engineering to purify these TMPEG-2000 NPs. Therefore we have examined the synthesis of TMPEG-2000 NPs for Pd, Cu, Ag and Au NPs upon reduction of TM salts by Na naphthalenide. These TMPEG-2000 NPs have been characterized by UV-vis. spectra, Transmission Electron Microscopy (TEM), and X-ray photoelectron spectroscopy (XPS), and the catalytic activities of all these TMPEG-2000 NPs have been compared for the standard catalysis of reduction of 4-nitrophenol (4-NP) to 4-aminophenol (4-AP). Finally, the catalytic activities of the PdNPs have been investigated for the Suzuki-Miyaura (PdNPs) and Sonogashira (Cu-Pd NPs) cross carbon-carbon coupling reactions. For the stabilization of the TMPEG-2000 NPs, the biocompatible polymer poly(ethyleneglycol)⁴⁴⁻⁴⁷ has been used here rather than toxic *N,N*-dimethylformamide (DMF), cetyltrimethylammonium bromide (CTAB), thiolate, phosphines that are toxic TMNP stabilizers.⁴⁸⁻⁵⁰

Results and discussion

Synthesis, purification and characterization of the TMPEG-2000 NPs. Small TMPEG-2000 NPs are synthesized for Pd, Cu, Ag and Au by reduction of the salts of these metal cations using Na naphthalenide in THF or acetonitrile in the presence of PEG-2000 as stabilizer according to equation 1.



equation 1

At the end of the reactions, the TMPEG-2000 NPs are obtained by two successive simple extractions with CH_2Cl_2 and H_2O under N_2 . In the first extraction, the nanoparticles are in the organic phase because of the salting-out effect,^[51] allowing to remove the Na^+ , Cl^- , SO_4^{2-} or PF_6^- ions in this step. In the second extraction that is conducted with CH_2Cl_2 and H_2O again, the TMPEG-2000 NPs transfer into the aqueous phase, and naphthalene is separated in the organic phase (Figure 1). Indeed, in all further catalytic experiments, the aqueous TMPEG-2000 NPs purified in this way (noted MPEG) perform better than the TMPEG-2000 NPs dissolved in water without purification (noted MPEG-1).

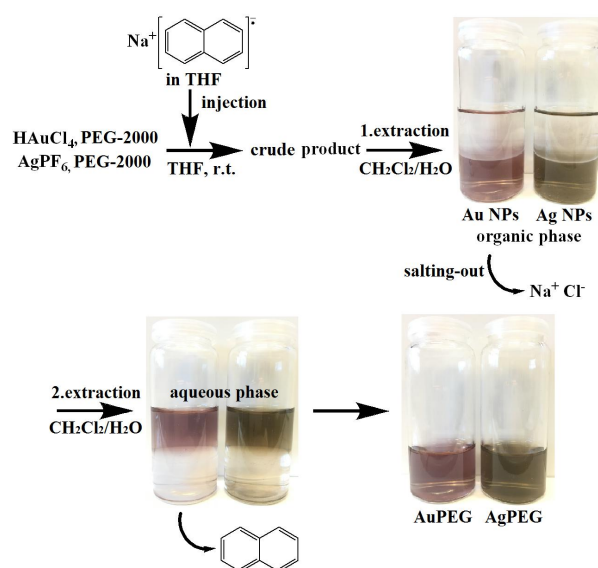


Figure 1. Synthesis and purification of AuPEG and AgPEG nanoparticles by salting-out effect.

This liquid-phase synthetic method is illustrated in Figure 1 for AuPEG and AgPEG as examples, and the synthetic details for the other TMPEG-2000 NPs are found in the Experimental Section. HAuCl₄ and AgPF₆ are reduced to Au and Ag nanoparticle by injection of Na naphthalenide, and then the color of Au is observed to change from faint yellow to brown whereas that of Ag changes from colorless to yellow brown.

Extraction is used to remove the excess of Na naphthalenide and salt. Because of the salting-out effect, AuPEG and AgPEG are dissolved in the organic phase in the first extraction. After removing the Na⁺ and Cl⁻ ions, the AuPEG and AgPEG dissolved well in the aqueous phase during the second extraction, and the color of pure AuPEG and AgPEG nanoparticles are purple and yellow green respectively. The surface plasmon bands (SPBs) of these two TMPEG-2000 NPs are shown in Figure 2 (a and b). AuPEG exhibits a SPB centered at 543 nm, and AgPEG shows a SPB centered at 415 nm. Upon comparing the SPBs of these two TMPEG-2000 NPs with the absorption bands of naphthalene (Figure 5, Experimental Section), it clearly appears that the bands of naphthalene are not found in the spectra of AuPEG and AgPEG, which means that naphthalene has been successfully wiped off. Other UV-vis. spectra of PdPEG and CuPEG were shown in Figures 6 and 7 (Experimental Section). And the XPS of the pure PdPEG shows the presence of about 40% Pd oxide in the sample (Figure 8, Experimental Section).

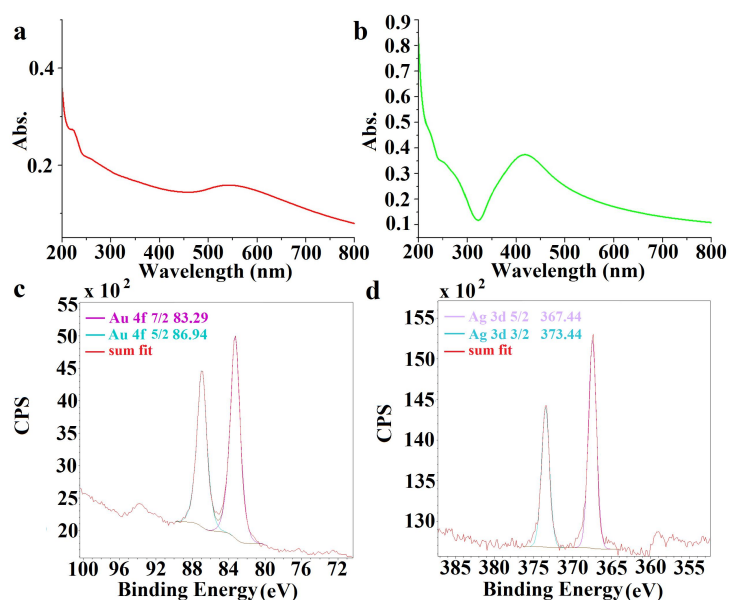


Figure 2. UV-vis. spectra of pure AuPEG (a) and pure AgPEG (b) and X-ray photoelectron spectra (XPS) of pure AuPEG (c) and pure AgPEG (d) NPs.

From the TEM of the as-prepared MPEG (Figure 3) and the size distribution (Figure 9, Experimental Section), it is noteworthy that well-dispersed and small (< 3 nm) AuPEG and PdPEG are synthesized by this method, whereas AgPEG and CuPEG are larger than 3 nm. The particles core sizes are almost unchanged before (Figure 10, Experimental Section) and after purification.

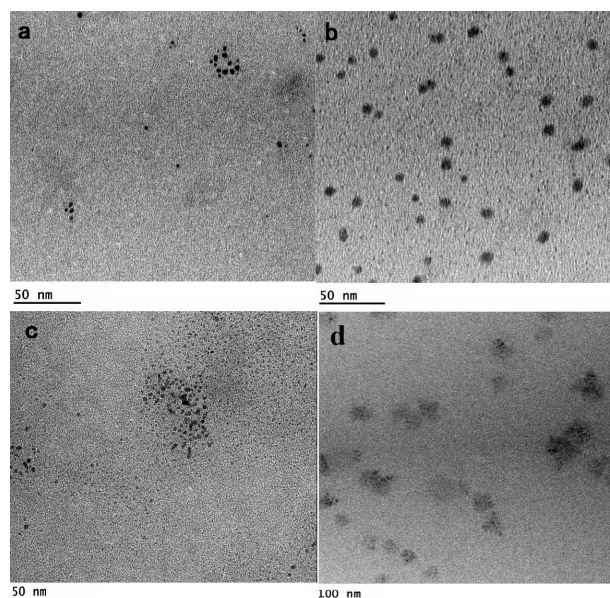
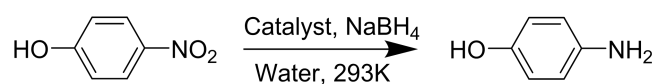


Figure 3. TEM of MPEG: a: AuPEG; b: AgPEG; c: PdPEG; d: CuPEG.

Compared catalytic test for all the TMPEG-2000 NPs using 4-nitrophenol reduction. The 4-nitrophenol (4-NP) reduction to 4-aminophenol (4-AP) with an excess amount of NaBH_4 is a model reaction allowing to evaluate the activity of the catalyst surface.⁵²⁻⁶⁶ Among the TM-catalyzed redox reactions, the reduction of nitroaromatics is among the most crucial ones.⁵⁸ Indeed, 4-NP is anthropogenic, toxic and inhibitory in nature. The reaction product, 4-aminophenol, is very useful for a wealth of applications that include analgesic and antipyretic drugs, photographic developers, corrosion inhibitors, and anticorrosion lubricants.⁵⁹⁻⁶¹ The mechanism reported by Ballauff's group involves rearrangement of the substrates 4-NP and NaBH_4 at the TMPEG-2000 NPs surface on the basis of the Langmuir–Hinshelwood (LH) kinetic model, i.e. the diffusion of the reactants is fast compared to the rate-limiting substrate rearrangement at the AuNP surface.⁶¹⁻⁶⁶ The presence of excess NaBH_4 insures pseudo-first order of the reaction. The absorption of 4-NP in the UV-vis. spectra at 400 nm thus facilitates the observation of the reaction kinetics by following the decrease of this band, whereas the increase of the absorption band at 300 nm shows the formation of 4-AP. The MPEG (or MPEG-1) NPs containing 0.2% mol or 0.5% mol catalyst are added according to the procedure that is described in details in the SI, and the reaction is monitored by UV-vis. spectroscopy. The kinetic constants of this reaction follows $k_{app} = -\ln(C/C_0)$, and they are shown in Table 1. In this category, the apparent reaction rate k_{app} decreases with the order of $\text{Pd} > \text{Au} > \text{Ag} > \text{Cu}$. PdPEG with an average core size of 1.69 nm is the most efficient catalyst ($k_{app} = 1.69 \times 10^{-2} \text{ s}^{-1}$), compared to other MPEG catalysts. In addition, no induction times are observed for PdPEG and AuPEG. Compared with the results of recent work,^{53,55,66}

PdPEG and AuPEG perform well for this reaction, but they are less active than some excellent recently reported catalysts.⁴⁷ Note that the purified MPEG perform better than non-purified MPEG-1 using the same amount of catalyst (Figures 11-18, Experimental Section). In the latter catalyst, the TMPEG-2000 NPs are additionally stabilized by the salts Na⁺ Cl⁻, 2Na⁺ SO₄²⁻ or Na⁺ PF₆⁻, and these stabilizers that are located near the TMPEG-2000 NPs surface partly inhibit the approach of the substrates to this catalyst surface. Logically purification that removed these salts from the TMPEG-2000 NPs improves the catalytic efficiency in MPEG. The characteristics of all the TMPEG-2000 NPs synthesized by Na naphthalenide reduction of the precursor TM salts after purification by salting-out and their catalytic data for 4-NP reduction are gathered in Table 1. Retention times that correspond to structural reorganization at the TMPEG-2000 NPs surface at the beginning of the catalytic reaction are found for the first-row transition metal CuNPs and AgNPs but not for the other noble metal NPs that are the most active nanocatalysts as expected.

Table 1. 4-NP reduction by NaBH₄ catalyzed by MPEG in water at 20°C.



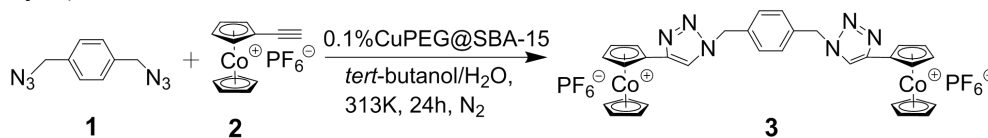
MPEG	Color	Amount ^[a] [mol%]	D _{core} ^[b] [nm]	t ₀ ^[c] [s]	k _{app} ^[d] [10 ⁻³ s ⁻¹]
AuPEG	Purple	0.2	2	0	15.8
AgPEG	yellow green	0.5	4	40	5.97
PdPEG	black	0.2	1.7	0	16.9
CuPEG	Faint yellow	0.5	3.2	120	4.95

[a] Amount of catalysts used in the catalyzed 4-NP reduction. NaBH₄ is in excess. [b] Core size (TEM) of the MPEG. [c] Induction time. [d] Rate constant.

CuNP catalysis. CuNP synthesized by Na naphthalenide reduction of CuSO₄ were previously characterized and characterized by TEM, XPS, UV-vis. and CuAAC reactions, and for these reactions aerobically oxidized Cu₂O NPs were shown to be more catalytically efficient than genuine Cu(0)NPs.⁴³ These most efficient Cu₂O NPs samples are now used here for further catalytic tests for the CuAAC reaction leading to the synthesis of the new dinuclear cobalticinium complex **3** and as co-catalyst of Sonogashira reactions.

CuAAC reaction applied to organometallic synthesis. The CuAAC synthesis of the new bis(cobalticinium) complex **3** is represented in equation 2 from the reaction

between **1** and **2**, and **3** has been characterized by ^1H and ^{13}C NMR, electrospray ionization mass spectrometry (Experimental Section) and cyclic voltammetry (*vide infra*).



equation 2

The bis(cobaltocenium) complex **3** is studied by cyclic voltammetry (CV) using decamethylferrocene (Cp^*_2Fe , $\text{Cp}^* = \eta^5\text{-C}_5\text{Me}_5$)⁶⁷⁻⁶⁹ as the internal reference and DMF as the solvent (Figure 4). It shows two chemically and electrochemically CV waves. The first reduction wave corresponding to the reduction of the 18-electron cobaltocenium moieties to the 19-electron cobaltocene ($\text{Co}^{\text{III/II}}$) takes place at $E_{1/2} = -0.81$ V vs. $\text{Cp}^*_2\text{Fe}^{+/0}$. The second wave corresponding to the reduction of cobaltocene to the 20-electron cobaltocenyl anion ($\text{Co}^{\text{II/I}}$)⁷⁰⁻⁷² appears at $E_{1/2} = -1.74$ V vs. $\text{Cp}^*_2\text{Fe}^{+/0}$ (Table 2). Both cobaltocenium groups in **3** are reduced in a single wave, because the cobaltocenium moieties are sufficiently distant, thus quite independent from each other. The envelope of the first redox wave ($\text{Co}^{\text{III/II}}$) is slightly broadened compared to a standard single-electron wave shape, however (compare with the second wave) which is due to electrostatic interaction very slightly differentiating the two single electron-transfer steps corresponding to the $\text{Co}^{\text{III/II}}$ redox change. This phenomenon is not apparent in the second wave dealing with the reduction of the neutral bis-cobaltocene species to the di-anion. Since the reduction of each Co^{III} to Co^{II} moiety corresponds to a single-electron reaction, the value of the number of electrons (n_p) involved in the first CV wave can be estimated by employing the Bard-Anson's equation 3 previously derived for conventional polarography:

$$n_p = (i_{dp}/C_p) / (i_{dm}/C_m) (M_p/M_m)^{0.275} \quad \text{equation 3}$$

Measurement of the respective intensities for the internal reference Cp^*_2Fe and the first wave (Figure 22, Experimental Section) leads to the data of $n_{p1} = 1.8 \pm 0.2$ that is close to the theoretical number of 2 electrons for compound **3**. The 2nd wave is slightly more intense than the 1st one ($i_{2c}/i_{1c} = 1.1$), giving $n_{p2} = 2.0 \pm 0.2$.

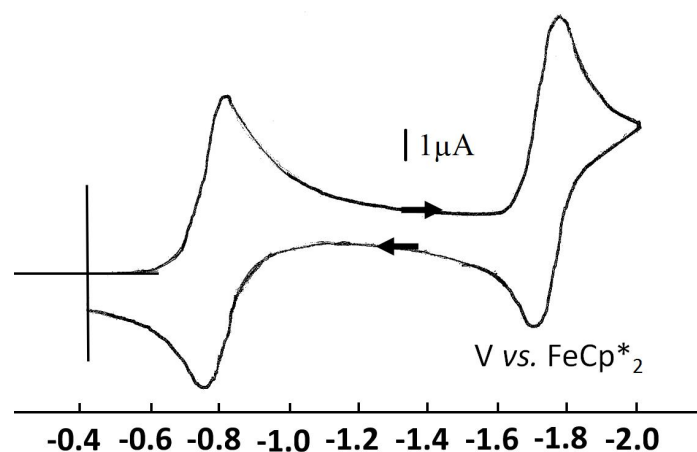


Figure 4. CV of the bis(cobalticinium) complex **3**. Internal reference: FeCp*₂ (see Figure 22, Experimental Section); solvent: DMF; 298 K; reference electrode: Ag; working and counter electrodes: Pt; scan rate: 0.2 V/s⁻¹; supporting electrolyte: [n-Bu₄N][PF₆] (0.1 M).

Table 2. Redox potentials, chemical (*i_a/i_c*) and electrochemical (*E_p_a* - *E_p_c* = ΔE) reversibility data for compound **3**; solvent: DMF.

	<i>E</i> _{1/2} (V)	ΔE (V)	<i>i_a/i_c</i>
Co ^{III/II}	-0.81	0.060	1
Co ^{III/I}	-1.74	0.060	0.8

Sonogashira reaction. The use of these Cu₂O NPs in Sonogashira reactions is indicated below. In these reactions, the Cu oxidation state was indicated to be Cu(I) by the band at 360 nm in the UV-vis. spectrum (*vide infra*). As in CuAAC reactions, the Cu(I) state is more efficient than the Cu(0) state for co-catalysis of Sonogashira reactions.⁷⁸⁻⁸⁰

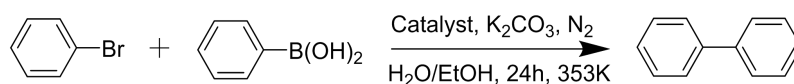
PdNP-catalyzed Suzuki and Sonogashira cross-coupling reactions. Palladium-catalyzed cross-coupling reactions, such as the Suzuki-Miyaura reaction^{74,75} and the Sonogashira reaction^[75-80] play a key role in constructing the carbon backbones, which has attracted research interest due to their extensive applications in organic synthesis.^{75,78-80}

Suzuki-Miyaura reaction. Attempts have been reported for Suzuki-Miyaura reactions with ppm mounts of catalyst.⁷⁹⁻⁹¹ PdNPs efficiently avoid the use of toxic ligands in the Suzuki-Miyaura reaction, and therefore PEG-stabilized PdPEG and PdPEG-1 nanoparticles are utilized here to test the Suzuki-Miyaura reaction between bromobenzene and phenylboronic acid at 80°C under N₂ (Table 3). 100 ppm PdPEG nanoparticles catalyze the quantitative Suzuki-Miyaura reaction and 50 ppm PdPEG provides a TON of 8400 and TOF of 350 h⁻¹. Furthermore, PdPEG is successfully

immobilized onto SBA-15 (Figure 27c and Figure 24, Experimental Section) for recycling experiments using 300 ppm of PdPEG@SBA-15. The Suzuki-Miyaura reaction between phenylboronic acid and bromobenzene under these conditions in the presence of the supported catalyst provides yields larger than 80% during at least three successive recycling experiments (Table 5, Experimental Section). The TEM image of PdPEG@SBA-15 after recycling (Figure 25, Experimental Section) shows that the PdNPs are partially aggregated, explaining why only a 65% isolated yield was obtained after recycling the 4th time.

The particle size of PdPEG is 1.85 nm in average on the SBA-15 support, and it noteworthy that the particles supported on SBA-15 retain a similar particle size of PdPEG (1.69 nm, Figure 3c). After work-up, the residual solution after centrifugation is used to test the Suzuki-Miyaura reaction, and only traces of final product are observed by thin-layer chromatography after first recycling run, which means that there is almost no catalyst leaching.

Table 3. Suzuki-Miyaura reaction catalyzed by the PdNPs. ^[a]



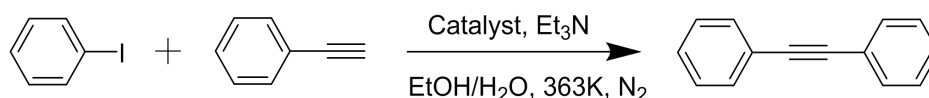
Catalysts	Amount ^[b]	Conversion (%) ^[c]	Yield (%) ^[d]	TON	TOF (h ⁻¹)
PdPEG	1000 ppm	100	98	980	40.8
PdPEG-1	1000 ppm	100	97	970	40.4
PdPEG	100 ppm	99	95	9500	395
PdPEG-1	100 ppm	91	85	8500	354
PdPEG	50 ppm	53	42	8400	350
PdPEG-1	50 ppm	32	23	4600	191

[a] Reaction conditions: bromobenzene (0.5 mmol), phenylboronic acid (0.75 mmol.), K₂CO₃ (1 mmol), H₂O/EtOH: 1 mL: 1 mL, 80°C, 24 h, under N₂. [b] Amount of catalysts used in the catalyzed Suzuki reduction. [c] ¹H NMR conversion. [d] Isolated yield.

Sonogashira reaction. 1 mol% PdPEG efficiently catalyzes the Sonogashira reaction between iodobenzene and phenylacetylene using H₂O/EtOH as the solvent at 90°C for 24 h in the presence of the base and 1 mol% CuPEG (Table 4). Recycling experiments using 1% of PdPEG@SBA-15 and 1% of CuPEG@SBA-15 provide yields larger than 85% during at least three successive recycling experiments (Table 6, Experimental Section). The residual solution after centrifugation is used to test the leaching problem, only traces of final product are observed by thin-layer chromatography after first

recycling run. Figures 27a and b (Experimental Section) show typical STEM and HRTEM (at the same position) images of CuPEG@SBA-15 respectively. The CuPEG nanoparticles are successfully immobilized onto the SBA-15 support and the particle size of CuPEG@SBA-15 is similar as that found in the starting CuPEG. The lattice spacing is about 2.4 Å, assuming that the crystallographic plane of the Cu₂O nanocrystal is {111}. This indicates that the CuPEG surface was oxidized by O₂ to form Cu₂O NPs, which are the active species of Sonogashira reaction. The purified catalysts provide better yields than the unpurified one, and this further shows that the salting-out purification method improves the activity of the catalyst surface of the TMNPs.

Table 4. Sonogashira reaction catalyzed by PdNPs and CuNPs.^[a]



Catalysts	Amount [b]	Conversion (%) [c]	Yield (%) [d]	TON	TOF (h ⁻¹)
PdPEG + CuPEG	1%+ 1%	97	90	45	1.9
PdPEG-1+ CuPEG-1	1%+ 1%	75	64	32	1.3
PdPEG	1%	90	81	81	3.4
PdPEG-1	1%	71	60	60	2.5

[a] reaction condition: iodobenzene (0.5 mmol), phenylacetylene (0.5 mmol) and Et₃N (1.5 mmol), H₂O/ EtOH: 2 mL: 2 mL, 90°C, 24 h, under N₂. [b] Amount of catalysts used in the catalyzed Sonogashira reaction. [c] ¹H NMR conversion. [d] Isolated yield.

Conclusions

Na naphthalenide reduction of late transition-metal salts is a valuable method for the synthesis of small PEG-protected late transition-metal nanoparticles because of the advantages of simplicity, very small size for Au and Pd nanoparticles, and purification by double extraction using the salting-out effect. Indeed, nanoparticles purified in this way are systematically more catalytically efficient than non-purified ones. Indeed good catalytic results are obtained with Pd, Cu and Au nanoparticles for various reactions including 4-nitrophenol reduction, fine click organometallic synthesis and supported co-catalysis (Cu(I)), and carbon-carbon cross coupling (Pd(0)). These Cu

and Pd nanoparticles yield excellent catalytic results including efficient recycling when they are supported on SBA-15. These methods are also potentially extendable to other types of catalysis.

Experimental Section

1. General data.

All solvents and chemicals were used as purchased, unless otherwise noted. UV-vis. absorption spectra were measured with a Perkin-Elmer Lambda 19 UV-vis. spectrometer. NMR spectra were recorded at 25 °C with a Bruker AC 400, or 300 (400 or 300 MHz). All the chemical shifts were reported in parts per million (δ , ppm) with reference to Me₄Si for the ¹H NMR spectra. Transmission Electron Microscopy (TEM), high-resolution TEM (HRTEM) and STEM images were recorded using A TEM JEOL JEM 1400 (120 kV) and a high-resolution TEM JEOL JEM 2100F (200 kV). X-ray photoelectron spectra (XPS): System: SPECS SAGE HR, X-Ray source: Mg K α non-monochromatic, operated at 12.5 kV and 250 W. Take-off angle 90°, at $\sim 10^{-8}$ Torr. Pass energy for survey spectra 30 eV, 15 eV for narrow scans. Analysis: spectra are calibrated to CC carbon 285 eV. Analysis consisted of Shirley background subtraction. Peaks were fitted with symmetrical Gaussian-Lorentzian (GL) line shapes. Sample was dispersed on silica substrate and evaporated prior to measurement. Electrospray-ionization mass spectrometry (ESI-MS) was performed on device of Applied Biosystems-QSTAR Elite. Cyclic voltammetry (CV) studies: all electrochemical measurements were recorded under nitrogen atmosphere. Conditions: supporting electrolyte: [*n*-Bu₄N][PF₆], 0.1 M; solvent: DMF; working and counter electrodes: Pt; reference electrode: Ag; internal reference: FeCp*₂ (Cp* = η^5 -C₅Me₅); scan rate: 0.200 V/s⁻¹. Flash column chromatography was performed using silica gel (300-400 mesh). Tetrahydrofuran (THF), acetonitrile (CH₃CN) and dichloromethane (CH₂Cl₂) were refluxed and freshly distilled, Milli-Q water was degassed by N₂ for 10 min to remove O₂ before use. Sodium naphthalenide was synthesized according to a known procedure.³⁴ Sodium metal (1.1 equiv) was dissolved in a solution of naphthalene (100 mg, 0.78 mmol) in THF (20 mL), the mixture was stirred for 12 h under N₂ atmosphere in a standard Schlenk flask, providing sodium naphthalenide with green color.

2. Synthesis of the TMPEG-2000 NPs.

2.1.1 AuPEG and AuPEG-1 nanoparticles. HAuCl₄ (2 mg, 3.72×10^{-3} mmol) and PEG-2000 (27 mg, 1.35×10^{-2} mmol) were dissolved in 20 mL THF under nitrogen in standard Schlenk and stirred for 30 min. Thereafter excess fresh sodium-naphthalenide solution was injected into the Schlenk flask, the color of the

solution changed from faint yellow to brown. The crude AuNPs were dried *in vacuo* and extracted with CH₂Cl₂ and H₂O under N₂, the water phase was removed, and the organic phase was dried. Extraction with CH₂Cl₂ and H₂O was continued and repeated 3 times, and pure aqueous AuNPs were then obtained (denoted as AuPEG). Crude AuNPs without purification dissolved in Milli-Q water (equal volume ratio, for cleaning excessive sodium-naphthalenide) are denoted AuPEG-1.

2.1.2 AgPEG and AgPEG-1 nanoparticles. The above procedure was applied using AgPF₆ (2 mg, 7.91×10⁻³ mmol) and PEG-2000 (42 mg, 2.1×10⁻² mmol) in 20 mL THF. Upon addition of excess fresh sodium-naphthalenide solution the color of the solution changed from colorless to yellow brown. Pure aqueous AgNPs are denoted as AgPEG. Crude AgNPs without purification dissolved in Milli-Q water as above to clean the excess sodium-naphthalenide are denoted AgPEG-1.

2.1.3 PdPEG and PdPEG-1 nanoparticles. The above procedure was applied using PdCl₂ (2 mg, 1.13×10⁻² mmol) and PEG-2000 (61 mg, 3.05×10⁻² mmol) in 20 mL CH₃CN. Upon addition of excess fresh sodium-naphthalenide solution the color of the solution changed from faint yellow to black. The pure aqueous PdNPs are denoted PdPEG, and crude PdNPs without purification dissolved in Milli-Q water to clean the excess sodium-naphthalenide are denoted as PdPEG-1.

2.1.4 CuPEG and CuPEG-1 nanoparticles. The above procedure was applied using CuSO₄·5H₂O (2 mg, 8×10⁻³ mmol) and PEG-2000 (43 mg, 2.15×10⁻² mmol) in 20 mL CH₃CN. Upon addition of excess fresh sodium-naphthalenide solution the color of the solution changed from colorless to faint yellow. The pure aqueous CuNP are noted CuPEG, and the crude CuNPs without purification dissolved in Milli-Q water to clean the excess sodium-naphthalenide are noted CuPEG-1.

2.2 Preparation of supported CuPEG@SBA-15 and PdPEG@SBA-15 catalysts. The CuPEG or PdPEG and SiO₂ with mol ratio 1:300 were dispersed in H₂O, and submitted to ultrasound for 1 h, then stirring was continued for 3 h under N₂. The mixture was kept overnight without stirring under N₂, then centrifugation was carried out with washing by deionized water three times, and the solid was dried at 323K.

3. Catalysis

3.1 4-NP reduction. 4-NP (1 equiv.) was mixed with excess NaBH₄ (81 equiv.) in water under air. The color of the solution changed from light yellow to dark yellow due to the formation of 4-nitrophenolate ion. Then a solution containing transition metal nanoparticles (0.2 or 0.5 mol%) was added to the mixture, and the solution quickly lost its dark yellow color with time. The kinetics of the reaction was monitored by UV-vis. spectroscopy (40 s for each run).

3.2 Azide-alkyne cycloaddition reaction between ethynylcobalticinium hexafluorophosphate, 1, and 1,4-bis (azidomethyl) benzene, 2, and catalyzed by

CuPEG@SBA-15 catalyst. A Schlenk flask equipped with a magnetic stir bar was charged with 1 mmol of **1** and 0.505 mmol of **2** and under N₂. The catalyst (0.1%), then 1 mL *tert*-butanol and 1 mL H₂O were added under N₂, and the reaction mixture was stirred for 24 h at 40 °C under N₂. After the reaction, the *tert*-butanol was removed *in vacuo* followed by extraction using CH₂Cl₂ and H₂O three times, the organic phase was dried over Na₂SO₄, and the solvent was removed *in vacuo*. The solids were washed with pentane and filtered, and the remaining solids were dried *in vacuo* yielding *p*-bis (cobalticinium hexafluorophosphate-1,2,3-triazolylmethyl) benzene, **3**, in yield (406 mg, 90% isolated yield). ¹H NMR (300 MHz, Acetone) δ 8.60 (s, 2H), 7.47 (s, 4H), 6.44 – 6.40 (m, 4H), 6.05 – 6.01 (m, 4H), 5.76 (s, 14H). ¹³C NMR (76 MHz, Acetone) δ 135.84 (s), 128.75 (s), 124.55 (s), 95.99 (s), 85.93 (s), 84.48 (s), 80.90 (s), 69.76 – 69.50 (m), 53.34 (s). ESI-MS: *p*-bis (cobalticinium-1,2,3-triazolylmethyl) benzene (904.03 Da – PF₆⁻ = 759.07 Da).

3.3 Suzuki-Miyaura reaction catalyzed by PdNPs. A dry Schlenk flask was charged with K₂CO₃ (1 mmol), phenylboronic acid (0.75 mmol.), and bromobenzene (0.5 mmol). Catalytic amounts of PdNPs solution were successively added, and then the solvents H₂O and EtOH were added in order to make a total of 2 mL of solvent (volume ratio of H₂O/ EtOH: 1/1). The suspension was then allowed to stir under N₂ for 24 hours at 80°C. After the reaction, the Schlenk flask was cooled to r.t., the mixture was extracted three times with 20 mL diethyl ether, the organic phase was dried over Na₂SO₄, and the solvent was removed *in vacuo*. The structure and purity of the crude product were verified using ¹H NMR, in particular in order to determine the conversion. In parallel, the reaction was checked using TLC in only petroleum ether as eluent. The purification by flash chromatography column was conducted with silica gel as the stationary phase and petroleum ether as the mobile phase. ¹H NMR (300 MHz, CDCl₃) δ 7.66 (d, J = 7.3 Hz, 4H), 7.57 – 7.45 (m, 4H), 7.41 (t, J = 7.3 Hz, 2H).

3.4 Sonogashira reaction catalyzed by PdNPs and CuNPs. A dry Schlenk tube equipped with a magnetic stir bar was charged with iodobenzene (0.5 mmol), phenylacetylene (0.5 mmol) and Et₃N (1.5 mmol) under N₂. Catalytic amounts of a solution of PdNPs and CuNPs were then successively added, and appropriate amount of H₂O and EtOH were added in order to adjust to a total of 4 mL of solvent (volume ratio of H₂O/ EtOH: 1/1). The mixture was stirred and heated at 90 °C for 24 h. After cooling to r.t., the mixture was extracted three times with 20 mL CH₂Cl₂, the organic phase was dried over Na₂SO₄, and the solvent was removed *in vacuo*. The crude product was checked by ¹H NMR to determine the conversion. In parallel, the reaction was checked using TLC. Purification by flash chromatography column was conducted in order to calculate the isolated yields. ¹H NMR (300 MHz, CDCl₃) δ 7.62 - 7.51 (m, 4H), 7.45 - 7.31 (m, 6H)

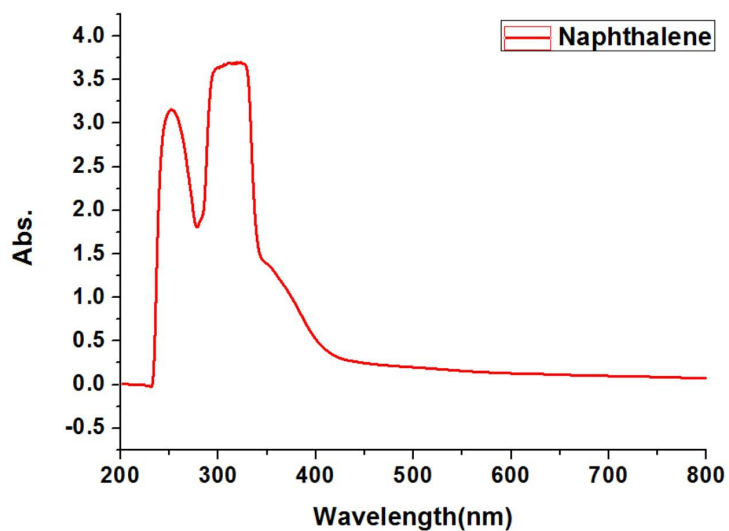


Figure 5. UV-vis. spectrum of naphthalene.

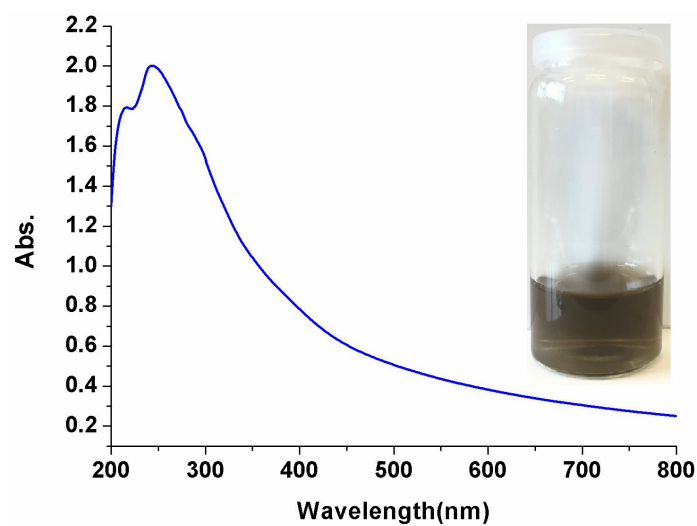


Figure 6. UV-vis. spectrum of pure PdPEG nanoparticles.

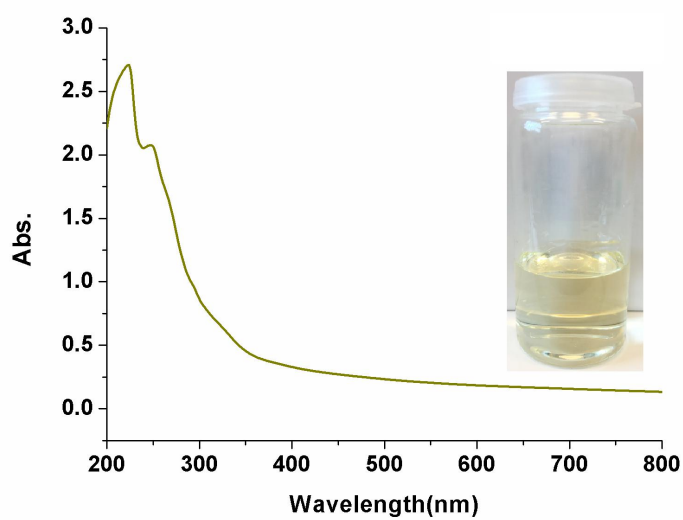


Figure 7. UV-vis. spectrum of pure CuPEG nanoparticles.

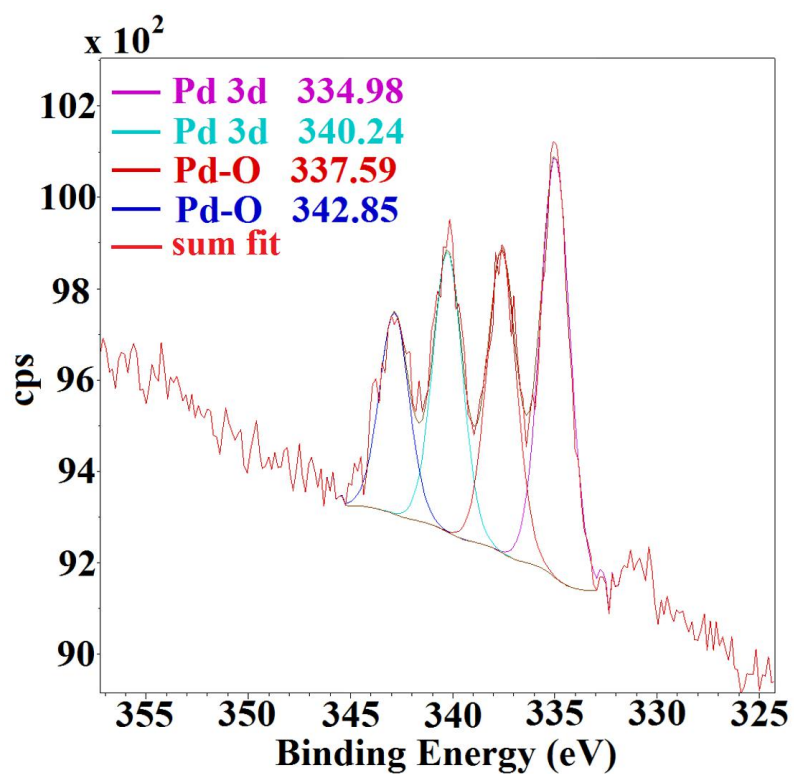


Figure 8. X-ray photoelectron spectroscopy (XPS) of pure PdPEG nanoparticles.

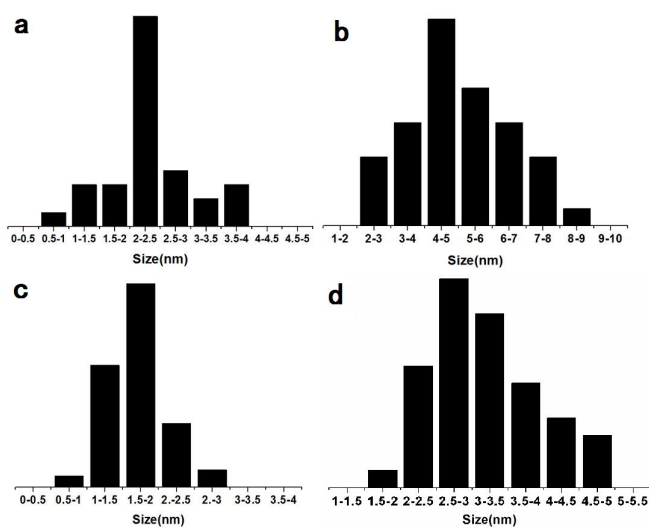


Figure 9. Size distribution of MPEG: a: AuPEG; b: AgPEG; c: PdPEG; d: CuPEG.

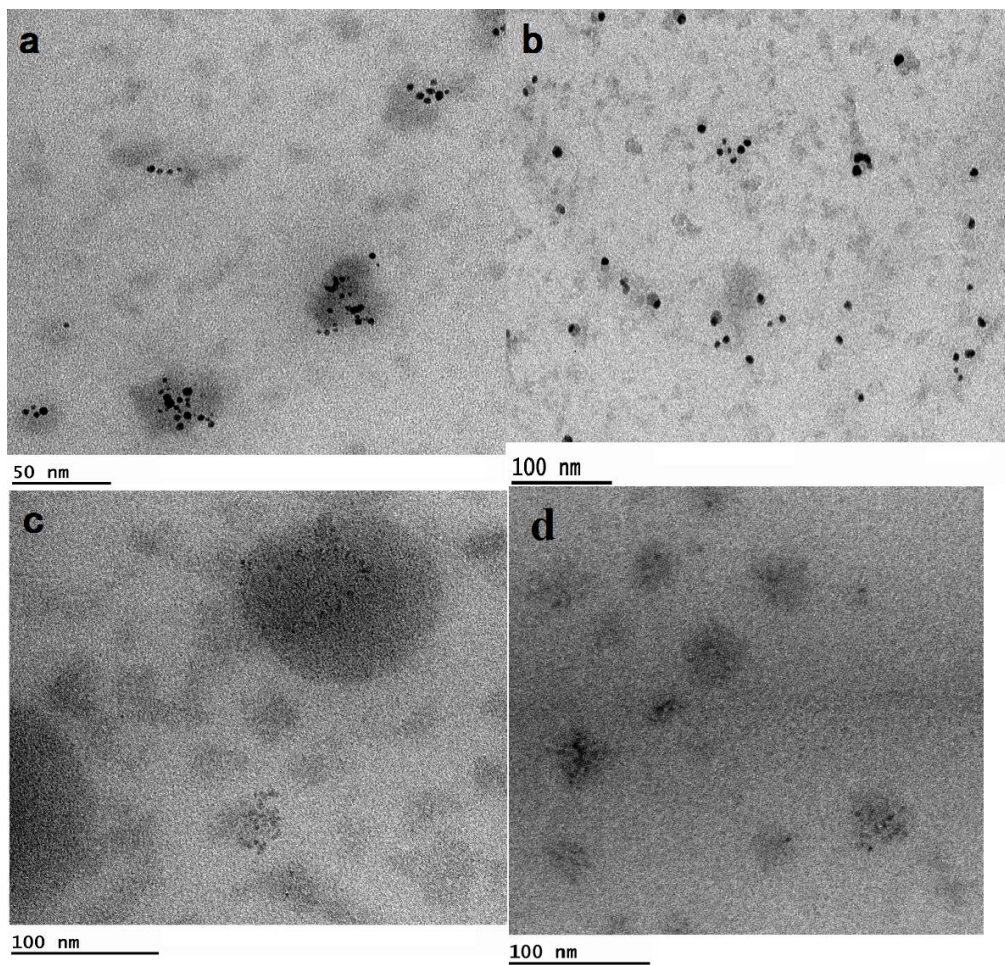


Figure 10. TEM of MPEG-1 (without purification): a: AuPEG-1; b: AgPEG-1; c: PdPEG-1; d: CuPEG-1.

UV-vis. spectrum of the 4-NP reduction and reaction rate (k_{app})

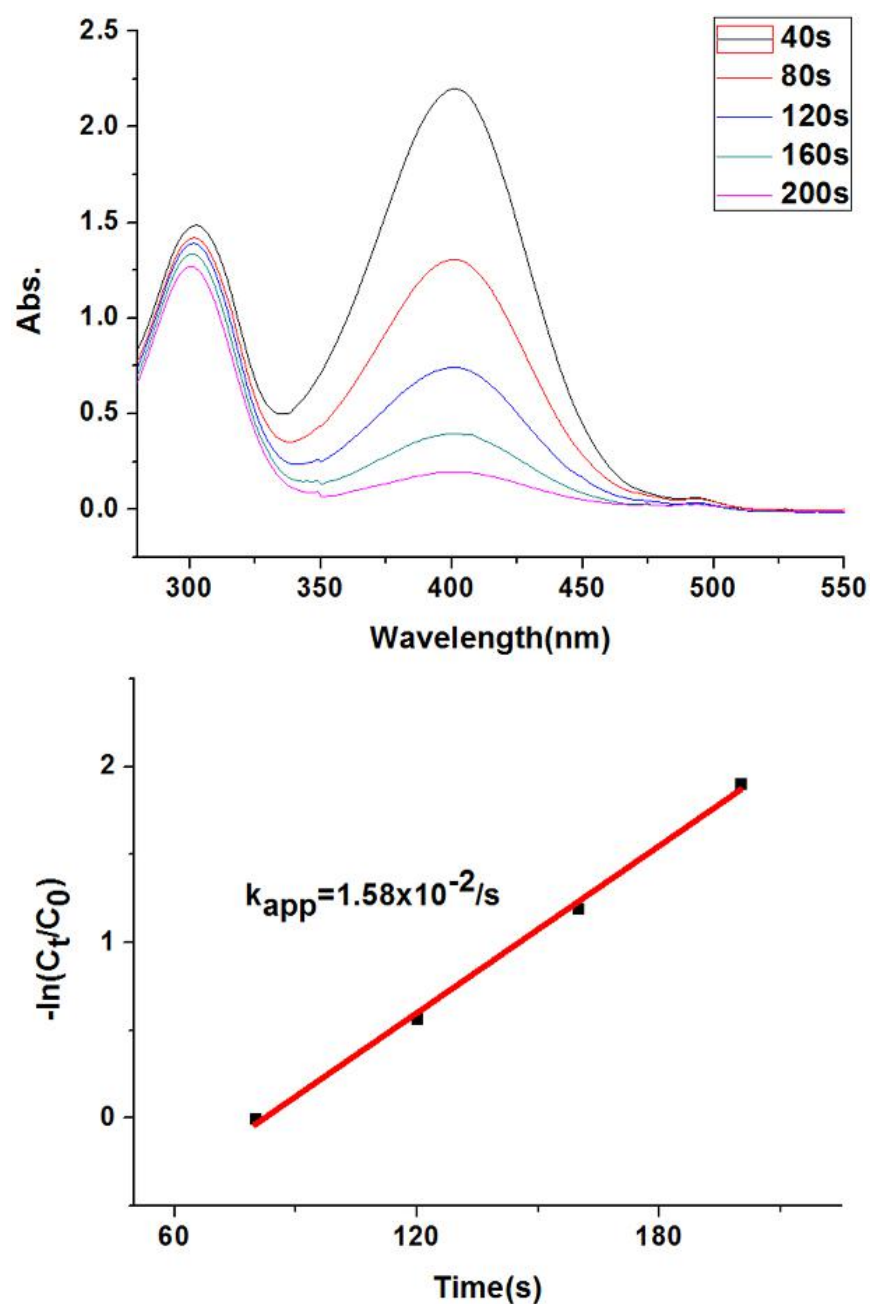


Figure 11. UV-vis. spectrum of the 4-NP reduction by NaBH_4 catalyzed by AuPEG (top); consumption rate of 4-NP: $-\ln(C_t/C_0)$ vs reaction time (bottom, $R^2 = 0.9963$).

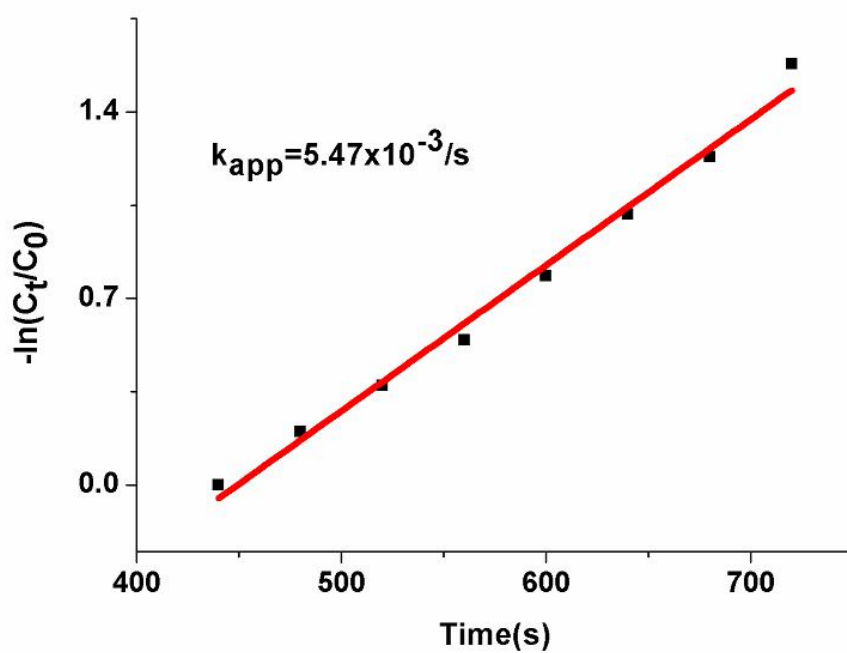
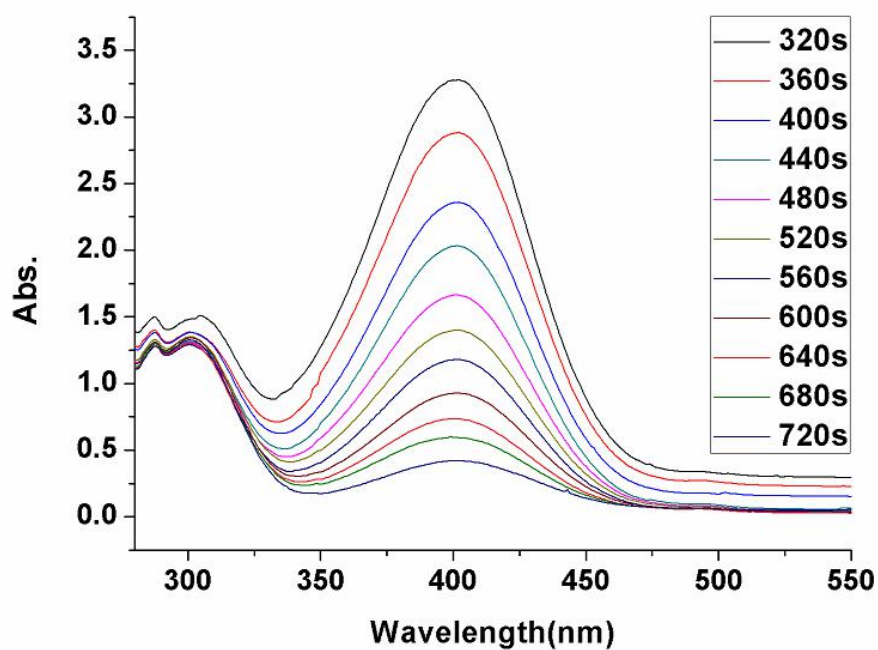


Figure 12. UV-vis. spectrum of the 4-NP reduction by NaBH₄ catalyzed by AuPEG-1 (top); consumption rate of 4-NP: $-\ln(C_t/C_0)$ vs reaction time (bottom, $R^2 = 0.9883$).

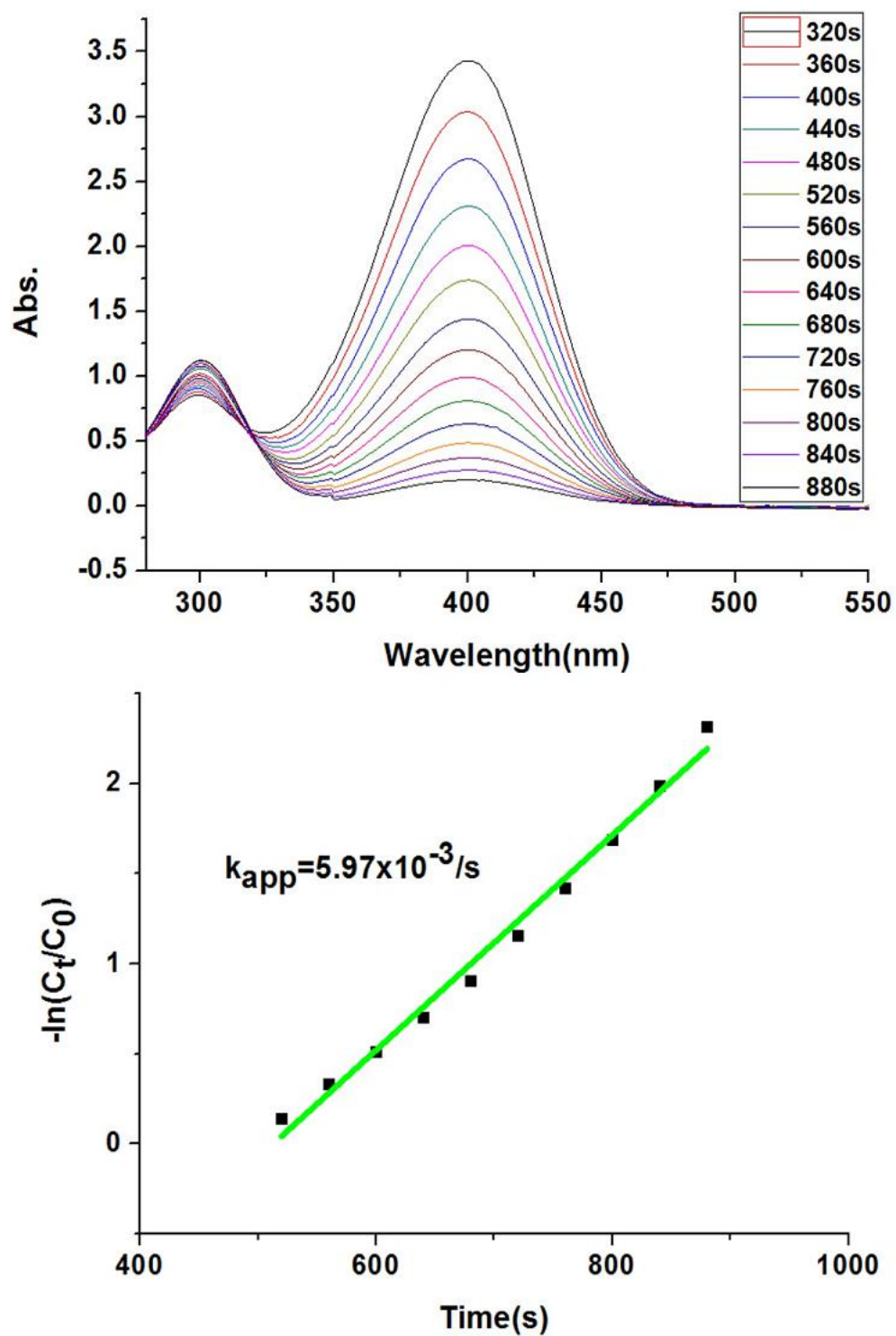


Figure 13. UV-vis. spectrum of the 4-NP reduction by NaBH_4 catalyzed by AgPEG (top); consumption rate of 4-NP: $-\ln(C_t/C_0)$ vs reaction time (bottom, $R^2 = 0.9882$).

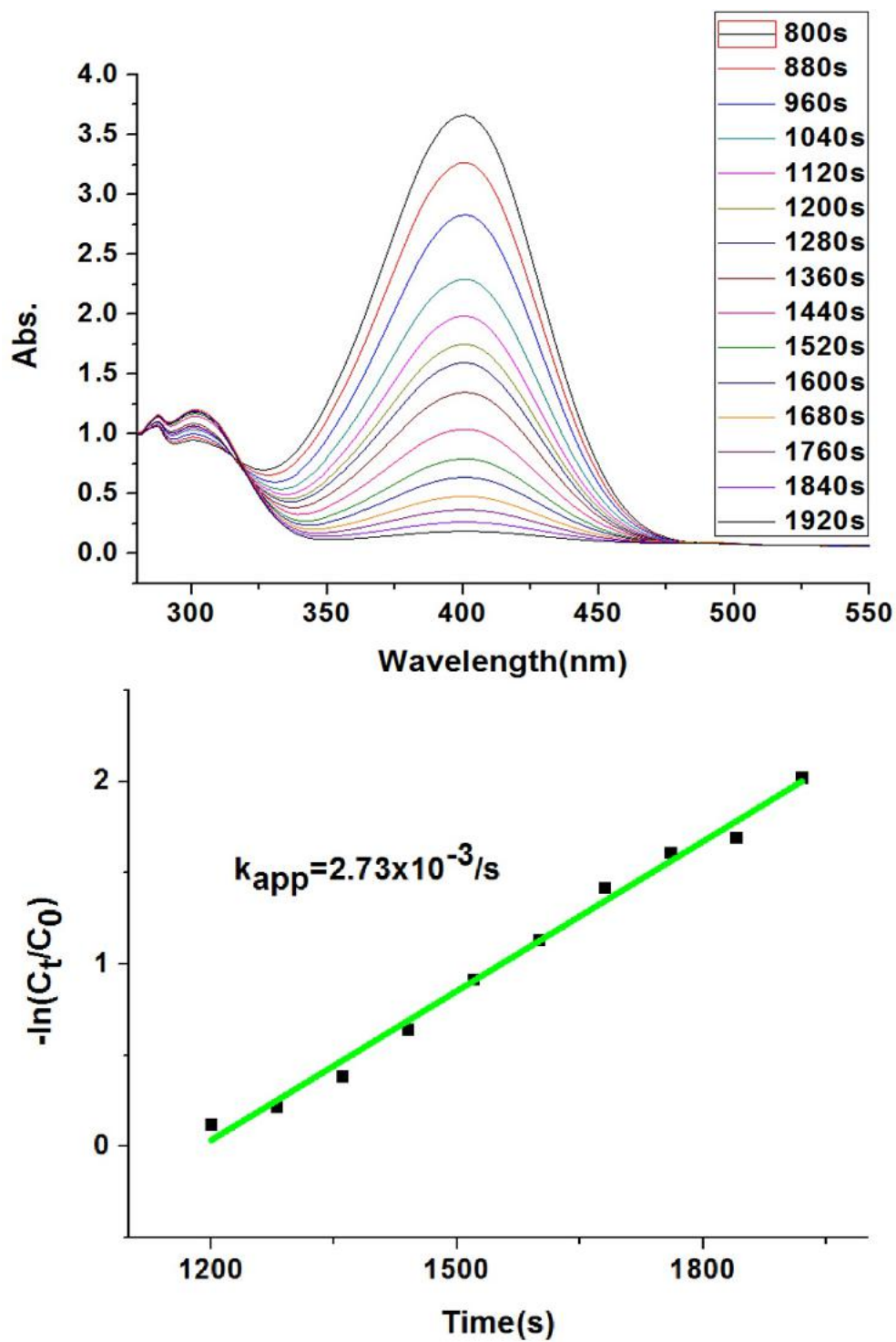


Figure 14. UV-vis. spectrum of the 4-NP reduction by NaBH_4 catalyzed by AgPEG-1 (top); consumption rate of 4-NP: $-\ln(C_t/C_0)$ vs reaction time (bottom, $R^2 = 0.9901$).

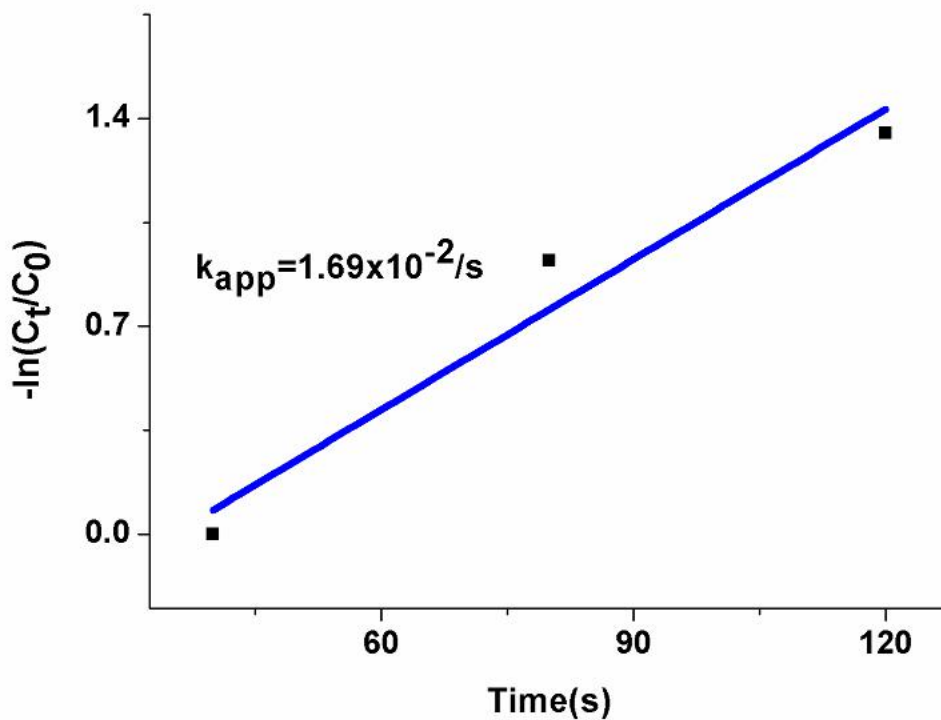
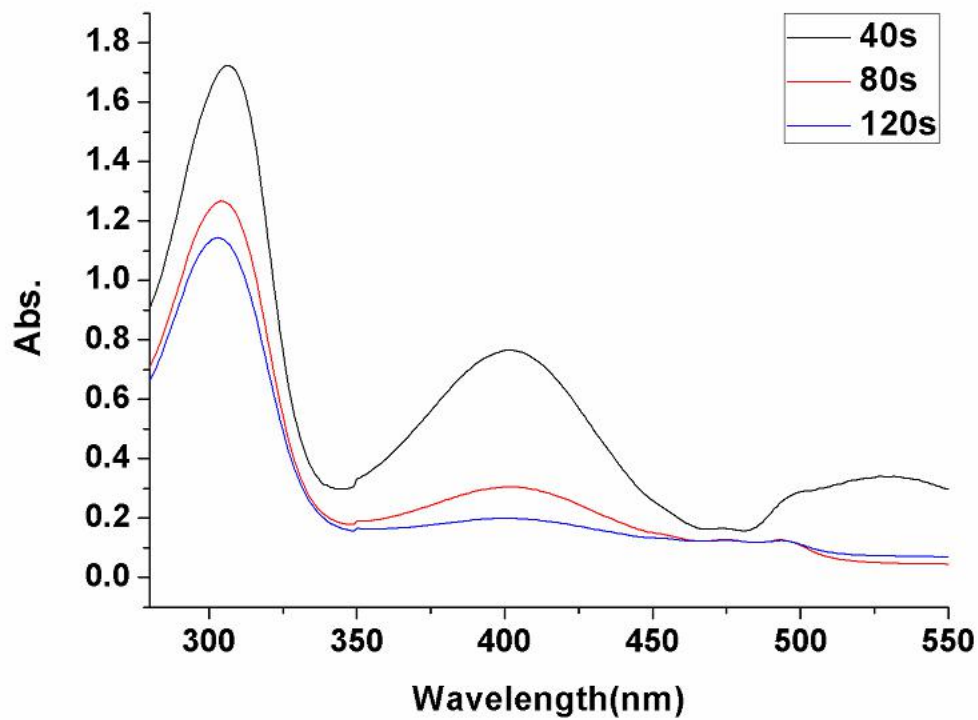


Figure 15. UV-vis. spectrum of the 4-NP reduction by NaBH₄ catalyzed by PdPEG (top); consumption rate of 4-NP: $-\ln(C_t/C_0)$ vs reaction time (bottom, $R^2 = 0.9157$).

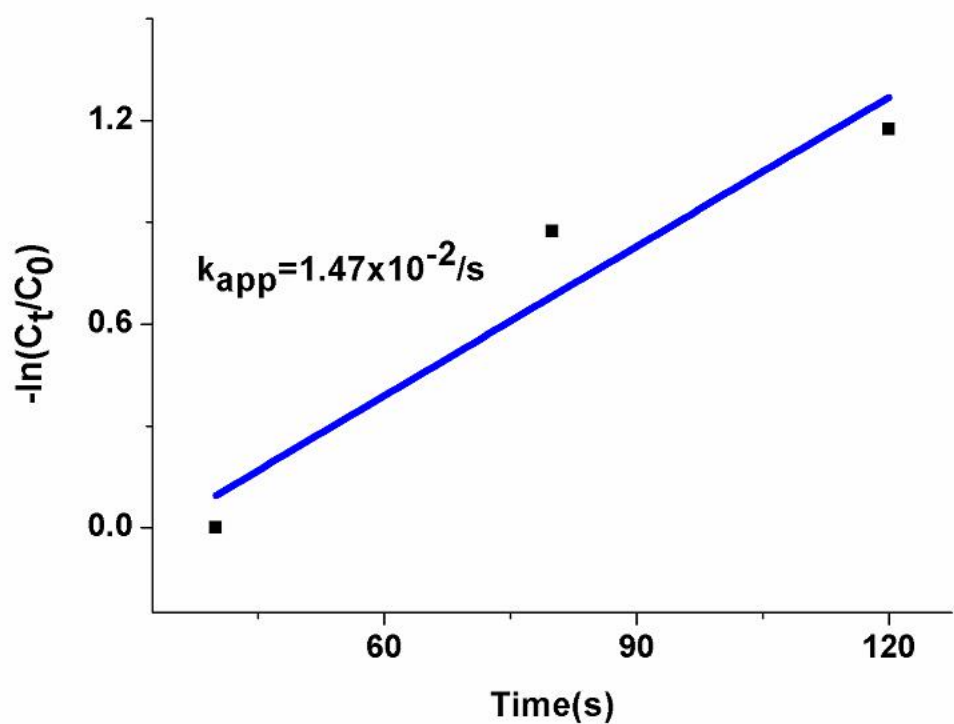
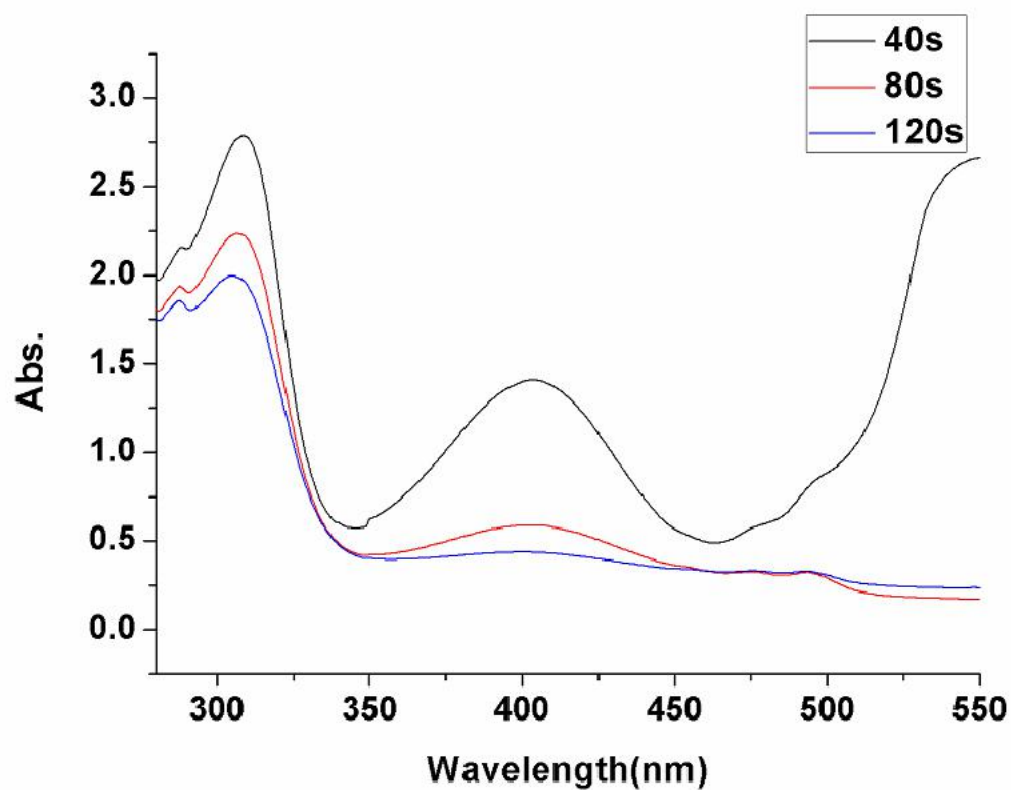


Figure 16. UV-vis. spectrum of the 4-NP reduction by NaBH₄ catalyzed by PdPEG-1 (top); consumption rate of 4-NP: $-\ln(C_t/C_0)$ vs reaction time (bottom, $R^2 = 0.8538$)

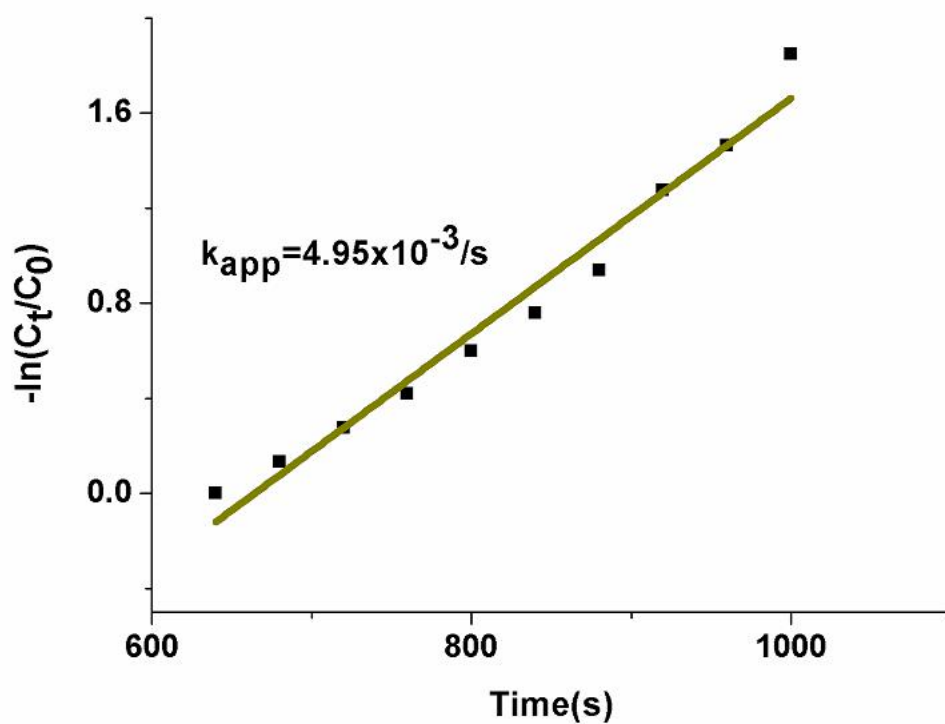
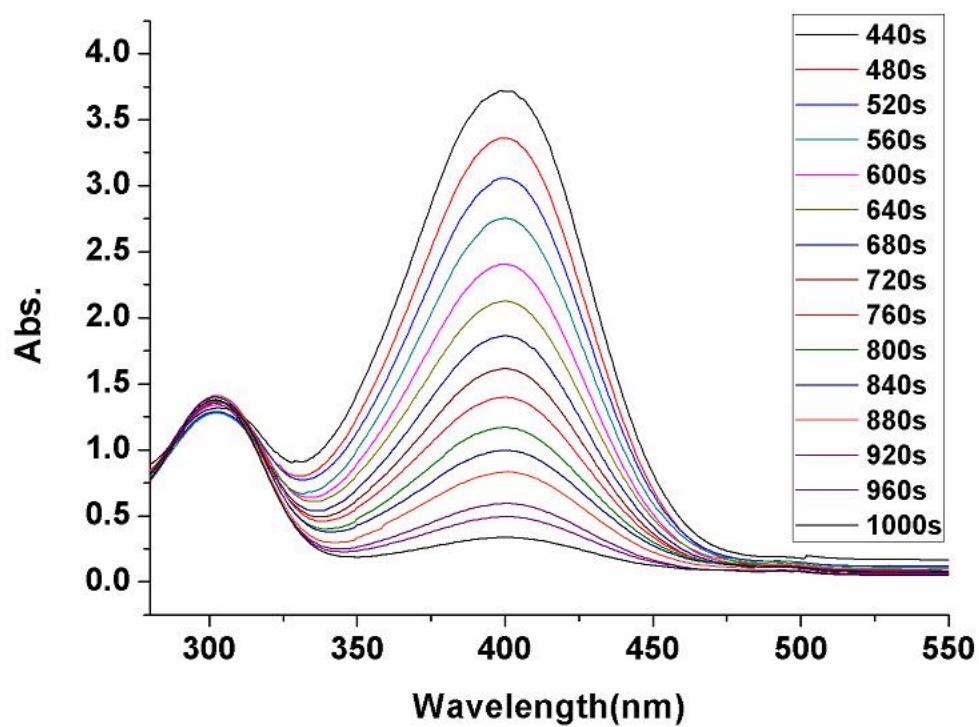


Figure 17. UV-vis. spectrum of the 4-NP reduction by NaBH₄ catalyzed by CuPEG (top); consumption rate of 4-NP: $-\ln(C_t/C_0)$ vs reaction time (bottom, $R^2 = 0.9698$).

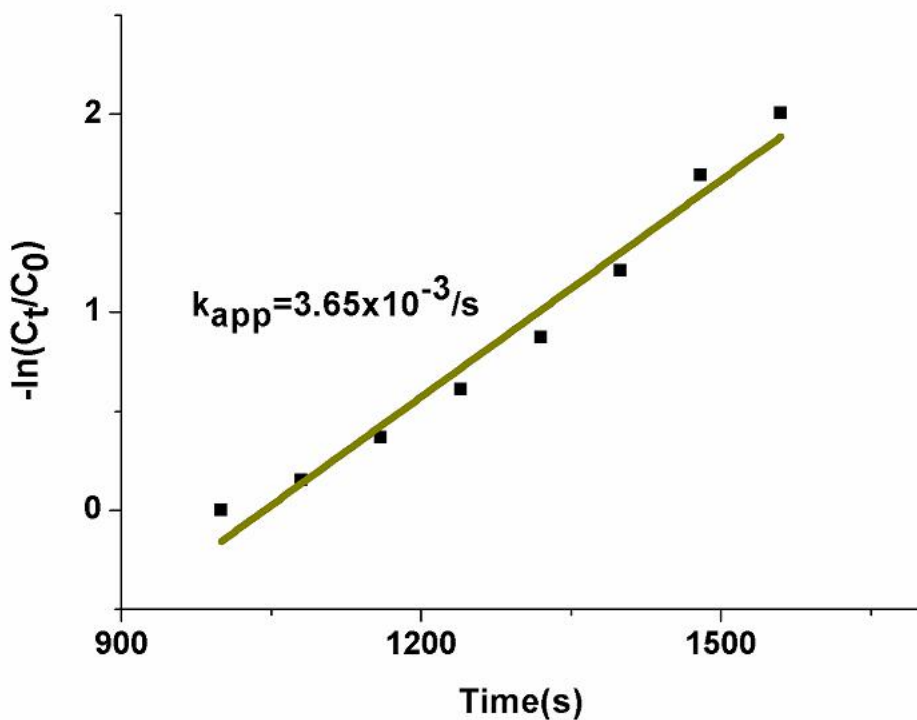
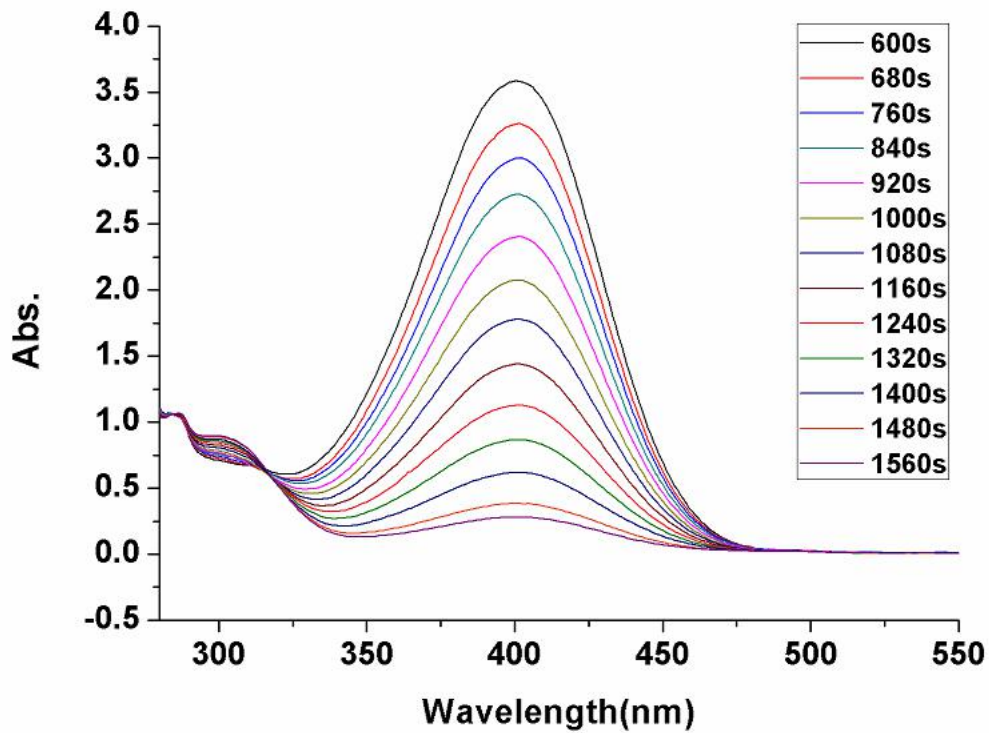


Figure 18. UV-vis. spectrum of the 4-NP reduction by NaBH_4 catalyzed by CuPEG-1 (top); consumption rate of 4-NP: $-\ln(C_t/C_0)$ vs reaction time (bottom, $R^2 = 0.9711$).

^1H , ^{13}C NMR, ESI-MS and CV of *p*-bis (cobalticinium-1,2,3-triazolylmethyl) benzene.

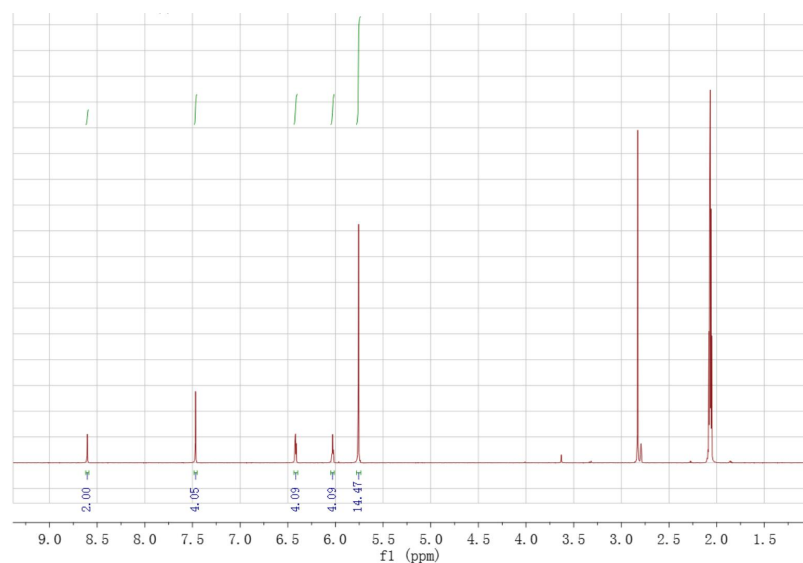


Figure 19. ^1H NMR spectrum of *p*-bis (cobalticinium-1,2,3-triazolylmethyl) benzene. ^1H NMR (300 MHz, Acetone) δ 8.60 (s, 2H), 7.47 (s, 4H), 6.44 – 6.40 (m, 4H), 6.05 – 6.01 (m, 4H), 5.76 (s, 14H).

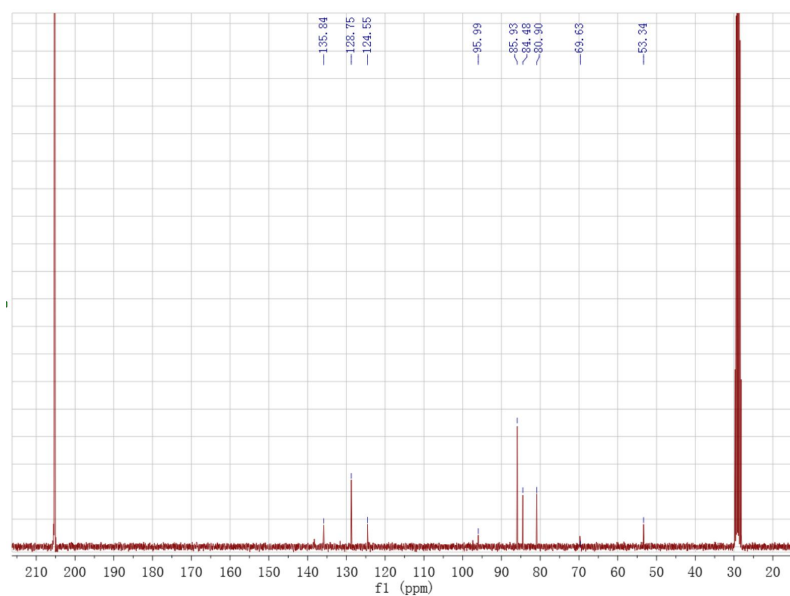


Figure 20. ^{13}C NMR spectrum of *p*-bis (cobalticinium-1,2,3-triazolylmethyl) benzene.

^{13}C NMR (76 MHz, Acetone) δ 135.84 (s), 128.75 (s), 124.55 (s), 95.99 (s), 85.93 (s), 84.48 (s), 80.90 (s), 69.76 – 69.50 (m), 53.34 (s).

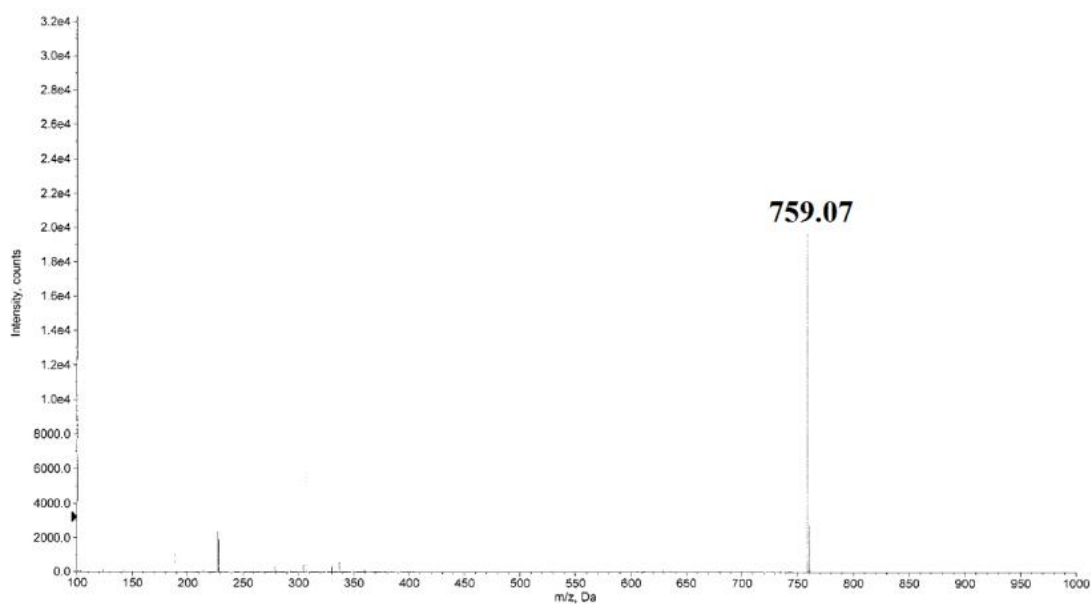


Figure 21. ESI-MS of *p*-bis (cobalticinium-1,2,3-triazolylmethyl) benzene. (759.07 Da= *p*-bis (cobalticinium-1,2,3-triazolylmethyl) benzene – PF_6^-)

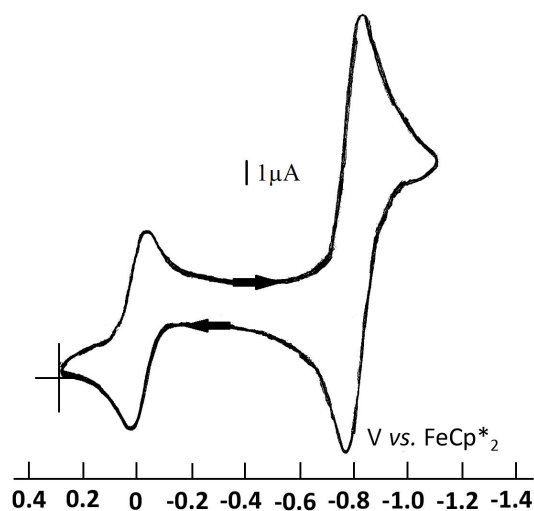


Figure 22. CV of decamethylferrocene reference and the first wave of *p*-bis (cobalticinium-1,2,3-triazolylmethyl) benzene. Internal reference: FeCp^*_2 ; Solvent: DMF; 298 K; reference electrode: Ag; working and counter electrodes: Pt; scan rate: 0.2 V/s^{-1} ; supporting electrolyte: $[\textit{n}\text{-Bu}_4\text{N}][\text{PF}_6]$ (1 M).

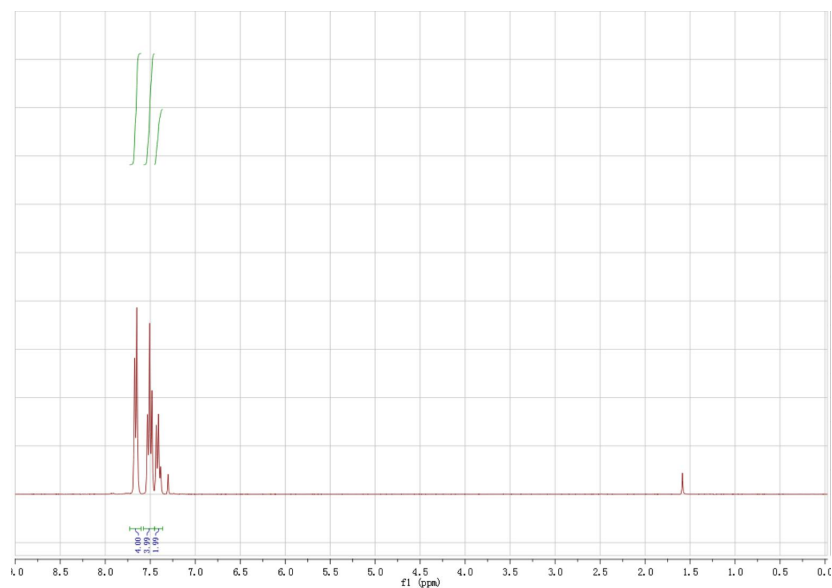


Figure 23. ^1H NMR spectrum of Biphenyl.

^1H NMR (300 MHz, CDCl_3) δ 7.66 (d, $J = 7.3$ Hz, 4H), 7.57 – 7.45 (m, 4H), 7.41 (t, $J = 7.3$ Hz, 2H).

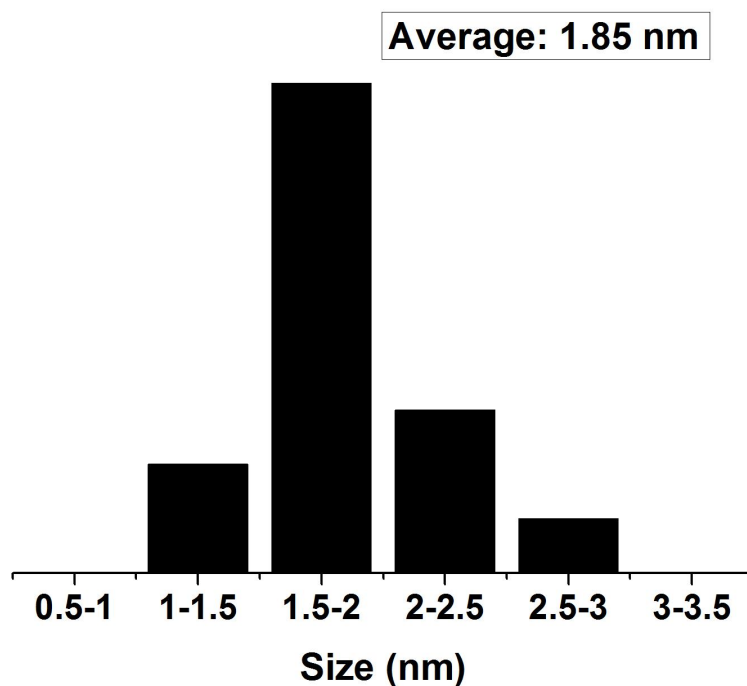


Figure 24. Size distribution of PdPEG@SBA-15.

Table 5. Recycling results of Suzuki reactions between phenylboronic acid and bromobenzene using 300 ppm of PdPEG@SBA-15 (ICP content:0.13%).

Catalytic runs	1 st	2 nd	3 rd	4 th
Yield (%)	96	85	80	65

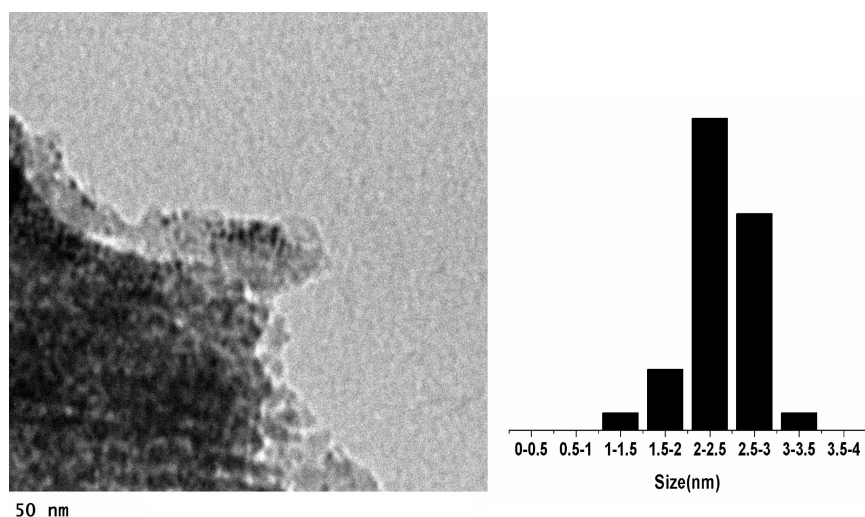


Figure 25. TEM image (left) and histogram (right) of PdPEG@SBA-15 after recycling.

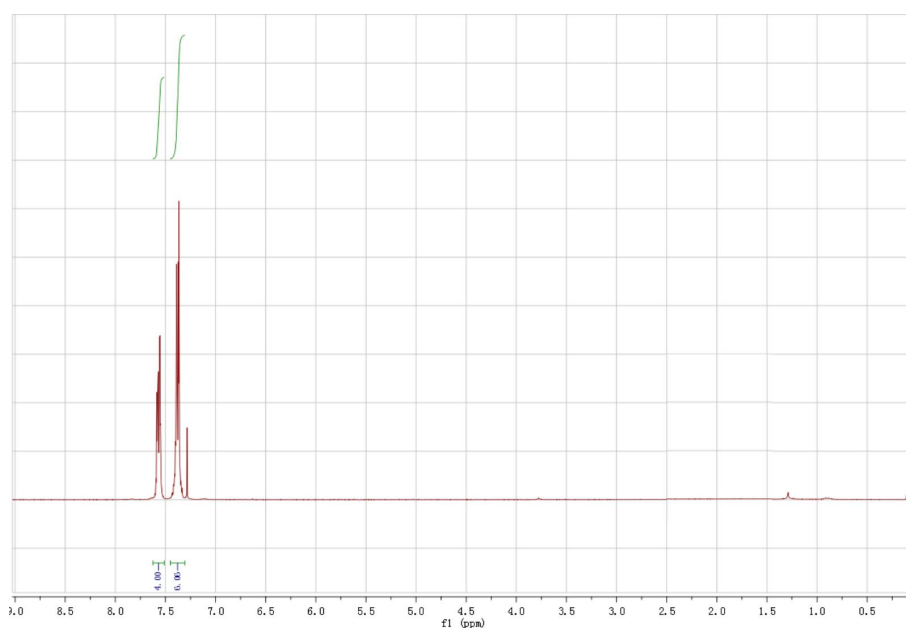


Figure 26. ^1H NMR spectrum of Diphenylacetylene.
 ^1H NMR (300 MHz, CDCl_3) δ 7.62 – 7.51 (m, 4H), 7.45 – 7.31 (m, 6H).

Table 6. Recycling results of Sonogashira reactions between iodobenzene, phenylacetylene using 1% of PdPEG@SBA-15 (ICP content:0.13 wt%) and 1% of CuPEG@SBA-15 (ICP content:0.06 wt%).

Catalytic runs	1 st	2 nd	3 rd	4 th
Yield (%)	95	92	85	70

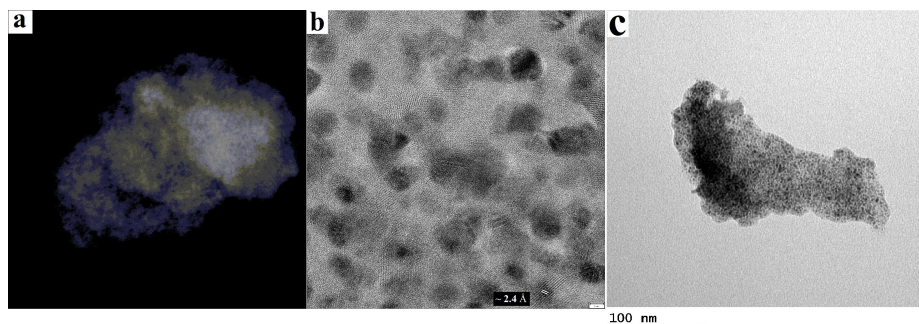


Figure 27. STEM (a) and HRTEM (b, at the same place of a) of CuPEG@SBA-15 (bar scale: 3 nm). TEM (c) of PdPEG@SBA-15.

References

- 1 Nanoparticles: From Theory to Application. Schmid, G., Ed; (Wiley-VCH, **2004**).
- 2 Y. N. Xia, Y. J. Xiong, B. Lim and S. E. Skrabalak, *Angew. Chem. Int. Ed. Engl.*, **2009**, 48, 60.
- 3 M.-C. Daniel and D. Astruc, *Chem. Rev.*, **2004**, 104, 293.
- 4 M. L. Brongersma, N. J. Halas and P. Nordlander, *Nat. Nanotechnol.*, **2015**, 10, 25.
- 5 M. Haruta, *Angew. Chem., Int. Ed.* **2014**, 53, 52.
- 6 A. Fihri, M. Bouhrara, B. Nekoueiahraki, J. M. Basset and V. Polshettiwar, *Chem. Soc. Rev.*, **2011**, 40, 5181.
- 7 A. Corma and H. Garcia, *Chem. Soc. Rev.*, **2008**, 37, 2096.
- 8 V. S. Myers, M. G. Weir, E. V. Carino, D. F. Yancey, S. Pande and R. M. Crooks, *Chem. Sci.*, **2011**, 2, 1632.
- 9 R. M. Crooks, M. Q. Zhao, L. Sun, V. Chechik and L. K. Yeung, *Acc. Chem. Res.*, **2001**, 34, 181.
- 10 E. Gross, J. H.-C. Liu, F. D. Toste and G. A. Somorjai, *Nat. Chem.*, **2012**, 4, 947.
- 11 M. Sankar, N. Dimitratos, P. J. Miedziak, P. P. Wells, C. J. Kiely and G. J. Hutchings, *Chem. Sci.*, **2012**, 3, 20.
- 12 L. M. Bronstein and Z. B. Shifrina, *Chem. Rev.*, **2011**, 111, 5301.
- 13 J. E. Mondloch, E. Bayram and R. G. Finke, *J. Mol. Catal. A*, **2012**, 355, 1.
- 14 M. T. Reetz and J. G. de Vries, *Chem. Commun.*, **2004**, 1559.
- 15 A. Balanta, C. Godard and C. Claver, *Chem. Soc. Rev.*, **2011**, 40, 4973.
- 16 C. Amiens, D. Ciuculescu-Pradines and K. Philippot, *Coord. Chem. Rev.*, **2016**, 308, 409.
- 17 V. Polshettiwar and R. S. Varma, *Green Chem.*, **2010**, 12, 743.
- 18 D. Astruc, F. Lu and J. Ruiz, *Angew. Chem. Int. Ed. Engl.*, **2005**, 44, 7852.
- 19 H. You, S. Yang, B. Ding and H. Yang, *Chem. Soc. Rev.*, **2013**, 42, 2880.
- 20 H. Goessmann and C. Feldmann, *Angew. Chem. Int. Ed.*, **2010**, 49, 1362.

- 21 M. R. Buck and R. E. Schaak, *Angew. Chem. Int. Ed.*, **2013**, 52, 6154.
- 22 Y. Lu and W. Chen, *Chem. Soc. Rev.*, **2012**, 41, 3594.
- 23 T. K. Sau and A. L. Rogach, *Adv. Mater.*, **2010**, 22, 1781.
- 24 S. Mourdikoudis and L. M. Liz-Marzan, *Chem. Mater.*, **2013**, 25, 1465.
- 25 C. Vollmer and C. Janiak, *Coord. Chem. Rev.*, **2011**, 255, 2039.
- 26 B. Lim and Y. Xia, *Angew. Chem. Int. Ed.*, **2011**, 50, 76.
- 27 J. M. Yan, X. B. Zhang, S. Han, H. Shioyama and Q. Xu, *Angew. Chem. Int. Ed.*, **2008**, 47, 2287.
- 28 L. Xiong and T. He, *Chem. Mater.*, **2006**, 18, 2211.
- 29 N. G. Connelly and W. E. Geiger, *Chem. Rev.*, **1996**, 96, 877.
- 30 H. Braunschweig, R. D. Dewhurst, K. Hammond, J. Mies, K. Radacki and A. Vargas, *Science*, **2012**, 336, 1420.
- 31 W. D. Woodul, E. Carter, R. Miller, A. F. Richards, A. Stasch, M. Kaupp, D. M. Murphy, M. Driess and C. Jones, *J. Am. Chem. Soc.*, **2011**, 133, 10074.
- 32 K. Suzuki, T. Matsuo, D. Hashizume, H. Fueno, K. Tanaka and K. Tamao, *Science*, **2011**, 331, 1306.
- 33 W. W. Brennessel, V. G. Young and J. E. Ellis, *Angew. Chem. Int. Ed.*, **2006**, 45, 7268.
- 34 C. Schottle, P. Bockstaller, R. Popescu, D. Gerthsen and C. Feldmann, *Angew. Chem. Int. Ed.*, **2015**, 54, 9866.
- 35 C. Schottle, D. E. Doronkin, R. Popescu, D. Gerthsen, J.-D. Grunwaldt and C. Feldmann, *Chem. Commun.*, **2016**, 52, 6316.
- 36 B. M. Leonard, Q. Zhou, D. Wu and F. J. DiSalvo, *Chem. Mater.*, **2011**, 23, 1136.
- 37 T. Ghosh, B. M. Leonard, Q. Zhou and F. J. DiSalvo, *Chem. Mater.*, **2010**, 22, 2190.
- 38 G. Saravanan, H. Abe, Y. Xu, N. Sekido, H. Hirata, S. Matsumoto, H. Yoshikawa and Y. Yamabe-Mitarai, *Langmuir*, **2010**, 26, 11446.
- 39 M. Schultz-Dobrick, S. K. Vijaya and M. Jansen, *J. Am. Chem. Soc.*, **2005**, 127, 12816.
- 40 Y. Tsuji, M. Kitano, K. Kishida, M. Sasase, T. Yokoyama, M. Hara and H. Hosono, *Chem. Commun.*, **2016**, 52, 14369.
- 41 D. Wang and D. Astruc, *Chem. Soc. Rev.*, **2017**, 46, 816.
- 42 C. Deraedt, L. Salmon, S. Gatard, R. Ciganda, R. Hernandez, J. Ruiz and D. Astruc, *Chem. Commun.*, **2014**, 50, 14194.
- 43 F. Fu, A. Martinez, C. Wang, R. Ciganda, L. Yate, A. Escobar, S. Moya, E. Fouquet, J. Ruiz and D. Astruc, *Chem. Commun.*, **2017**, 53, 5384.
- 44 F. E. Bailey and J. V. Koleske, *Alkylene oxides and their polymers*, Dekker, New-York, 1991, vol. **1991**, p. 27.
- 45 J. V. Jokerst, T. Lobovkina, R. N. Zare and S. S. Gambhir, *Nanomedicine*, **2011**, 6,

- 715.
- 46 J. S. Suk, Q. Xu, N. Kim, J. Hanes and L. M. Ensign, *Adv. Drug Deliv. Rev.*, **2016**, 99A, 28.
 - 47 C. Wang, R. Ciganda, L. Salmon, D. Gregurec, J. Irigoyen, S. Moya, J. Ruiz and D. Astruc, *Angew. Chem. Int. Ed.*, **2016**, 55, 1.
 - 48 X. Liu, C. Li, J. Xu, J. Lv, M. Zhu, Y. Guo, S. Cui, H. Liu, S. Wang and Y. J. Li, *Phys.Chem. C*, **2008**, 112, 10778.
 - 49 H. Kawasaki, H. Yamamoto, H. Fujimori, R. Arakawa, M. Inada and Y. Iwasaki, *Chem. Commun.*, **2010**, 46, 3759.
 - 50 R. Jin, *Nanoscale*, **2010**, 2, 343.
 - 51 A. Loupy, B. Tchoubar and D. Astruc, *Chem. Rev.*, **1992**, 92, 1141.
 - 52 N. Pradhan, A. Pal and T. Pal, *Colloids Surf. A*, **2002**, 196, 247.
 - 53 T. Aditya, A. Pal and T. Pal, *Chem. Commun.*, **2015**, 51, 9410.
 - 54 K. Esumi, K. Miyamoto and T. Yoshimura, *J. Colloid Interface Sci.*, **2002**, 254, 402.
 - 55 P. Zhao, X. Feng, D. Huang, G. Yang and D. Astruc, *Coord. Chem. Rev.*, **2015**, 287, 114.
 - 56 K. Kuroda, T. Ishida and M. Haruta, *J. Mol. Catal. A: Chem.*, **2009**, 298, 7.
 - 57 R. Ciganda, N. Li, C. Deraedt, S. Gatard, P. Zhao, L. Salmon, R. Hernandez, J. Ruiz and D. Astruc, *Chem. Commun.*, **2014**, 50, 10126.
 - 58 A. Corma and P. Serna, *Science*, **2006**, 313, 332.
 - 59 Z. Zhang, C. Shao, P. Zou, P. Zhang, M. Zhang, J. Mu, Z. Guo, X. Li and C. Wang, *Chem. Commun.*, **2011**, 47, 3906.
 - 60 A. Gangula, R. Podila, M. Ramakrishna, L. Karanam, C. Janardhana and A. M. Rao, *Langmuir*, **2011**, 27, 15268.
 - 61 I. Biondi and G. Laurenczy, *Inorg. Chem.*, **2011**, 50, 8038.
 - 62 Y. Mei, Y. Lu, F. Polzer, M. Ballauff and M. Drechsler, *Chem. Mater.*, **2007**, 19, 1062.
 - 63 S. Wunder, F. Polzer, Y. Lu, Y. Mei and M. Ballauff, *J. Chem. Phys.*, **2010**, 114, 8814.
 - 64 S. Wunder, Y. Lu, M. Albrecht and M. Ballauff, *ACS Catal.*, **2011**, 1, 908.
 - 65 P. Herves, M. Perez-Lorenzo, L. M. Liz-Marzan, J. Dzubiel, Y. Lu and M. Ballauff, *Chem. Soc. Rev.*, **2012**, 41, 5577.
 - 66 Y. Lu and M. Ballauff, *Prog. Polym. Sci.*, **2016**, 59, 86.
 - 67 J. Ruiz and D. Astruc, *D. C. R. Acad. Sci., Paris, t. 1, Série II c*, **1998**, 21.
 - 68 I. Noviantri, K. N. Brown, D. S. Fleming, P. T. Gulyas, P. A. Lay, A. F. Masters and L. Phillips, *J. Phys. Chem. B*, **1999**, 103, 6713.
 - 69 J. Ruiz, M.-C. Daniel and D. Astruc, *Can. J. Chem.*, **2006**, 84, 288.
 - 70 W. E. Geiger, *J. Am. Chem. Soc.*, **1974**, 96, 2632.

- 71 W. E. Geiger, W. L. Bowden and N. El Murr, *Inorg. Chem.*, **1979**, 18, 2358.
- 72 W. E. Geiger, *Organometallics*, **2007**, 26, 5738.
- 73 J. B. Flanagan, S. Margel, A. J. Bard and F. C. Anson, *J. Am. Chem. Soc.*, **1978**, 100, 4248.
- 74 N. Miyaura and A. Suzuki, *Chem. Rev.*, **1995**, 95, 2457.
- 75 A. Suzuki, In *Modern Arene Chemistry*; D. Astruc, Ed.; Wiley- VCH: Weinheim, Germany, **2002**; pp. 53.
- 76 K. Sonogashira, Y. Tohda and N. Hagihara, *Tetrahedron Lett.*, **1975**, 16, 4467.
- 77 K. Sonogashira, T. Yatake, Y. Tohda, S. Takahashi and N. Hagihara, *Chem. Commun.*, **1977**, 291.
- 78 R. Chinchilla and C. Najera, *Chem. Rev.*, **2007**, 107, 874.
- 79 R. Chinchilla and C. Najera, *Chem. Rev.*, **2014**, 114, 1783.
- 80 H. Doucet and J.-C. Hierso, *Angew. Chem., Int. Ed.*, **2007**, 46, 834.
- 81 A. Alimardanov, L. Schmieder-van de Vondervoort, A. H. M. de Vries and J. G. de Vries, *Adv. Synth. Catal.*, **2004**, 346, 1812.
- 82 S. Ogasawara and S. Kato, *J. Am. Chem. Soc.*, **2010**, 132, 4608.
- 83 C. Deraedt, N. Pinaud and D. Astruc, *J. Am. Chem. Soc.*, **2014**, 136, 12092.
- 84 C. Deraedt and D. Astruc, *Acc. Chem. Res.*, **2014**, 47, 494.
- 85 I. Maluendra and O. Navarro, *Molecules*, **2014**, 20, 7528.
- 86 G. M. Scheurmann, L. Rumi, P. Steurer, W. Bannwarth and R. Mulhaupt, *J. Am. Chem. Soc.*, **2009**, 131, 8262.
- 87 S.-Y. Ding, J. Gao, Q. Wang, Y. Zhang, W. G. Song, C. Y. Su and W. Wang, *J. Am. Chem. Soc.*, **2011**, 133, 19816.
- 88 A. K. Rathi, M. B. Gawande, J. Pechousek, J. Tuck, C. Airicio, M. Petr, O. Tomanec, R. Krikavova, R. S. Varma and R. Zboril, *Green Chem.*, **2016**, 18, 2363.
- 89 S. Handa, Y. Wang, F. Gallou and B. H. Lipshutz, *Science*, **2015**, 349, 1087.
- 90 S. Huebner, J. G. de Vries and V. Farina, *Adv. Syn. Catal.*, **2016**, 358, 3.
- 91 P. Das and W. Linert, *Coord. Chem. Rev.*, **2016**, 311, 1.

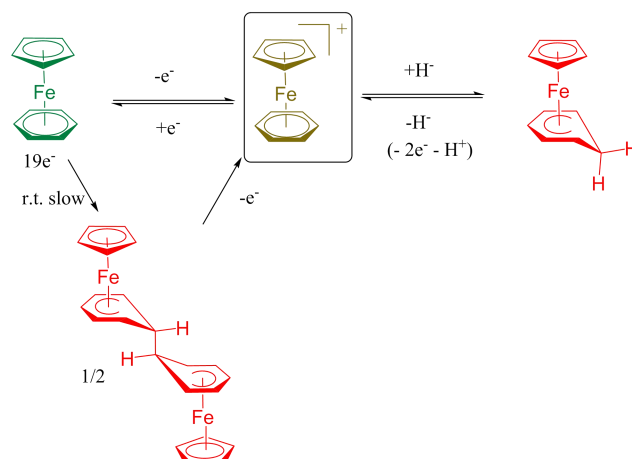
Part II: Electron- and Hydride-Reservoir Organometallics as Precursors of Catalytically Efficient Transition Metal Nanoparticles and reduced neutral gold clusters to robust nanocomposite with 18-electron sandwich complexes as counter cations.

**Chapter 3. Electron- and Hydride-Reservoir Organometallics as
Precursors of Catalytically Efficient Transition Metal
Nanoparticles in Water.**

Introduction

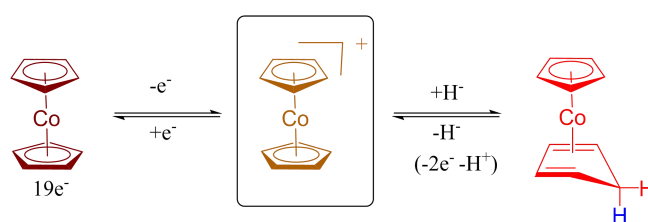
Nanoparticles (NPs) have increasingly been shown to be an essential part of academic research in catalysis; their methods of synthesis are crucial for their catalytic efficiency, and are still constantly investigated and optimized.^[1] So far, sodium borohydride has been the most frequently used reductant of precursor metal salts for the synthesis of transition metal nanoparticles (TMNPs),^[2] but organoboranes formed in organic solutions and borates formed in aqueous solution partly inhibit the catalytic activity of the TMNP surface.^[3] Therefore, a number of other reductants have been probed successfully, including H₂, NaBH₄, (SiMe₂)₆, Mg, Li or Na in liquid NH₃, and Li or Na naphthalenide in the presence of a stabilizer.^[1],4]

Here, we use as reductants electron-rich^[5] and hydride-rich neutral organometallics,^[6] for which both the reduced and oxidized forms are stable. Thus, following the reduction of the metal salts, these organometallics are found to be relatively bulky cationic stabilizers of the TMNPs. This strategy has recently been probed with ferrocenes upon the reduction of HAuCl₄ to form AuNPs with various late transition metal salts.^[7] With ferrocene itself, large AuNPs were formed owing to the weak driving force resulting from the weak reducing power of ferrocene.^[7] Here, the goal is to compare various electron-reservoir systems with very negative redox potentials with hydride donors of closely related structures. The electron-reservoir systems are known 19-electron Fe^I sandwich complexes of the [FeCp(η⁶-arene)] series (Cp = η⁵-cyclopentadienyl).^[5] The parent compound [FeCp(η⁶-C₆H₆)] is not stable at room temperature (RT) and disproportionates in THF to ferrocene and iron metal, and dimerizes slowly in pentane at RT.^[8] Derivatives with methyl groups on the arene ligand are more stable but behave similarly, except the hexamethylbenzene complex [FeCp(η⁶-C₆Me₆)], which is stable up to 100 °C and for which the X-ray crystal structure and very low ionization potential determined by He^I photoelectron spectroscopy are known (inter alia).^[5,9] Here, both the benzene and hexamethylbenzene iron complexes are used, as well as the dimer of the mesitylene complex and the hydride adducts. The three types of neutral iron sandwich compounds, 19-electron complex, dimer, and hydride derivative, all give the cationic structure upon reduction of a substrate such as the TM precursor salt, as shown in Scheme 1.



Scheme 1. Inter-relations between the CpFe (benzene) structures involved in the reduction of metal salt precursors of metal NPs.

These Fe complexes are compared to ferrocene (FeCp_2) and cobaltocene (CoCp_2)^[10] and its hydride derivative [$\text{CoCp}(\eta^4\text{-C}_5\text{H}_5)$], which also give the same cobalticinium salt upon substrate reduction (Scheme 2).^[11] Decamethylferrocene is avoided because it combines both disadvantages of a poor reductant (given its weak driving force) and bulky donor (providing long-distance, slow electron transfer), leading to the formation of large NPs, which therefore cannot be competitive in catalysis. All these organometallic complexes are used here to reduce HAuCl_4 and K_2PdCl_4 , and the AuNPs^[12] and PdNPs^[11] formed are subsequently characterized. Their formation is discussed as a function of the nature and driving force,^[13] steric constraints, and other factors provided by the organometallic reductant, and these NPs are examined as catalysts in the reduction of 4-nitrophenol by NaBH_4 ^[14] (AuNPs and PdNPs) and Suzuki-Miyaura cross C-C coupling reactions (PdNPs).^[15]



Scheme 2. Interactions between the cobalt sandwich complexes involved in the reduction of metal salts of metal salts precursors of metal NPs.

Results and Discussion

We first examine the characteristics of the organometallic reductants, in particular with the use of cyclic voltammetry. We then investigate the AuNP and PdNP syntheses and finally the reactions catalyzed by these NPs, before concluding by

comparing the qualities of the reductants. To follow the discussion, note that the NPs bear the same numbers as their organometallic precursors in Figure 1. For instance $\text{Au}^{\text{III}} + \text{R1}$ gives Au1 , and so on.

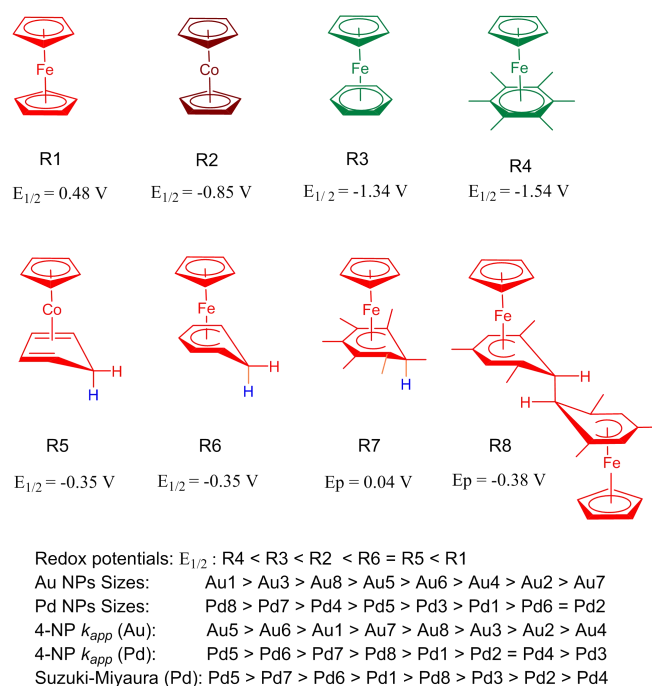


Figure 1. Various neutral electron-reservoir and hydride-reservoir organometallic sandwich complexes, denoted R1 to R8, used for the reduction of Au^{III} and Pd^{II} to AuNPs and PdNPs, respectively, their potentials $E_{1/2}$ of reversible oxidation (or E_p for irreversible oxidation), ranking of the TMNP sizes obtained using these reductants, and ranking of the TMNP efficiencies in the catalysis of 4-nitrophenol reduction (rate constants k_{app} with AuNPs and PdNPs) and Suzuki-Miyaura cross C-C coupling reactions (TONs with PdNPs). The nanoparticles are denoted by the atom (Au or Pd) followed by the same number as the number n of the reductant Rn used for their synthesis.

Electron-reservoir and hydride-reservoir reductants

Known neutral electron-reservoir and hydride-reservoir organometallic reducing agents with iron^[5,8,10] and cobalt^[11] sandwich structures were chosen as reductants of late TM salts to generate catalytically active late TMNPs. These organometallic reductants are the three 19-electron complexes of Fe and Co (electron reservoirs R2, R3, and R4) and three hydride-reservoir compounds of closely related structures (hydride reservoirs R5, R6, and R7). We wished to compare single-electron donors and single-hydride donors yielding, after reaction, the same cationic full sandwich structure. In addition, an organometallic dimer R8^[16] was included in the series of reductants, because it also provides a cationic sandwich complex similarly to the

electron-reservoir and hydride-reservoir complexes after oxidation. Finally, ferrocene^[10b,17] was also compared with the more electron-rich complexes to examine the influence of the reaction driving force with the same metallocenic molecular structure. In Figure 1, these reductants are represented with their oxidation potentials (from Refs. [5], [18], [19], or new cyclic voltammetry measurements). At the bottom of Figure 1, the reducing power ranking is shown. The ranking of the catalytic efficiencies of the TMNPs synthesized with these reductants was further determined in the present work in the reduction of 4-nitrophenol (AuNPs and PdNPs) and the Suzuki-Miyaura reaction (PdNPs). The numbers indicated for the TMNPs correspond to those of the reductants used for their synthesis (Figure 1).

The redox potentials indicated in Figure 1 are exclusively the oxidation potentials of the neutral organometallic compounds. These values were recorded using decamethylferrocene (FeCp*₂) as the internal reference^[20] or another permethylated sandwich compound as reference with the measured potential in the same region as decamethylferrocene.^[20b] All the redox potential values are indicated versus FeCp*₂.^[20] The cyclic voltammetry (CV) of complexes R5, R6, R7, and R8 that had not been reported earlier and were recorded specifically for the present study are given in Figure 2 a-d for R5-R8, respectively. The oxidation potentials of R1, R2, R3, and R4 are known,^[5,17,18] and they are recorded here as well as in Figure 2 a-d with values that are found to be analogous to those reported in the literature.

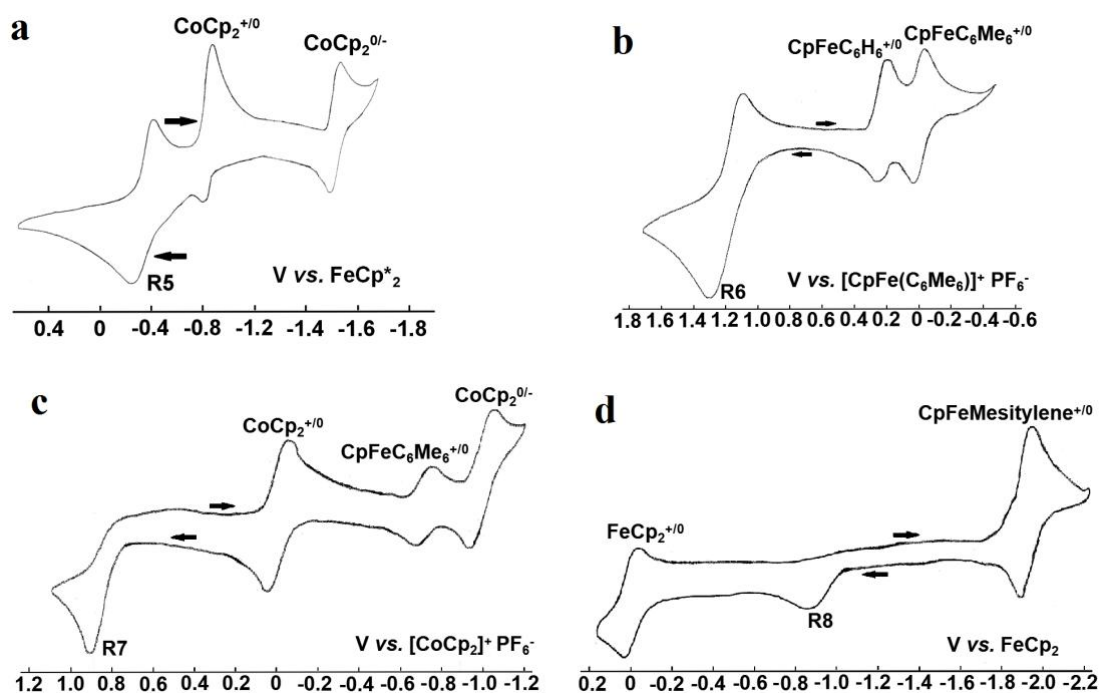


Figure 2. a: CV of R5. Internal reference: FeCp*₂; b: CV of the R6. Internal reference: [CpFeC₆Me₆] [PF₆]; E_{1/2} (R6) vs. E_{1/2} ([CpFeC₆Me₆] [PF₆]) = 1.19 V; E_{1/2} ([CpFeC₆Me₆] [PF₆]) vs. E_{1/2} (FeCp*₂) = -1.54 V, so E_{1/2} (R6) = -0.35 V; c: CV of the

R7. Internal reference: [CoCp₂] [PF₆]; E_p (R7) vs. E_{1/2} ([CoCp₂] [PF₆]) = 0.89 V, E_{1/2} ([CoCp₂] [PF₆]) vs. E_{1/2} (FeCp*₂) = -0.85 V, so E_p (R7) = 0.04 V; d: CV of the R8. Internal reference: ferrocene; E_p (R8) vs. E_{1/2} (ferrocene) = -0.86 mV, E_{1/2} (ferrocene) vs. E_{1/2} (FeCp*₂) = 0.48 mV, so E_p (R8) = -0.38 mV. Solvent: DMF; 298 K; reference electrode: Ag; working and counter electrodes: Pt; scan rate: 0.2 V · s⁻¹; supporting electrolyte: [*n*-Bu₄N][PF₆] (0.1 M).

The CV of R5 in DMF (Figure 2a) shows a partly chemically reversible wave at -0.35 V versus FeCp*₂. At this scan rate (0.2 V s⁻¹), the 17-electron species formed upon monoelectronic oxidation of R5 is shown on the CV to decompose partly with cleavage of a C-H bond of the methylene group, to give back the 18-electron cobalticinium cation. The two CV waves of the latter (Co^{III/II} and Co^{II/I}) are electrochemically reversible, as reported by Geiger.^[18] This CV shows the relatively fast oxidation of R5, but the partial chemical reversibility allows access to the E_{1/2} redox potential.^[21]

The CV of R6 (Figure 2b) shows a very similar situation to that of R5, that is, the CV wave of R6 is partly chemically reversible, allowing both the determination of the E_{1/2} redox potential of R6 at -0.35 V versus FeCp*₂, and observation of the decomposition product R3⁺ (presumably formed by *exo*-cyclic C-H bond cleavage by comparison to the oxidation of R7, *vide infra*), which appears as an electrochemically reversible wave of R3⁺⁰. The E_{1/2} values are accessible using the internal reference R4⁺ as its PF₆⁻ salt.

The CV of R7 (Figure 2c) shows an essential difference from that of its parent analogue R6, in that the CV wave of R7 is completely irreversible at the working scan rates up to 1 V s⁻¹. This indicates that the decomposition of R7 by *exo*-cyclic C-H bond cleavage to form R4⁺ is much faster than that of R6. The result is the same in both cases R6 and R7, however, in that the oxidation product is observed in the CV as a reversible wave. For R7, this oxidation product is R4⁺. A convenient internal reference in this case was cobalticinium R2⁺ introduced as the PF₆⁻ salt.

The CV of R8 (Figure 2d), similarly to that of R7, shows an irreversible wave and the appearance of a reversible wave for the oxidation product [FeCp(η⁶-mesitylene)]⁺,^[10] resulting from *exo*-cyclic C-C bond cleavage in R8 following oxidation, with the bond cleavage faster than the electrochemical timescale. It is difficult to state whether C-C cleavage occurs after the first or the second monoelectronic anodic oxidation, but the oxidation wave of R8 is very broad, which favors the second hypothesis, with an electrostatic factor provoking the second monoelectronic oxidation at a more positive potential than the first.

The knowledge of the oxidation potential order, R4 > R3 > R2 > R8 > R6 = R5 > R7 > R1, will be useful in examining the influence of the driving force of the

reductant on the AuNP and PdNP sizes and catalytic efficiencies.

Synthesis and characterization of the AuNPs and PdNPs

HAuCl_4 and K_2PdCl_4 were reduced by the organometallic reductants R1-R8 to examine the influence of the characteristics of these reductants on the sizes and catalytic efficiencies of the TMNPs formed in this way. The reductant stoichiometry in the reduction of HAuCl_4 and K_2PdCl_4 matches that of the chloride numbers in the precursor. In the case of AuNPs and PdNPs obtained by reduction using R2 (for details, see Experimental Section), the four required equivalents of CoCp_2 were injected quickly into the aqueous solution of precursor [$\text{HAuCl}_4 \cdot 3\text{H}_2\text{O}$ (1 mg) or K_2PdCl_4 (0.83 mg), 2.54×10^{-3} mmol] and poly(vinylpyrrolidone) (PVP-10000) under N_2 at RT. The solution color changed immediately after reactant mixing, indicating the formation of TMNPs. The TMNPs were further named Aux and Pdy, with x or y denoting the number of the organometallic precursor Rx or Ry in Figure 1. The UV-vis. spectra of these TMNPs are shown in Figure 6 and Figures 8-14 and 33 (Experimental Section). For example, the UV-vis. spectrum of Au2 shows both the surface plasmon band (SPB)^[12] at 500 nm, characteristic of the Au2 core, and the cobalticinium absorption at 393 nm, which is also observed in Pd2. In all cases, metalocenium absorptions are present in the UV-vis. spectra, showing that all the organometallic reductants are oxidized by the metal cations to form the metaloceniums and the metal(0) NPs, in accord with the favorable driving forces and with the CV studies.

Au7, which showed the smallest and best dispersed NPs among all the AuNPs according to the TEM (see below), was chosen for XPS measurements. The Au 4f_{7/2} peak of Au7 in the XPS spectrum (Figure 3) at around 83.3 eV is assigned to Au^0 , which is confirmed by the AuNP SPB. The XPS of Pd7 reduced by the same reductant (R7) shows that there is approximately 51 % Pd^0 and 49 % Pd^{II} .

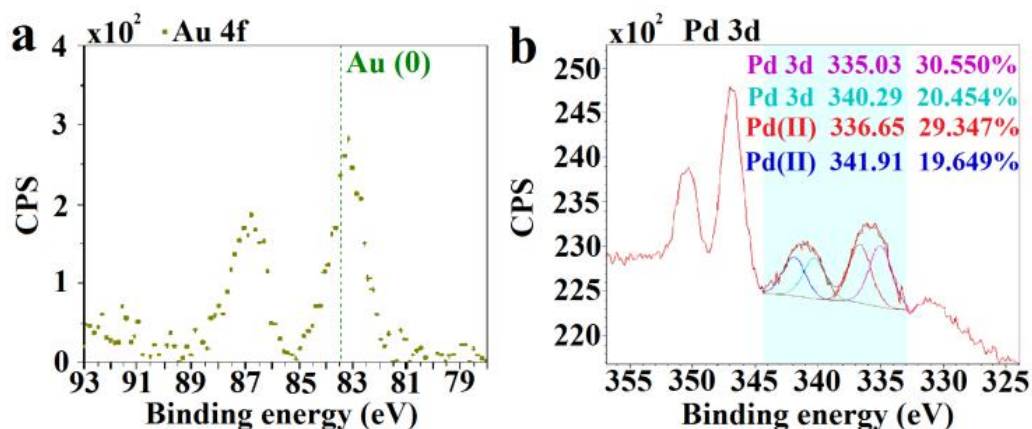


Figure 3. X-ray photoelectron spectroscopy of Au7 (a) and Pd7 (b) NPs.

All the TMNPs were characterized by TEM (Figures 4 and 5; see Figures 15 and 16,

Experimental Section, for the histograms). R1 (ferrocene)^[17] is the weakest reductant among the organometallic reductants R1–R8,^[18] and therefore, not surprisingly, large AuNPs are formed with R1. Au1 NPs were obtained with an average size of 19 nm. Except for Au1, however, it is difficult to establish a correlation between the driving force and the AuNP core size. Concerning the PdNPs, the driving force and nature, that is, electron reservoir versus hydride reservoir, does not seem to have any significant influence on the PdNP core size, which is between 3.0 and 3.8 nm; only the bulk of the reductant appears to be responsible for the formation of relatively large PdNPs in the cases of R7 (Pd7: 4.7 nm) and R8 (Pd8: 9.1 nm). The reaction between R1 and Au^{III} appears to be relatively fast, however. Conversely, no color change was observed upon injection of R1 into aqueous K₂PdCl₄; the blue color corresponding to ferricinium appeared after 1 h, indicating that more than 1h is required to obtain the Pd1 NPs.

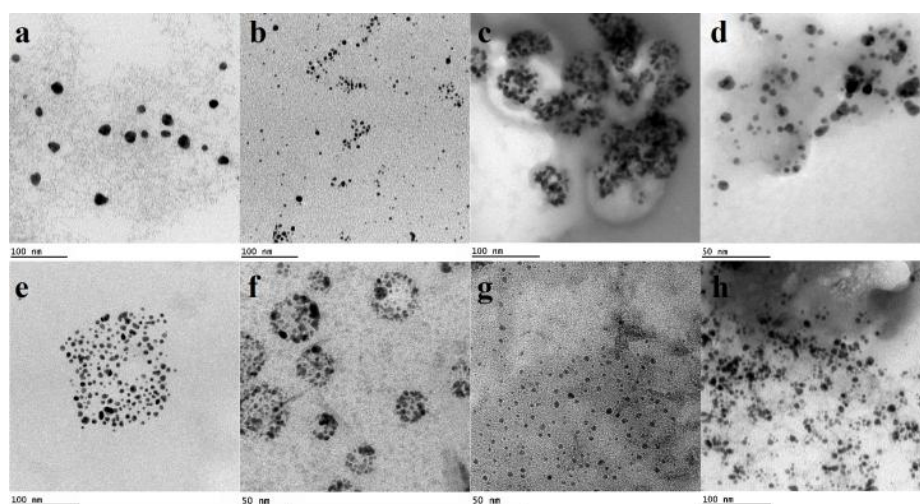


Figure 4. TEM pictures of the AuNPs: a, Au1; b, Au2; c, Au3; d, Au4; e, Au5; f, Au6; g, Au7; h, Au8.

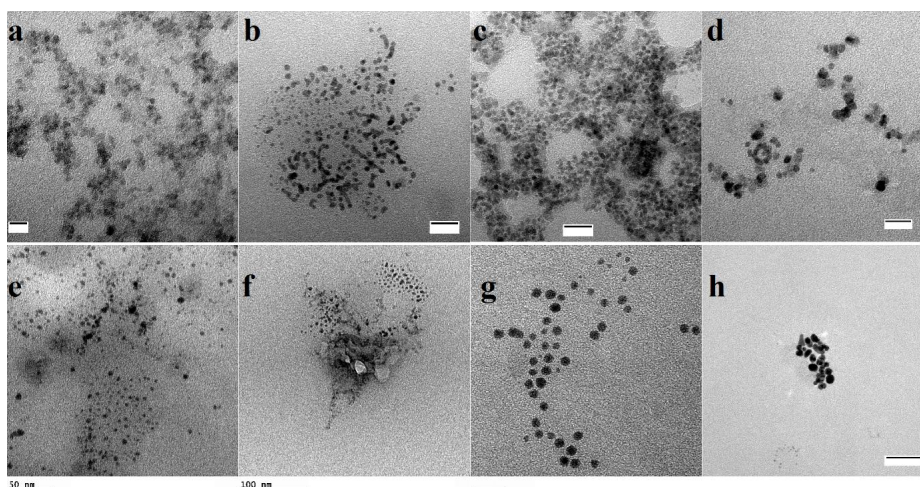
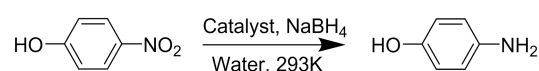


Figure 5. TEM pictures of the PdNPs: a, Pd1 (scale bar: 10 nm); b, Pd2 (scale bar: 20 nm); c, Pd3 (scale bar: 20 nm); d, Pd4 (scale bar: 15 nm); e, Pd5 ; f, Pd6 ; g, Pd7 (scale bar: 20 nm); h, Pd8 (scale bar: 50 nm).

Comparison of catalytic efficiencies of AuNPs and PdNPs for 4-nitrophenol reduction

The reduction of nitroaromatics, including nitrophenols, which are toxic and anthropogenic, to aminoaromatics, which are very useful for a wealth of applications, is an essential TM-catalyzed redox reaction.^[14,22,23] In particular, the reduction of 4-nitrophenol (4-NP) to 4-aminophenol (4-AP) by NaBH₄ is a model reaction allowing the evaluation of the activity of the catalyst surface.^[14] The absorption of 4-NP in the UV-*vis.* spectra at 400 nm thus facilitates the observation of the reaction kinetics by following the decrease of this band, whereas the increase in the absorption band at 300 nm shows the formation of 4-AP. The AuNPs (0.5 mol % Au) or PdNPs (0.02 mol % Pd) were added according to the procedure described in the Experimental Section, and the reactions were monitored by UV-*vis.* spectroscopy (Figures S17-S32, Experimental Section). The kinetic rate constants for this reaction follow the equation $k_{app} \times t = -\ln(C/C_0)$, and are shown in Table 1. The value of k_{app} decreases in the order Au5 > Au6 > Au1 > Au7 > Au8 > Au3 > Au2 > Au4 and Pd5 > Pd6 > Pd7 > Pd8 > Pd1 > Pd2 = Pd4 > Pd3. The TMNPs Au5 and Pd5 obtained from R5 are therefore the most efficient catalysts. In addition, no induction times are observed in all cases, and the PdNPs work better than the AuNPs. Pd5, with an average particle size of 3.5 nm, exhibits the highest reaction rate, $k_{app} = 38 \times 10^{-3} \text{ s}^{-1}$, with 200 ppm catalytic metal, which is the most efficient catalyst compared with recent literature concerning AuNP and PdNP catalysis in 4-NP reduction reactions (Table 2).

Table 1. 4-NP reduction by NaBH₄ catalyzed by TMNPs in water at 20°C.



Catalyst	Amount ^[a] [mol%]	D _{core} ^[b] [nm]	t ₀ ^[c] [s]	k _{app} ^[d] [10 ⁻³ s ⁻¹]
Au1	0.5	18.83	0	15.0
Au1-1	0.5	17.38	-	-
Au2	0.5	4.19	0	4.75
Au3	0.5	6.82	0	7.87
Au4	0.5	4.47	0	3.26
Au5	0.5	5.15	0	22.7
Au6	0.5	4.77	0	17.4
Au7	0.5	3.59	0	12.5
Au8	0.5	5.75	0	8.84
Pd1	0.02	3.26	0	14.6
Pd2	0.02	2.99	0	11.3
Pd3	0.02	3.31	0	7.56

Pd4	0.02	3.83	0	11.3
Pd5	0.02	3.47	0	38.0
Pd6	0.02	2.99	0	21.3
Pd7	0.02	4.72	0	16.9
Pd8	0.02	9.02	0	15.8

[a] Amount of catalysts used in the catalyzed 4-NP reduction. NaBH₄ is in excess (81 equiv.). [b] Core size (TEM) of the TMNPs. [c] Induction time. [d] Rate constant.

Table 2. Comparison of 4-NP reduction by NaBH₄ using various Pd and Au NPs catalysts in the recent literature.

Catalysts	Stabilizer	Catalyst amount (mol %)	NaBH ₄ (equiv.)	k_{app} ($\times 10^{-3}/s$)	Ref.
Pd NPs	PVP10000	0.02	81	38	This work
	PEDOT-PPS	77	excess	65.8	24
	CeO ₂	0.56	83	8	25
	G0-27 TEG dendrimer	0.2	100	4	26
	CNT/PiHP	4	80	5	27
	Fe ₃ O ₄	10	139	33	28
	Microgels	2.1	100	1.5	29
	Ppy/TiO ₂	2.6	11	12.2	30
	SBA-15	100	1000	12	31
	SPB	0.36	100	4.41	32
	Glycodendrimers	0.2	81	4.4	33
	Tristrz-PEG2000	0.2	81	24.8	34
	PEG2000	0.2	81	16.9	35
Au NPs	Tristrz-PEG2000	0.2	81	43.7	34
	PEG2000	0.2	81	15.8	35
	DMF	15	2000	7	36
	CTAB	1.25	500	6.1	37
	PEO-b-PAA	0.5	300	9.5	38
	PVP	1.56	147	10.2	39
	Cyclodextrin	17.6	44	4.56	40
	Polyaniline	17.6	44	11.7	41
	Methyl-imidazolium-based ionic polymer	20	88	33	42
	PAMAM	0.1	100	7.91	43
	PPI	0.1	100	14.7	44
	Dendritic 1,2,3-triazole terminated with peg2000	0.5	80	7	45
	Fc ⁺ -trz-Cl ⁻	0.5	80	1.1	46
	Mono-trz-PEG2000	0.2	81	14	47

	Nano-PEG550	0.2	81	7.5	47
	Polymer trz-PEG	0.2	81	11	47
	NaBH ₄	1	100	20	3b
	Abroma augusta Linnbark extract	4.3	300	7	48
	1,4-bis(terpyridine-4-yl) benzene	Not provided (0.5 mg catalyst)	100	1.9	49
	GO@NH ₂	4.5	80	35.6	50
	Fe ₂ O ₃ -GO	5	50	4.2	51
	Triazoletemini PEO	0.5	81	5.2	52

Even though Au1 is large (19 nm), it performs well and exhibits a higher reaction rate ($k_{app} = 15 \times 10^{-3} \text{ s}^{-1}$) than some Au NPs of smaller size (for instance, Au7, Au8, Au3, Au2, Au4) in the 4-NP reduction reaction. Remarkably, if ferricinium chloride is removed from the Au1 surface by dialysis (Figure 6 b, noted Au1-1), however, Au1-1 loses its activity in the reaction (no reaction in 6 h), although its SPB changes only from 600 for Au1 to 586 nm after dialysis in Au1. Then no clear color change appears, because the color is dominated by the blue plasmonic absorption, even if in the same time the absorption at 616 nm corresponding to ferricinium, which is hidden by the broad Au SPB band, is removed upon dialysis. Upon dialysis of Pd1 to Pd1-1 (Figure 33, Experimental Section), however, the color changes from green (owing to ferricinium) to faint yellow, and the clear disappearance of the ferricinium absorption in the UV-*vis.* spectrum is characteristic of the removal of ferricinium. Interestingly, the average AuNP core size does not change significantly from Au1 to Au1-1 (Figure 34, Experimental Section), indicating that the removal of ferricinium chloride and cancelling of catalytic properties in 4-NP reduction upon dialysis does not influence the AuNP core size. Although the reaction mechanism of 4-NP reduction is not precisely known,^[14] Ballauff's group suggested rearrangement of the substrates 4-NP and NaBH₄ at the NPs surface on the basis of the Langmuir-Hinshelwood (LH) kinetic model.^[22] Ferricinium appears to be an excellent electrostatic stabilizer, which, using its large bulk, protects the core surface from inhibition by the PVP polymer. If ferricinium is close to the surface, it is not bonded to it, allowing easy approach and binding by the substrate and hydride, and the PVP stabilizer appears to be remote from the surface, which allows free approach of the substrate and hydride. On the other hand, in the absence of ferricinium, the PVP binds the AuNP core surface directly, provoking inhibition of the catalysis of 4-NP reduction.

The effect of cobalticinium in this reaction was researched with the best Au5 NPs upon dialysis (Figure 6 c,d). Following this process, the UV-*vis.* absorption at 394 nm (cobalticinium) is missing, which indicates that cobalticinium is also removed by dialysis. Then the NPs become PVP-stabilized Au5-1. Even though the SPB and color

do not change much, the k_{app} value of the 4-NP reduction reaction decreases from $22.7 \times 10^{-3} \text{ s}^{-1}$ (Au5) to $3.1 \times 10^{-3} \text{ s}^{-1}$ (Au5-1) with the same catalytic amount (Figure 35, Experimental Section). The disappearance of the electrostatically protecting metallocenium upon dialysis provokes the cancellation or decrease of the catalytic properties of the AuNPs, which shows the unique role of the metallocenium in NP catalysis. It also illustrates the fact that approach to the NP core surface is crucial for the catalytic reaction and is facilitated by the presence of the metallocenium cation.

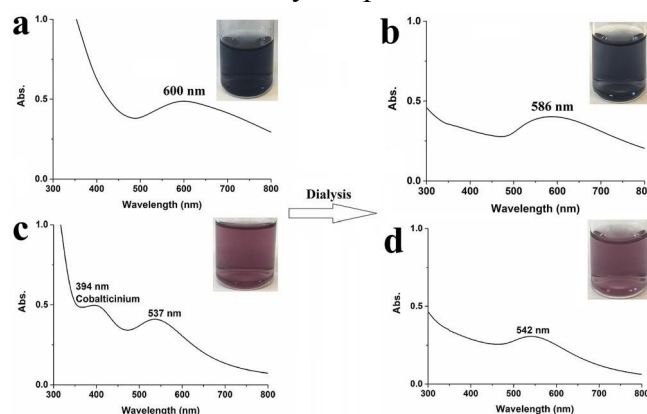
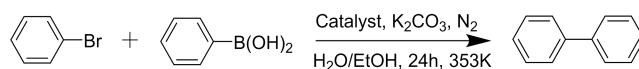


Figure 6. UV-*vis* spectra and photographs of Au1 and Au5 before (a and c) and Au1-1 and Au5-1 after (b and d) dialysis.

Comparison of catalytic efficiency of PdNPs for the Suzuki–Miyaura coupling reaction

The catalytic activities of PdNPs were examined in one of the representative Pd-catalyzed reactions, the Suzuki-Miyaura cross C-C bond coupling, which plays a key role in the construction of carbon backbones and has attracted research interest with extensive applications in organic synthesis.^[15] The amounts of Pd catalysts reported in the literature are very variable, and there are several examples of Suzuki-Miyaura reactions reported with catalyst amounts of the order of parts per million.^[53]

Indeed, the minimization of the amount of Pd catalyst in these reactions is an essential goal toward possible applications in industrial synthesis. Another key parameter for “green chemistry” is the avoidance of the use of toxic and expensive ligands such as phosphines, which are often found in organometallic catalysts. This is achieved well with PdNPs, especially if they are used in very small amounts. PVP-stabilized Pd1-Pd8 NPs are utilized here to catalyze the Suzuki-Miyaura reaction between bromobenzene and phenylboronic acid at 80 °C under N₂ with 300 ppm Pd catalyst (Table 3). The three PdNPs synthesized from the hydride reservoirs R5, R6, and R7 are the three best catalysts in the series, with Pd5 again the best catalyst. Pd5 catalyzes the Suzuki-Miyaura cross C-C bond coupling between bromobenzene and phenylboronic acid with 99 % isolated yield and a TOF of 13.8 h⁻¹ (Table 3).

Table 3. Suzuki–Miyaura reaction catalyzed by PdNPs.^[a]

Catalysts	Conversion (%) ^[b]	Yield (%) ^[c]	TON	TOF (h ⁻¹)
Pd1	58	52	173.3	7.2
Pd2	30	26	86.7	3.6
Pd3	32	27	90	3.8
Pd4	15	10	33.3	1.4
Pd5	100	99	330	13.8
Pd6	70	64	213.3	8.9
Pd7	87	81	270	11.3
Pd8	45	42	140	5.8

[a] Reaction conditions: bromobenzene (0.5 mmol), phenylboronic acid (0.75 mmol), K₂CO₃ (1 mmol), 300 ppm catalysts, H₂O/EtOH: 1:1 mL, 80 °C, 24 h, under N₂. [b] ¹H NMR conversion. [c] Isolated yield.

From the comparison of all the AuNPs and PdNPs in the 4-NP reduction and Suzuki-Miyaura reactions, Au5 and Pd5 always show the best activities. On the other hand, the activities of Au2 and Pd2 are rather poor. R2 is a stronger electron-transfer reductant than R5 according to the CV data, and the NP size orders Au2 < Au5 and Pd2 < Pd5 (Figures 4 and 5) are fully consistent with the order of the driving forces. The oxidized form of R2 and R5 is the same, for example, cobalticinium (Figure 2a, and Figures 8 and 11, Experimental Section), showing that the hydride reservoirs give better results than electron reservoirs for the catalytic activity of AuNPs and PdNPs in these catalytic reactions. A possible explanation is that hydride reservoirs transfer hydrides to transition metal cations, which is followed by fast reductive elimination to metal(0), and further hydride transfer makes the NP surface very reactive. On the other hand, electron transfer to cationic transition metals is followed by more significant structural reorganization before the metal(0) state is reached.

Conclusions

The parameters of the organometallic reductants of HAuCl₄ and K₂PdCl₄ to form AuNPs and PdNPs, including driving force, bulk, and electron- versus hydride-reservoir nature, have been scrutinized for their potential influence on the catalytic efficiency. The hydride-reservoir complexes [CoCp(η⁴-C₅H₆)], [FeCp(η⁵-C₆H₇)], and [FeCp(η⁵-C₆H₆H)] are shown here to form AuNPs and PdNPs in

the presence of PVP, giving better catalytic results than those formed using the electron-reservoir complexes FeCp_2 , CoCp_2 , $[\text{FeCp}(\eta^6\text{-C}_6\text{H}_6)]$, and $[\text{FeCp}(\eta^6\text{-C}_6\text{Me}_6)]$ under the same conditions. The best results for both 4-nitrophenol reduction by NaBH_4 and Suzuki-Miyaura cross C-C coupling are obtained with AuNPs and PdNPs synthesized through reduction of the precursors HAuCl_4 and K_2PdCl_4 by $[\text{CoCp}(\eta^4\text{-C}_5\text{H}_6)]$. For the former reaction, the PdNPs are somewhat more efficient than the AuNPs. Indeed, the PdNPs obtained from this complex show the high reaction rate constant $k_{\text{app}} = 38 \times 10^{-3} \text{ s}^{-1}$ with 200 ppm catalyst. This data shows that it is the most efficient catalyst compared with recent literature concerning AuNPs and PdNPs in the catalysis of 4-NP reduction. These PdNPs also catalyze the Suzuki-Miyaura coupling between bromobenzene and phenylboronic acid with 99 % isolated yield and a TOF of 13.8 h^{-1} . The bulky reductants R4 and R7 with a permethylated ring and the dimer R8 give less satisfactory catalytic efficiencies than the parent complexes, apparently because of steric problems around the NP core. The presence of the PVP stabilizer in the NP synthesis decreases the catalytic activities of the NP catalysis considerably. The presence of the cationic sandwich complex that surrounds the NP cores is responsible for the high catalytic efficiency, seemingly because the sandwich salt inhibits close contact between the PVP polymer and the NP core. Meanwhile, a certain proportion of the chloride counter anions of the cationic sandwich units are coordinated to the AuNP core. For instance, dialysis of the NPs removes the metallocenium chloride, leaving the PVP-stabilized NP core size unchanged, and these metallocenium-free AuNPs then show a loss of or decrease in the catalytic efficiency. This shows that the carefully optimized mode of NP synthesis is excellent and very efficient for catalytic applications. Note that all the organometallic sandwich complexes surrounding the NPs have absolutely no catalytic activities by themselves, because they are robust 18-electron cationic complexes that do not undergo any decoordination to active 16- electron species.^[10c]

Experimental Section

General data

UV-vis. absorption spectra were measured with a Perkin-Elmer Lambda 19 UV-vis. spectrometer. NMR spectra were recorded at 25 °C with a Bruker AC 400, or 300 (400 or 300 MHz). All the chemical shifts were reported in parts per million (δ , ppm) with reference to Me_4Si for the ^1H NMR spectra. Transmission Electron Microscopy (TEM) images were recorded using A TEM JEOL JEM 1400 (120 kV). X-ray photoelectron spectra (XPS): System: SPECS SAGE HR, X-Ray source: Mg $\text{K}\alpha$ non-monochromatic, operated at 12.5 kV and 250 W. Take-off angle 90°, at $\sim 10^{-8}$ Torr.

Pass energy for survey spectra 30 eV, 15 eV for narrow scans. Analysis: spectra are calibrated to CC carbon 285 eV. Analysis consisted of Shirley background subtraction. Peaks were fitted with symmetrical Gaussian-Lorentzian (GL) line shapes. Sample was dispersed on silica substrate and evaporated prior to measurement. Cyclic voltammetry (CV) studies: all electrochemical measurements were recorded under nitrogen atmosphere. Conditions: supporting electrolyte: [*n*-Bu₄N][PF₆], 0.1 M; solvent: DMF; working and counter electrodes: Pt; reference electrode: Ag; internal reference: FeCp*₂ (Cp* = η⁵-C₅Me₅); scan rate: 0.200 V · s⁻¹. Flash column chromatography was performed using silica gel (300-400 mesh).

Tetrahydrofuran (THF) and pentane were heated at reflux and freshly distilled, and milli-Q water (18.2 MΩ) was used for all the NP preparations.

Synthesis of Au and Pd nanoparticles

From 19 e sandwich complexes; example of R2: In a Schlenk flask, Na/Hg amalgam was prepared in dry THF under N₂ at RT. Then, cobalticinium hexafluorophosphate [CoCp₂][PF₆] (Cp = η⁵-C₅H₅) (50 mg) and THF (20 mL) were added, and the mixture was stirred for 2 h. The solution changed color progressively from yellow to brown, indicating the formation of cobaltocene [CoCp₂]. The solvent was removed in vacuo, providing the crude product, which was redissolved in pentane to eliminate the insoluble NaPF₆ salt by cannula filtration.

Finally, pentane was removed in vacuo, and the product was redissolved again in dry THF (20 mL) for further use. HAuCl₄·3H₂O (1 mg, 2.54 × 10⁻³ mmol) or K₂PdCl₄ (0.83 mg, 2.54 × 10⁻³ mmol) and PVP-10000 (2 equiv.) were dissolved in 20 mL milli-Q water under nitrogen in a standard Schlenk flask and stirred for 30 min. Then a fresh [CoCp₂] solution (4 equiv.) was injected quickly into the Schlenk flask, and the color change of the solution indicated the formation of the NPs Au₂ or Pd₂.

The syntheses of AuNPs and PdNPs from the other 19e sandwich compounds [FeCp(η⁶-C₆H₆)] (R3, synthesized from [FeCp(η⁶-C₆H₆)] [PF₆] as starting materials at 0°C) and [FeCp(η⁶-C₆Me₆)] (R4, synthesized from [FeCp(η⁶-C₆Me₆)] [PF₆] as starting materials at RT), and from ferrocene (R1, used as purchased) were performed in a similar way, except that the reaction between R1, K₂PdCl₄, and PVP-10000 required stirring for 2h to form the Pd₁ NPs.

From hydride-reservoir sandwich complexes; example of R5: Cobalticinium hexafluorophosphate [CoCp₂][PF₆] (Cp = η⁵-C₅H₅) (50 mg) and THF (20 mL) were added in a Schlenk flask under N₂ at RT. Then, NaBH₄ (5 equiv.) was added, and the mixture was stirred for 2 h. The solution changed color progressively from yellow to red, indicating the formation of R5. The solvent was removed in vacuo, providing the crude product, which was redissolved in pentane to eliminate the insoluble NaPF₆ salt by cannula filtration. Finally, pentane was removed in vacuo, and the product was redissolved again in dry THF (20 mL) for further use.

H₂AuCl₄·3H₂O (1 mg, 2.54 × 10⁻³ mmol) or K₂PdCl₄ (0.83 mg, 2.54 × 10⁻³ mmol) and PVP10000 (2 equiv.) were dissolved in Milli-Q water (20 mL) under nitrogen in a standard Schlenk flask and stirred for 30 min. Then, a fresh R5 solution (4 equiv.) was injected quickly into the Schlenk flask, and the color change of the solution indicated the formation of Au5 or Pd5 nanoparticles.

Au and Pd NPs were formed similarly from other H-donor sandwich compounds, R6 (synthesized from [FeCp(η⁶-C₆H₆)]PF₆) as starting materials at 0 °C) and R7 (synthesized from [CpFe(η⁶-C₆Me₆)]PF₆) as starting materials at 50 °C).

From the dimer R8: In a Schlenk flask, Na/Hg amalgam was prepared in dry THF under N₂ at RT. Then, [CpFe(η⁶-mesitylene)]PF₆ (50 mg) and THF (20 mL) were added, and the mixture was stirred for 2 h at 0 °C. The solution changed color progressively from yellow to forest green, indicating the formation of [CpFe(η⁶-mesitylene)]. The solvent was removed in vacuo, providing the crude product, which was redissolved in pentane to eliminate the insoluble NaPF₆ salt by cannula filtration. Then, the pentane solution was kept overnight to allow spontaneous dimerization to occur. Finally, pentane was removed in vacuo, and the red product (R8) was redissolved in dry THF (20 mL) for further use.

H₂AuCl₄·3H₂O (1 mg, 2.54 × 10⁻³ mmol) or K₂PdCl₄ (0.83 mg, 2.54 × 10⁻³ mmol) and PVP-10000 (2 equiv.) were dissolved in milli-Q water (20 mL) under nitrogen in a standard Schlenk flask and stirred for 30 min. Then, a fresh R8 solution (4 equiv.) was injected quickly into the Schlenk flask, and the color change of the solution indicated the formation of Au8 or Pd8 NPs.

Reduction of 4-NP by NaBH₄ (at 20 °C)

Generally, 4-NP (1 equiv.) was mixed with excess NaBH₄ (81 equiv.) in water under air. The color of the solution changed from light yellow to dark yellow owing to the formation of the 4-nitrophenolate ion. Then, a solution containing AuNPs (0.5 mol %) or Pd NPs (200 ppm) was added to the mixture. The solution quickly lost its dark yellow color with time, and the progress of the reaction was monitored by UV-vis. spectroscopy (40 s for each run).

Suzuki-Miyaura reaction catalyzed by PdNPs

A dry Schlenk flask was charged with phenylboronic acid (0.75 mmol), bromobenzene (0.5 mmol), and K₂CO₃ (1 mmol). Catalytic amounts of a solution of PdNPs were added successively, then H₂O and EtOH were added to make a total solvent volume of 2 mL (H₂O/EtOH = 1:1, vol/vol). The suspension was then allowed to stir under N₂ for 24 h at 80 °C. After the reaction, the Schlenk flask was cooled to RT, the mixture was extracted three times with diethyl ether (3 × 20 mL), the organic phase was dried over Na₂SO₄, and the solvent was removed in vacuo. The crude product was checked by ¹H NMR to calculate the conversion. In parallel, the reaction

was checked using TLC in only petroleum ether as eluent. Purification by flash chromatography column was conducted with silica gel as the stationary phase and petroleum ether as the mobile phase.

Cyclic voltammetry (CV) of the decamethylferrocene reference, [CpFeC₆Me₆] [PF₆] and the first wave of [CoCp₂] [PF₆].

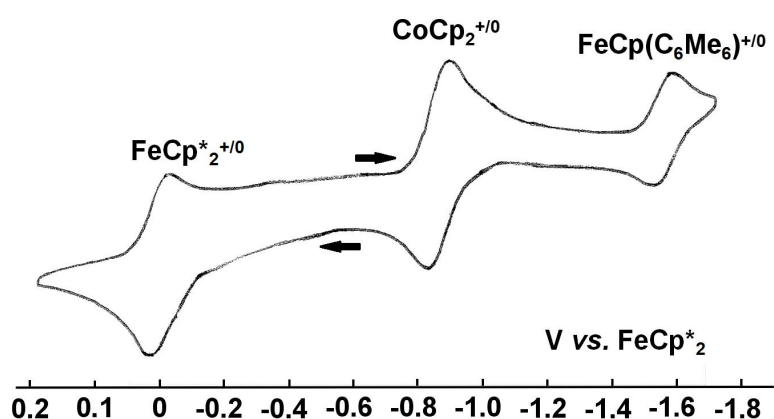


Figure 7. CV of the decamethylferrocene reference, [CpFeC₆Me₆] [PF₆] and the first wave of [CoCp₂] [PF₆]. Internal reference: FeCp*₂; solvent: DMF; 298 K; reference electrode: Ag; working and counter electrodes: Pt; scan rate: 0.2 V/s⁻¹; supporting electrolyte: [*n*-Bu₄N][PF₆] (0.1 M).

UV-vis spectra of the Au and Pd nanoparticles.

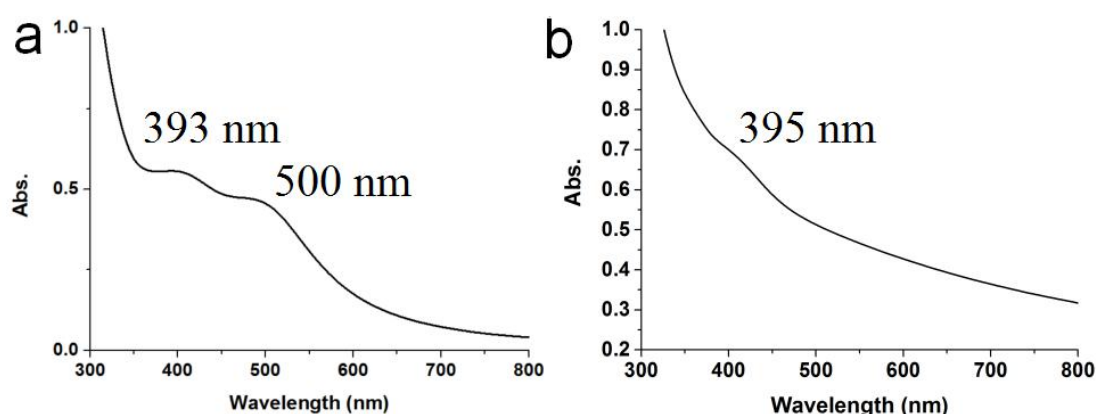


Figure 8. UV-vis spectra of Au₂(a) and Pd₂(b) nanoparticles.

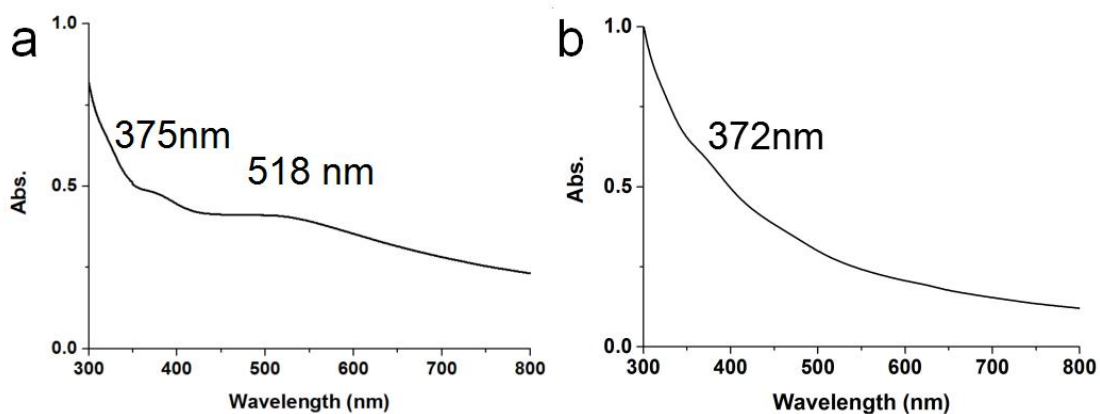


Figure 9. UV-*vis* spectra of Au₃(a) and Pd₃(b) nanoparticles.

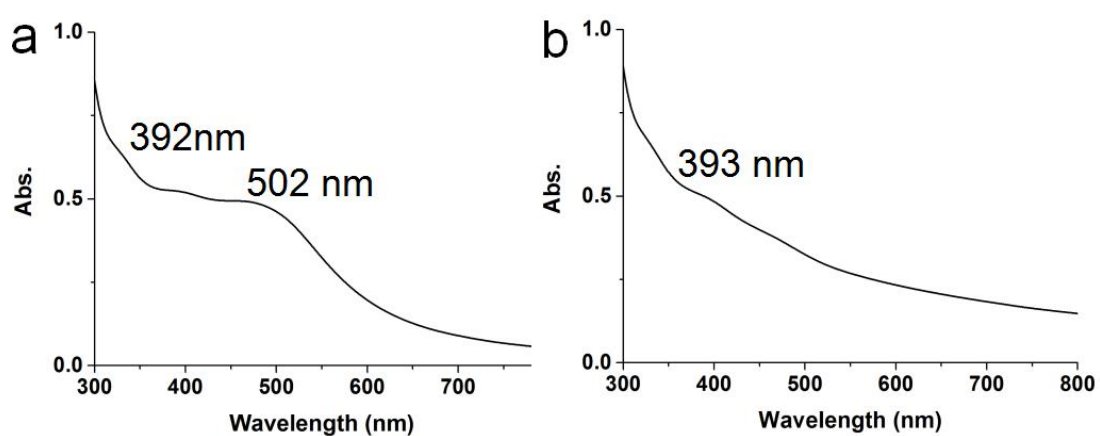


Figure 10. UV-*vis* spectra of Au₄(a) and Pd₄(b) nanoparticles.

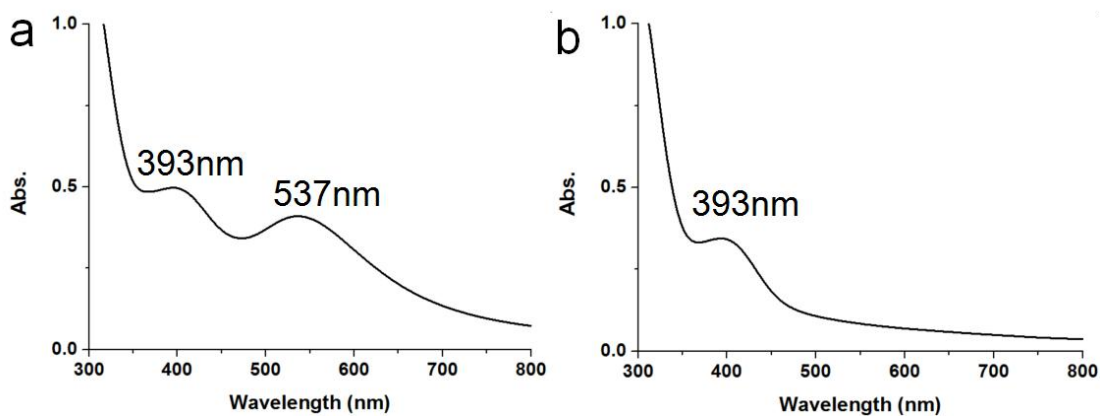


Figure 11. UV-*vis* spectra of Au₅(a) and Pd₅(b) nanoparticles.

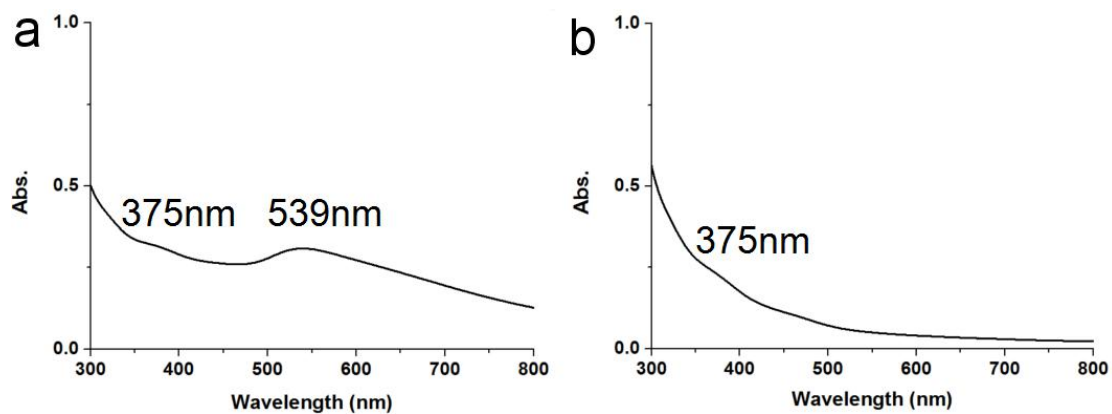


Figure 12. UV-*vis* spectra of Au6(a) and Pd6(b) nanoparticles.

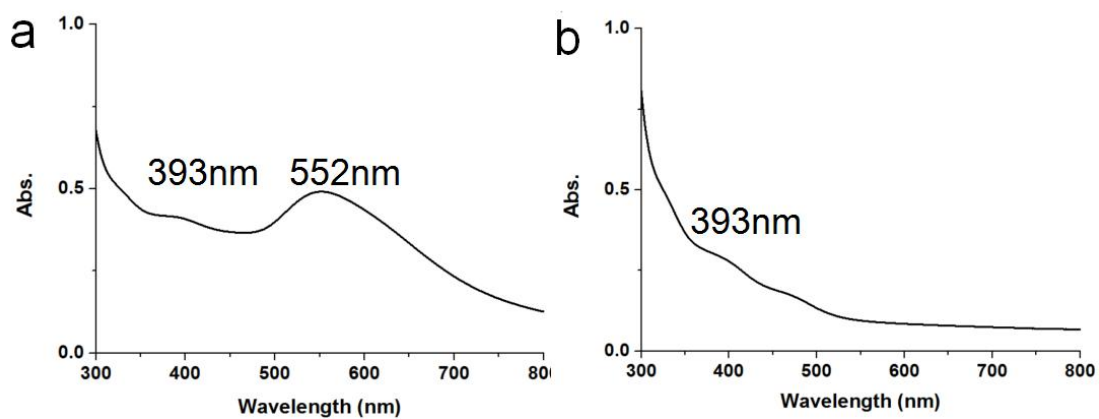


Figure 13. UV-*vis* spectra of Au7(a) and Pd7(b) nanoparticles.

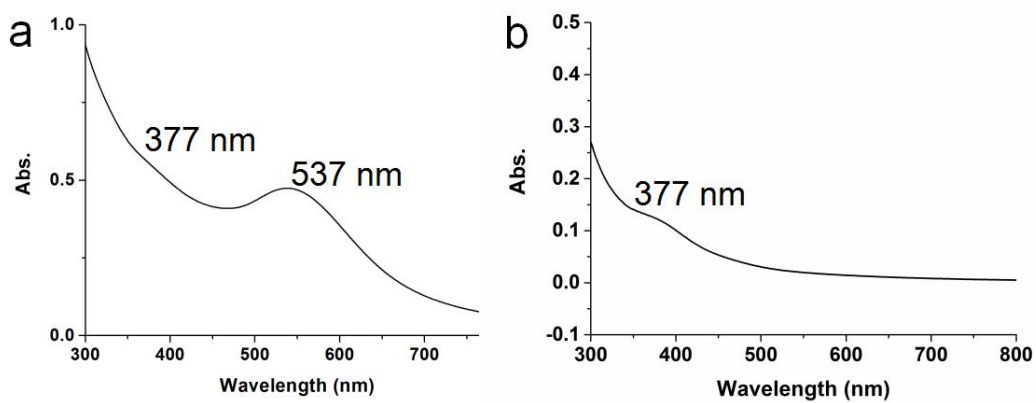


Figure 14. UV-*vis* spectra of Au8(a) and Pd8(b) nanoparticles.

Histograms of the Au and Pd nanoparticles

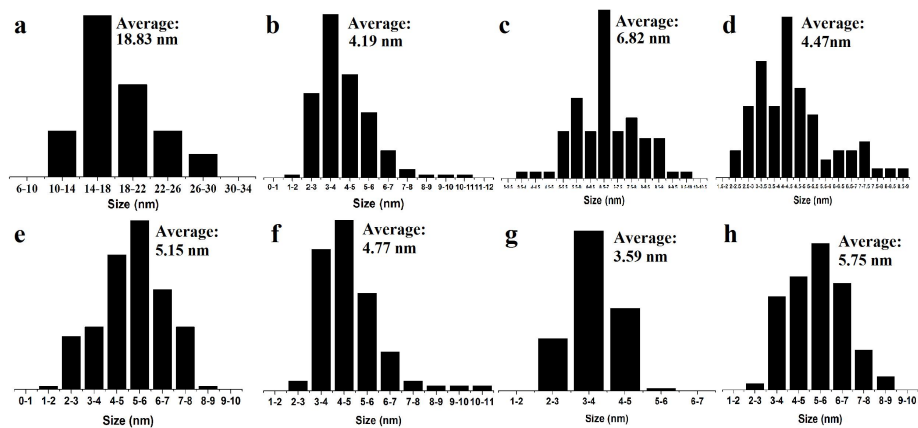


Figure 15. Histogram of Au nanoparticles: a, Au1; b, Au2; c, Au3; d, Au4; e, Au5; f, Au6; g, Au7; h, Au8.

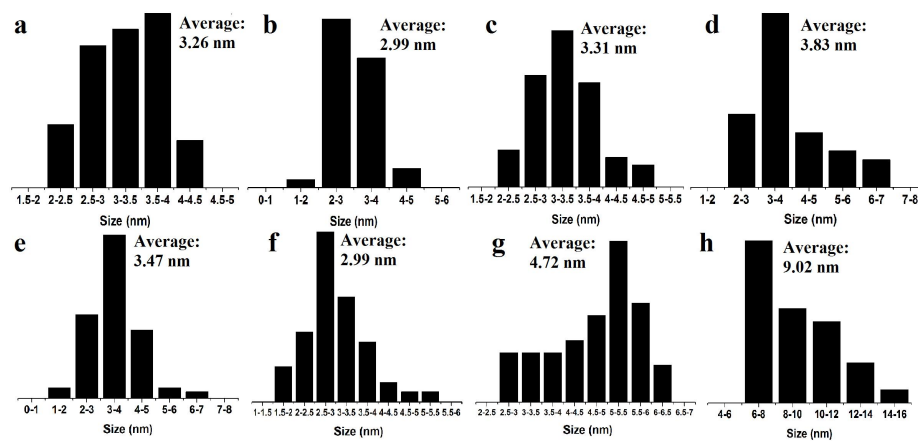


Figure 16. Histogram of Pd nanoparticles: a, Pd1; b, Pd2; c, Pd3; d, Pd4; e, Pd5; f, Pd6; g, Pd7; h, Pd8.

UV-vis. spectra of the 4-NP reduction and reaction rate (k_{app})

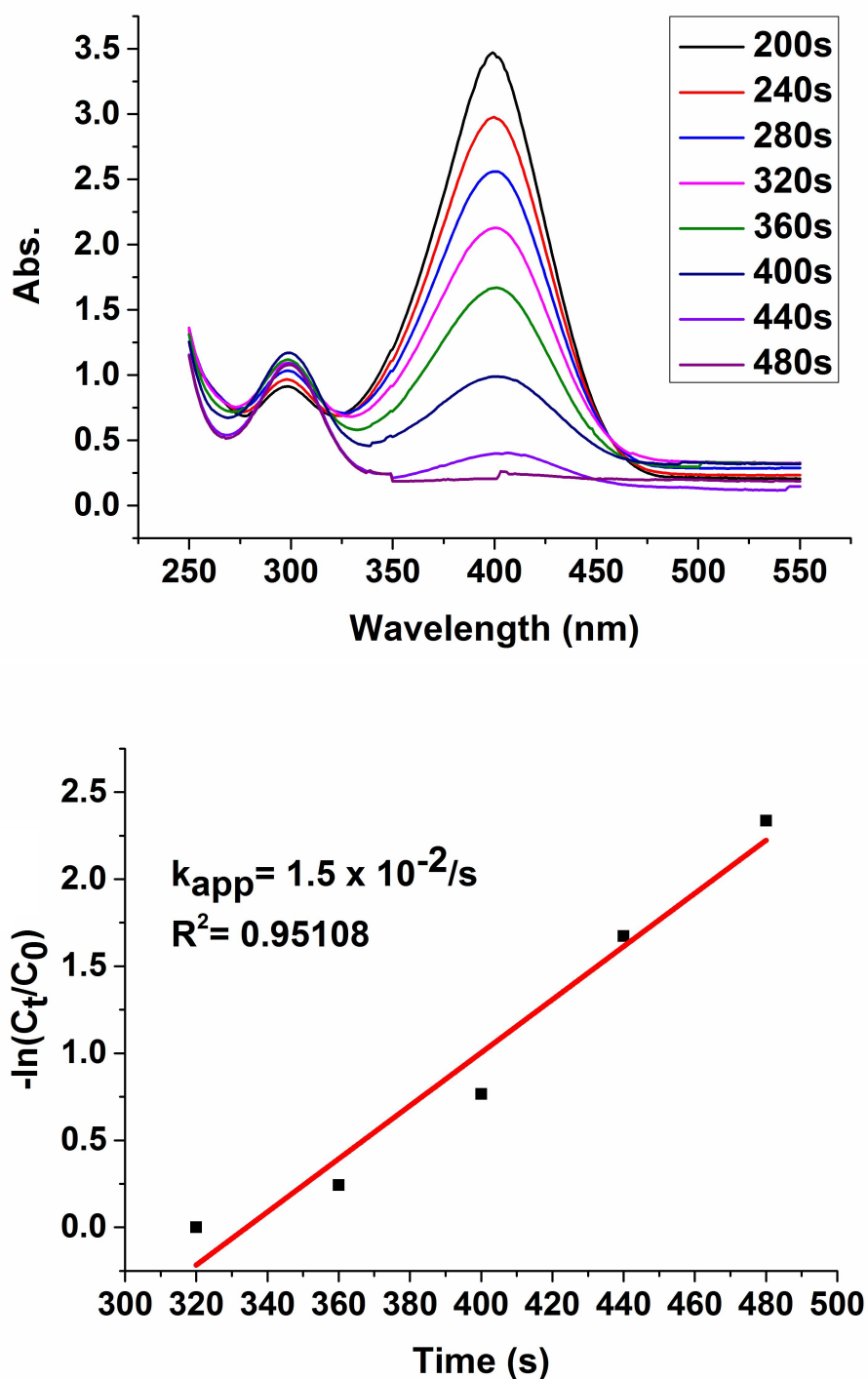


Figure 17. UV-vis. spectra of the 4-NP reduction by NaBH_4 catalyzed by AuI (top); consumption rate of 4-NP: $-\ln(C_t/C_0)$ vs reaction time (bottom).

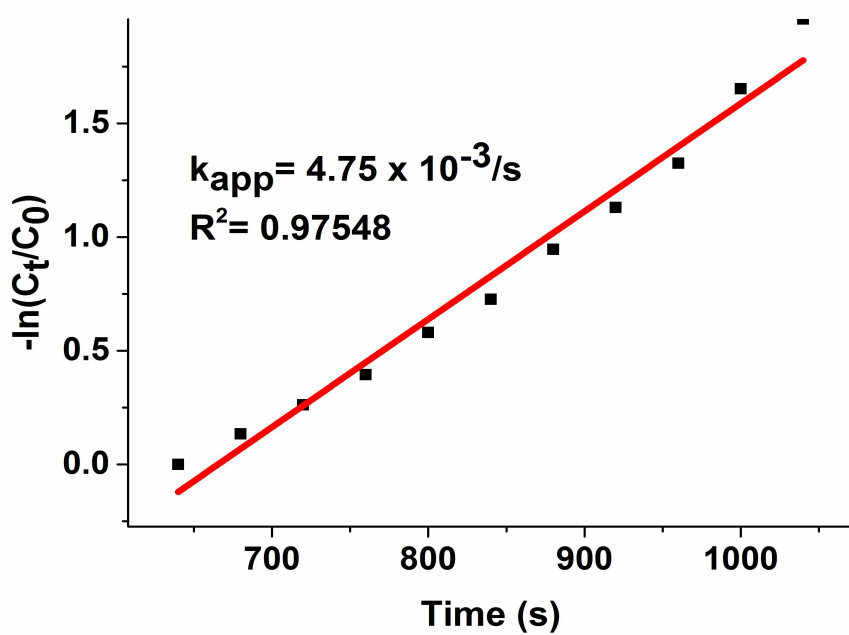
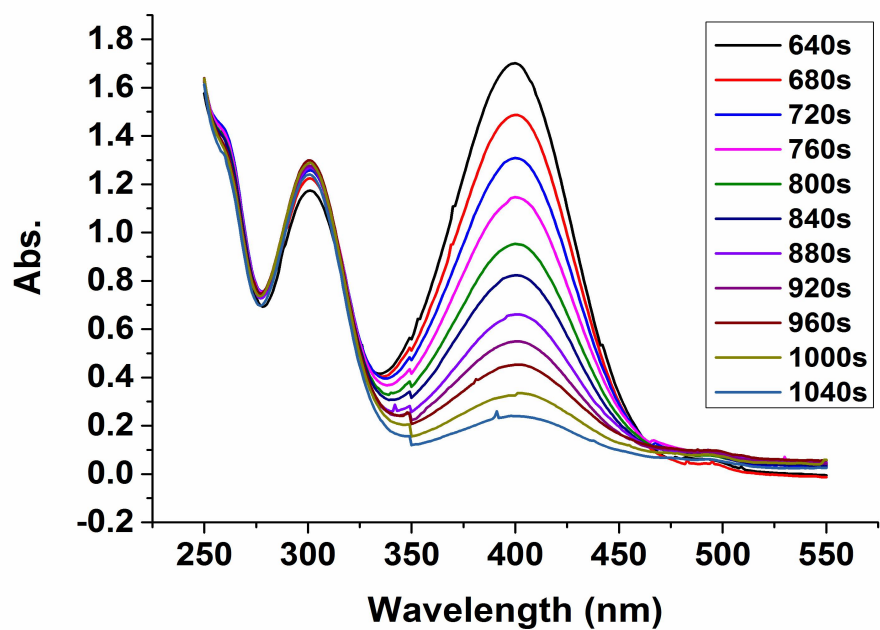


Figure 18. UV-*vis.* spectra of the 4-NP reduction by NaBH₄ catalyzed by Au₂ (top); consumption rate of 4-NP: $-\ln(C_t/C_0)$ vs reaction time (bottom).

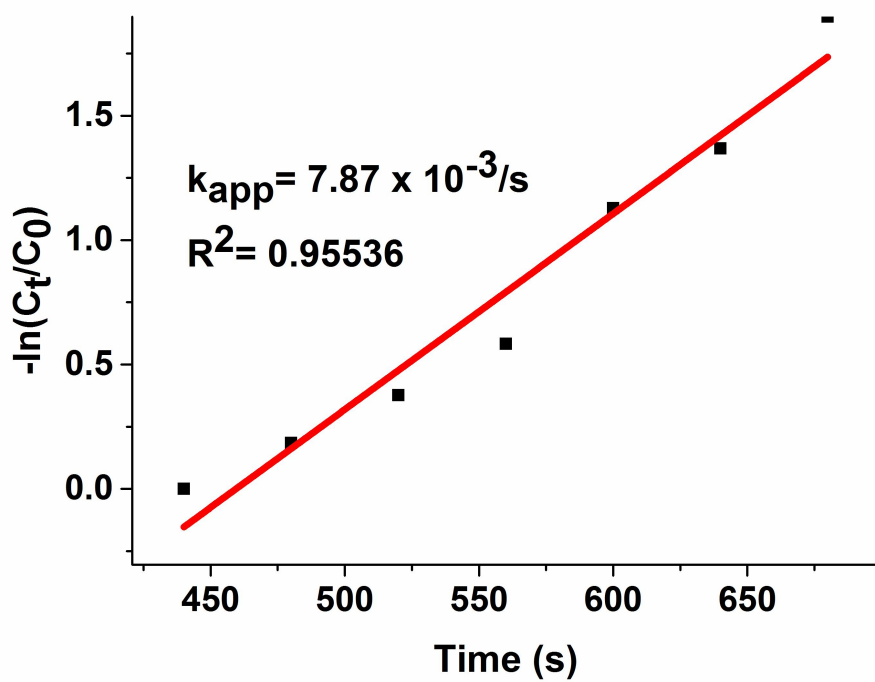
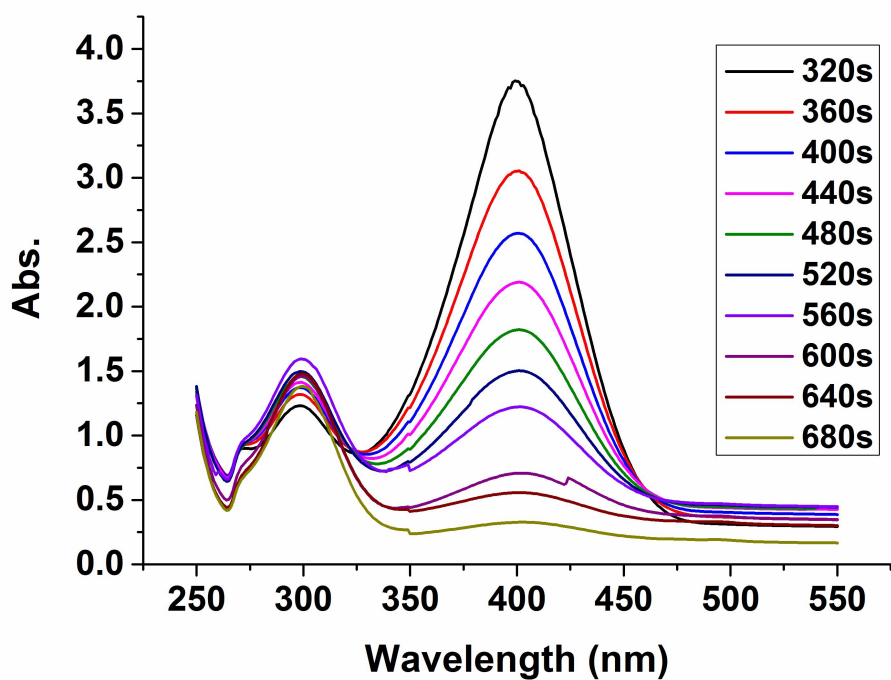


Figure 19. UV-*vis.* spectra of the 4-NP reduction by NaBH₄ catalyzed by Au₃ (top); consumption rate of 4-NP: $-\ln(C_t/C_0)$ vs reaction time (bottom).

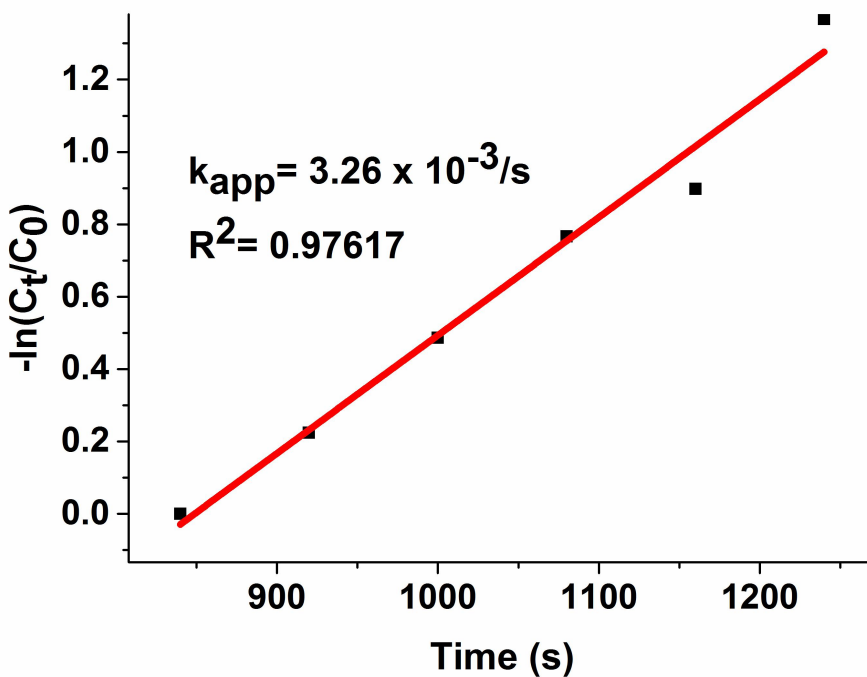
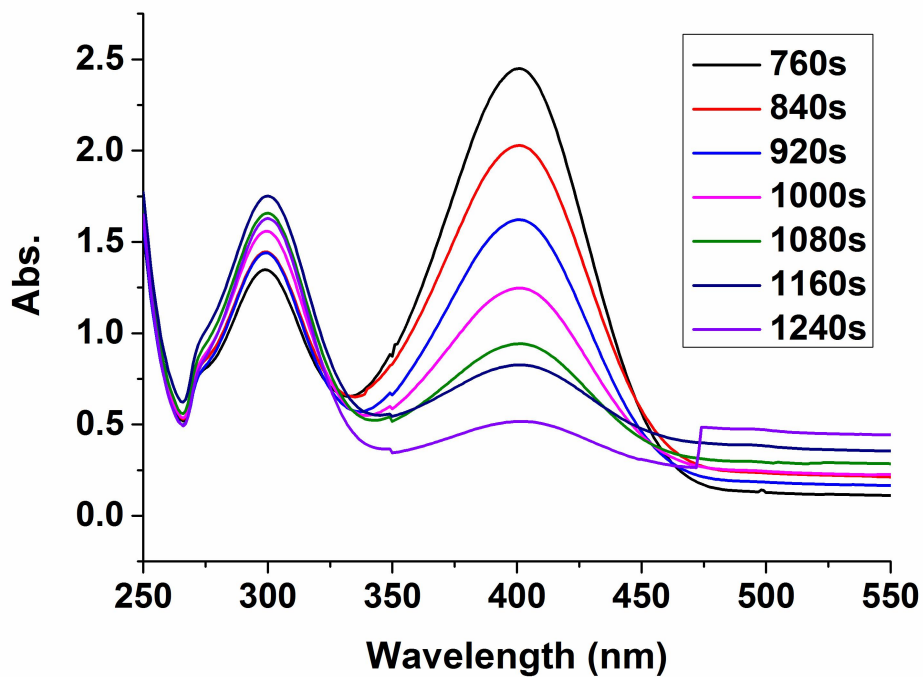


Figure 20. UV-*vis.* spectra of the 4-NP reduction by NaBH₄ catalyzed by Au₄ (top); consumption rate of 4-NP: $-\ln(C_t/C_0)$ vs reaction time (bottom).

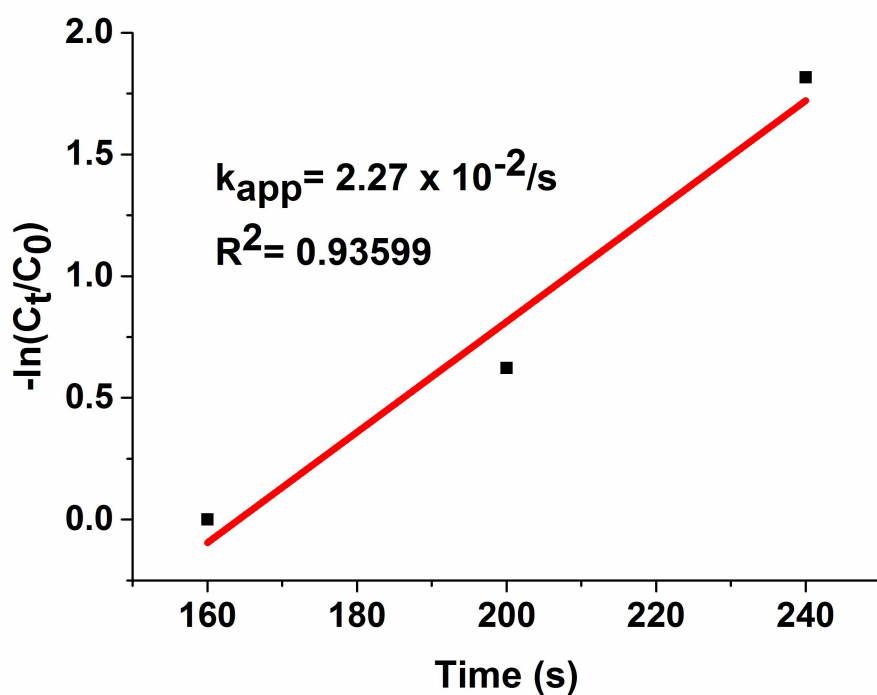
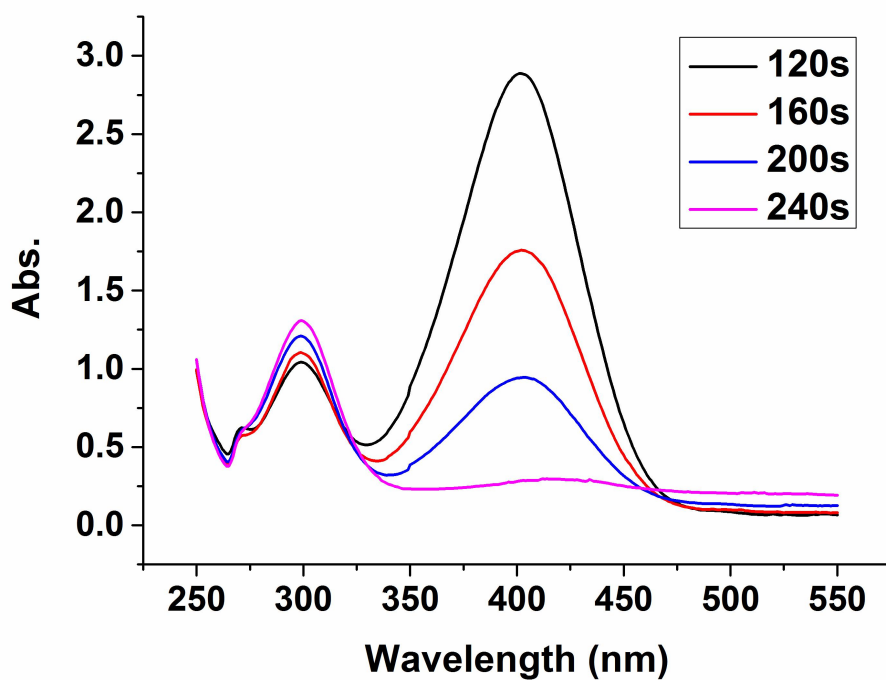


Figure 21. UV-*vis.* spectra of the 4-NP reduction by NaBH₄ catalyzed by Au5 (top); consumption rate of 4-NP: $-\ln(C_t/C_0)$ vs reaction time (bottom).

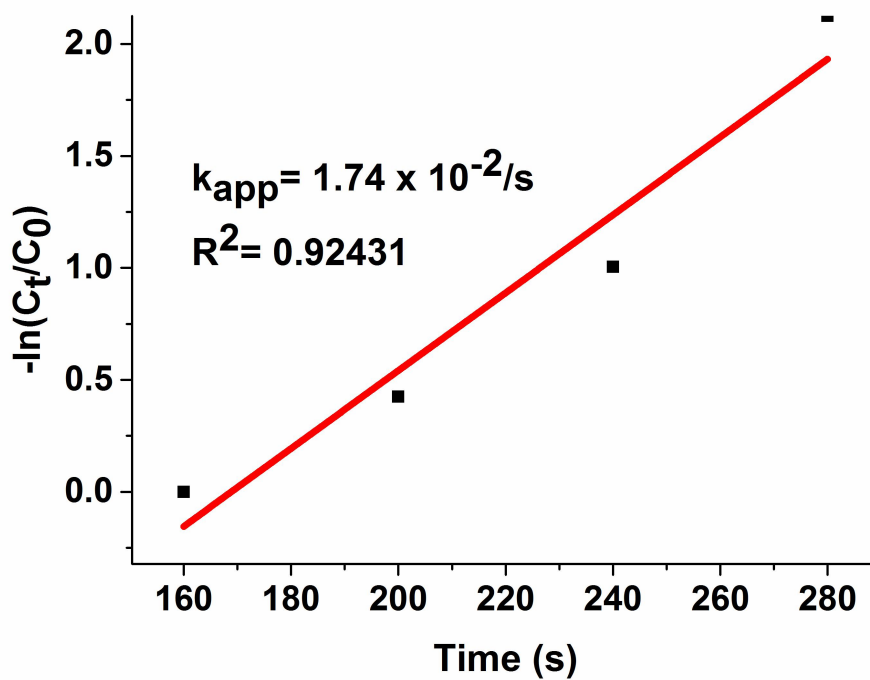
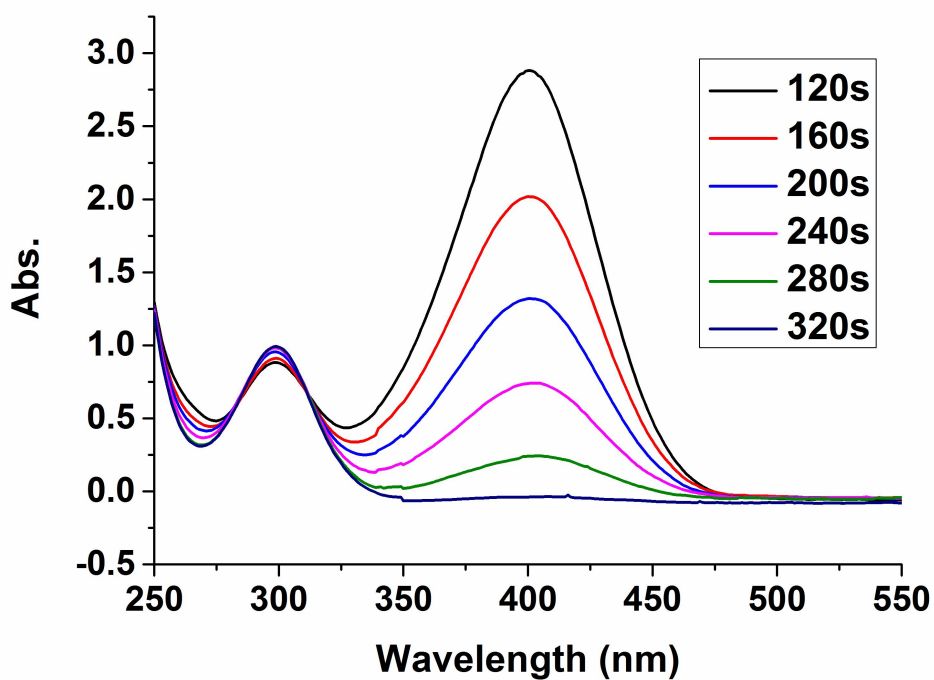


Figure 22. UV-*vis.* spectra of the 4-NP reduction by NaBH₄ catalyzed by Au₆ (top); consumption rate of 4-NP: $-\ln(C_t/C_0)$ vs reaction time (bottom).

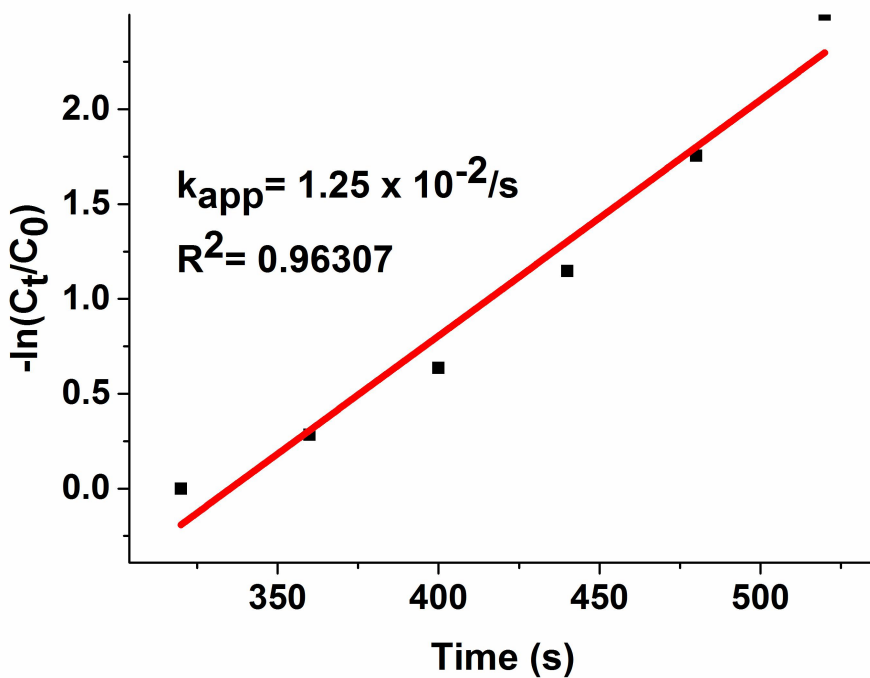
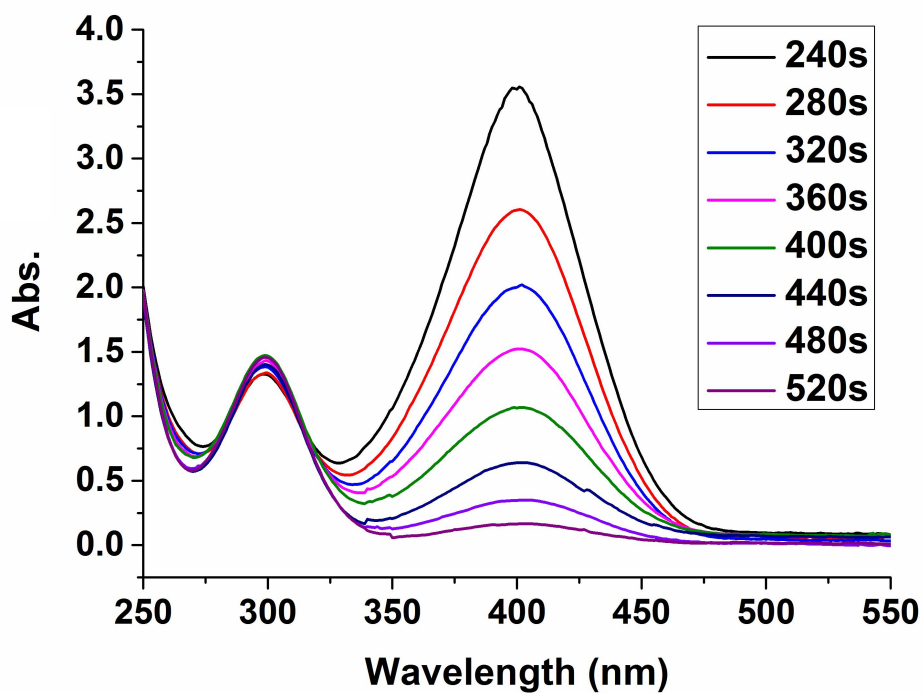


Figure 23. UV-*vis.* spectra of the 4-NP reduction by NaBH₄ catalyzed by Au7 (top); consumption rate of 4-NP: $-\ln(C_t/C_0)$ vs reaction time (bottom).

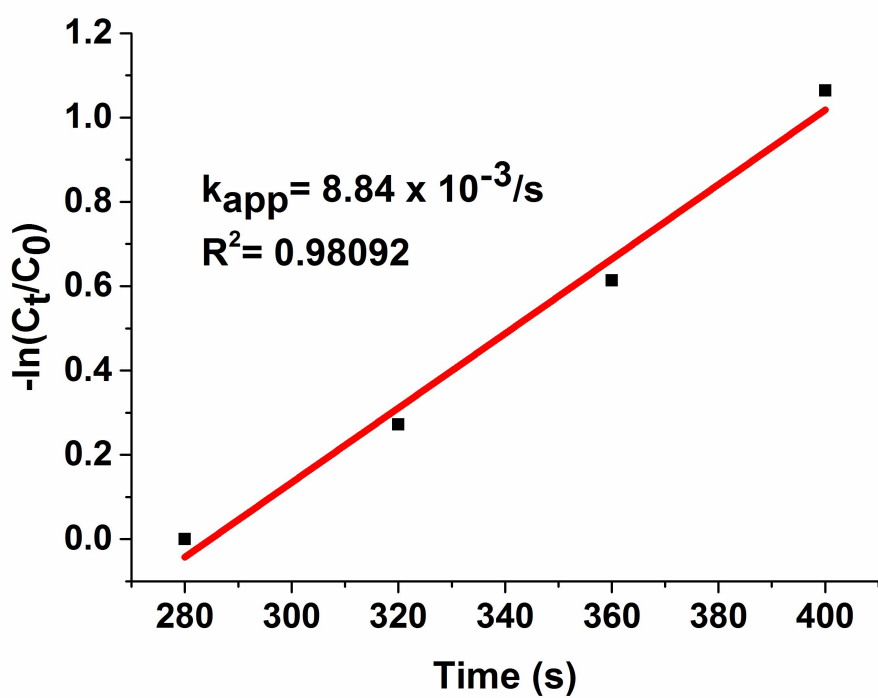
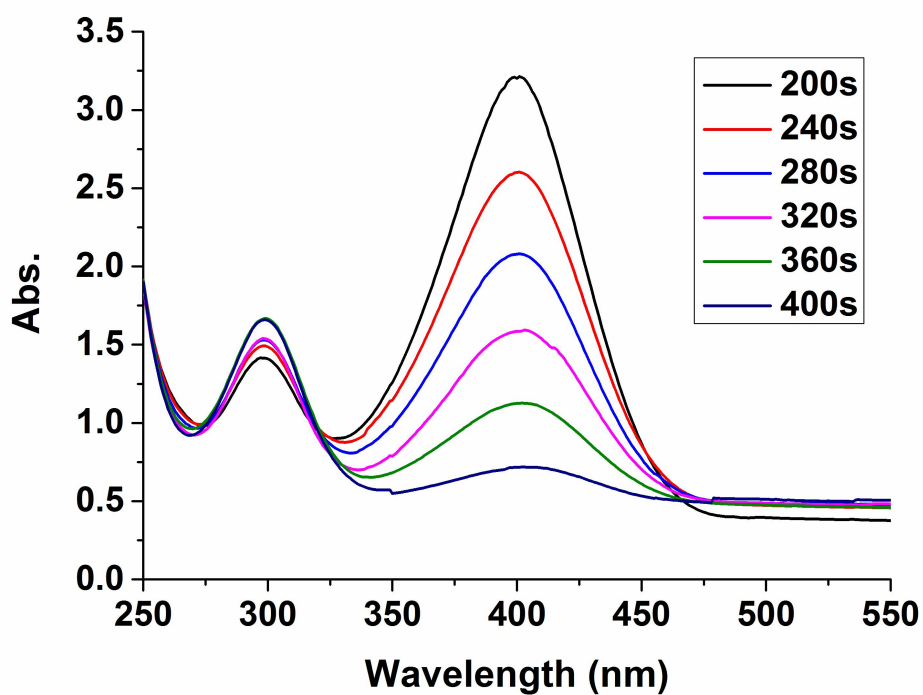


Figure 24. UV-*vis.* spectra of the 4-NP reduction by NaBH₄ catalyzed by Au₈ (top); consumption rate of 4-NP: $-\ln(C_t/C_0)$ vs reaction time (bottom).

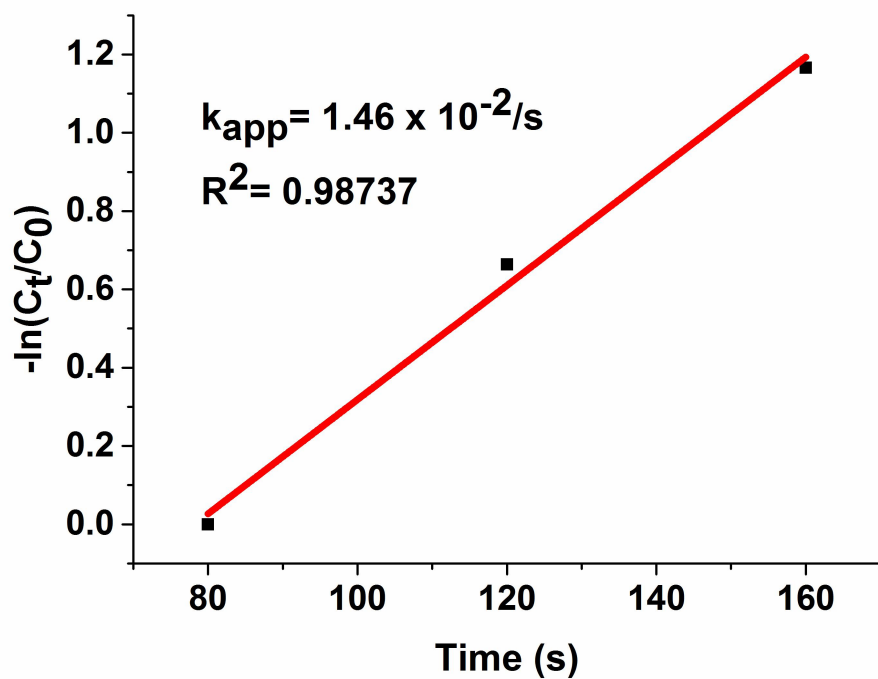
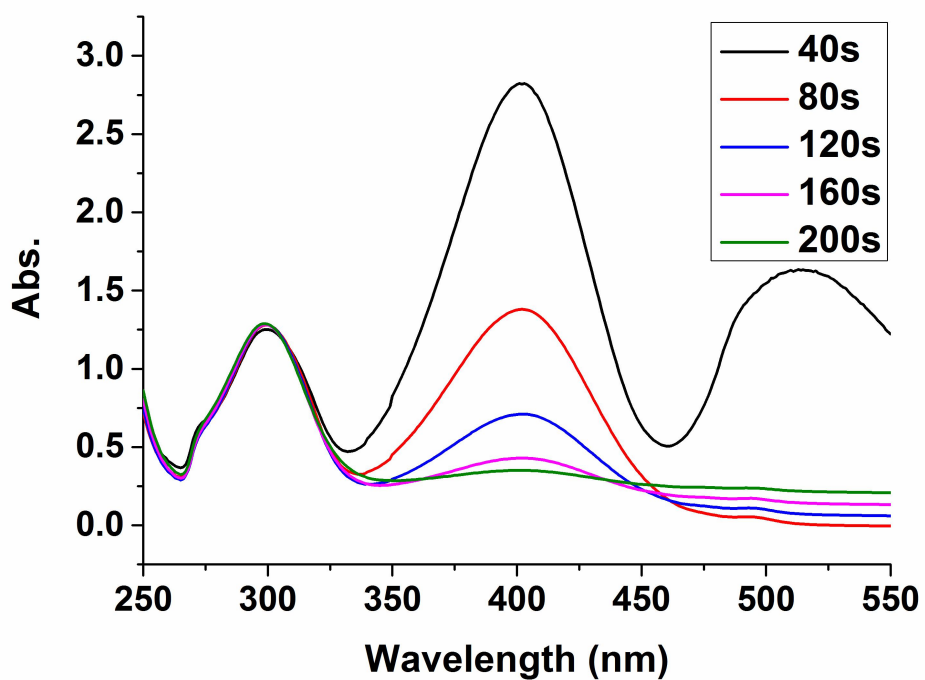


Figure 25. UV-*vis.* spectra of the 4-NP reduction by NaBH₄ catalyzed by Pd1 (top); consumption rate of 4-NP: $-\ln(C_t/C_0)$ vs reaction time (bottom).

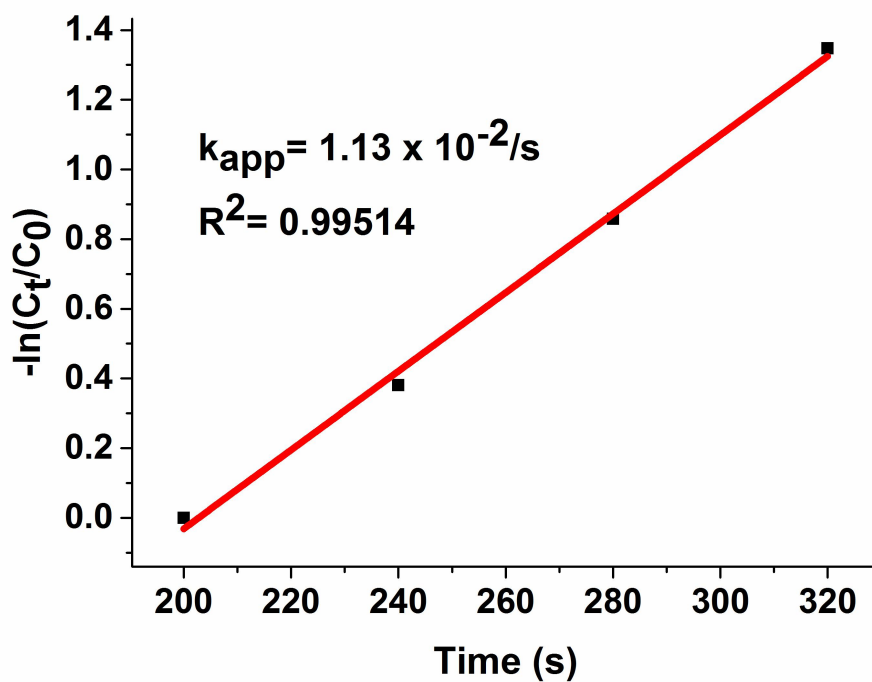
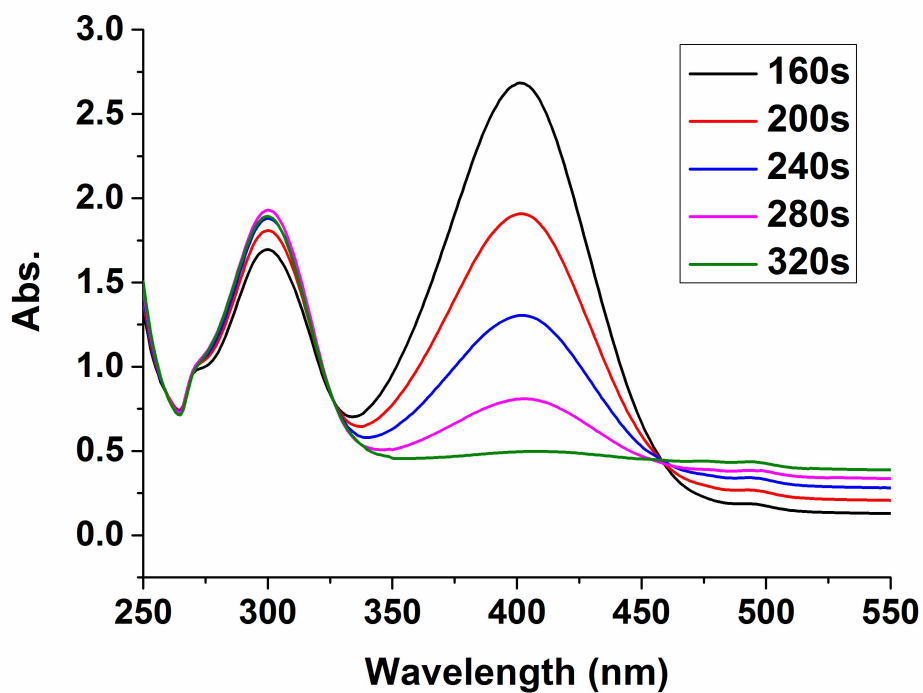


Figure 26. UV-*vis.* spectra of the 4-NP reduction by NaBH₄ catalyzed by Pd₂ (top); consumption rate of 4-NP: $-\ln(C_t/C_0)$ vs reaction time (bottom).

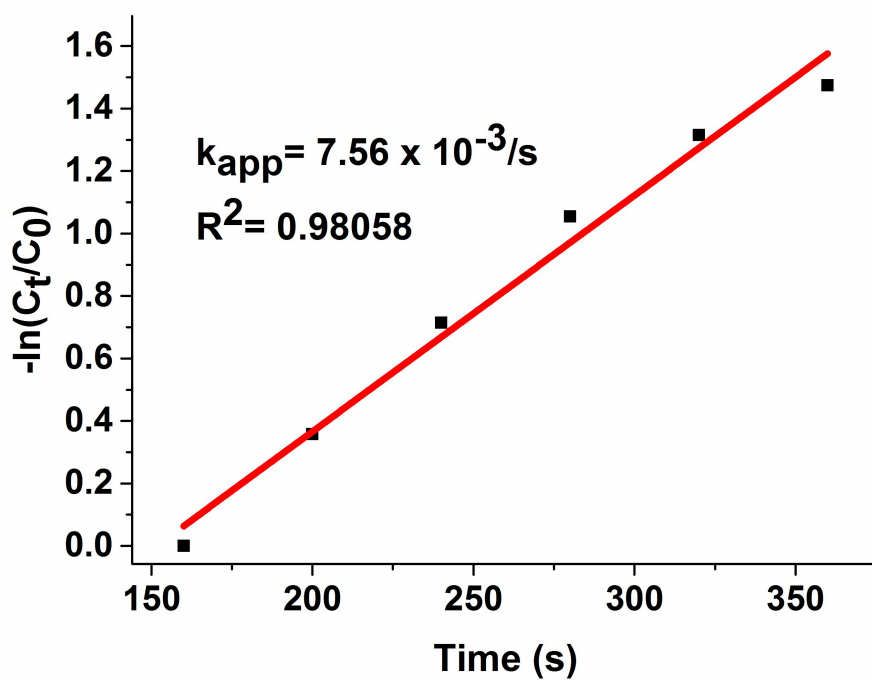
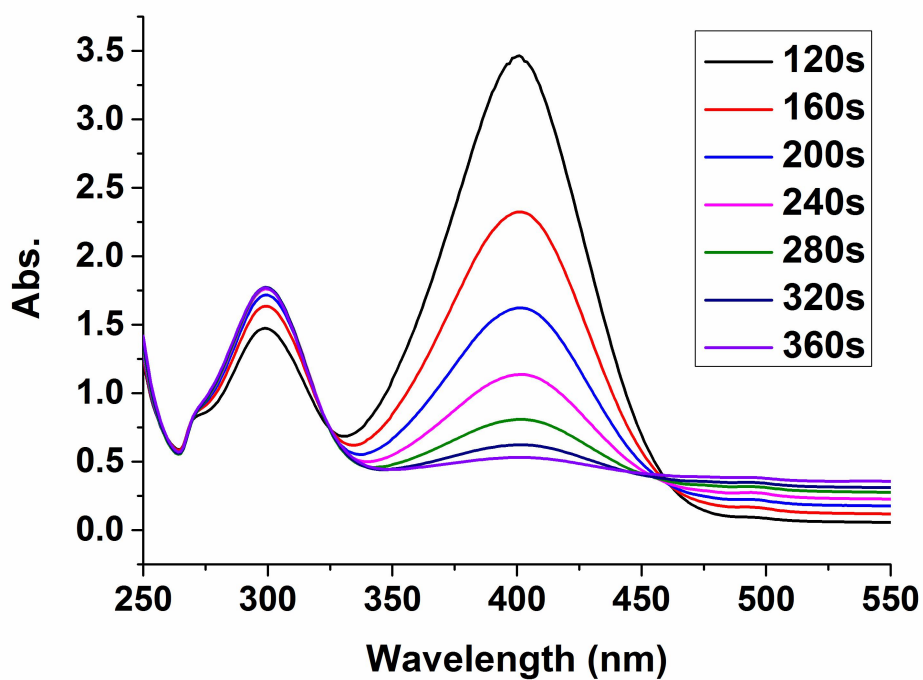


Figure 27. UV-*vis.* spectra of the 4-NP reduction by NaBH₄ catalyzed by Pd₃ (top); consumption rate of 4-NP: $-\ln(C_t/C_0)$ vs reaction time (bottom).

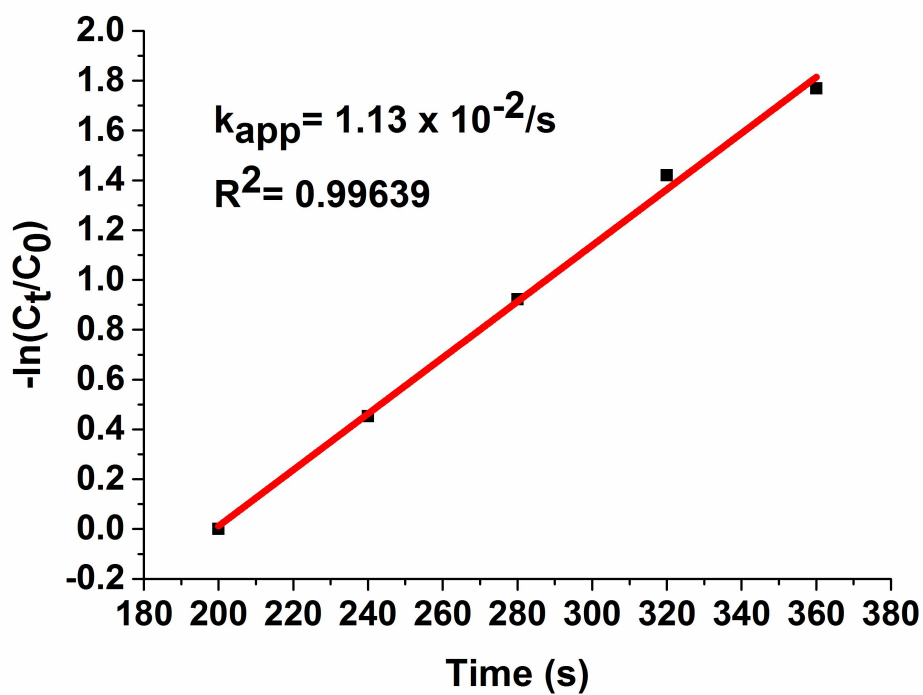
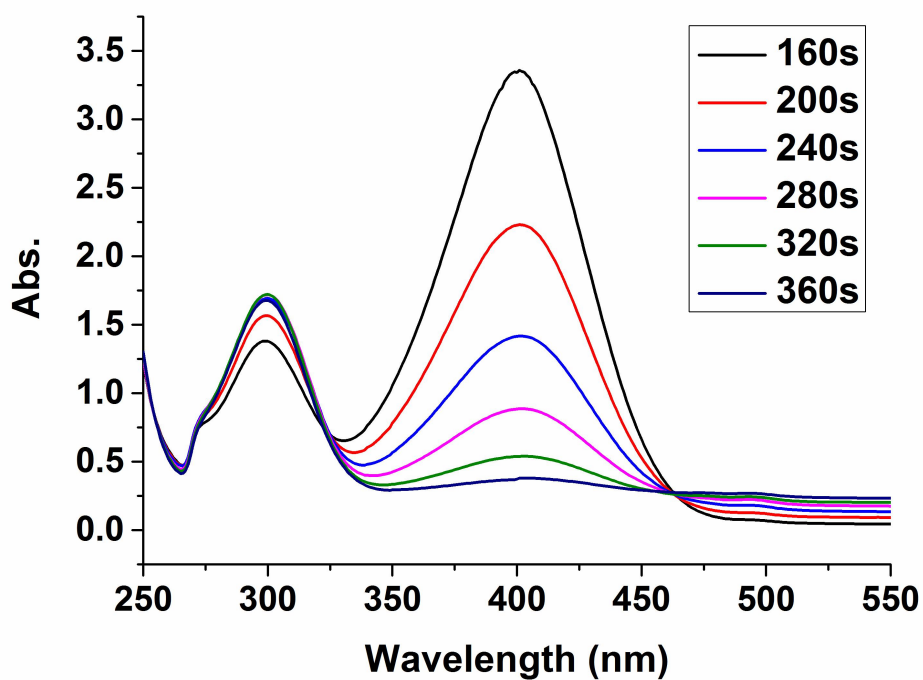


Figure 28. UV-*vis.* spectra of the 4-NP reduction by NaBH₄ catalyzed by Pd₄ (top); consumption rate of 4-NP: $-\ln(C_t/C_0)$ vs reaction time (bottom).

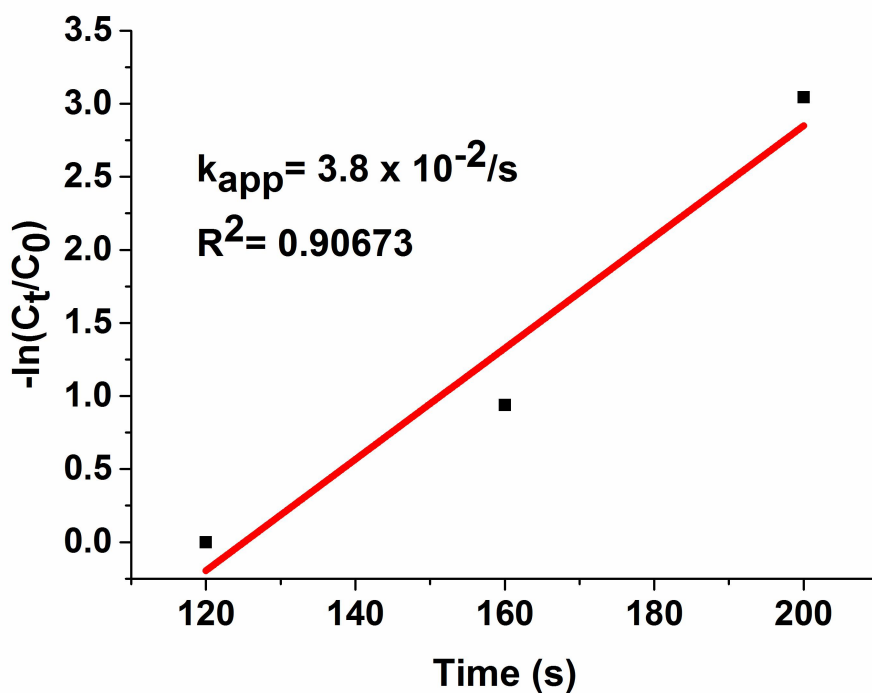
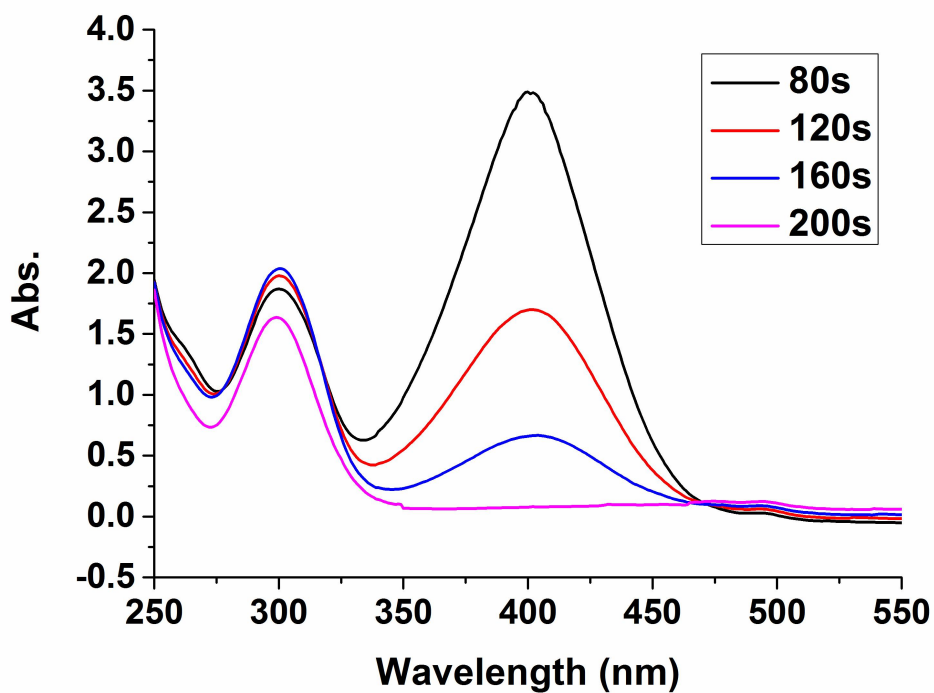


Figure 29. UV-*vis.* spectra of the 4-NP reduction by NaBH₄ catalyzed by Pd5 (top); consumption rate of 4-NP: $-\ln(C_t/C_0)$ vs reaction time (bottom).

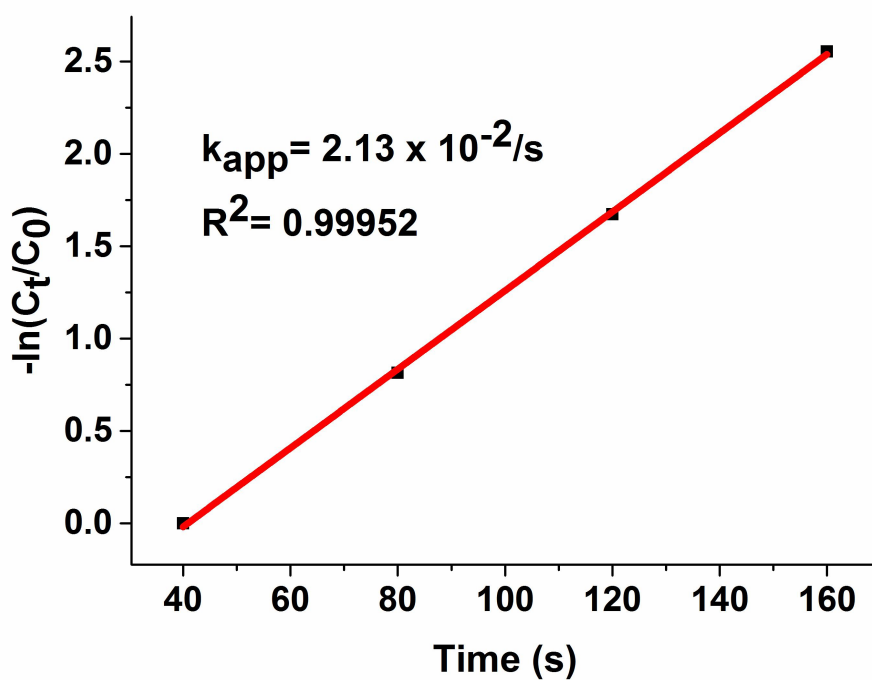
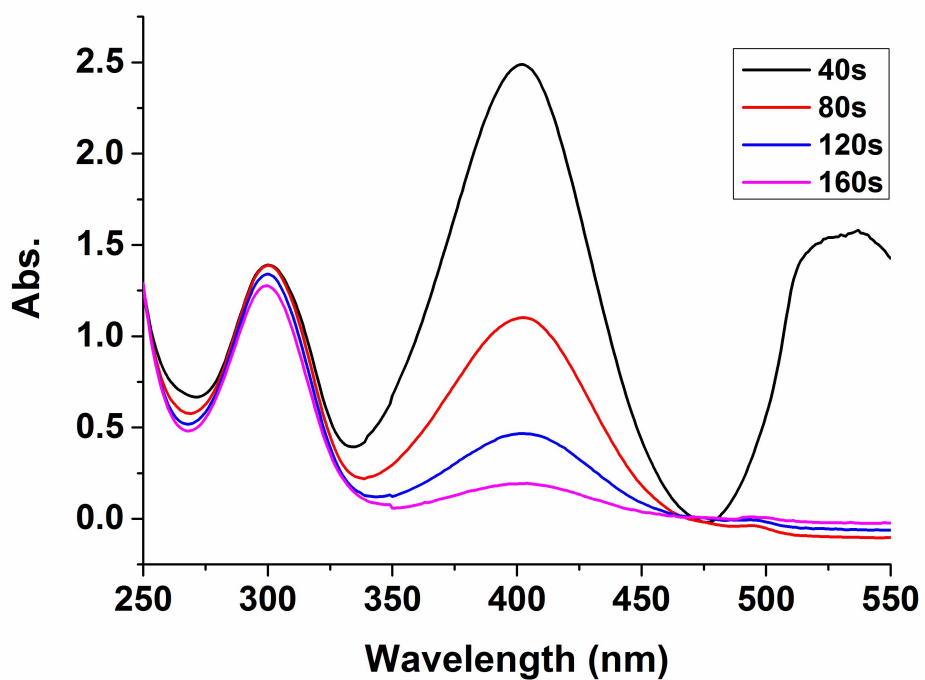


Figure 30. UV-*vis.* spectra of the 4-NP reduction by NaBH₄ catalyzed by Pd6 (top); consumption rate of 4-NP: $-\ln(C_t/C_0)$ vs reaction time (bottom).

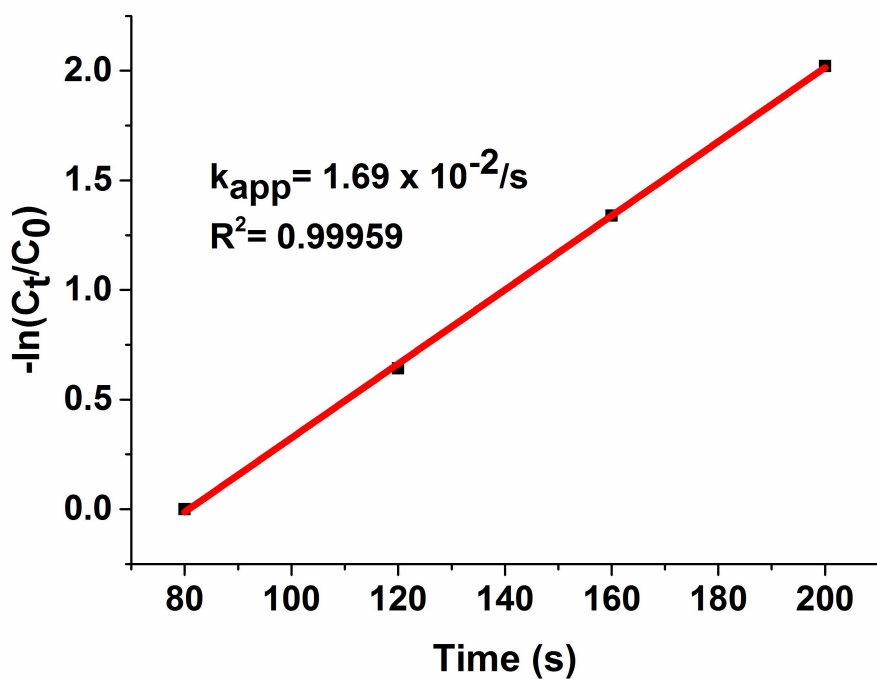
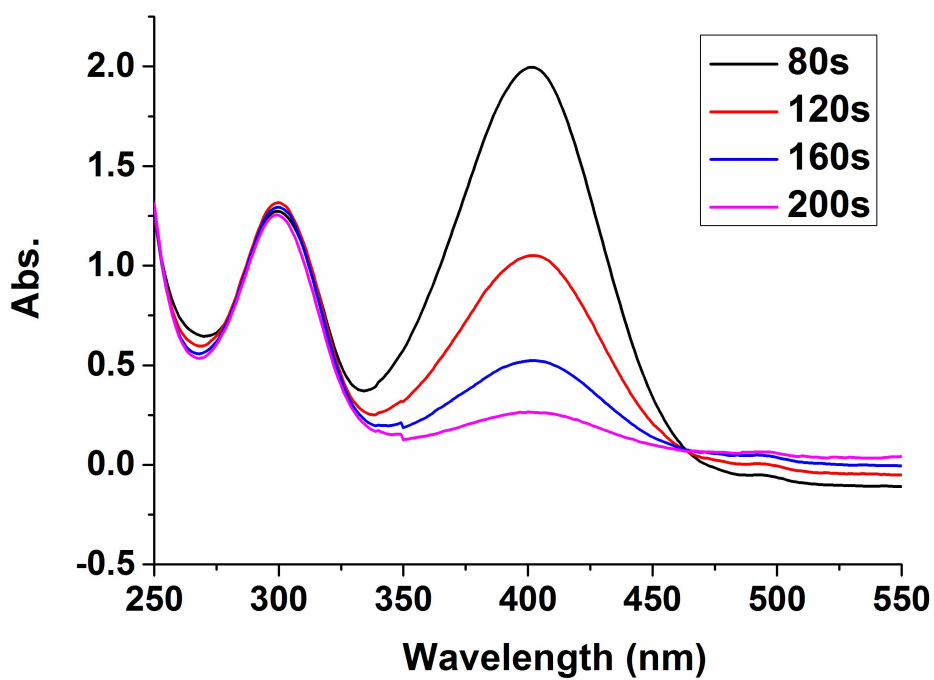


Figure 31. UV-*vis.* spectra of the 4-NP reduction by NaBH₄ catalyzed by Pd7 (top); consumption rate of 4-NP: $-\ln(C_t/C_0)$ vs reaction time (bottom).

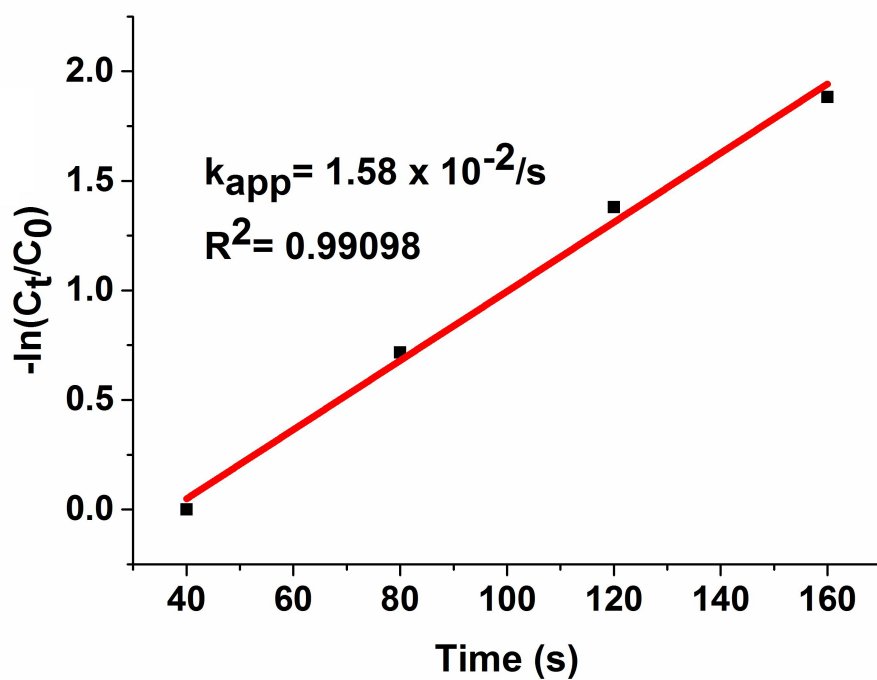
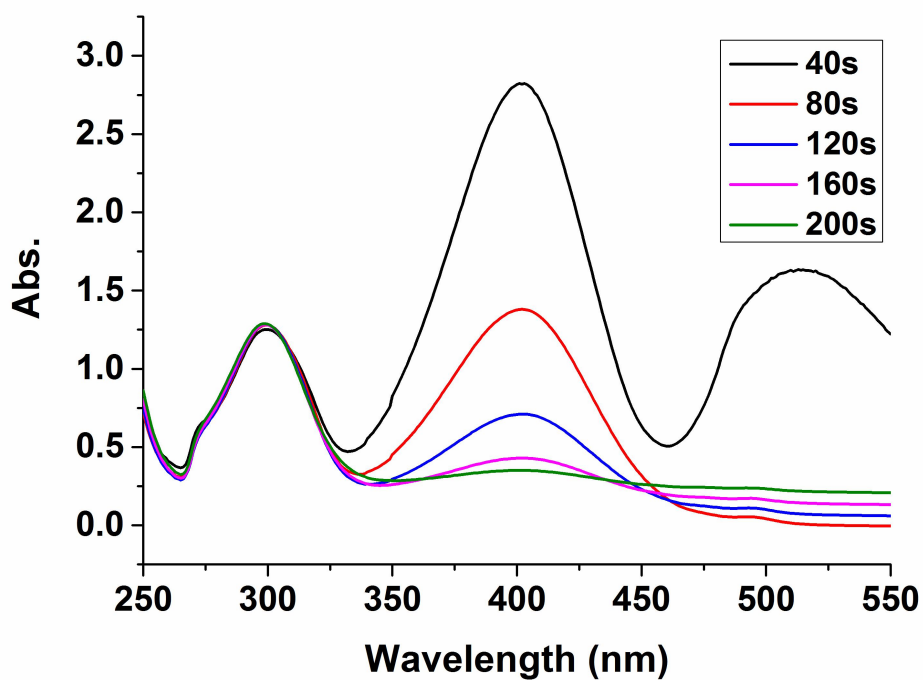


Figure 32. UV-*vis.* spectra of the 4-NP reduction by NaBH₄ catalyzed by Pd8 (top); consumption rate of 4-NP: $-\ln(C_t/C_0)$ vs reaction time (bottom).

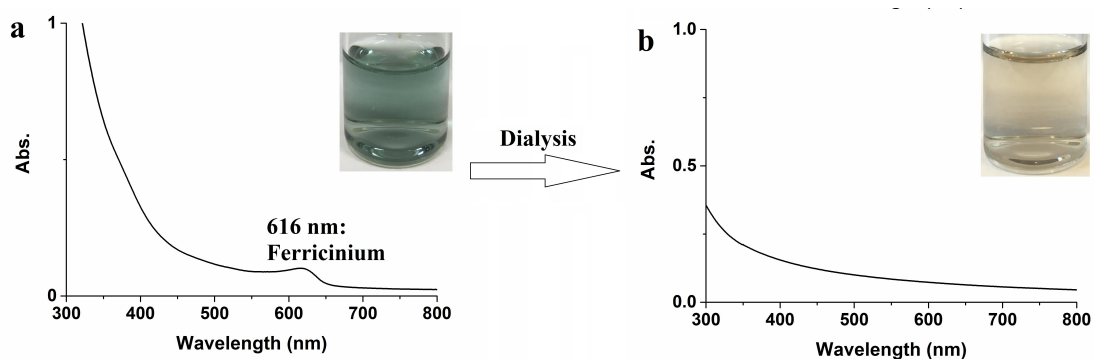


Figure 33. UV-*vis.* spectra and photographs of Pd1 before (a) and Pd1-1 after (b) dialysis.

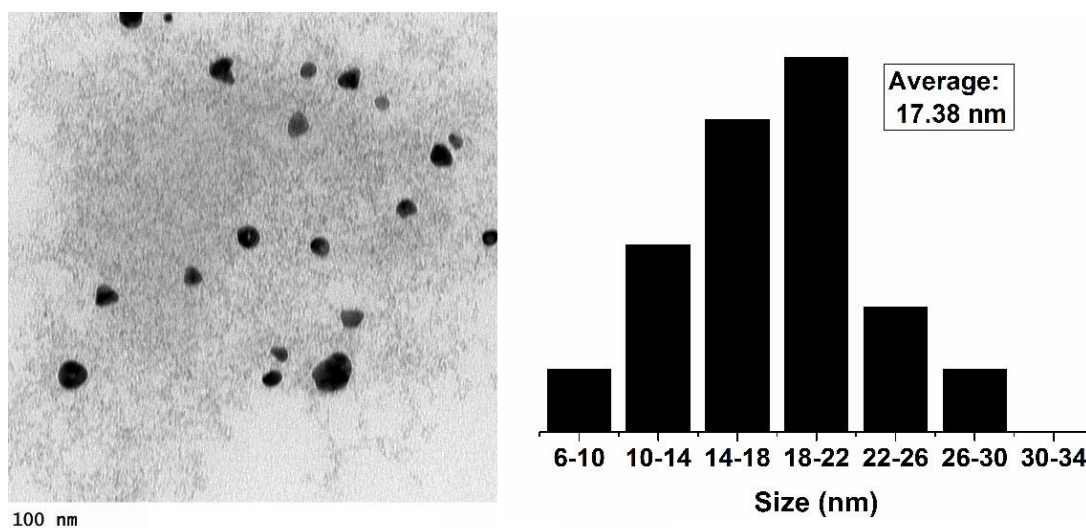


Figure 34. TEM picture (left) and histogram (right) of Au1-1.

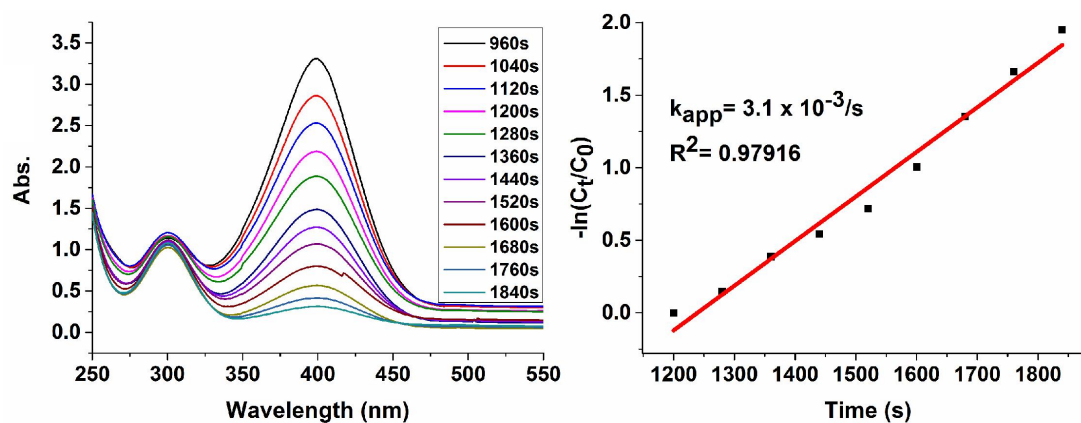


Figure 35. UV-*vis.* spectra of the 4-NP reduction by NaBH₄ catalyzed by Au5-1 (left); consumption rate of 4-NP: $-\ln(C_t/C_0)$ vs reaction time (right).

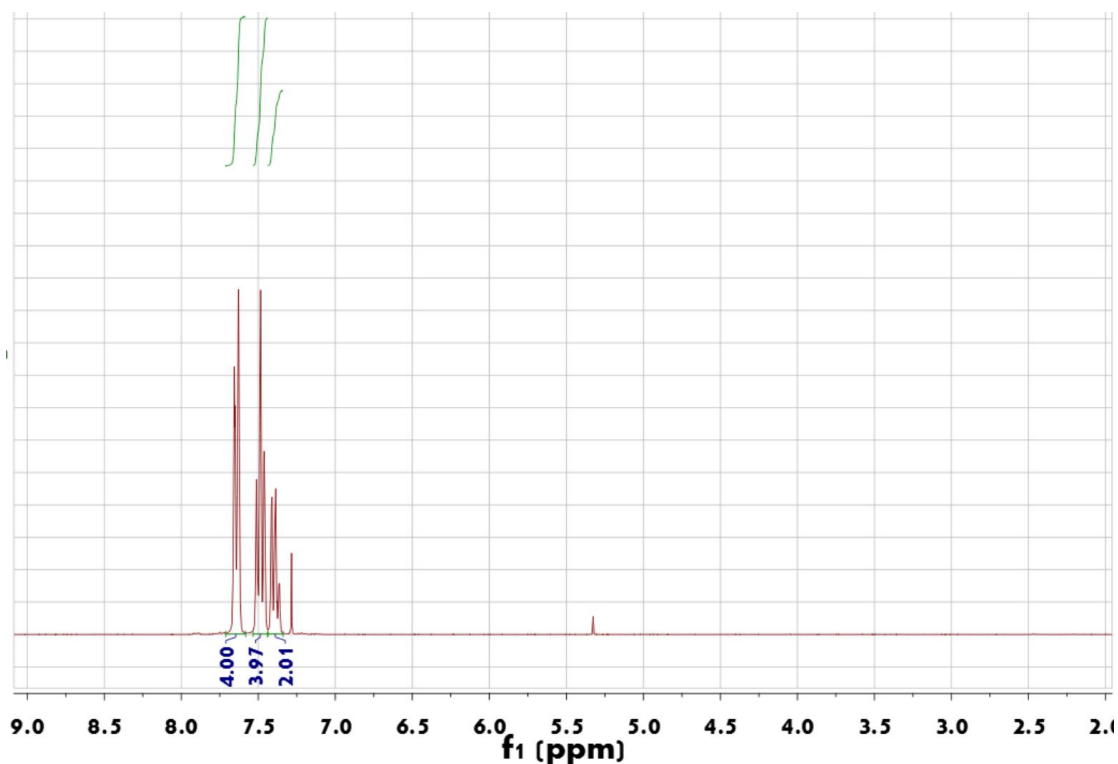


Figure 36. ^1H NMR spectrum of Biphenyl.

^1H NMR (300 MHz, CDCl_3) δ 7.71 – 7.58 (m, 4H), 7.53 – 7.44 (m, 4H), 7.44 – 7.34 (m, 2H).

References

- a) R. Ye, B. Yuan, J. Zhao, W. T. Ralston, C. Y. Wu, E. U. Bari, F. D. Toste, G. A. Somorjai, *J. Am. Chem. Soc.* **2016**, 138, 8533-8537; b) M. Haruta, *Angew. Chem. Int. Ed.* **2014**, 53, 52-56 ; *Angew. Chem.* **2014**, 126, 54–58 ; c) M. Sankar, N. Dimitratos, P. J. Miedziak, P. P. Wells, C. J. Kiely, G. J. Hutchings, *Chem. Soc. Rev.* **2012**, 41, 8099-8139 ; d) A. Corma, A. Leyva- Perez, J. M. Sabater, *Chem. Rev.* **2011**, 111, 1657-1712; e) L. M. Bronstein, Z. B. Shifrina, *Chem. Rev.* **2011**, 111, 5301-5344 ; f) V. S. Myers, M. G. Weier, E. V. Carino, D. F. Yancey, S. Pande, R. M. Crooks, *Chem. Sci.* **2011**, 2, 1632-1646; g) A. Balanta, C. Godard, C. Claver, *Chem. Soc. Rev.* **2011**, 40, 4973-4985; h) J.-M. Basset, R. Psaro, D. Roberto, R. Ugo, *Modern Surface Organometallic Chemistry*, Wiley-VCH, Weinheim, **2009**; i) V. Polshettiwar, R. S. Varma, *Green Chem.* **2010**, 12, 743-754; j) D. Astruc, F. Lu, J. Ruiz, *Angew. Chem. Int. Ed.* **2005**, 44, 7852-7872; *Angew. Chem.* **2005**, 117, 8062-8083; k) M. T. Reetz, J. G. de Vries, *Chem. Commun.* **2004**, 1559-1563.
 - a) M. Brust, M. Walker, D. Bethel, D. J. Schiffrin, R. Whyman, *J. Chem. Soc. Chem. Commun.* **1994**, 801-802; b) Y. G. Sun, Y. N. Xia, *Nano Lett.* **2003**, 3, 675-679; c) Y. P. Sun, X. Q. Li, J. S. Qao, W. X. Zhang, H. P. Wang, *Adv. Colloid*

- Interface Sci.* **2006**, 120, 47-56; d) M. P. Mallin, C. J. Murphy, *Nano Lett.* **2002**, 2, 1235-1237; e) S. H. Chen, K. Kimura, *Langmuir* **1999**, 15, 1075-1082 ; f) Y. M. Mohan, K. Lee, T. Premkumar, K. E. Geckeler, *Polymer* **2007**, 48, 158-164.
- 3 a) M. He, Q. Wang, R. Wang, Y. Xie, W. F. Zhao, C. S. Zhao, *ACS Appl. Mater. Interfaces* **2017**, 9, 15962-15974; b) C. Deraedt, L. Salmon, S. Gatard, R. Ciganda, R. Hernandez, J. Ruiz, D. Astruc, *Chem. Commun.* 2014, 50, 14194-14196.
- 4 a) J. M. Yan, X. B. Xhang, S. Han, H. Shioyama, Q. Xu, *Angew. Chem. Int. Ed.* **2008**, 47, 2287-2289 ; *Angew. Chem.* **2008**, 120, 2319-2321; b) C. Schçttle, P. Bockstaller, R. Popescu, D. Gerthsen, C. Feldmann, *Angew. Chem. Int. Ed.* **2015**, 54, 9866-9870; *Angew. Chem.* **2015**, 127, 10004-10008 ; c) C. Schçttle, D. E. Doronkin, R. Popescu, D. Gerthsen, J. D. Grenwald, C. Feldmann, *Chem. Commun.* **2016**, 52, 6316-6319.
- 5 a) J.-R. Hamon, D. Astruc, P. Michaud, *J. Am. Chem. Soc.* **1981**, 103, 758-766; b) J. C. Green, M. R. Kelly, M. P. Payne, E. A. Seddon, D. Astruc, J.-R. Hamon, P. Michaud, *Organometallics* **1983**, 2, 211-218; c) M. V. Rajasekharan, S. Giezynski, J. H. Ammeter, N. Oswald, J.-R. Hamon, P. Michaud, D. Astruc, *J. Am. Chem. Soc.* **1982**, 104, 2400-2407; d) D. Astruc, *Acc. Chem. Res.* **1986**, 19, 377-383.
- 6 A. Rapakousiou, C. Belin, L. Salmon, J. Ruiz, D. Astruc, *Chem. Commun.* **2017**, 53, 6267-6270.
- 7 a) R. Ciganda, J. Irigoyen, D. Gregurec, R. Hernández, S. Moya, C. Wang, J. Ruiz, D. Astruc, *Inorg. Chem.* **2016**, 55, 6361-6363 ; b) R. Ciganda, H. Gu, R. Hernández, A. Escobar, A. Martínez, L. Yate, S. Moya, J. Ruiz, D. Astruc, *Inorg. Chem.* **2017**, 56, 2784-2791.
- 8 A. N. Nesmeyanov, N. A. Volkenau, I. N. Bolesova, *Dokl. Akad. Nauk SSSR* **1974**, 217, 104-106.
- 9 a) D. Astruc, J.-R. Hamon, G. Althoff, E. Román, P. Batail, P. Michaud, J.-P. Mariot, F. Varret, D. Cozak, *J. Am. Chem. Soc.* **1979**, 101, 5445-5447; b) C. Moinet, E. Román, D. Astruc, *J. Electroanal. Chem.* **1981**, 121, 241-253.
- 10 a) I. U. Khand, P. L. Pauson, W. E. Watts, *J. Chem. Soc. C* **1968**, 2257-2259; b) For redox and hydride transfer reactions of organometallic sandwich complexes, see Ref. [10 c], chapt. 12; c) D. Astruc, *Organometallic Chemistry and Catalysis*, Springer, Berlin, **2007**.
- 11 M. L. H. Green, L. Pratt, G. Wilkinson, *J. Chem. Soc.* **1959**, 3753-3767.
- 12 M.-C. Daniel, D. Astruc, *Chem. Rev.* **2004**, 104, 293-346.
- 13 For an analysis of the role of the driving force in electron transfer reactions, see a) R. A. Marcus, N. Sutin, *Biochim. Biophys. Acta Rev. Bioenerg.* **1985**, 811, 265-322 ; b) D. Astruc, *Electron Transfer and Radical Processes in Transition Metal Chemistry*, Wiley-VCH, New York, **1995**.

- 14 a) N. Pradhan, A. Pal, T. Pal, *Colloids Surf. A* **2002**, 196, 247-257; b) P. Hervés, M. Perez-Lorenzo, L. M. Luiz-Marzan, J. Dzubiella, M. Ballauff, *Chem. Soc. Rev.* **2012**, 41, 5577-5587; c) T. Aditya, A. Pal, T. Pal, *Chem. Commun.* **2015**, 51, 9410-9431; d) P. Zhao, X. Feng, D. S. Huang, G. Y. Yang, D. Astruc, *Coord. Chem. Rev.* **2015**, 287, 114-136.
- 15 a) N. Miyaura, A. Suzuki, *Chem. Rev.* **1995**, 95, 2457-2483; b) A. Suzuki, in *Modern Arene Chemistry* (Ed.: D. Astruc), Wiley-VCH, Weinheim, **2002**, pp. 53.
- 16 A. N. Nesmeyanov, S. P. Solodovnikov, N. A. Vol'kenau, L. S. Kotesova, N. A. Sinitsina, *J. Organomet. Chem.* **1978**, 148, C5-C7.
- 17 a) E. O. Fischer, W. Pfab, *Z. Naturforsch. B* **1952**, 7, 377-379; b) G. Wilkinson, M. Rosenblum, M. C. Whiting, R. B. Woodward, *J. Am. Chem. Soc.* **1952**, 74, 2125-2126.
- 18 N. G. Connelly, W. E. Geiger, *Chem. Rev.* **1996**, 96, 877-910.
- 19 W. E. Geiger, *J. Am. Chem. Soc.* **1974**, 96, 2632-2634.
- 20 a) I. Noviadri, K. N. Brown, D. S. Fleming, P. T. Gulyas, P. A. Lay, A. F. Masters, L. Phillips, *J. Phys. Chem. B* **1999**, 103, 6713-6722; b) J. Ruiz Aranzaes, M.-C. Daniel, D. Astruc, *Can. J. Chem.* **2006**, 84, 288-299.
- 21 For chemical and electrochemical reversibilities of CV waves, see A. J. Bard, L. R. Faulkner, *Electrochemical Methods: Fundamentals and Applications*, 2nd ed., Ref. [13 b], chapt. 1, Wiley, New York **2001**.
- 22 a) Mei, Y. Lu, F. Polzer, M. Ballauff, M. Dreshler, *Chem. Mat.* **2007**, 19, 1062-1069; b) S. Wunder, F. Polzer, Y. Lu, Y. Mei, M. Ballauff, *J. Phys. Chem. C* **2010**, 19, 8814-8820; c) S. Wunder, Y. Lu, M. Albrecht and M. Ballauff, *ACS Catal.* **2011**, 1, 908-916; d) Y. Lu, M. Ballauff, *Prog. Polym. Sci.* **2016**, 59, 86-104.
- 23 a) J. Lee, J. Park, H. Song, *Adv. Mater.* **2008**, 20, 1523-1528; b) Z. Zhang, C. Shao, P. Zou, P. Zhang, M. Zhang, J. Mu, Z. Guo, X. Li and C. Wang, *Chem. Commun.* **2011**, 47, 3906-398; c) A. Gangula, R. Podila, M. Ramakrishna, L. Karanam, C. Janardhana and A. M. Rao, *Langmuir* **2011**, 27, 15268-15274; d) C. Wang, R. Ciganda, L. Yate, S. Moya, L. Salmon, J. Ruiz, D. Astruc, *J. Mater. Sci. A* **2017**, 52, 9465-9476.
- 24 S. Harish, J. Mathiyarasu, K. L. N. Phani, V. Yegnaraman, *Catal. Lett.* **2009**, 128, 197-202.
- 25 B. Liu, S. Yu, Q. Wang, W. Hu, P. Jing, Y. Liu, W. Jia, Y. Liu, L. Liu, J. Zhang, *Chem. Commun.* **2013**, 49, 3757-3759.
- 26 C. Deraedt, L. Salmon, D. Astruc, *Adv. Synth. Catal.* **2014**, 356, 2525-2538.
- 27 H. Li, L. Han, J. Cooper-White, I. Kim, *Green Chem.* **2012**, 14, 586-591.
- 28 K. Jiang, H. X. Zhang, Y. Y. Yang, R. Mothes, H. Lang, W. B. Cai, *Chem. Commun.* **2011**, 47, 11924-11926.

- 29 X. Lu, X. Bian, G. Nie, C. Zhang, C. Wang, Y. Wei, *J. Mater. Chem.* **2012**, *22*, 12723-12730.
- 30 J. MorHre, M. J. Tenorio, M. J. Torralvo, C. Pando, J. A. R. Renuncio, A. Cabanas, *J. Supercrit. Fluids* **2011**, *56*, 213-222.
- 31 R. Bhandari, M. R. Knecht, *ACS Catal.* **2011**, *1*, 89-98.
- 32 Y. Mei, G. Sharma, Y. Lu, M. Ballauff, M. Dreshler, T. Irrgang, R. Kempe, *Langmuir* **2005**, *21*, 12229-1234..
- 33 S. Gatard, L. Salmon, C. Deraedt, J. Ruiz, D. Astruc, S. Bouquillon, *Eur. J. Inorg. Chem.* **2014**, 4369-4375.
- 34 C. Wang, R. Ciganda, L. Salmon, D. Gregurec, J. Irigoyen, S. Moya, J. Ruiz, D. Astruc, *Angew. Chem. Int. Ed.* **2016**, *55*, 3091-3095; *Angew. Chem.* **2016**, *128*, 3143-3147.
- 35 F. Fu, A. M. Martinez-Villacorta, A. Escobar, J. Irigoyen, S. Moya, E. Fouquet, J. Ruiz, D. Astruc, *Inorg. Chem. Front.* **2017**, *4*, 2037-2044.
- 36 H. Yamamoto, H. Yano, H. Kouchi, Y. Obora, R. Arakawa, H. N. Kawasaki, *Nanoscale* **2012**, *4*, 4148-4154.
- 37 R. Fenger, E. Fertitta, H. Kirmse, A. F. Thunemann, K. Rademann, *Phys. Chem. Chem. Phys.* **2012**, *14*, 9343-9349.
- 38 E. Seo, J. Kim, Y. Hong, Y. S. Kim, D. Lee, B. S. Kim, *J. Phys. Chem. C* **2013**, *117*, 11686-11693.
- 39 C. Xiao, S. Chen, L. Zhang, S. Zhou, W. Wu, *Chem. Commun.* **2012**, *48*, 11751-11753.
- 40 T. Huang, F. Meng, L. Qi, *J. Phys. Chem. C* **2009**, *113*, 13636-13642.
- 41 J. Han, L. Li, R. Guo, *Macromolecules* **2010**, *43*, 10636-10644.
- 42 I. Biondi, G. Laurenczy, P. J. Dyson, *Inorg. Chem.* **2011**, *50*, 8038-8045.
- 43 K. Esumi, K. Miyamoto, T. Yoshimura, *J. Colloid Interface Sci.* **2003**, *268*, 501-506.
- 44 K. Hayakawa, T. Yoshimura, K. Esumi, *Langmuir* **2003**, *19*, 5517-5521.
- 45 N. Li, P. Zhao, N. Liu, M. Echeverria, S. Moya, L. Salmon, J. Ruiz, D. Astruc, *Chem. Eur. J.* **2014**, *20*, 8363-8369.
- 46 N. Li, M. Echeverria, S. Moya, J. Ruiz, D. Astruc, *Inorg. Chem.* **2014**, *53*, 11802-11808.
- 47 R. Ciganda, N. Li, C. Deraedt, S. Gatard, P. Zhao, L. Salmon, R. Hernández, J. Ruiz, D. Astruc, *Chem. Commun.* **2014**, *50*, 10126-10129.
- 48 S. Das, B. G. Bag, R. Basu, *Appl. Nanosci.* **2015**, *5*, 867-873.
- 49 A. G. Majouga, E. K. Beloglazkina, E. A. Manzheliy, D. A. Denisov, E. G. Evtushenko, K. I. Maslakov, E. V. Golubina, N. V. Zyk, *Appl. Surf. Sci.* **2015**, *325*, 73-78.
- 50 Y. Ju, X. Li, J. Feng, Y. Ma, J. Hu, X. Chen, *Appl. Surf. Sci.* **2014**, *316*, 132-140.

- 51 H. Woo, J. W. Kim, M. Kim, S. Park, K. H. Park, *RSC Adv.* **2015**, *5*, 7554-7558.
- 52 P. Zhao, N. Li, N. Liu, L. Salmon, J. Ruiz, D. Astruc, *Chem. Commun.* **2013**, *49*, 3218-3220.
- 53 a) C. Deraedt, L. Salmon, L. Etienne, J. Ruiz, D. Astruc, *Chem. Commun.* 2013, *49*, 8169-8171; b) C. Deraedt, D. Astruc, *Acc. Chem. Res.* 2014, *47*, 494-503; c) S. Handa, Y. Wang, F. Gallou, B. H. Lipshutz, *Science* 2015, *349*, 1087-1091.

**Chapter 4. Cobaltocene Reduction of Cu and Ag Salts and
Catalytic Behavior of the Nanoparticles Formed.**

Introduction

Transition metal nanoparticles (TMNPs) are an essential part of the nanoworld because of their fundamental aspects and multiple applications in biomedicine, sensing, optoelectronics,¹⁻⁴ and particularly in catalysis.⁵⁻¹⁴ Although organometallic chemistry has provided efficient transition-metal catalysts, they include expensive and sometimes toxic ligands.¹⁵ The advantages of TMNP catalysts are the lack of such ligands and the simplicity of preparation and fixation onto supports.¹⁶⁻¹⁹ It is necessary, however, that the synthesis be well controlled and that for efficiency the TMNPs be small enough so that most atoms are located at the periphery.²⁰ Usually, the TMNPs are synthesized by reduction of TM salts using reducing agents such as H₂, NaBH₄, (SiMe₂)₆, Mg, Li or Na in liquid NH₃ and Li or Na naphthalenide in the presence of a stabilizer.²⁰⁻²³ Key parameters in the TMNP synthesis are the control of the reductant stoichiometry, its driving force and the nature of the stabilizer that define the size, shape and protection type of the TMNPs. Very often the oxidized form of the reductant is not removed and its combination with the TMNP is uncertain, so that it can partly inhibit the TMNP surface activity.

We propose the use of cobaltocene, CoCp₂^{24,25} (Cp = η⁵-C₅H₅), because it presents many advantages that solve the above problems. It is a commercially available electron-reservoir compound,²⁶⁻²⁸ and its amount and reaction product, [CoCp₂][X],^{24,25,29} are well controlled. CoCp₂ provides a strong driving force with a standard redox potential of -1.4 V vs. SCE^{27,28} for the reduction of CuSO₄·5H₂O and Ag salts insuring the fast formation of very small CuNPs and AgNPs respectively.

Following immediate reactions between CoCp₂ and CuSO₄·5H₂O or Ag salts, the cationic groups [CoCp₂]⁺ obtained along with the metal NP form an encapsulating network around the NP that is an excellent NP stereoelectronic and electrostatic stabilizer. This protecting network does not bind the NP surface atoms that remain available for catalytic substrate binding and activation. The activity of the NP surface will be investigated in order to know if it is appropriate for excellent catalytic conditions. The AgNP plasmonic absorption and kinetics of AgNP-catalyzed 4-nitrophenol reduction by NaBH₄ are both therefore excellent tests. Overall the major interest is the facile, fast and clean reduction under ambient conditions of standard commercial salts to catalytically very efficient CuNPs for alkyne azide cycloaddition (CuAAC) reaction.³⁰

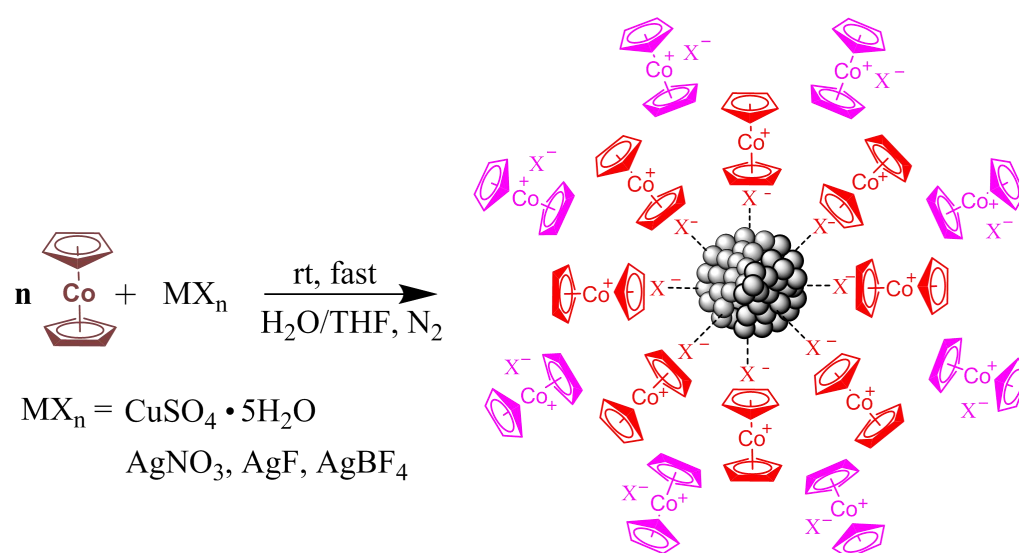
“Click” reactions were highlighted by Sharpless as a privileged way to couple two molecular fragments for practical use in organic chemistry, biochemistry and nanomaterials science.³⁰ The most currently used “click” reaction, Cu(I)-catalyzed alkyne azide cycloaddition (CuAAC),³¹ was proposed with high amount of CuSO₄ that is toxic for biomedical usage³² or with sophisticated nitrogen ligands.^{33,34} CuNPs

can also work as catalyst, although the catalytic amounts are usually far higher than those of the reported molecular Cu(I) catalysts.³⁴⁻³⁸

Here we have used CoCp₂ to reduce and stabilize CuNPs with small particle size and narrow histogram in water and tetrahydrofuran (THF). The CuNPs are characterized by UV-vis. spectra, Transmission Electron Microscopy (TEM) and X-ray photoelectron spectra (XPS). The CuNPs are examined for their catalytic activity in the CuAAC reaction in neat water with low catalytic amounts, and their use is extended to various alkynes and organic azides for CuAAC “click” reactions. Interestingly these CuNPs are in particular successfully used to prepare functional biomedical substrates in neat water.

Results and discussion

Synthesis and Characterizations of the AgNPs. Quick addition of cobaltocene in THF to an aqueous solution of the commercial salt AgNO₃ at room temperature (rt) under N₂ results in instantaneous color change (*vide infra*) indicating the formation of AgNPs (Scheme 1, see details in Experimental Section). The cobaltocene stoichiometry matches that of the number of electrons necessary to reduce the metal cation of the precursor salt to metal (0) atoms precursors of nanoparticles. Thus no additional stabilizing agent is needed, and these AgNPs are more stable than other non- or less-protected TMNPs synthesized by other means, which shows the protecting role of the cobalticinium salt network.



Scheme 1. Synthesis of CuNPs and AgNPs by reaction of CuSO₄·5H₂O or an Ag salt with cobaltocene. For CuNPs, n = 2 and MX_n = CuSO₄. For AgNPs, n = 1, and MX_n = AgX (X = NO₃, F or BF₄).

Dependence of the AgNP surface plasmon band and 4-nitrophenol reduction rate constants on the precursor counter anion

Various Ag salts (NO_3^- , F^- and BF_4^-) were probed for reduction by CoCp_2 in order to characterize the effects of the coordination of the anions on a plasmonic NP surface by variations of the AgNP surface plasmon band (SPB).³⁹ XPS analysis (Figure 5, Experimental Section) and UV-vis. spectroscopy show that the AgNPs are in the zero oxidation state, and the average size of the AgNPs prepared by AgNO_3 , AgF and AgBF_4 are 3.0, 3.1 and 3.2 nm respectively according to the measurements made by TEM (Figures 9-11, Experimental Section). The variations of color and SPB maximum are dramatic upon anion variation. Reduction of the precursor salts AgNO_3 , AgF and AgBF_4 respectively yield orange, dark-brown and light brown AgNPs (Figure 1) with SPB maxima at 423, 439 and 410 nm respectively (Figures 6-8, Experimental Section). These strong anion effects are best taken into account as suggested above by the coordination of a good proportion of the anions onto the AgNP surface that differently perturbs the electronic state of the surface.

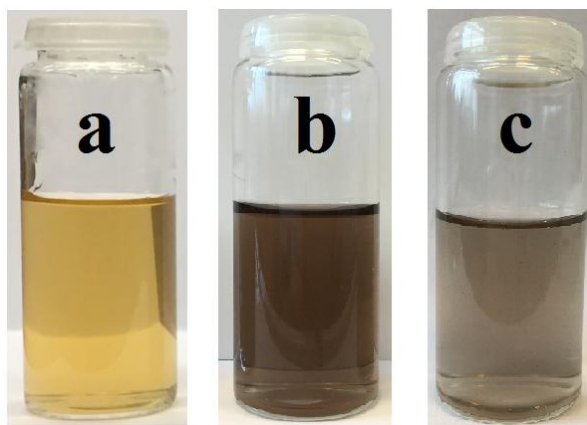


Figure 1. Photographs of the AgNPs obtained using cobaltocene for the reduction of AgX precursor salts: (a) AgNO_3 ; (b) AgF ; (c) AgBF_4 .

This coordination of the anion is corroborated by the variation of the effects of the nature of anion coordination in the surface restructuring involved in surface catalysis as shown below. The nature of this anion also influences the AgNP-catalyzed 4-nitrophenol reduction by NaBH_4 ⁴⁰ as anticipated from the influence of the anion coordination on the SPB (*vide supra*). This reaction is a useful test to investigate the restructuring of the NP surface during a catalytic reaction according to a Langmuir-Hinshelwood model that involves adsorption of the substrates on the NP surface as shown by Ballauff's group.⁴¹ Indeed starting from AgBF_4 , AgNO_3 and AgF , the k_{app} values of the pseudo-first order rate constant of this reaction measured by the disappearance of the nitrophenolate absorption band at 400 nm are respectively 0.0010 s^{-1} , 0.0017 s^{-1} and 0.0036 s^{-1} without any retention time (Figures 12-14,

Experimental Section). These rate constants are very different from an anion to another. Their comparison indicates that the catalytic reaction with the small F^- anion is more favorable than those involving other larger anions. Also the reaction is fast with the three anions, even compared to the best catalysts, i. e. the reported classic PdNPs and AuNPs, confirming the excellent catalytic properties of the NPs synthesized using this method

Synthesis and Characterizations of the CuNPs

Reduction of $CuSO_4 \cdot 5H_2O$ by cobaltocene at rt under N_2 results in instantaneous color change from colorless to black indicating the formation of the CuNPs (Scheme 1, see details in Experimental section). The stoichiometry is 2 equivalents of cobaltocene per Cu atom. The CuNPs obtained by this method are stable as the AgNPs above and are characterized by TEM pictures showing the very small NP core size and narrow histogram with a distribution around 1.7 nm (Figure 2). The very small CuNP size results from the strong driving force provided by the reducing agent resulting in fast reduction of Cu(II) to Cu(0) followed by efficient electrostatic and anion ligand stabilization by cobalticinium sulfate.

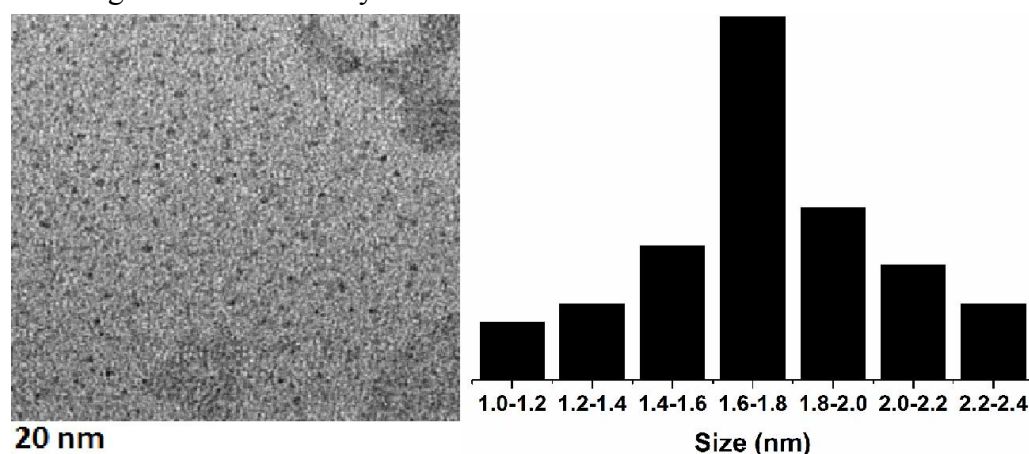


Figure 2. TEM picture (left) and histogram (right) of the 1.7 nm CuNPs prepared by reduction of $CuSO_4$ by cobaltocene.

The XPS spectrum of the CuNPs essentially confirms their zero oxidation state in the core and on the surface. The Cu 2p spectrum shows the Cu $2p_{3/2}$ and $2p_{1/2}$ peaks. The fitting of the Cu $2p_{3/2}$ part of the spectrum reveals the presence of Cu(0) at around 932.5 eV, without Cu(II) species (Figure 3).

The absence of the absorption band in the UV-*vis.* spectra confirms that these CuNPs are zero-valent Cu species, the CuNP plasmon band being only observable for large CuNPs, contrary to those of AgNPs and AuNPs.⁴ On the other hand, the cobalticinium moiety is well characterized by the broad absorption band at 397 nm in the UV-*vis.* spectrum (Figure 4).⁴²

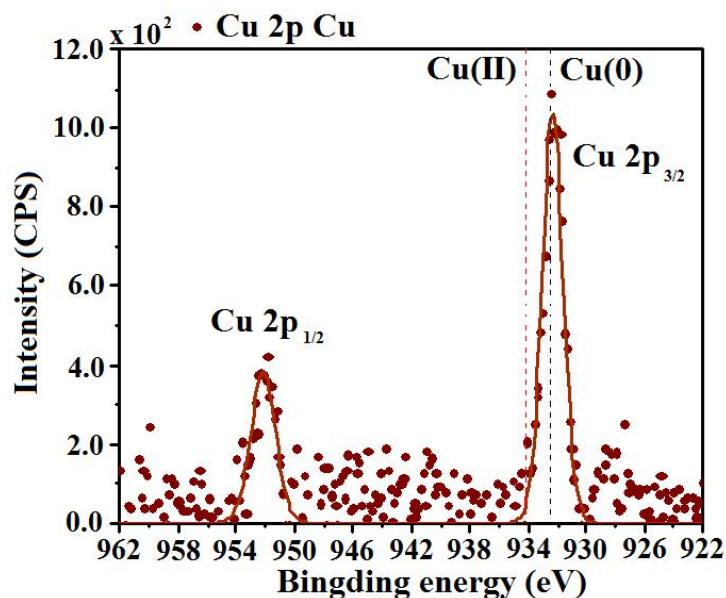


Figure 3. XPS spectrum of the CuNPs prepared from CuSO₄ and cobaltocene.

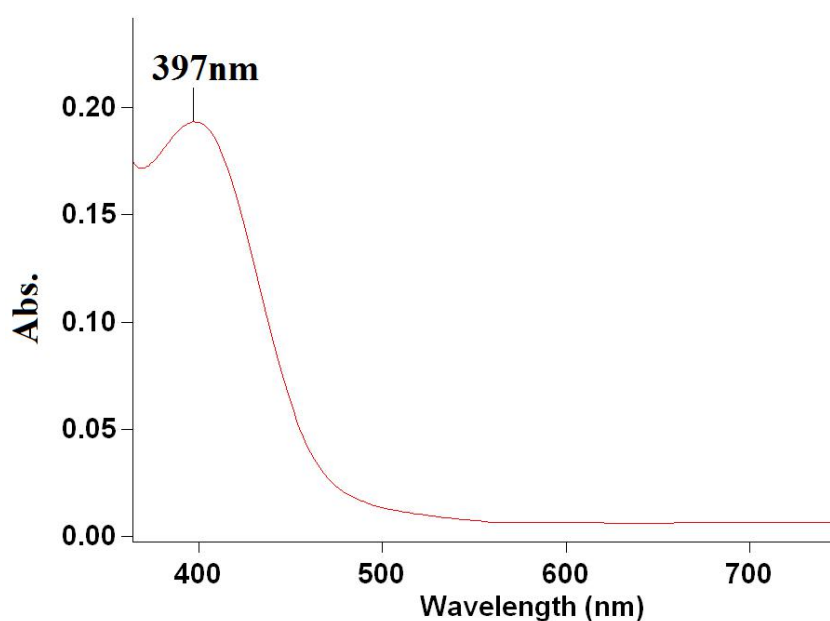


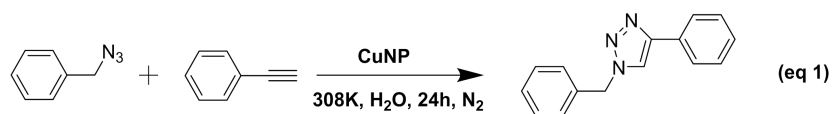
Figure 4. UV-vis. spectrum of the CuNPs obtained by reduction of CuSO₄ by cobaltocene.

Some of the SO₄²⁻ anions formed in these reactions are weak “L₂-type” (formally 4e) ligands²⁵ for the zero-valent surface metal atoms in order to equilibrate the cobalticinium charges (*vide infra*). The number of SO₄²⁻ ligands is limited by the number of surface metal atoms. Since there are more SO₄²⁻ species than surface metal atoms many SO₄²⁻ anions remain only electrostatically bonded to cobalticinium groups without binding the CuNP surface. The SO₄²⁻ anions weakly bonded to the surface electrostatically attract cobalticinium counter cations that are close to the NP

surface to form the stabilizing network. These considerations are confirmed by the above experiments for AgNPs.

Efficient Cu(NP)-catalyzed alkyne azide cycloaddition in water. The CuNPs obtained by reduction of CuSO₄ by cobaltocene were probed for their catalytic activity in CuAAC reaction between benzyl azide and phenylacetylene in neat water (Table 1). This reaction produced 99% isolated yield with 0.1% catalytic amount for 24 h at 35°C and a TOF of 250 with 50 ppm of CuNP catalyst. The scope of the application of this low level amount of the water-soluble CuNP catalyst was explored with other CuAAC reactions between various alkynes and organic azides in water. Good isolated yields were achieved in the CuAAC reaction of a wide variety of alkynes with organic azides using 0.1% or 0.2% catalysts (Table 2). Moreover, one-pot three-components “click” reactions have been conducted from benzyl bromide, sodium azide and phenylacetylene yielding 93% isolated yield with 0.2% Cu of this CuNP nanocatalyst (Experimental Section). The water-soluble CuNP catalyst was also easily recycled by simple filtration at least 4 times with only very slight yield decrease, the click products being insoluble in water (Experimental Section).

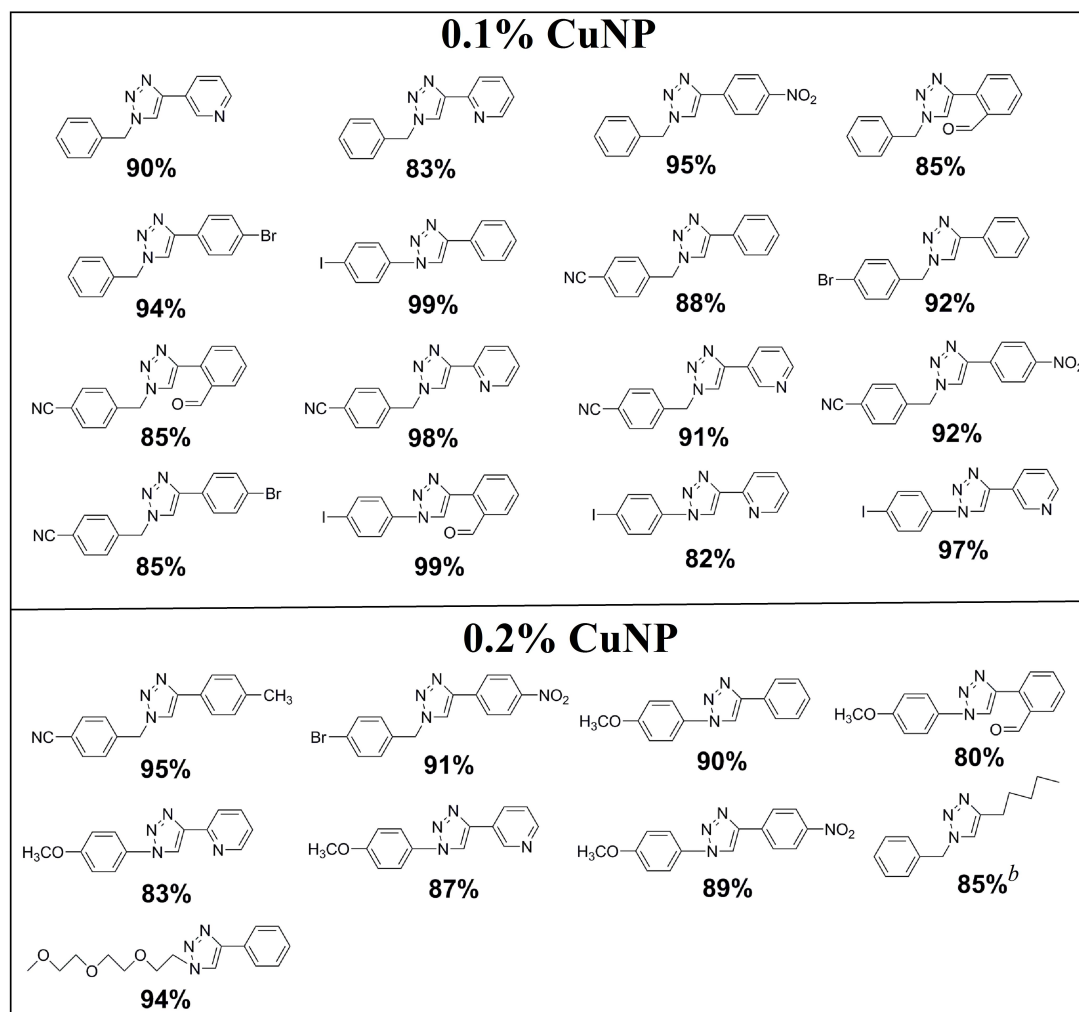
Table 1. “CuAAC” reaction catalyzed by the CuNP ^a



Entry	Amount (%) ^b	Yield (%) ^c	TON	TOF (h ⁻¹)
1	0.005	30	6000	250
2	0.01	48	4800	200
3	0.05	76	1520	63.3
4	0.1	99	990	41.3
5	0.2	99	495	20.6

^a Reaction conditions: 0.5 mmol of benzyl azide, 0.505 mmol of phenylacetylene, and 2 mL of H₂O, 35 °C, 24 h, under N₂. ^b Amount of catalysts used in the “CuAAC” reduction. ^c Isolated yield.

Table 2. “CuAAC” reactions between various azides and alkynes using the 0.1% or 0.2% CuNP catalyst.^a

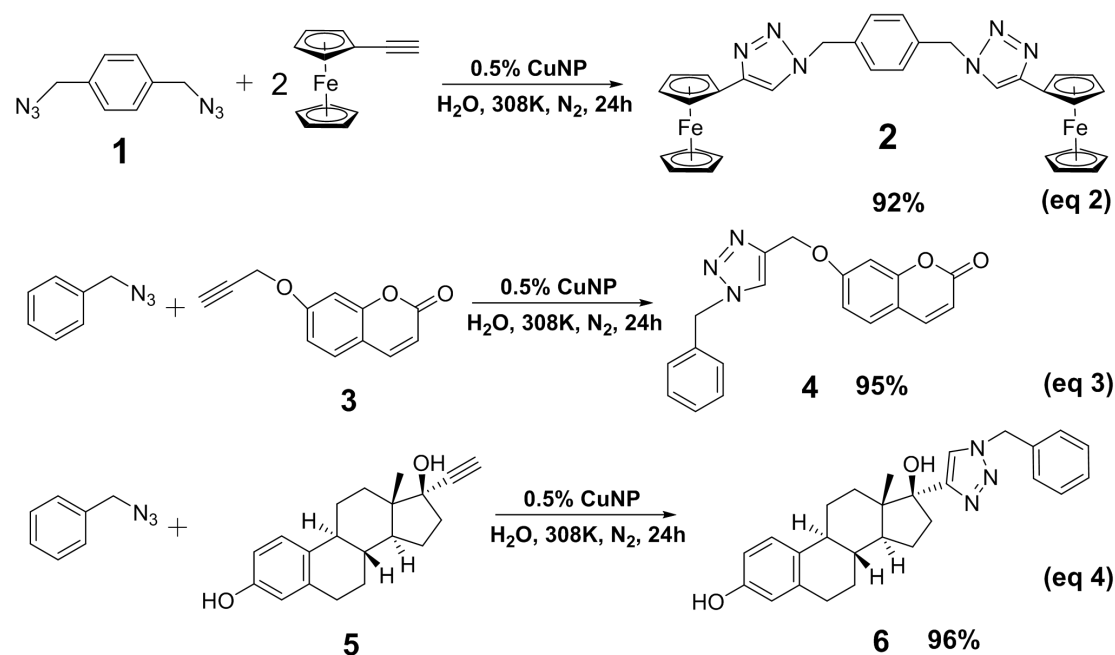


^a Reaction conditions: 0.5 mmol of azide, 0.505 mmol of alkyne, 2 mL H₂O, 35°C, 24 h, under N₂. ^b Solvent: 1 mL H₂O and 1 mL *tert*-butanol.

Functional substrates of biomedical interest were also successfully prepared using this CuNP catalyst. In eq 2, *p*-bis (ferrocenyl-1,2,3-triazolylmethyl) benzene (**2**) was synthesized by the click reaction between compound **1** and ethynylferrocene⁴³ using 0.25% per branch at 35 °C for 24 h with 92% isolated yield in water. This product **2** is of interest, because host-guest molecular interactions between β-CD and ferrocene derivatives⁴⁴ are currently used to synthesize nanocatalysts and AuNPs for photothermal therapy.⁴⁵

Coumarin derivatives are often used in the perfume industry. They also are fluorophores and have been applied as fluorescent probes to visualize the metabolism of cysteine in living cells.⁴⁶ Thus the click-triazole functionalized 7-(propargyloxy)-coumarin **4** was synthesized from **3** in H₂O in 95% isolated yield upon using this CuNP catalyst (0.5% Cu) for 24 h at 35 °C.

Another key natural product, estradiol, is known as a medication and naturally occurring steroid hormone. Estradiol is an estrogen that is mainly used in menopausal hormone therapy and to treat low sex hormone levels in women. It has several biological functions such as sexual development, reproduction, skeletal system, and nervous system. Besides, the natural alkyne of estradiol also discloses various medicinal applications. Here, the CuAAC click reaction between ethynyl estradiol (**5**) and benzyl azide using CuNP (0.5%) in water at 35 °C for 24 h provides **6** in 96% isolated yield (eq 4).



Conclusion

The reduction of Cu and Ag salts to metal NPs by cobaltocene, a common commercial product, provides a range of possibilities for further use of CuNPs and AgNPs that have large catalytic applications. The reduction of these salts to NPs shows that cobaltocene should in fact reduce a good number of transition metal salts to zero-valent metal NPs. Cobaltocene being a neutral 19-electron complex is an electron-reservoir system that indeed provides a large driving force leading to the formation of very small NPs ideal for catalysis. This stands in contrast with isostructural ferrocene providing a weak driving force that produces large NPs that have little catalytic activity.^{47,48} Another advantage of cobaltocene here is that its oxidized cobalticinium form is perfectly defined and robust, contrary to the oxidized forms of most other reductants.

The remarkable variation of the SPB wavelength and kinetics of the AgNP-catalyzed 4-nitrophenol reduction as a function of the nature of the counter anion of the precursor Ag(I) salt shows the stabilization of the AgNPs by this counter anion acting as a weak ligand for the AgNP surface. This means that the cobalticinium salts works

as a nanoreactor around the NPs, leaving the NP surface rather free for catalytic interactions with substrates at this NP surface. This is corroborated by the high catalytic activity of the AgNP surface in 4-nitrophenol reduction by NaBH₄.

Application of this principle to CuNPs synthesized by reduction of CuSO₄ by cobaltocene provides new possibilities in useful catalysis that have already been partly exploited in this work. A variety of heterogeneous click CuAAC reactions have been shown to proceed very efficiently with water-insoluble substrates using the water-soluble CuNP catalyst synthesized in this way including click CuAAC synthesis of biologically relevant compounds.

Such CuNP catalysis is advantageous compared to that using sophisticated pre-synthesized Cu(I) complexes. Yet the mechanism of CuAAC reactions is well known to proceed via Cu(I) active species, whereas the CuNPs synthesized here have been shown by UV-vis. and XPS spectroscopy to involve Cu(0) atoms on the CuNP surface as well as in the core. It is probable, however, that terminal alkynes, whose coordination in complex Cu species has been demonstrated earlier, react with the Cu(0)NP surface to form surface Cu(I)-alkynyl intermediate species.⁴⁹⁻⁵¹ These principles of nanocatalyst design should be extended to various other very efficient mono- and polymetallic nanocatalysts in the close future.

Experimental Section

General data

All the solvents and chemicals were used as received.

- The **UV-vis.** absorption spectra were measured with a Perkin-Elmer Lambda 19 UV-vis. spectrometer.
- **NMR spectra** : Its were recorded at 25 °C with a Bruker AC 200, or 300 (200 or 300 MHz). All the chemical shifts are reported in parts per million (δ , ppm) with reference to Me₄Si for the ¹H NMR spectra.
- **Transmission Electron Microscopy (TEM)**: The sizes of TMNPs were determined by TEM using a JEOL JEM 1400 (120 kV) microscope. The TEM samples were prepared by deposition of the nanoparticle suspension (10 μ L) onto a carbon-coated microscopy copper grid.
- **X-ray Photoelectron Spectroscopy (XPS)**: System: SPECS SAGE HR; X-Ray source: Al K α non-monochromatic; operated at 12.5 kV and 300 W. Take off angle 90°, at \sim 10⁻⁸ Torr. Pass energy for survey spectra 30 eV, 10 eV for narrow scans analysis; spectra are calibrated to CC carbon 285 eV. Analysis is consisted of Shirley background subtraction. Peaks are fitted with symmetrical Gaussian-Lorentzian (GL) line shapes. Samples are prepared by

dehydration on the titania coated glass or silica substrates. Titania is selected as a substrate to avoid the overlap of Si and Au.

- **Flash column chromatography:** It was performed using silica gel (300-400 mesh).

Nanoparticle synthesis. $\text{CuSO}_4 \cdot 5\text{H}_2\text{O}$ (1 mg, 4×10^{-3} mmol) was dissolved in 19 mL milli-Q water under nitrogen in a standard Schlenk flask and degassed for 10 min., then $[\text{CoCp}_2]^{52}$ (1.5 mg, 8×10^{-3} mmol) in dry THF (1 mL) was quickly injected under nitrogen into the Schlenk flask. The color of the solution changed from colorless to black indicating the formation of the CuNPs. This synthesis has also been scaled up 10 times. AgNPs were synthesized similarly.

4-Nitrophenol reduction kinetics: 4-NP (7 mg, 5×10^{-2} mmol) was mixed with NaBH_4 (154 mg, 4.0 mmol) in water under nitrogen. The color of the solution changed from light yellow to dark yellow due to the formation of the sodium 4-nitrophenolate salt. Then a solution containing 2 mol% Ag nanoparticles was added to the mixture under nitrogen. Then the solution lost its dark yellow color with time, and the progress of the reaction kinetics was monitored by UV-*vis.* spectroscopy (40 s for each run).

CuAAC reactions: A Schlenk flask equipped with a magnetic stir bar was charged with benzyl azide (66.5 mg, 0.5 mmol) and phenylacetylene (51.5 mg, 0.505 mmol) under N_2 . The catalyst was added into the Schlenk flask under N_2 , and degassed water was added in order to obtain a 2 mL volume of aqueous solution. The reaction heterogeneous mixture was then stirred for 24 h at 35 °C under N_2 , then the product was extracted with CH_2Cl_2 (3 x 15 mL). The organic layer was dried over Na_2SO_4 and filtered, and the solvent was removed *in vacuo* to give crude 1-benzyl-4-phenyl-1H-[1,2,3]triazole. This product was then purified by silica gel column chromatography using petroleum ether/ethyl acetate: 10/1 for elution to give a 99% isolated yield (116 mg). ^1H NMR (300 MHz, CDCl_3): δ 7.89 – 7.77 (m, 2H), 7.68 (s, 1H), 7.49 – 7.37 (m, 5H), 7.38 – 7.30 (m, 3H), 5.60 (s, 2H) (SI). The other CuAAC reactions were conducted analogously, the reaction being carried out on 0.5 mmol or 0.2 mmol scale. The products were purified by silica gel column chromatography using petroleum ether/ethyl acetate: 10/1 for elution or washed with pentane. The yields are given in tables 1 and 2, and the data and spectra for all the products are provided in the Experimental Section.

2. Characterization of the NPs.

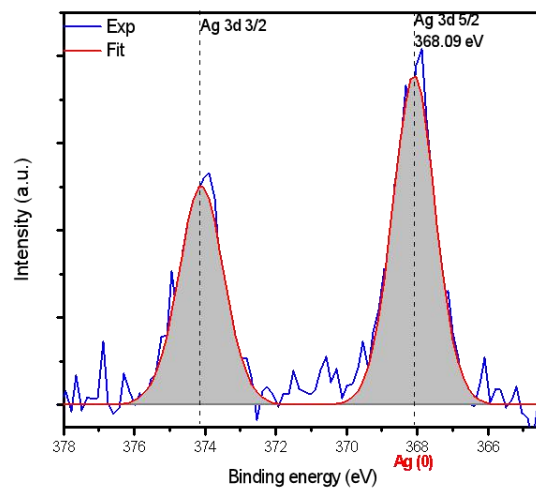


Figure 5. XPS spectrum of the AgNP obtained upon reduction of AgNO_3 by cobaltocene.

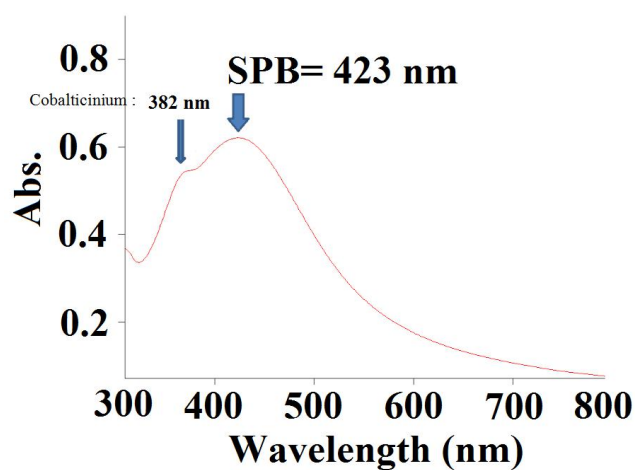


Figure 6. UV-*vis.* spectrum of AgNP obtained upon reduction of AgNO_3 by cobaltocene.

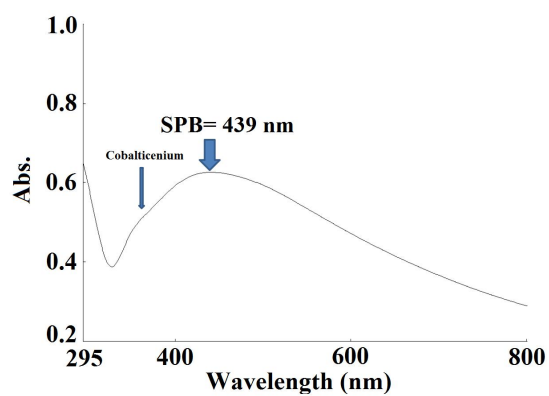


Figure 7. UV-*vis.* spectrum of AgNPs obtained upon reduction of AgF by cobaltocene.

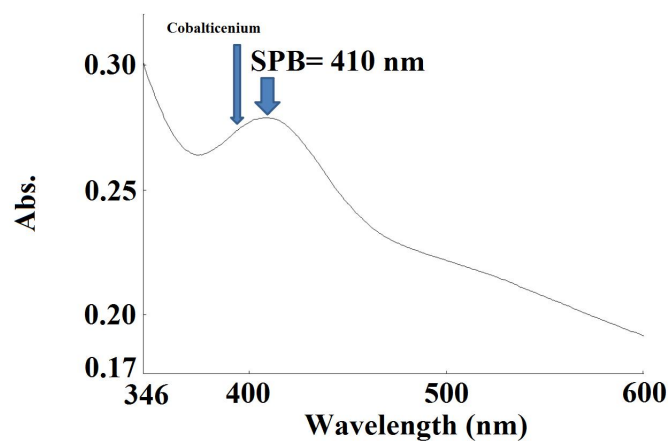


Figure 8. UV-*vis.* Spectra of AgNP obtained upon reduction of AgBF₄ by cobaltocene.

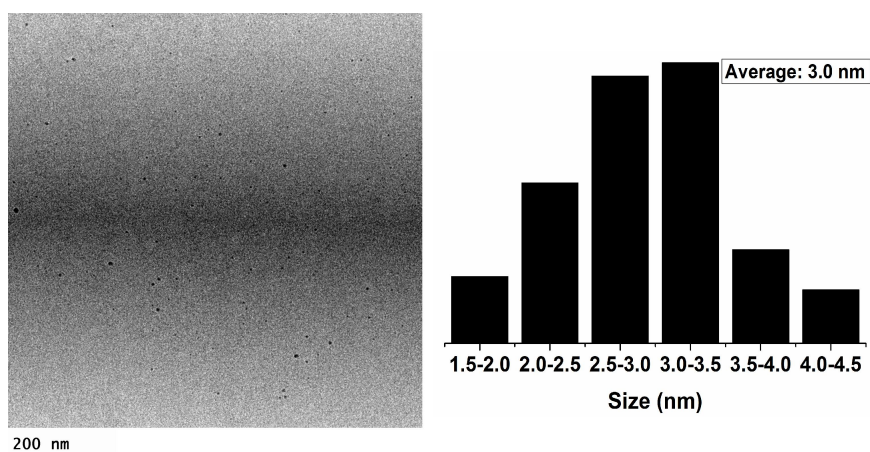


Figure 9. TEM (left) and histogram (right) of AgNP obtained upon reduction of AgNO₃ by cobaltocene.

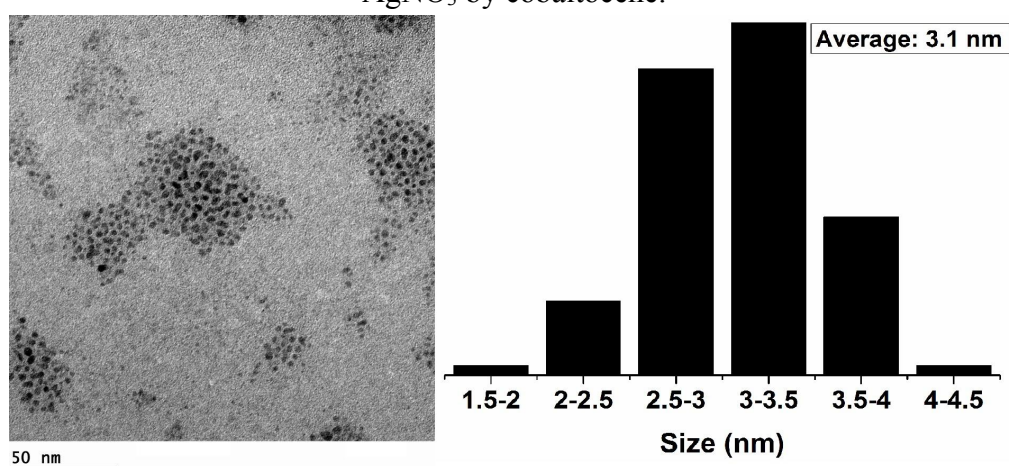


Figure 10. TEM (left) and histogram (right) of AgNP obtained upon reduction of AgF by cobaltocene.

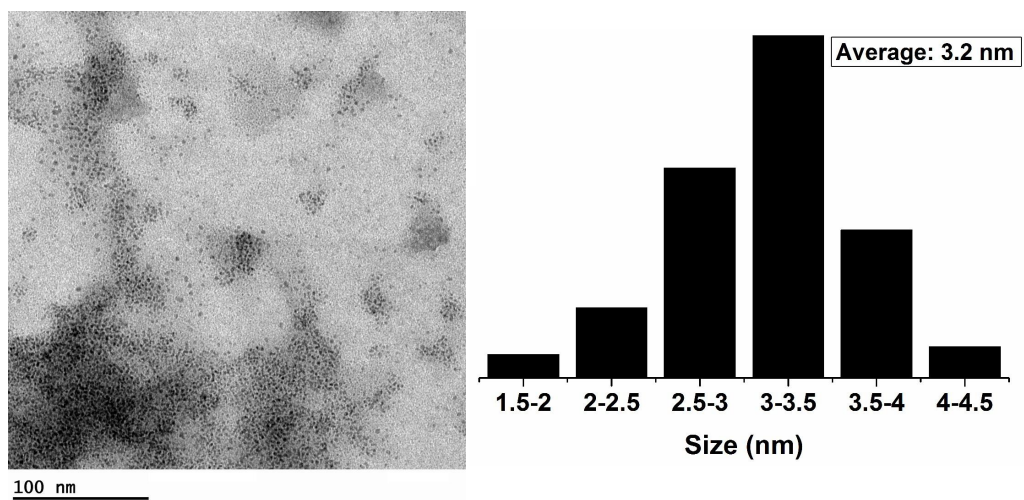


Figure 11. TEM (left) and histogram (right) of AgNP obtained upon reduction of AgBF_4 by cobaltocene.

3. Reduction of 4-nitrophenol catalyzed by AgNPs with NaBH₄ (at 20

°C)

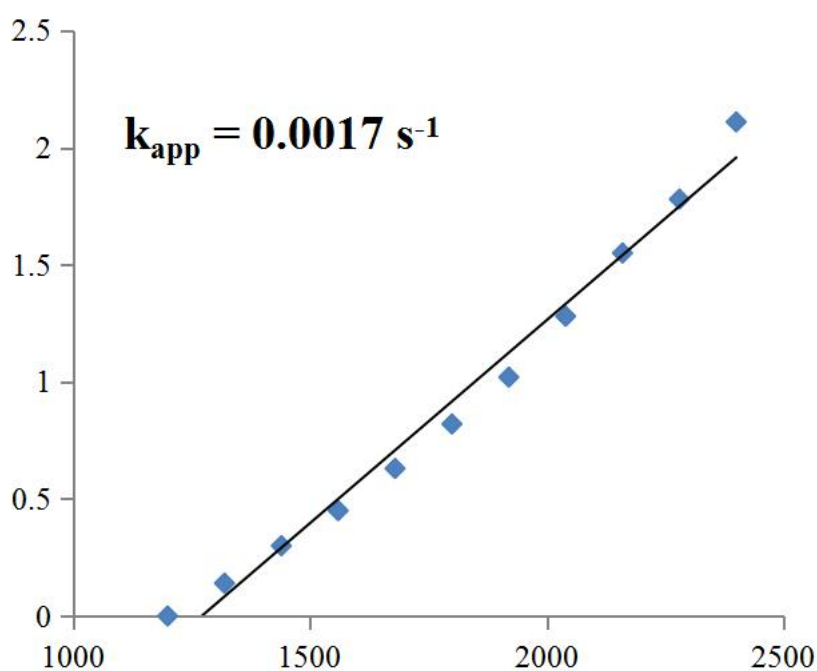
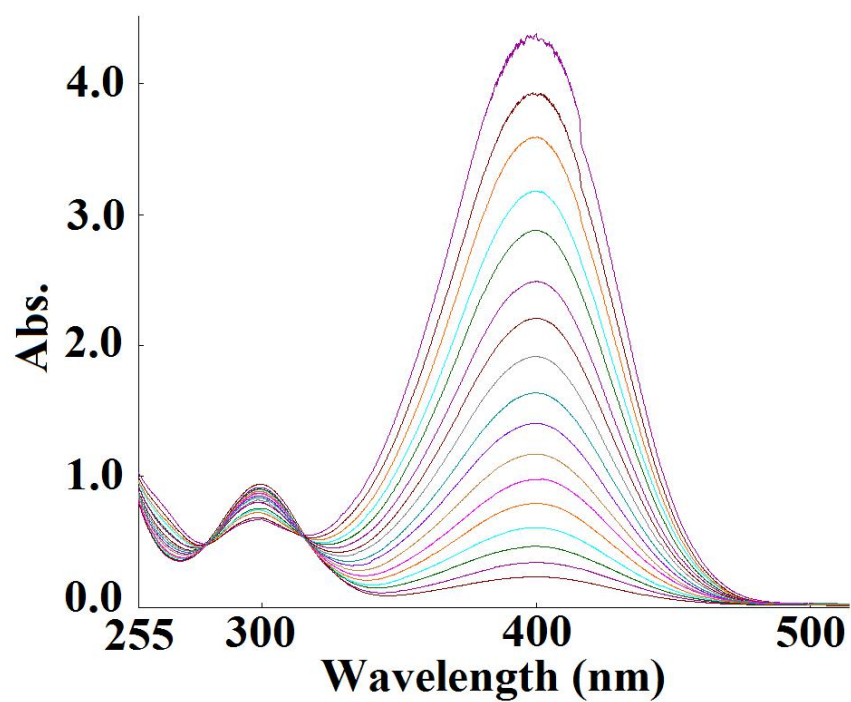


Figure 12. UV-vis. spectra of the 4-NP reduction by NaBH₄ catalyzed by AgNPs obtained upon reduction of AgNO₃ by cobaltocene (top); consumption rate of 4-NP: $-\ln(C_t/C_0)$ vs. reaction time (bottom).

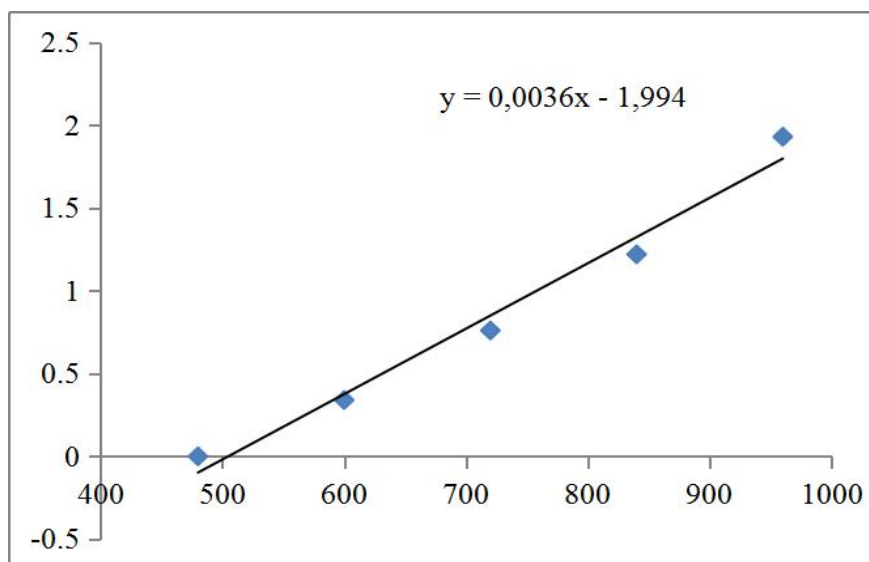
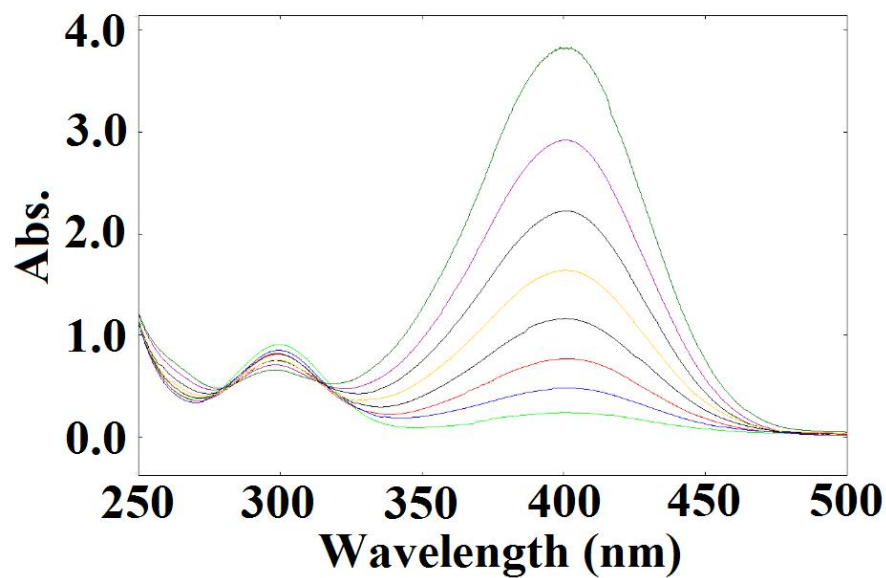


Figure 13. UV-vis. spectra of the 4-NP reduction by NaBH₄ catalyzed by AgNPs obtained upon reduction of AgF by cobaltocene (top); consumption rate of 4-NP: $-\ln(C_t/C_0)$ vs. reaction time (bottom).

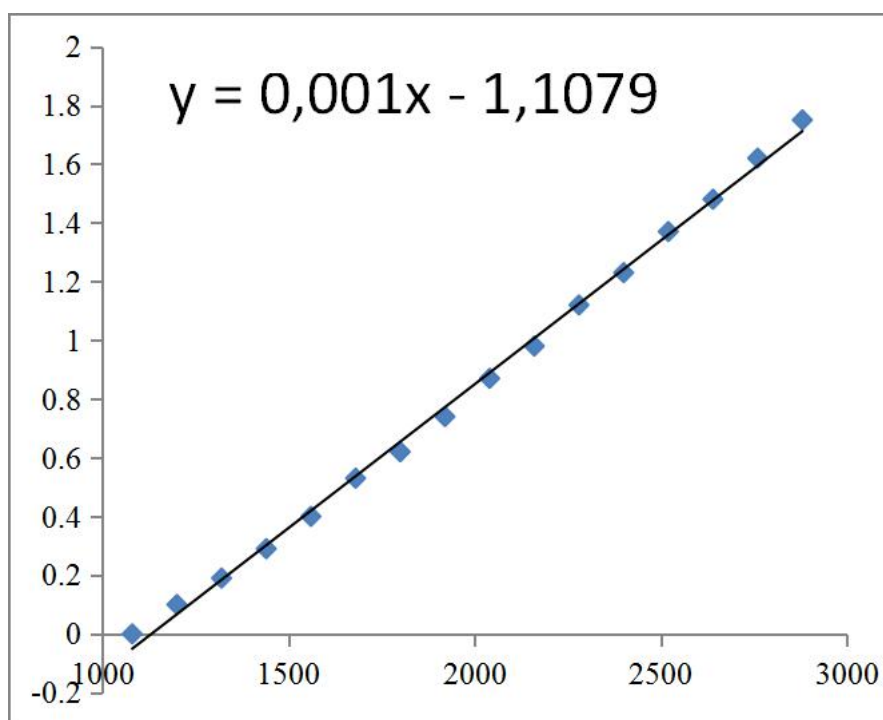
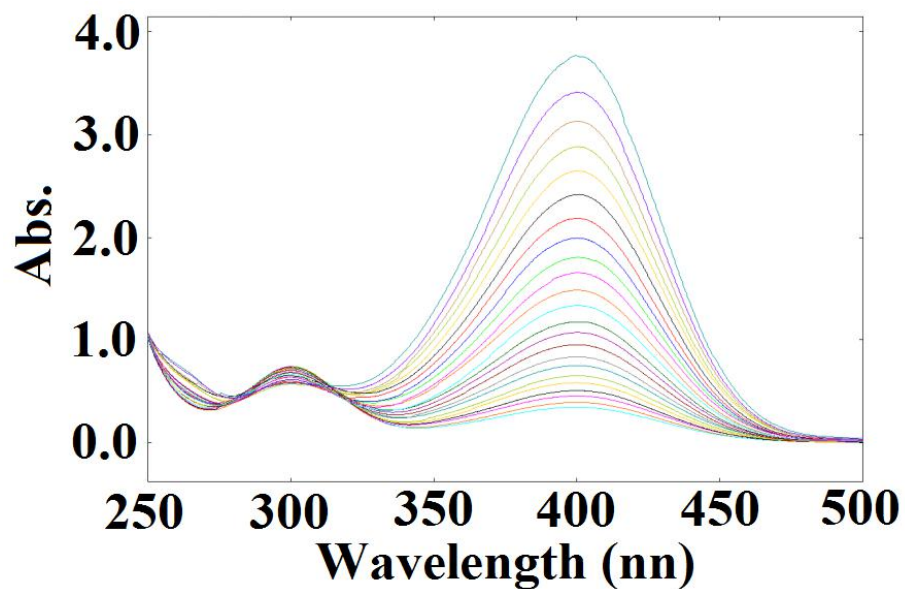


Figure 14. UV-vis. spectra of the 4-NP reduction by NaBH₄ catalyzed by AgNPs obtained upon reduction of AgBF₄ by cobaltocene (top); consumption rate of 4-NP: $-\ln(C_t/C_0)$ vs. reaction time (bottom).

4. Procedure for CuAAC reactions

General procedure for the CuAAC reactions

A Schenk flask equipped with a magnetic stir bar was charged with azide and alkyne under N₂. The catalyst was added into the Schlenk flask under N₂, and degassed water was added in order to obtain a 2 mL volume of aqueous solution. The heterogeneous reaction mixture was then stirred for 24 h at 35 °C under N₂, then the product was extracted with CH₂Cl₂ (3 x 15 mL). The organic layer was dried over Na₂SO₄ and filtered, and the solvent was removed *in vacuo* to provide the crude product. This product was then purified by silica gel column chromatography using petroleum ether/ethyl acetate: 10/1 for elution or washed with pentane to give an isolated yield indicated in the main text tables 1 and 2. The data for each reaction and product are given below each ¹H NMR spectrum.

Procedure for the one pot three components CuAAC reaction

A Schlenk flask equipped with a magnetic stir bar was charged with benzyl bromide (85.5 mg, 0.5 mmol), sodium azide (35.8 mg, 0.55 mmol) and phenylacetylene (51.5 mg, 0.505 mmol) under N₂. The catalyst was added into the Schlenk flask under N₂, and degassed water was added in order to obtain a 2 mL volume of aqueous solution. The reaction heterogeneous mixture was then stirred for 24 h at 35 °C under N₂, then the product was extracted with CH₂Cl₂ (3 x 15 mL). The organic layer was dried over Na₂SO₄ and filtered, and the solvent was removed *in vacuo* to give crude 1-benzyl-4-phenyl-1H-[1,2,3]triazole. This product was then purified by silica gel column chromatography using petroleum ether/ethyl acetate: 10/1 for elution to give a 93% isolated yield (108 mg).

Procedure for the recycling of the CuNPs.

In the recycling test, we used 0.5% CuNPs at the beginning and the reaction being carried out on 0.2 mmol scale:

After the reaction, the system was allowed to cool to r.t.. And the water soluble CuNPs catalysts were filtered to a new flask which was charging with another run of substrates under N₂. During those processes, cautions should be taken to avoid the air in order to ensure the catalytic active nanoparticles during the catalysis. And then the organic solids were extracted with CH₂Cl₂ and water, the organic layer was dried over Na₂SO₄ and filtered, and the solvent was removed *in vacuo* to give crude 1-benzyl-4-phenyl-1H-[1,2,3] triazole. This product was then purified by silica gel column chromatography using petroleum ether/ethyl acetate: 10/1 for elution to give the isolated yield.

Catalytic Runs	1 st	2 nd	3 rd	4 th
Yield	99%	95%	87%	86%

Procedure for the CuAAC synthesis for the compound (2)

CuAAC for the synthesis of p-bis (ferrocenyl-1,2,3-triazolylmethyl) benzene (2) :

A Schlenk flask equipped with a magnetic stir bar was charged with ethynylferrocene (84.8 mg, 0.404 mmol) and **1** (37.6 mg, 0.2 mmol) and under N₂. The catalyst (0.5%) and 2 mL H₂O were added under N₂, and the reaction mixture was stirred for 24 h at 35 °C under N₂. After the reaction, the crude product was extracted by using CH₂Cl₂ and H₂O three times, the organic phase was dried over Na₂SO₄, and the solvent was removed *in vacuo*. The solids were washed with pentane and filtered, and the remaining solids were dried *in vacuo* yielding *p*-bis (ferrocenyl-1,2,3-triazolylmethyl) benzene (**2**) (92%, 112 mg).

5. Characterization of the click products by ¹H NMR spectroscopy.

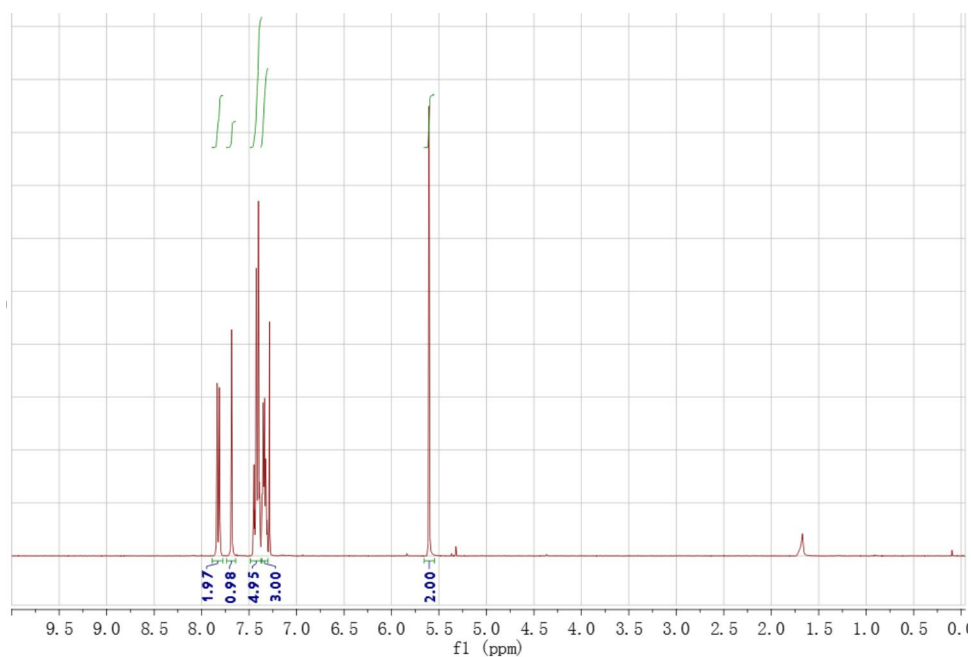


Figure 15. ¹H NMR spectrum of 1-benzyl-4-phenyl-1H-[1,2,3]triazole.

¹H NMR (300 MHz, CDCl₃) δ 7.89 – 7.77 (m, 2H), 7.68 (s, 1H), 7.49 – 7.37 (m, 5H), 7.38 – 7.30 (m, 3H), 5.60 (s, 2H). Reaction conditions: see experimental section.

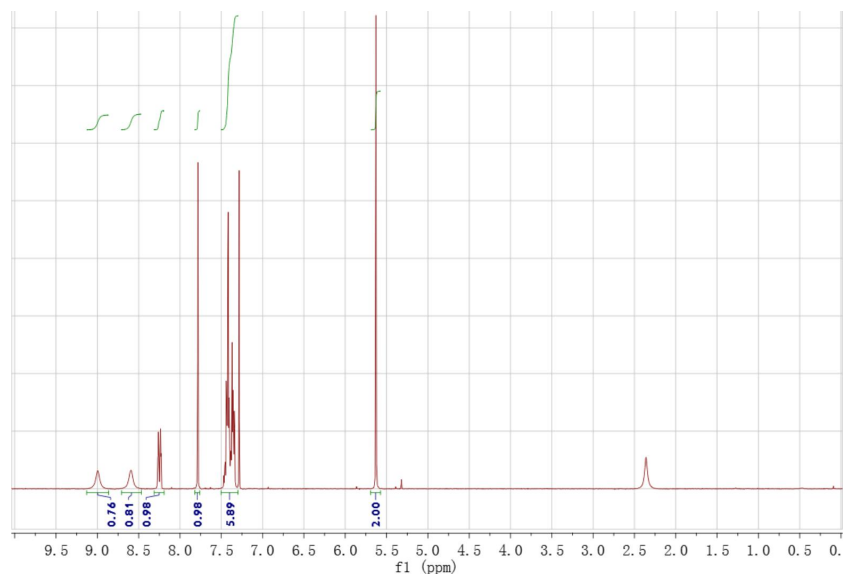


Figure 16. ^1H NMR spectrum of 3-(1-benzyl-1H-1,2,3-triazol-4-yl)pyridine.

^1H NMR (300 MHz, CDCl_3) δ 9.00 (s, 1H), 8.59 (s, 1H), 8.25 (dt, $J = 7.9, 1.8$ Hz, 1H), 7.78 (s, 1H), 7.50 – 7.30 (m, 6H), 5.63 (s, 2H).

Reaction conditions: 0.5 mmol (66.5 mg) of benzyl azide, 0.505 mmol (52 mg) of 3-ethynylpyridine, and 2 mL of H_2O , 0.1 mol% CuNPs, 35°C , 24 h, under N_2 . Isolated yield (106 mg, 90%).

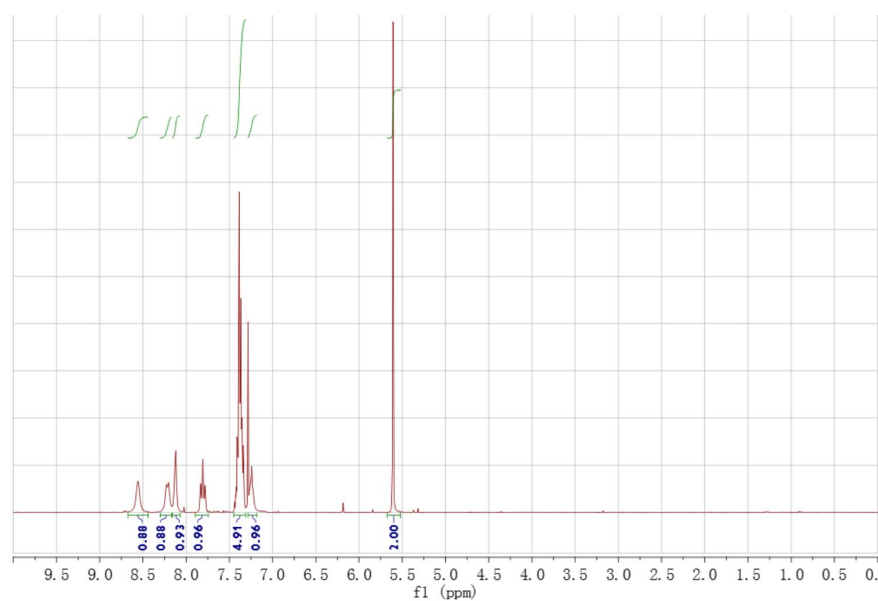


Figure 17. ^1H NMR spectrum of 2-(1-benzyl-1H-1,2,3-triazol-4-yl)pyridine.

^1H NMR (300 MHz, CDCl_3) δ 8.56 (s, 1H), 8.22 (d, $J = 6.7$ Hz, 1H), 8.12 (s, 1H), 7.89 – 7.74 (m, 1H), 7.45 – 7.31 (m, 5H), 7.24 (s, 1H), 5.61 (s, 2H).

Reaction conditions: 0.5 mmol (66.5 mg) of benzyl azide, 0.505 mmol (52 mg) of 2-ethynylpyridine, and 2 mL of H_2O , 0.1 mol% CuNPs, 35°C , 24 h, under N_2 . Isolated yield (98 mg, 83%).

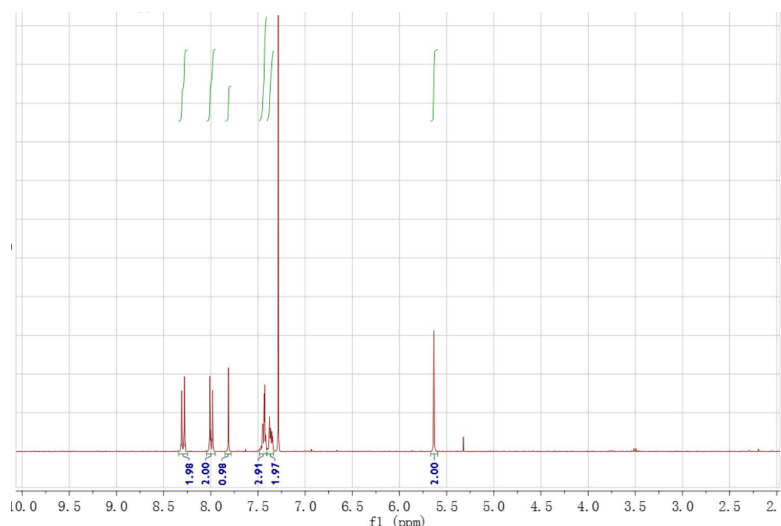


Figure 18. ^1H NMR spectrum of 1-benzyl-4-(4-nitrophenyl)-1H-1,2,3-triazole.

^1H NMR (300 MHz, CDCl_3) δ 8.34 – 8.25 (m, 2H), 8.05 – 7.95 (m, 2H), 7.81 (s, 1H), 7.48 – 7.41 (m, 3H), 7.41 – 7.33 (m, 2H), 5.64 (s, 2H).

Reaction conditions: 0.5 mmol (66.5 mg) of benzyl azide, 0.505 mmol (74.2 mg) of 1-ethynyl-4-nitrobenzene, and 2 mL of H_2O , 0.1 mol% CuNPs, 35°C , 24 h, under N_2 . Isolated yield (133 mg, 95%).

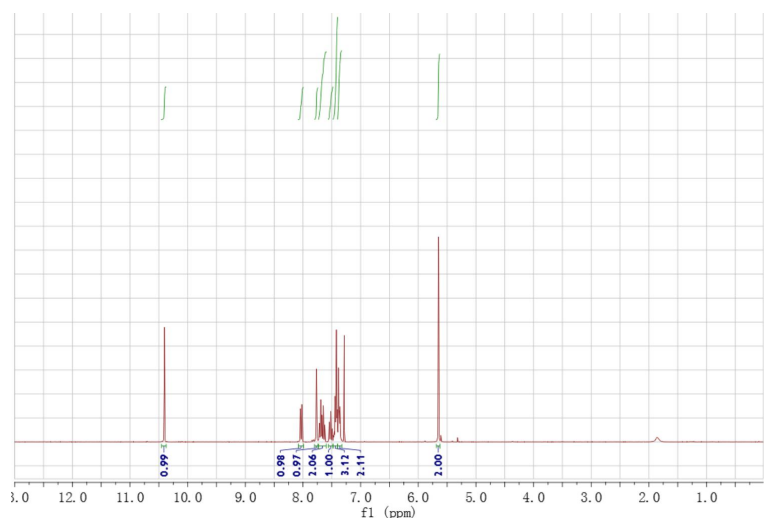


Figure 19. ^1H NMR spectrum of 2-(1-benzyl-1H-1,2,3-triazol-4-yl)benzaldehyde.

^1H NMR (300 MHz, CDCl_3) δ 10.40 (d, $J = 0.6$ Hz, 1H), 8.03 (dd, $J = 7.7, 1.2$ Hz, 1H), 7.77 (s, 1H), 7.73 – 7.60 (m, 2H), 7.52 (ddd, $J = 7.8, 7.1, 0.7$ Hz, 1H), 7.48 – 7.40 (m, 3H), 7.40 – 7.33 (m, 2H), 5.65 (s, 2H).

Reaction conditions: 0.5 mmol (66.5 mg) of benzyl azide, 0.505 mmol (65.6 mg) of 2-ethynylbenzaldehyde, and 2 mL of H_2O , 0.1 mol% CuNPs, 35°C , 24 h, under N_2 . Isolated yield (100 mg, 85%).

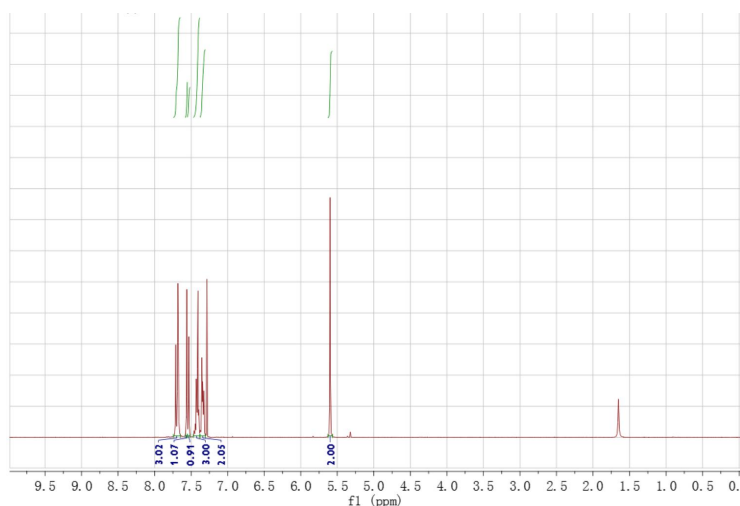


Figure 20. ^1H NMR spectrum of 1-benzyl-4-(4-bromophenyl)-1H-1,2,3-triazole. ^1H NMR (300 MHz, CDCl_3) δ 7.69 (dd, $J = 8.7, 1.9$ Hz, 3H), 7.58 – 7.55 (m, 1H), 7.53 (d, $J = 1.7$ Hz, 1H), 7.47 – 7.38 (m, 3H), 7.38 – 7.31 (m, 2H), 5.60 (s, 2H). Reaction conditions: 0.5 mmol (66.5 mg) of benzyl azide, 0.505 mmol (90.9 mg) of 1-bromo-4-ethynylbenzene, and 2 mL of H_2O , 0.1 mol% CuNPs, 35°C , 24 h, under N_2 . Isolated yield (233 mg, 94%).

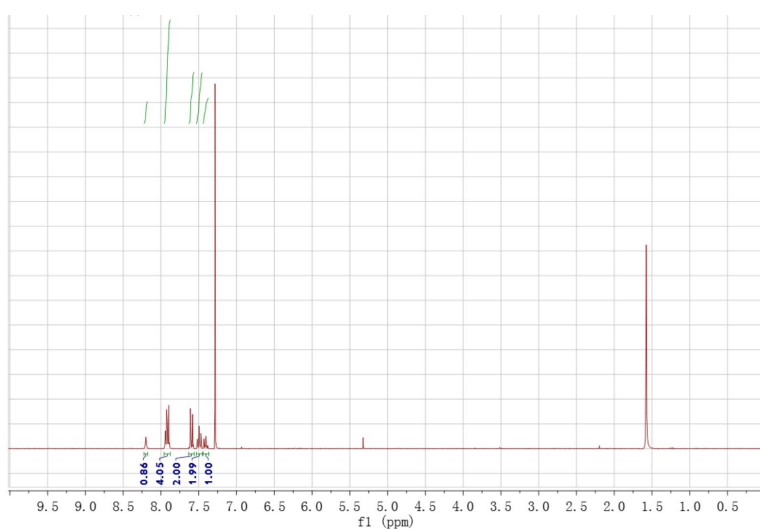


Figure 21. ^1H NMR spectrum of 1-(4-iodophenyl)-4-phenyl-1H-1,2,3-triazole. ^1H NMR (300 MHz, CDCl_3) δ 8.20 (s, 1H), 7.96 – 7.88 (m, 4H), 7.63 – 7.56 (m, 2H), 7.53 – 7.45 (m, 2H), 7.41 (dd, $J = 8.5, 6.2$ Hz, 1H). Reaction conditions: 0.5 mmol (122.5 mg) of 1-azido-4-iodobenzene, 0.505 mmol (51.5 mg) of phenylacetylene, and 2 mL of H_2O , 0.1 mol% CuNPs, 35°C , 24 h, under N_2 . Isolated yield (172 mg, 99%).

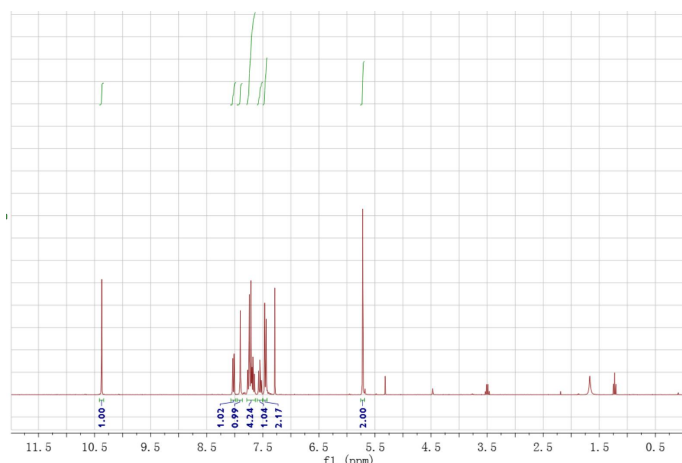


Figure 24. ^1H NMR spectrum of 4-((4-(2-formylphenyl)-1H-1,2,3-triazol-1-yl)methyl) benzonitrile.

^1H NMR (300 MHz, CDCl_3) δ 10.41 – 10.34 (m, 1H), 8.03 (dd, $J = 7.7, 1.4$ Hz, 1H), 7.90 (s, 1H), 7.79 – 7.63 (m, 4H), 7.56 (dd, $J = 11.1, 3.9$ Hz, 1H), 7.45 (d, $J = 8.5$ Hz, 2H), 5.72 (s, 2H).

Reaction conditions: 0.5 mmol (79 mg) of 4-(azidomethyl)benzonitrile, 0.505 mmol (65.6 mg) of 2-ethynylbenzaldehyde, and 2 mL of H_2O , 0.1 mol% CuNPs, 35°C , 24 h, under N_2 . Isolated yield (122 mg, 85%).

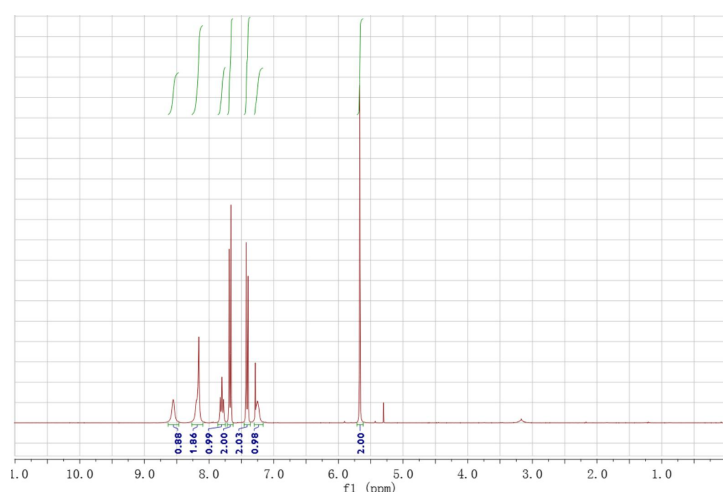


Figure 25. ^1H NMR spectrum of 4-((4-(pyridin-2-yl)-1H-1,2,3-triazol-1-yl)methyl) benzonitrile.

^1H NMR (300 MHz, CDCl_3) δ 8.56 (s, 1H), 8.18 (d, $J = 10.9$ Hz, 2H), 7.80 (t, $J = 7.7$ Hz, 1H), 7.72 – 7.63 (m, 2H), 7.41 (d, $J = 8.4$ Hz, 2H), 7.27 (d, $J = 9.8$ Hz, 1H), 5.67 (s, 2H).

Reaction conditions: 0.5 mmol (79 mg) of 4-(azidomethyl)benzonitrile, 0.505 mmol (52 mg) of 2-ethynylpyridine, and 2 mL of H_2O , 0.1 mol% CuNPs, 35°C , 24 h, under N_2 . Isolated yield (128 mg, 98%).

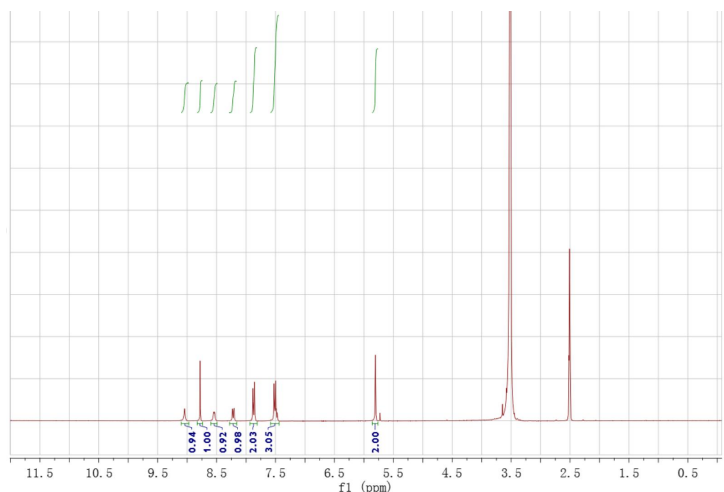


Figure 26. ^1H NMR spectrum of 4-((4-(pyridin-3-yl)-1H-1,2,3-triazol-1-yl)methyl)benzonitrile.

^1H NMR (300 MHz, DMSO) δ 9.04 (s, 1H), 8.78 (s, 1H), 8.54 (d, $J = 3.4$ Hz, 1H), 8.28 – 8.16 (m, 1H), 7.93 – 7.81 (m, 2H), 7.58 – 7.44 (m, 3H), 5.80 (s, 2H).

Reaction conditions: 0.5 mmol (79 mg) of 4-(azidomethyl)benzonitrile, 0.505 mmol (52 mg) of 3-ethynylpyridine, and 2 mL of H_2O , 0.1 mol% CuNPs, 35°C, 24 h, under N_2 . Isolated yield (119 mg, 91%).

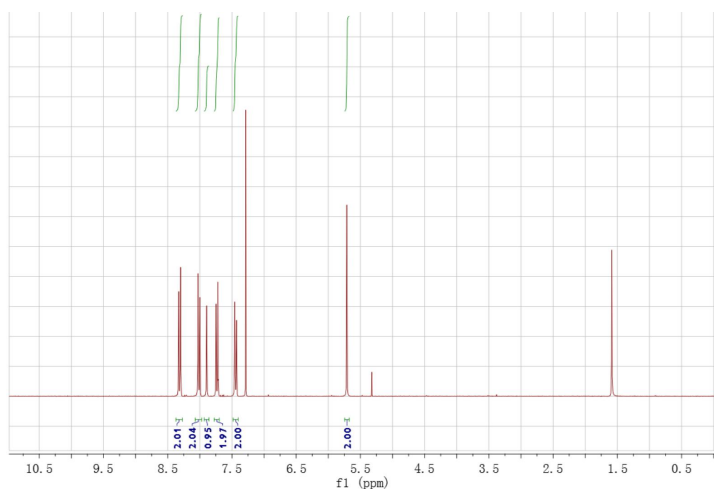


Figure 27. ^1H NMR spectrum of 4-((4-(4-nitrophenyl)-1H-1,2,3-triazol-1-yl)methyl)benzonitrile.

^1H NMR (300 MHz, CDCl_3) δ 8.37 – 8.27 (m, 2H), 8.07 – 7.97 (m, 2H), 7.89 (s, 1H), 7.78 – 7.70 (m, 2H), 7.44 (d, $J = 8.6$ Hz, 2H), 5.71 (s, 2H).

Reaction conditions: 0.5 mmol (79 mg) of 4-(azidomethyl)benzonitrile, 0.505 mmol (74.2 mg) of 1-ethynyl-4-nitrobenzene, and 2 mL of H_2O , 0.1 mol% CuNPs, 35°C, 24 h, under N_2 . Isolated yield (140 mg, 92%).

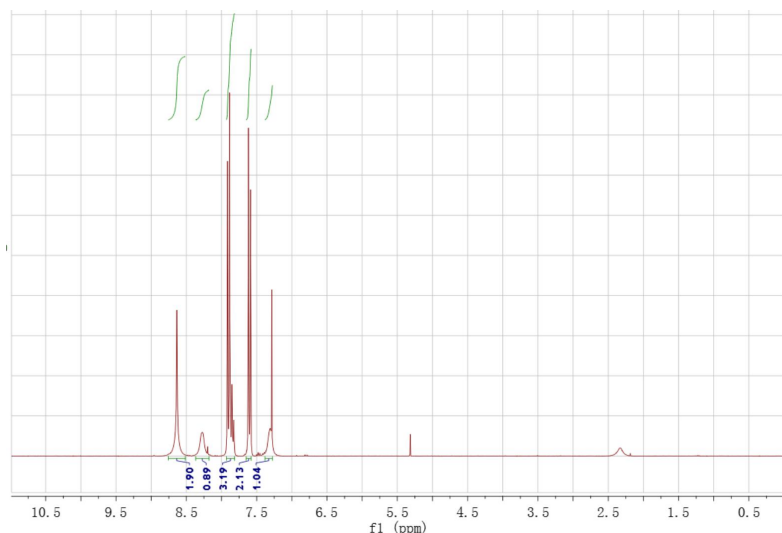


Figure 30. ^1H NMR spectrum of 2-(1-(4-iodophenyl)-1H-1,2,3-triazol-4-yl)pyridine. ^1H NMR (300 MHz, CDCl_3) δ 8.63 (s, 2H), 8.23 (d, $J = 22.6$ Hz, 1H), 7.93 – 7.82 (m, 3H), 7.65 – 7.58 (m, 2H), 7.30 (d, $J = 6.5$ Hz, 1H).
 Reaction conditions: 0.5 mmol (122.5 mg) of 1-azido-4-iodobenzene, 0.505 mmol (52 mg) of 2-ethynylpyridine, and 2 mL of H_2O , 0.1 mol% CuNPs, 35°C , 24 h, under N_2 . Isolated yield (143 mg, 82%).

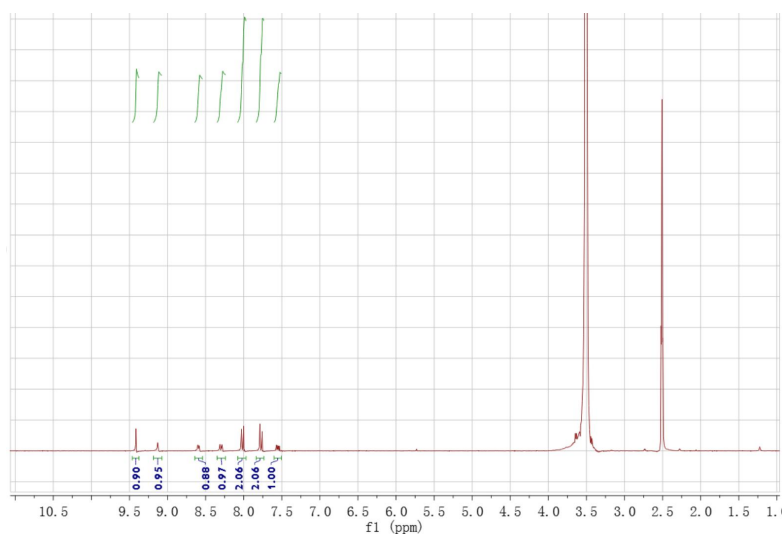


Figure 31. ^1H NMR spectrum of 3-(1-(4-iodophenyl)-1H-1,2,3-triazol-4-yl)pyridine. ^1H NMR (300 MHz, DMSO) δ 9.41 (d, $J = 2.4$ Hz, 1H), 9.12 (d, $J = 8.0$ Hz, 1H), 8.59 (dd, $J = 6.5, 3.2$ Hz, 1H), 8.29 (ddd, $J = 6.5, 4.3, 2.2$ Hz, 1H), 8.08 – 7.97 (m, 2H), 7.84 – 7.73 (m, 2H), 7.55 (dd, $J = 8.0, 4.8$ Hz, 1H).
 Reaction conditions: 0.5 mmol (122.5 mg) of 1-azido-4-iodobenzene, 0.505 mmol (52 mg) of 3-ethynylpyridine, and 2 mL of H_2O , 0.1 mol% CuNPs, 35°C , 24 h, under N_2 . Isolated yield (169 mg, 97%).

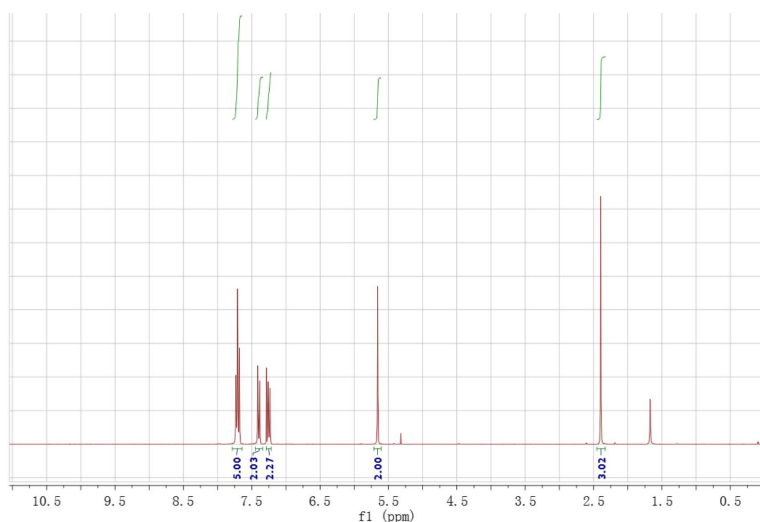


Figure 32. ^1H NMR spectrum of 4-((4-(p-tolyl)-1H-1,2,3-triazol-1-yl)methyl)benzonitrile.

^1H NMR (300 MHz, CDCl_3) δ 7.78 – 7.64 (m, 5H), 7.40 (d, $J = 8.5$ Hz, 2H), 7.29 – 7.22 (m, 2H), 5.66 (s, 2H), 2.40 (s, 3H).

Reaction conditions: 0.5 mmol (79 mg) of 4-(azidomethyl)benzonitrile, 0.505 mmol (56.8 mg) of 1-ethynyl-4-methylbenzene, and 2 mL of H_2O , 0.2 mol% CuNPs, 35°C , 24 h, under N_2 . Isolated yield (130 mg, 95%).

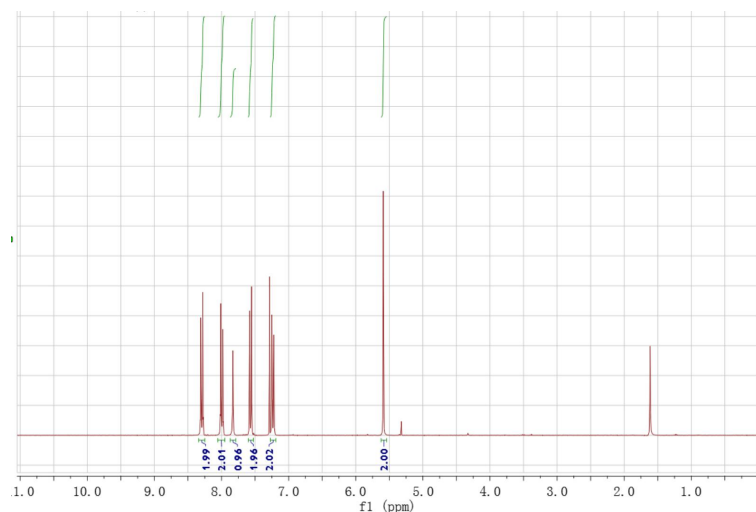


Figure 33. ^1H NMR spectrum of 1-(4-bromobenzyl)-4-(4-nitrophenyl)-1H-1,2,3-triazole.

^1H NMR (300 MHz, CDCl_3) δ 8.34 – 8.25 (m, 2H), 8.05 – 7.95 (m, 2H), 7.83 (s, 1H), 7.60 – 7.53 (m, 2H), 7.27 – 7.19 (m, 2H), 5.59 (s, 2H).

Reaction conditions: 0.5 mmol (105 mg) of 1-(azidomethyl)-4-bromobenzene, 0.505 mmol (74.2 mg) of 1-ethynyl-4-nitrobenzene, and 2 mL of H_2O , 0.2 mol% CuNPs, 35°C , 24 h, under N_2 . Isolated yield (163 mg, 91%).

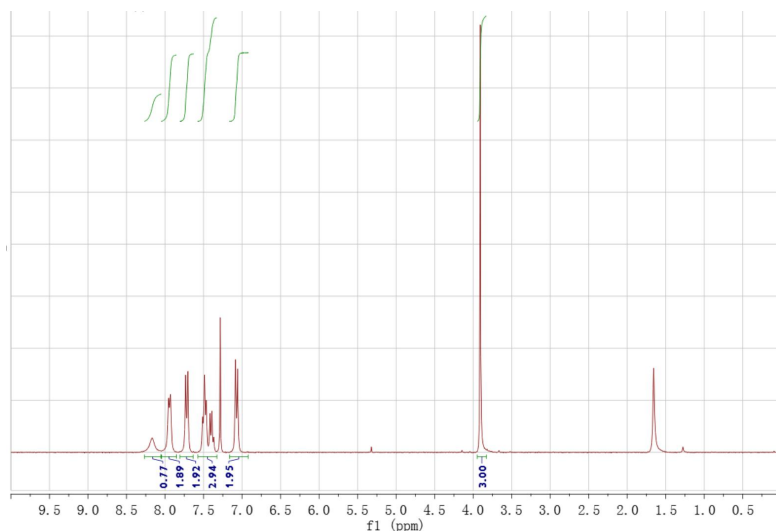


Figure 34. ^1H NMR spectrum of 1-(4-methoxyphenyl)-4-phenyl-1H-1,2,3-triazole.

^1H NMR (300 MHz, CDCl_3) δ 8.17 (s, 1H), 7.94 (d, $J = 6.9$ Hz, 2H), 7.72 (d, $J = 8.8$ Hz, 2H), 7.44 (dt, $J = 29.1, 7.2$ Hz, 3H), 7.07 (d, $J = 8.6$ Hz, 2H), 3.91 (s, 3H).

Reaction conditions: 0.5 mmol (74.5 mg) of 1-azido-4-methoxybenzene, 0.505 mmol (51.5 mg) of phenylacetylene, and 2 mL of H_2O , 0.2 mol% CuNPs, 35°C , 24 h, under N_2 . Isolated yield (113 mg, 90%).

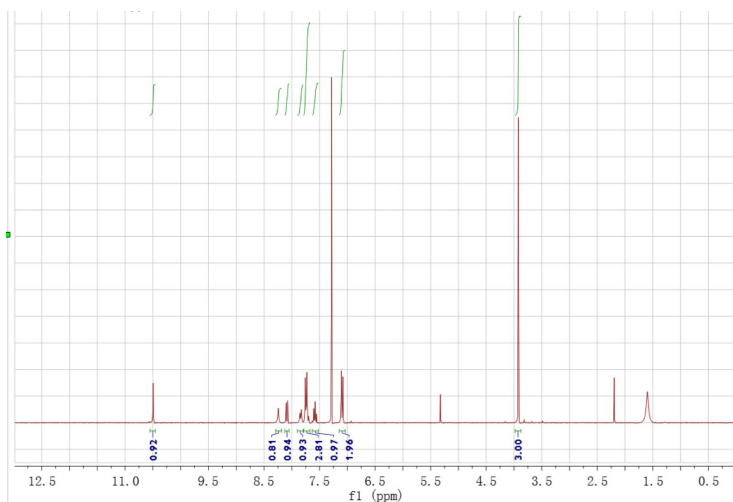


Figure 35. ^1H NMR spectrum of 2-(1-(4-methoxyphenyl)-1H-1,2,3-triazol-4-yl)benzaldehyde.

^1H NMR (300 MHz, CDCl_3) δ 10.50 (s, 1H), 8.24 (s, 1H), 8.09 (dd, $J = 7.8, 1.3$ Hz, 1H), 7.84 (d, $J = 7.4$ Hz, 1H), 7.73 (t, $J = 9.4$ Hz, 3H), 7.58 (t, $J = 7.5$ Hz, 1H), 7.09 (d, $J = 9.0$ Hz, 2H), 3.92 (s, 3H).

Reaction conditions: 0.5 mmol (74.5 mg) of 1-azido-4-methoxybenzene, 0.505 mmol (65.6 mg) of 2-ethynylbenzaldehyde, and 2 mL of H_2O , 0.2 mol% CuNPs, 35°C , 24 h, under N_2 . Isolated yield (112 mg, 80%).

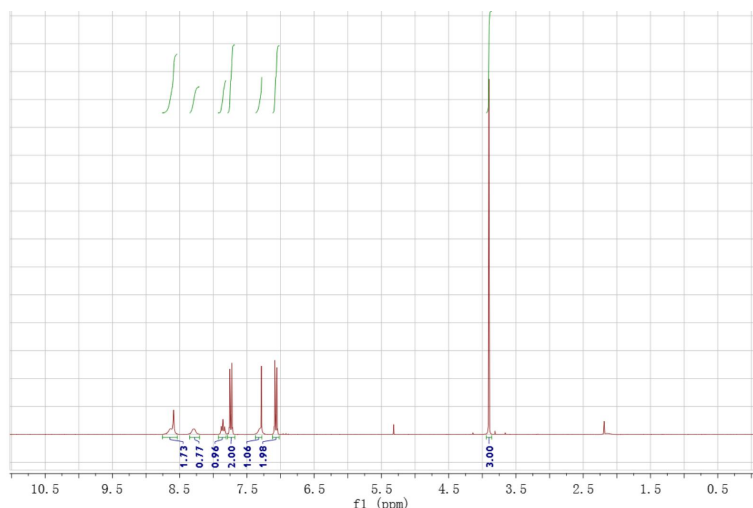


Figure 36. ^1H NMR spectrum of 2-(1-(4-methoxyphenyl)-1H-1,2,3-triazol-4-yl)pyridine.

^1H NMR (300 MHz, CDCl_3) δ 8.61 (d, $J = 13.7$ Hz, 2H), 8.28 (s, 1H), 7.86 (t, $J = 7.7$ Hz, 1H), 7.79 – 7.68 (m, 2H), 7.28 (s, 1H), 7.12 – 7.02 (m, 2H), 3.90 (s, 3H).

Reaction conditions: 0.5 mmol (74.5 mg) of 1-azido-4-methoxybenzene, 0.505 mmol (52 mg) of 2-ethynylpyridine, and 2 mL of H_2O , 0.2 mol% CuNPs, 35°C, 24 h, under N_2 . Isolated yield (105 mg, 83%).

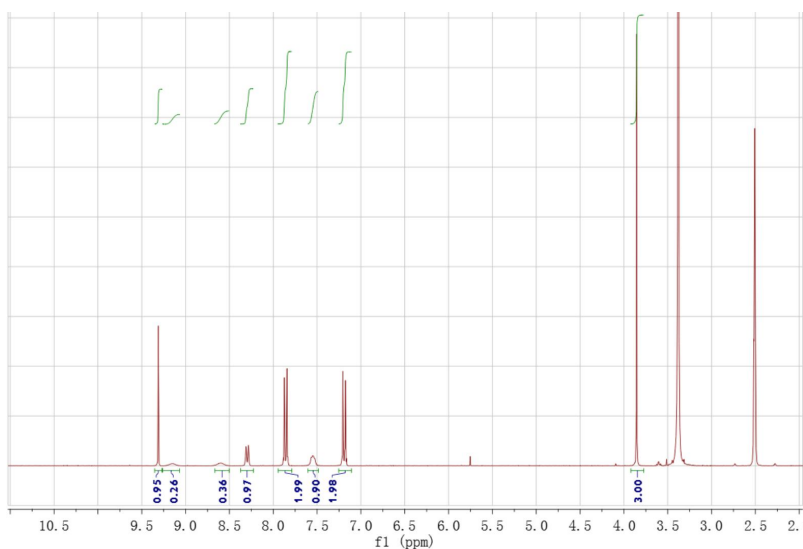


Figure 37. ^1H NMR spectrum of 3-(1-(4-methoxyphenyl)-1H-1,2,3-triazol-4-yl)pyridine.

^1H NMR (300 MHz, DMSO) δ 9.31 (s, 1H), 9.15 (s, 1H), 8.60 (s, 1H), 8.30 (d, $J = 8.0$ Hz, 1H), 7.94 – 7.79 (m, 2H), 7.56 (d, $J = 4.5$ Hz, 1H), 7.25 – 7.11 (m, 2H), 3.85 (s, 3H).

Reaction conditions: 0.5 mmol (74.5 mg) of 1-azido-4-methoxybenzene, 0.505 mmol (52 mg) of 3-ethynylpyridine, and 2 mL of H_2O , 0.2 mol% CuNPs, 35°C, 24 h, under N_2 . Isolated yield (110 mg, 87%).

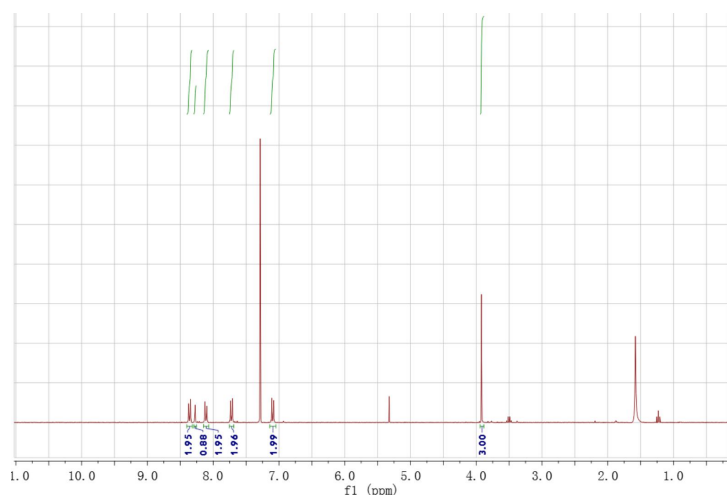


Figure 38. ^1H NMR spectrum of 1-(4-methoxyphenyl)-4-(4-nitrophenyl)-1H-1,2,3-triazole.

^1H NMR (300 MHz, CDCl_3) δ 8.36 (d, $J = 8.9$ Hz, 2H), 8.27 (s, 1H), 8.11 (d, $J = 8.9$ Hz, 2H), 7.75 – 7.68 (m, 2H), 7.14 – 7.05 (m, 2H), 3.92 (s, 3H).

Reaction conditions: 0.5 mmol (74.5 mg) of 1-azido-4-methoxybenzene, 0.505 mmol (74.2 mg) of 1-ethynyl-4-nitrobenzene, and 2 mL of H_2O , 0.2 mol% CuNPs, 35°C , 24 h, under N_2 . Isolated yield (132 mg, 89%).

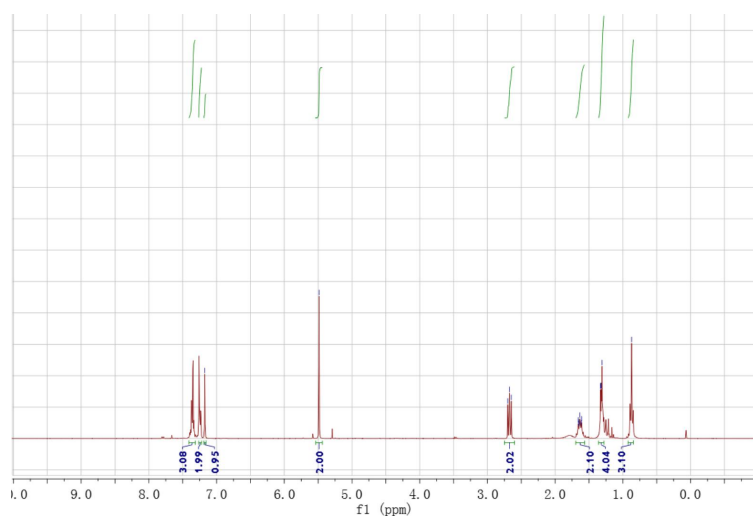


Figure 39. ^1H NMR spectrum of 1-benzyl-4-pentyl-1H-1,2,3-triazole.

^1H NMR (300 MHz, CDCl_3) δ 7.41 – 7.32 (m, 3H), 7.26 – 7.22 (m, 2H), 7.17 (s, 1H), 5.49 (s, 2H), 2.75 – 2.60 (m, 2H), 1.70 – 1.57 (m, 2H), 1.36 – 1.28 (m, 4H), 0.87 (s, 3H).

Reaction conditions: 0.5 mmol (66.5 mg) of benzyl azide, 0.505 mmol (48.6 mg) of 1-heptyne, and 1 mL H_2O and 1 mL *tert*-butanol, 0.2 mol% CuNPs, 35°C , 24 h, under N_2 . Isolated yield (97 mg, 85%).

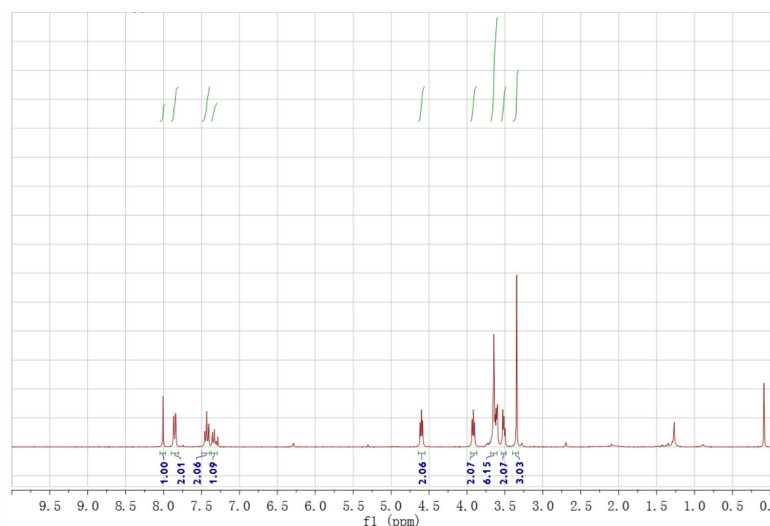


Figure 40. ^1H NMR spectrum of 1-(2-(2-(2-methoxyethoxy)ethoxy)ethyl)-4-phenyl-1H-1,2,3-triazole.

^1H NMR (300 MHz, CDCl_3) δ 8.01 (s, 1H), 7.90 – 7.80 (m, 2H), 7.43 (t, $J = 7.4$ Hz, 2H), 7.33 (t, $J = 7.3$ Hz, 1H), 4.64 – 4.55 (m, 2H), 3.95 – 3.87 (m, 2H), 3.69 – 3.60 (m, 6H), 3.55 – 3.49 (m, 2H), 3.34 (s, 3H).

Reaction conditions: 0.5 mmol (94.6 mg) of 1-azido-2-(2-(2-methoxyethoxy)ethoxy)ethane, 0.505 mmol (51.5 mg) of phenylacetylene, and 2 mL of H_2O , 0.2 mol% CuNPs, 35°C , 24 h, under N_2 . Isolated yield (137 mg, 94%).

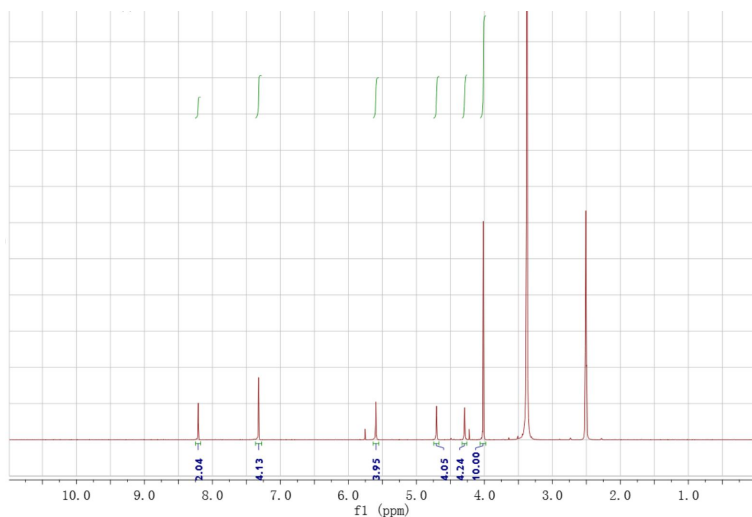


Figure 41. ^1H NMR spectrum of compound **2**.⁵³

^1H NMR (300 MHz, DMSO) δ 8.22 (d, $J = 8.1$ Hz, 2H), 7.32 (s, 4H), 5.60 (s, 4H), 4.70 (t, $J = 1.8$ Hz, 4H), 4.33 – 4.26 (m, 4H), 4.02 (d, $J = 3.1$ Hz, 10H).

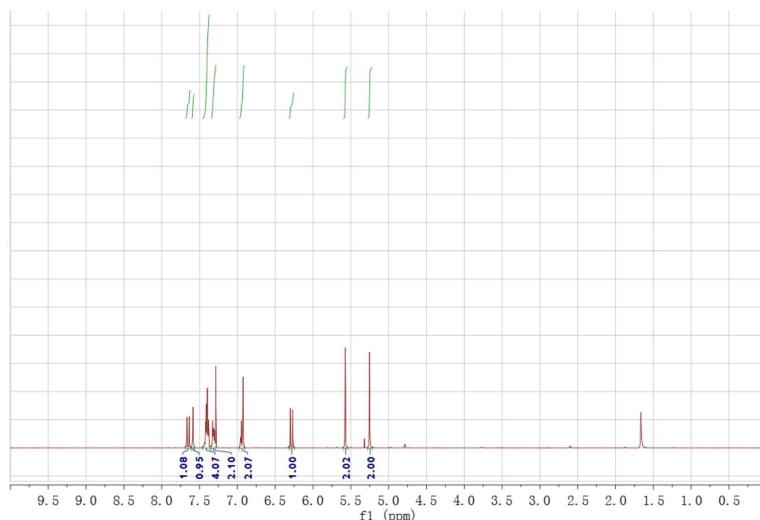


Figure 42. ^1H NMR spectrum of compound **4**.⁵³

^1H NMR (300 MHz, CDCl_3) δ 7.66 (dd, $J = 9.4, 5.6$ Hz, 1H), 7.59 (s, 1H), 7.46 – 7.36 (m, 4H), 7.35 – 7.29 (m, 2H), 6.94 (dd, $J = 7.7, 2.0$ Hz, 2H), 6.32 – 6.25 (m, 1H), 5.57 (s, 2H), 5.25 (s, 2H).

Reaction conditions: 0.2 mmol (26.6 mg) of benzyl azide, 0.205 mmol (41.1 mg) of compound **3**, and 2 mL of H_2O , 0.5 mol% CuNPs, 35°C, 24 h, under N_2 . Isolated yield (64 mg, 95%).

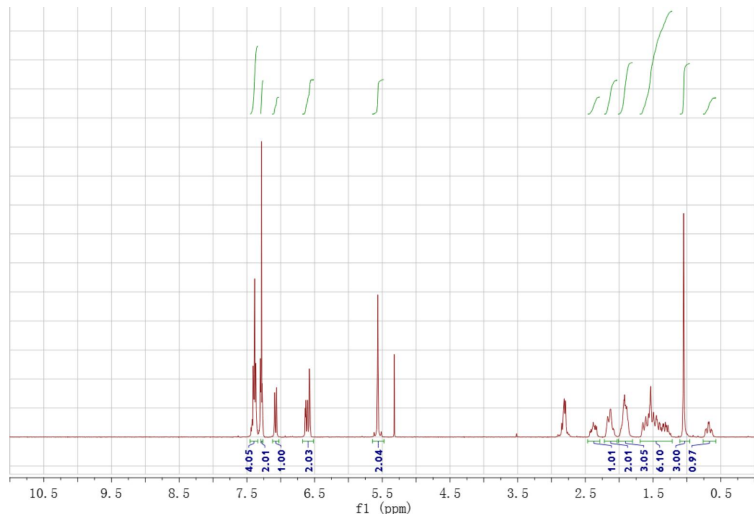


Figure 43. ^1H NMR spectrum of compound **6**.⁵³

^1H NMR (300 MHz, CDCl_3) δ 7.45 – 7.34 (m, 4H), 7.28 (q, $J = 1.9$ Hz, 2H), 7.08 (d, $J = 8.3$ Hz, 1H), 6.68 – 6.51 (m, 2H), 5.65 – 5.48 (m, 2H), 2.47 – 2.29 (m, 1H), 2.13 (dd, $J = 14.0, 11.0$ Hz, 2H), 2.01 – 1.80 (m, 3H), 1.69 – 1.22 (m, 6H), 1.05 (s, 3H), 0.68 (dd, $J = 12.9, 9.0$ Hz, 1H).

Reaction conditions: 0.2 mmol (26.6 mg) of benzyl azide, 0.205 mmol (60.7 mg) of compound **5**, and 2 mL of H_2O , 0.5 mol% CuNPs, 35°C, 24 h, under N_2 . Isolated yield (82 mg, 96%).

References

- 1 Schmid, G. *Nanoparticles: From Theory to Application*; Wiley-VCH: Weinheim, Germany, **2004**.
- 2 Xia, Y. N.; Xiong, Y. J.; Lim, B.; Skrabalak, S. E. Shape-controlled Synthesis of Metal Nanocrystals: Simple Chemistry Meets Complex Physics? *Angew. Chem. Int. Ed. Engl.* **2009**, *48*, 60–103.
- 3 Brongersma, M. L.; Halas, N. J.; Nordlander, P. Plasmon-induced Hot Carrier Science and Technology. *Nat. Nanotechnol.* **2015**, *10*, 25–34.
- 4 Daniel, M. –C.; Astruc, D. Gold Nanoparticles: Assembly, Supramolecular Chemistry, Quantum-Size-Related Properties, and Applications toward Biology, Catalysis, and Nanotechnology. *Chem. Rev.* **2004**, *104*, 293–346.
- 5 Basset, J. –M.; Psaro, R.; Roberto, D.; Ugo, R. *Modern Surface Organometallic Chemistry*; Wiley-VCH: Weinheim, 2009.
- 6 Meyers, V. S.; Weier, M. G.; Carino, E. V.; Yancey, D. F.; Pande, S.; Crooks, R. M. Dendrimer-encapsulated Nanoparticles: New Synthetic and Characterization Methods and Catalytic Applications. *Chem. Sci.* **2011**, *2*, 1632–1646.
- 7 Bronstein, L. M.; Shifrina, Z. B. Dendrimers as Encapsulating, Stabilizing, or Directing Agents for Inorganic Nanoparticles. *Chem. Rev.* **2011**, *111*, 5301–5344.
- 8 Ye, R.; Yuan, B.; Zhao, J.; Ralston, W. T.; Wu, C. Y.; Bari, E. U.; Toste, F. D.; Somorjai, G. A. Metal Nanoparticles Catalyzed Selective Carbon–Carbon Bond Activation in the Liquid Phase. *J. Am. Chem. Soc.* **2016**, *138*, 8533–8537.
- 9 Reetz, M. T.; de Vries, J. G. Ligand-free Heck Reactions Using Low Pd-loading. *Chem. Commun.* **2004**, 1559–1563.
- 10 Haruta, M. Chance and Necessity: My Encounter with Gold Catalysts. *Angew. Chem., Int. Ed.* **2014**, *53*, 52–56.
- 11 Sankar, M.; Dimitratos, N.; Miedziak, P. J.; Wells, P. P.; Kiely, C. J.; Hutchings, G. J. Designing Bimetallic Catalysts for a Green and Sustainable Future. *Chem. Sci.* **2012**, *3*, 20–44.
- 12 Balanta, A.; Godard, C.; Claver, C. Pd Nanoparticles for C–C Coupling Reactions. *Chem. Soc. Rev.* **2011**, *40*, 4973–4985.
- 13 Polshettiwar, V.; Varma, R. S. Green Chemistry by Nano-catalysis. *Green Chemistry* **2010**, *12*, 743–754.
- 14 Corma, A.; Leyva-Perez, A.; Maria Sabater, J. Gold-Catalyzed Carbon–Heteroatom Bond-Forming Reactions. *Chem. Rev.* **2011**, *111*, 1657–1712.

- 15 Cornils, B.; Herrmann, W. A. *Applied Homogeneous Catalysis with Organometallic Compounds*; Wiley-VCH: Weinheim, 1996.
- 16 Bell, A. T. The Impact of Nanoscience on Heterogeneous Catalysis. *Science* 2003, *299*, 1688–1691.
- 17 Cui, C. H.; Gan, L.; Heggen, M.; Rudi, S.; Strasser, P. Compositional Segregation in Shaped Pt Alloy Nanoparticles and their Structural Behaviour During Electrocatalysis. *Nat. Mater.* 2013, *12*, 765–771.
- 18 Prieto, G.; Zečević, J.; Friederich, H.; de Jong, K. P.; de Jongh, P. E. Towards Stable Catalysts by Controlling Collective Properties of Supported Metal Nanoparticles. *Nat. Mater.* 2013, *12*, 34–39.
- 19 Na, K.; Choi, M.; Yaghi, O. M.; Somorjai, G. A. Metal Nanocrystals Embedded in Single Nanocrystals of MOFs Give Unusual Selectivity as Heterogeneous Catalysts. *Nano Letters* 2014, *14*, 5979–5983.
- 20 Astruc, D.; Lu, F.; Ruiz, J. Nanoparticles as Recyclable Catalysts: the Frontier between Homogeneous and Heterogeneous Catalysis. *Angew. Chem. Int Ed. Engl.* 2005, *44*, 7852–7872.
- 21 Yan, J. M.; Zhang, X. B.; Han, S.; Shioyama, H.; Xu, Q. Iron-nanoparticle-catalyzed Hydrolytic Dehydrogenation of Ammonia Borane for Chemical Hydrogen Storage. *Angew. Chem. Int. Ed.* 2008, *47*, 2287–2289.
- 22 Schöttle, C.; Bockstaller, P.; Popescu, R.; Gerthsen, D.; Feldmann, C. Sodium - Naphthalenide - Driven Synthesis of Base - Metal Nanoparticles and Follow - up Reactions. *Angew. Chem., Int Ed.* **2015**, *54*, 9866–9870.
- 23 Schöttle, C.; Doronkin, D. E.; Popescu, R.; Gerthsen, D.; Grünwald, J. D.; Feldmann, C. Ti⁰ Nanoparticles via Lithium-naphthalenide-driven Reduction. *Chem. Commun.* **2016**, *52*, 6316–6319.
- 24 Wilkinson, G. The Preparation and Some Properties of Ruthenocene and Ruthenicinium Salts. *J. Am. Chem. Soc.* **1952**, *74*, 6148–6150.
- 25 Astruc, D. *Organometallic Chemistry and Catalysis*; Springer: Heidelberg, 2007.
- 26 Astruc, D. Organoiron Electron-reservoir Complexes. *Acc. Chem. Res.* 1986, *19*, 377–383.
- 27 Connelly, N. G.; Geiger, W. E. Chemical Redox Agents for Organometallic Chemistry. *Chem. Rev.* 1996, *96*, 877–910.
- 28 Geiger, W. E. Electroreduction of Cobaltocene. Evidence for a Metallocene Anion. *J. Am. Chem. Soc.* 1974, *96*, 2632–2634.
- 29 Sheats, J. E.; Rausch, M. D. Synthesis and Properties of Cobalticinium Salts. I. Synthesis of Monosubstituted Cobalticinium Salts. *J. Org. Chem.* 1970, *35*,

- 3245–3255.
- 30 Kolb, H. C.; Finn, M. G.; Sharpless, K. B. Click Chemistry: Diverse Chemical Function from a Few Good Reactions. *Angew. Chem., Int. Ed.* **2001**, *40*, 2004–2021.
- 31 For selected reviews, see: (a) Meldal, M.; Tornøe, C. W. Cu-Catalyzed Azide–Alkyne Cycloaddition. *Chem. Rev.* **2008**, *108*, 2952–3015; (b) Hein, J. E.; Fokin, V. V. Copper-catalyzed Azide-alkyne Cycloaddition (CuAAC) and Beyond: New Reactivity of Copper(I) Acetylides. *Chem. Soc. Rev.* **2010**, *39*, 1302–1315; (c) Haldón, E.; Nicasio, M. C.; Pérez, P. Copper-catalysed Azide-alkyne Cycloadditions (CuAAC): An Update. *J. Org. Biomol. Chem.* **2015**, *13*, 9528–9550; (d) Castro, V.; Rodríguez, H.; Albericio, F. CuAAC: An Efficient Click Chemistry Reaction on Solid Phase. *ACS Comb. Sci.* **2016**, *18*, 1–14; (e) Wang, C.; Ikhlef, D.; Kahlal, S.; Saillard, J.; Astruc, D. Metal-Catalyzed Azide-Alkyne “Click” Reactions: Mechanistic Overview and Recent Trends. *Coord. Chem. Rev.* **2016**, *316*, 1–20; (f) Singh, M. S.; Chowdhury, S.; Koley, S. Advances of Azide-alkyne Cycloaddition-click Chemistry over the Recent Decade. *Tetrahedron* **2016**, *72*, 5257–5283.
- 32 Rostovtsev, V. V.; Geen, L. G.; Fokin, V. V.; Sharpless, K. B. A Stepwise Huisgen Cycloaddition Process: Copper(I)-catalyzed Regioselective "Ligation" of Azides and Terminal Alkynes. *Angew. Chem., Int. Ed.* **2002**, *114*, 2708–2711.
- 33 Etayo, P.; Ayats, C.; Pericas, M. A. Synthesis and Catalytic Applications of C3-symmetric Tris(triazolyl)methanol Ligands and Derivatives. *Chem. Commun.* **2016**, *52*, 1997–2010.
- 34 Liu, X.; Gregurec, D.; Irigoyen, J.; Martinez, A.; Moya, S.; Ciganda, R.; Hermange, P.; Ruiz, J.; Astruc, D. Precise Localization of Metal Nanoparticles in Dendrimer Nanosnakes or Inner Periphery and Consequences in Catalysis. *Nat. Commun.* **2016**, *7*, 13152.
- 35 Fu, F.; Martinez, A.; Wang, C.; Ciganda, R.; Yate, L.; Escobar, A.; Moya, S.; Fouquet, E.; Ruiz, J.; Astruc, D. Exposure to Air Boosts CuAAC Reactions Catalyzed by PEG-stabilized Cu Nanoparticles. *Chem. Commun.* **2017**, *53*, 5384–5387.
- 36 Alonso, F.; Moglie, Y.; Radivoy, G. Copper Nanoparticles in Click Chemistry. *Acc. Chem. Res.* **2015**, *48*, 2516–2528.
- 37 Gawande, M. B.; Goswami, A.; Felpin, F. X.; Asefa, T.; Huang, X. X.; Silva, R.; Zou, X. X.; Zboril, R.; Varma, R. S. Cu and Cu-Based Nanoparticles: Synthesis and Applications in Catalysis. *Chem. Rev.* **2016**, *116*, 3722–3811.
- 38 Decan, M. R.; Impellizzeri, S.; Marin, M. L.; Scaiano, J. C. Copper Nanoparticle Heterogeneous Catalytic ‘Click’ Cycloaddition Confirmed by Single-molecule

- Spectroscopy. *Nat. Commun.* **2014**, *5*, 4612.
- 39 Rycenga, M.; Cobley, C. M.; Zeng, J.; Li, W. Y.; Moran, C. H.; Zhang, Q.; Qin, D.; Xia, X. N. Controlling the Synthesis and Assembly of Silver Nanostructures for Plasmonic Applications. *Chem. Rev.* **2011**, *111*, 3669–3712.
- 40 (a) Sau, T. K.; Pal, A.; Pal, T. Size Regime Dependent Catalysis by Gold Nanoparticles for the Reduction of Eosin. *J. Phys. Chem. B* **2001**, *105*, 9266–9272. (b) Hervés, P.; Pérez-Lorenzo, M.; Liz-Marzan, L. M.; Dzubielia, J.; Lu, Y.; Ballauff, M. Catalysis by Metallic Nanoparticles in Aqueous Solution: Model Reactions. *Chem. Soc. Rev.* **2012**, *41*, 5577–5587. (c) Aditya, T.; Pal, A.; Pal, T. Nitroarene Reduction: A Trusted Model Reaction to Test Nanoparticle Catalysts. *Chem. Commun.* **2015**, *51*, 9410–9431. (d) Zhao, P.; Feng, X.; Huang, D.; Yang, G.; Astruc, D. Basic Concepts and Recent Advances in Nitrophenol Reduction by Gold- and Other Transition Metal Nanoparticles. *Coord. Chem. Rev.* **2015**, *287*, 114–136.
- 41 (a) Wunder, S.; Lu, Y.; Albrecht, M.; Ballauff, M. Catalytic Activity of Faceted Gold Nanoparticles Studied by a Model Reaction: Evidence for Substrate-Induced Surface Restructuring. *ACS Catal.* **2011**, *1*, 908–916; (b) Lu, Y.; Ballauff, M. Spherical Polyelectrolyte Brushes as Nanoreactors for the Generation of Metallic and Oxidic Nanoparticles: Synthesis and Application in Catalysis. *Prog. Polym. Sci.* **2016**, *59*, 86–104.
- 42 Fu, F.; Wang, Q.; Ciganda, R.; Martínez-Villacorta, A. M.; Escobar, A.; Moya, S.; Fouquet, E.; Ruiz, J.; Astruc, D. Electron- and Hydride-Reservoir Organometallics as Precursors of Catalytically Efficient Transition Metal Nanoparticles in Water. *Chem. Eur. J.* **2018**, *24*, 6645–6653.
- 43 Ornelas, C.; Ruiz, J.; Cloutet, E.; Alves, S.; Astruc, D. Click Assembly of 1,2,3 - Triazole - Linked Dendrimers, Including Ferrocenyl Dendrimers, Which Sense Both Oxo Anions and Metal Cations. *Angew. Chem. Int. Ed.* **2007**, *46*, 872–877.
- 44 Liu, J.; Mendoza, S.; Román, E.; Lynn, M. J.; Xu, R.; Kaifer, A. E. Cyclodextrin-Modified Gold Nanospheres. Host–Guest Interactions at Work to Control Colloidal Properties. *J. Am. Chem. Soc.* **1999**, *121*, 4304–4305.
- 54 Wang, Y.; Li, H.; Jin, Q.; Ji, J. Intracellular Host–guest Assembly of Gold Nanoparticles Triggered by Glutathione. *Chem. Commun.* **2016**, *52*, 582–585.
- 46 Yue, Y.; Huo, F.; Ning, P.; Zhang, Y.; Chao, J.; Meng, X.; Yin, C. Dual-Site Fluorescent Probe for Visualizing the Metabolism of Cys in Living Cells. *J. Am. Chem. Soc.* **2017**, *139*, 3181–3185.

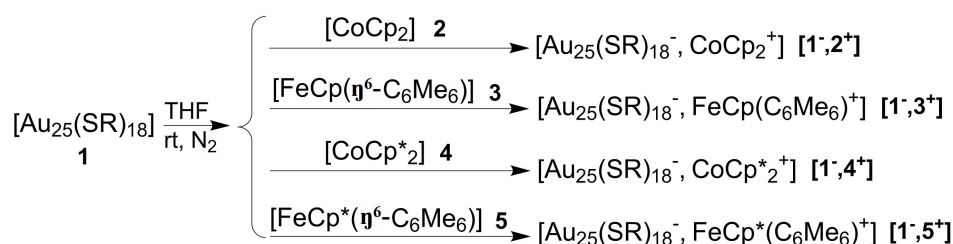
- 47 Ciganda, R.; Irigoyen, J.; Gregurec, D.; Hernández, R.; Moya, S.; Wang, C.; Ruiz, J.; Astruc, D. Liquid–Liquid Interfacial Electron Transfer from Ferrocene to Gold(III): An Ultrasimple and Ultrafast Gold Nanoparticle Synthesis in Water under Ambient Conditions. *Inorg. Chem.* **2016**, *55*, 6361–6363.
- 48 Astruc, D. Why is Ferrocene so Exceptional? *Eur. J. Inorg. Chem.* **2017**, 6–29.
- 49 Hu, P. G.; Chen, L. M.; Kang, X. W.; Chen, S. W. Surface Functionalization of Metal Nanoparticles by Conjugated Metal–Ligand Interfacial Bonds: Impacts on Intraparticle Charge Transfer. *Acc. Chem. Res.* **2016**, *49*, 2251–2260.
- 50 Judai, K.; Numao, S.; Nishijo, J.; Nishi, N. In Situ Preparation and Catalytic Activation of Copper Nanoparticles from Acetylide Molecules. *J. Mol. Catal. A-Chemical* **2011**, *347*, 28–33.
- 51 Yam, W. W. W.; Lo, K. K. W.; Fung, W. K. M.; Wang, C. R. Design of Luminescent Polynuclear Copper(I) and Silver(I) Complexes with Chalcogenides and Acetylides as the Bridging Ligands. *Coord. Chem. Rev.* **2010**, *171*, 17–41.
- 52 Cobaltocene, a purple black solid, is available at Sigma-Aldrich or is readily best synthesized by reaction between CoBr_2 and NaCp in THF. See (a) Sheats, J. E. A Comprehensive Review up to 1976 of Cobalt Sandwich Compounds. *J. Organomet. Chem. Library* **1979**, *7*, 461-521; (b) Kemmitt, R. D. W.; Russell D. R. *Comprehensive Organometallic Chemistry*, Wilkinson, J.; Stone, F. G. A.; Abel, E. W. Eds., Pergamon, New York, 1982, Vol. 5, p. 244.
- 53 Wang, C.; Wang, D.; Yu, S.; Cornilleau, T.; Ruiz, J.; Salmon, L.; Astruc, D. Design and Applications of an Efficient Amphiphilic “Click” CuI Catalyst in Water. *ACS Catal.* **2016**, *6*, 5424–5431.

Chapter 5. Synthesis of New Gold Nanoparticle Salts with Organometallic Counter Cations

Introduction

Precisely defined thiolate-protected gold nanoclusters have recently attracted significant research interest because of their unique catalytic, optical, and electronic properties.¹ In this category, the spherical nanocluster $\text{Au}_{25}(\text{SR})_{18}$ {R = $(\text{CH}_2)_2\text{Ph}$ }, **1**,² has been the most extensively studied.¹ It is viewed as a typical “superatom”, and its neutral and anionic forms have been shown by X-ray crystal structures to contain similar cores² and are reversibly interconverted.³ Liu *et al* reported electron transfer between $[\text{Au}_{25}(\text{SR})_{18}]^- \text{TOA}^+$ {TOA⁺ = $\text{N}(n\text{-C}_8\text{H}_{17})_4^+$ } and TEMPO⁺ BF₄⁻, {TEMPO⁺ BF₄⁻ = 2,2,6,6-tetramethylpiperidin-1-oxoammonium tetrafluoroborate},^{4a} and Chong et al showed that $[\text{Au}_{25}(\text{SR})_{18}]^- \text{TOA}^+$ served as electron-transfer chain catalyst⁵ for cascade reaction of 2-nitrobenzotrile under ambient conditions.⁶ Although the nanocluster $[\text{Au}_{25}(\text{SR})_{18}]^- \text{TOA}^+$ is stable in the solid state, however, it suffers from some kinetic instability in solution, and therefore it is only stable for a few hours in CH_2Cl_2 solution under ambient conditions.^{3b} Thus, new syntheses of stable salts of $[\text{Au}_{25}(\text{SR})_{18}]^-$ in both solid state and solution are needed in order to provide access to new mixed nanocomposites and understand the structure-property relationship at the atomic level. Therefore we have envisaged using electron-reservoir and hydride reservoir Fe and Co sandwich complexes as reducing agents of the neutral nanocluster **1** forming complex salts of the nanocluster anion **1**⁻ (Scheme 1).

The principle of electron-reservoir complexes is that both the reduced and oxidized forms are robust and isostructural, thus readily interconverted, and that the reduced form is very electron-rich, being only oxidized at very negative redox potentials.⁷ The 19-electron complexes $[\text{Fe}(\eta^5\text{-C}_5\text{R}_5)(\eta^6\text{-arene})]$ ⁸ and $\text{Co}(\eta^5\text{-C}_5\text{R}_5)_2$ ⁹ {R = H or Me} belong to this family; in particular the ring ligand permethylation (i.e. R = Me, arene = C_6Me_6) strengthens the bulk, robustness and reducing power of these complexes.¹⁰ The bulk of such electron-reservoir sandwich complexes not only stabilizes small nanoparticles, but also contributes to their excellent catalytic activity.¹¹ Here we are using the 19-electron complexes cobaltocene (Cp_2Co), **2**, $[\text{FeCp}(\eta^6\text{-C}_6\text{Me}_6)]$, **3**, (Cp = $\eta^5\text{-C}_5\text{H}_5$), decamethyl cobaltocene, CoCp^*_2 , (Cp* = $\eta^5\text{-C}_5\text{Me}_5$), **4** and $[\text{FeCp}^*(\eta^6\text{-C}_6\text{Me}_6)]$, **5** to stoichiometrically reduce the neutral nanocluster **1** to **1**⁻, “metallocenium”⁺ & (Scheme 1). The formal potentials of $[\text{Au}_{25}(\text{SR})_{18}]^{0/-1}$ is -0.39 V vs. ferrocene^{+0,4} and +0.11V vs. decamethylferrocene, FeCp^*_2 ,¹² so that **1** is exergonically reduced to **1**⁻ by these four strong organometallic reductants. The exergonicity of these reactions (Figure 1) insures fast single-electron transfer.¹³



Scheme 1. Synthesis of the salts $[\text{Au}_{25}(\text{SR})_{18}]^-, \text{metalloecenium}^+$.

Results and discussion

The driving force of the electron transfer is almost exclusively governed by the respective standard redox potentials E° of the donors and acceptor (Figure 1),¹³ because the electrostatic factor in the Rehm-Weller equation is very weak due to the low charges involved and rather large sizes of the electron-transfer substrates.¹⁴ The 19-electron complexes have oxidation potentials far more negative than the reduction potential of **1**, therefore they all reduce **1** in a fast reaction. On the other hand, decamethylferrocene, FeCp^*_2 , **6**, whose redox potential is almost the same as that of **1**, does not reduce **1** at room temperature for kinetic reasons in a situation of too weak driving force. The fast reaction between **1** and 1 equiv of organometallic sandwich complex **2-5** under N_2 at rt leads to instantaneous color change from yellow brown to red brown at the equivalence point of the reaction (Figure 6, Experimental Section).

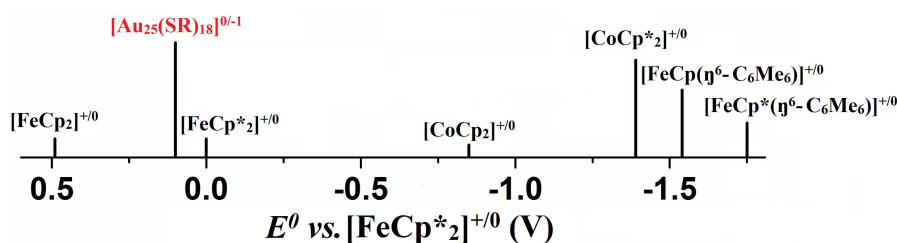


Figure 1. Standard redox potentials of Fe and Co sandwich complexes vs. $[\text{FeCp}^*_2]^{+/0}$.

UV-vis. absorption spectroscopy, which is a convincing physical technique to distinguish salts of diamagnetic $\mathbf{1}^-$ from paramagnetic $\mathbf{1}$,^{3b} was used before and after reduction of **1** (Figure 9, Experimental Section). The shoulder at 630 nm in the spectrum of **1** disappears, while the characteristic absorption band of $\mathbf{1}^-$ emerges at 800 nm. Simultaneously, the intensities of the 400-nm band decreases and that of the 450-nm band increases during these electron-transfer reactions.

^1H NMR was also used to characterize these four new compounds. The ^1H NMR spectra of the diamagnetic TOA^+ salt was first reproduced in CD_2Cl_2 .^{3a} The ^1H NMR spectra of the four diamagnetic salts $[\mathbf{1}^-, \text{“metalloecenium”}^+]$ present sharp peaks and

are similar to that of $[1^-, \text{TOA}^+]$, except for the obvious differences for the cations (Figure 10, Experimental Section). This contrasts with the ^1H NMR spectrum of **1** that presents broad bands due to the paramagnetism resulting from its electronic structure with an unpaired electron in the HOMO.³

The matrix assisted laser desorption ionization mass spectra (MALDI-MS) and electrospray ionization mass spectra (ESI-MS) confirm the formula of the salts $[1^-, 2^+]$, $[1^-, 3^+]$, $[1^-, 4^+]$ and $[1^-, 5^+]$. The Figures 2a and 11 (Experimental Section) reveal prominent peaks at $m/z = 7392.44$, 7391.91 , 7391.91 and 7392.03 Da that are assigned to the anion **1**⁻ (cal. 7392.93 Da) of the salt $[1^-, \text{metalloocenium}^+]$ (the other peaks are assigned to its fragments). In Figure 2b, a peak at $m/z = 354.19$ Da is observed in positive mode of ESI-MS, showing the cation **5**⁺ (cal. 354.19 Da) in $[1^-, 5^+]$. In the same way, peaks at 189.07, 283.20 and 329.27 Da are present in Figures 11 a, b and c (Experimental Section), related to **2**⁺ (cal. 189.01 Da), **3**⁺ (cal. 283.11 Da), **4**⁺ (cal. 329.17 Da) in $[1^-, 2^+]$, $[1^-, 3^+]$ and $[1^-, 4^+]$, respectively.

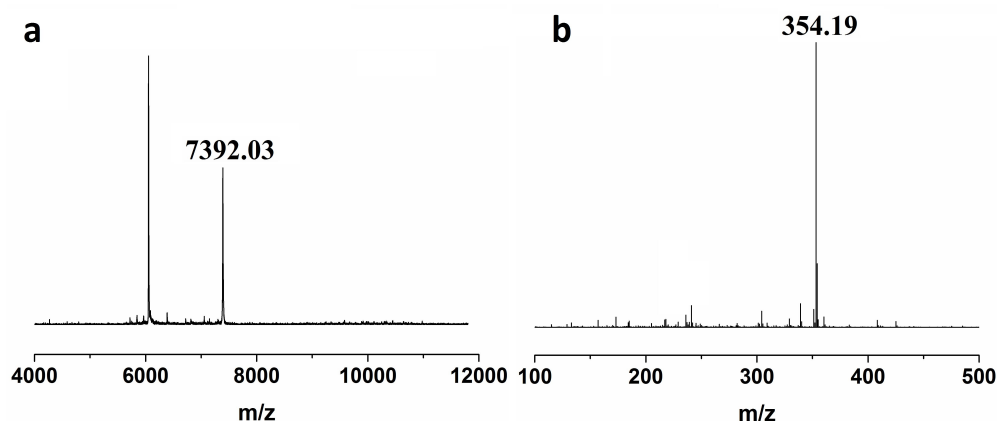


Figure 2. MALDI-MS (a) and ESI-MS (b) analysis of the $[1^-, 5^+]$.

UV-vis. absorption spectroscopy allowed studying the counter cation effect on the stability to air of these nanocluster anion salts in THF solution under ambient conditions. The parent cobalticinium salt $[1^-, 2^+]$ was stable in air in THF for 2 days, and the iron sandwich salt $[1^-, 3^+]$, that possess 6 methyl groups on the benzene ring, exhibited the same aerobic stability (Figure 12, Experimental Section). This 2-day stabilization is a great progress compared to the salt $[1^-, \text{TOA}^+]$ that is stable only for a few hours at rt. However, when methyl groups are present on both ligand rings, i.e. in the cations **4**⁺ of $[1^-, 4^+]$ (Figure 13, Experimental Section) and **5**⁺ of $[1^-, 5^+]$ (Figure 3), these salts both resisted to aerobic oxidation by O_2 from air for 14 days at rt in THF solution.

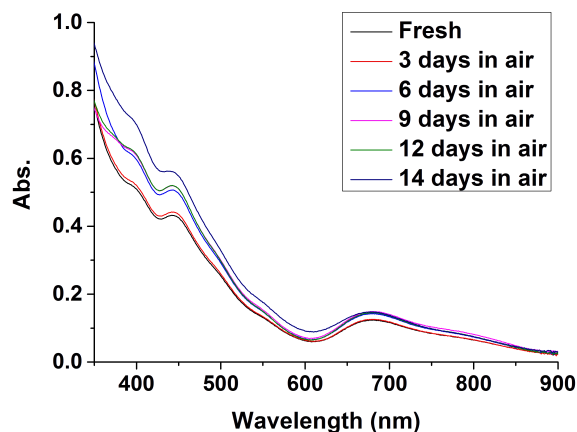


Figure 3. UV-vis. spectra of the nanocluster composite $[1^-, 5^+]$ exposed to air at rt in THF solution.

The similarity between the aerobic stability periods in solution of $[1^-, 2^+]$ and $[1^-, 3^+]$ that have in common a Cp ligand, and a large size difference of the other ligand (Cp in **2** and C_6Me_6 in **3**) is remarkable. The permethylation of only one ring in **3**⁺ in which the six methyl groups introduce a large additional bulk on one side of the sandwich does not bring about any aerobic stability advantage compared to cobalticinium, **2**⁺. In addition the dichotomy between the aerobic stability times of the two sub-families (2 days for $[1^-, 2^+]$ and $[1^-, 3^+]$ vs. 14 days for $[1^-, 4^+]$ and $[1^-, 5^+]$) shows a key point for strong aerobic stability increase. These features indicate that the smaller Cp ligand is facing the Au_{25} cluster anion in the two former salts (Figures 4a vs. 4b), whereas both ring permethylations force one of the two permethylated Cp* ligands to face the Au cluster in the two latter complexes (Figure 4c). This trend takes into account the large aerobic stability increase to 14 days for these two latter salts. It is the bulk of both sandwich ligands that protects the anionic Au_{25}^- core. On the other hand the bulk of only one sandwich ligand does not play a decisive role in the Au cluster protection, because it does not directly face the Au cluster anion.

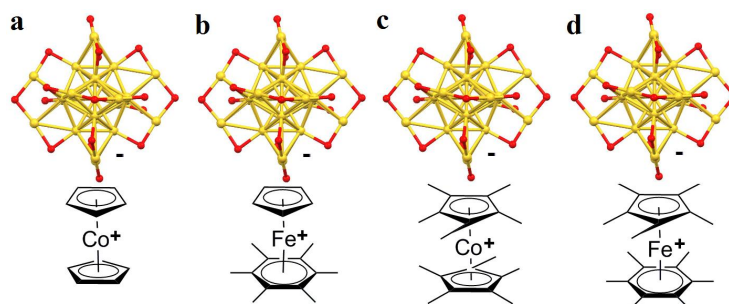


Figure 4. Proposed stabilization mode of the anion 1^- in the salts a, $[1^-, 2^+]$, b, $[1^-, 3^+]$, c, $[1^-, 4^+]$ and d, $[1^-, 5^+]$.

This nanocluster composites [**1**⁻, **4**⁺] and [**1**⁻, **5**⁺] are also stable in air for more than half a year in the solid state under ambient conditions, which surpasses the stability of [**1**⁻, TOA⁺]. By comparison, [**1**⁻, Na⁺], synthesized by NaBH₄ reduction of **1**, is oxidized by air within a few minutes to **1** in THF solution (Figure 14, Experimental Section).

Finally we have also examined the electron-transfer properties to **1** of the 18-electron complexes [CoCp(η⁴-C₅H₆), **7**, [FeCp(η⁵-C₆Me₆H), **8** and [CoCp*(η⁴-C₅Me₅H), **9** (Figure 5) that are hydride reservoirs, i.e. good reductants and reversibly interconverted by hydride transfer from the cations **2**⁺, **3**⁺ and **4**⁺ respectively.¹⁵ For instance reaction of **2**⁺PF₆⁻ with NaBH₄ is known to yield **7** via a single-electron transfer pathway via **2**,¹⁶ but electron-transfer reactions of **7** yielding a salt of **2**⁺ are not known. The complexes **7**, **8** and **9** indeed rapidly react with **1** to form exactly the same nanocomposite salts [**1**⁻,**2**⁺], [**1**⁻,**3**⁺] and [**1**⁻,**4**⁺], respectively, as those obtained by reactions of **2**, **3** and **4** with **1**, as shown by UV-vis. and ¹H NMR spectroscopies and mass spectrometry (Figure 15 and 16, Experimental Section).

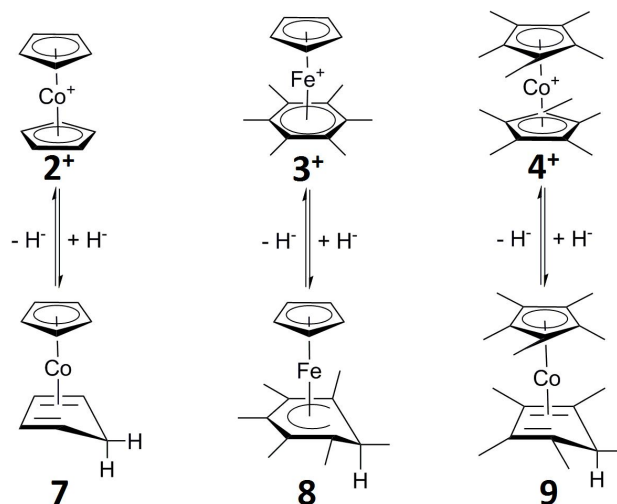


Figure 5. Three stable hydride-reservoir sandwich complexes. Their syntheses involve reactions of the organometallic cations with NaBH₄. Hydride abstraction from the neutral complexes yielding the cations is usually conducted with a Ph₃C⁺ salt.¹⁵

The hydride reservoir complexes **7**, **8** and **9** have oxidation potentials (resp. -0.35 V, 0.04 V and -0.89 V vs. Cp*₂Fe⁺⁰) that are less cathodic than those of the related 19-electron complexes **2**, **3**, and **4**, respectively, but about the same or more cathodic than the standard reduction potential of **1** (Figure 1). Their reactions with **1** are also driven by the irreversibility of the redox reactions, which adds to the exergonicity to provoke fast electron transfer to **1**. For

instance, **8**^{15c} has the same redox potential as decamethylferrocene that does not react with **1**. The mechanism of these latter reactions is either single electron transfer to **1** followed by hydrogen atom loss or direct hydride transfer to **1** followed by hydrogen atom loss. The preserved identity of the gold cluster ligand shell disclosed by mass spectrometry discards hydride substitution of a thiolate ligand, favoring the former hypothesis. The advantages of the use of **7**, **8** and **9** over **2**, **3**, and **4** is that their synthesis is somewhat easier by reaction of the salts of the cations **2**, **3** and **4** with NaBH₄, and **7** and **8** benefit from stability in air at rt.

Conclusion

In conclusion a new method of synthesis of nanocluster anions has been developed involving a strategy that uses the reduced form of electron-reservoir and hydride-reservoir complexes. In this situation, the hydride-reservoir complexes behave as electron-transfer reagents as the electron-reservoir complexes. Their hydride transfer properties will be illustrated later in other processes. The flexibility of this method includes the choice of the metal and the ligand bulk of the reducing agent, allowing comparison of the aerobic stabilities provided depending on the geometrical electron-reservoir parameters. The aerobic stability studies conducted by UV-vis. spectroscopy show that the best protection against the kinetic instability in air is brought about by **4**⁺ or **5**⁺ involving the largest bulk protection by permethylated Cp* rings near the nanocluster surface. This strategy illustrates some of the applications of the concepts of electron reservoir and hydride reservoir complexes. It could be generalized to the synthesis and stabilization of most cluster anions that present reversibly interconverted redox states, affording structure-reactivity relationship studies towards catalysis, optics and molecular electronic applications.

Experimental Section

General data

All solvents and chemicals were used as purchased, unless otherwise noted.

- UV-vis. absorption spectra were measured with a Perkin-Elmer Lambda 19 UV-vis. spectrometer.
- NMR spectra were recorded at 25 °C with a Bruker AC 400, or 300 (400 or 300 MHz). All the chemical shifts are reported in parts per million (δ , ppm) with reference to Me₄Si for the ¹H NMR spectra.
- Matrix assisted laser desorption ionization mass spectrometry (MALDI-MS) was performed on an Applied Biosystems Voyager DE-STR MALDI-TOF equipped with a

nitrogen laser (337 nm). The mass spectra of negative ions were collected in the linear mode at an acceleration voltage of 25 kV and a delay time of 350 ns. Trans - 2 - [3 - (4 - tert - Butyl - phenyl) - 2 - methyl - 2 - propenylidene] malononitrile (DCTB) was used as the MALDI matrix.

- Electrospray ionization (ESI) mass spectra were acquired using a Bruker Q-TOF mass spectrometer equipped with ESI source.

Details for the synthesis of $\text{Au}_{25}(\text{SR})_{18}^-$ metallocenium⁺ nanoclusters

Synthesis of the nanocluster $[\mathbf{1}^-, \mathbf{2}^+]$ from the 19e complex **2** as example:

In a Schlenk flask, Na/Hg amalgam was prepared in dry THF under N_2 at r.t., then 10 mg of cobalticenium hexafluorophosphate $[\text{CoCp}_2][\text{PF}_6]$ ($\text{Cp} = \eta^5\text{-C}_5\text{H}_5$) and THF (10 mL) were added, and the mixture was allowed to stir for 2 h. The solution progressively changed color from yellow to brown indicating the formation of cobaltocene **2**. The solvent was removed *in vacuo* providing the crude product that was redissolved in 10 mL dry pentane to eliminate the insoluble NaPF_6 salt by cannula filtration. Finally, pentane was removed *in vacuo*, and the product was redissolved again in dry THF (10 mL) for further use. 5 mg **1** (which was synthesized according to ref 17) was dissolved in 10 mL dry THF under nitrogen in a standard Schlenk flask and stirred at room temperature. Then a fresh **2** solution (1 equivalent was required) was quickly injected into the Schlenk flask after 5 min degassed, the color change of the solution from yellow brown to red brown (Figure S1) indicating the formation of the $[\mathbf{1}^-, \mathbf{2}^+]$ from **1**. The THF solvent was removed *in vacuo* and the products were extracted by toluene and then filtered, and the toluene solution was dried *in vacuo* at 30 °C to get the pure [nanocluster composite $\mathbf{1}^-, \mathbf{2}^+$]. The nanocluster nanocomposites $[\mathbf{1}^-, \mathbf{3}^+]$, $[\mathbf{1}^-, \mathbf{4}^+]$ and $[\mathbf{1}^-, \mathbf{5}^+]$ were synthesized from the other organometallic 19e complexes by a similar process.

Synthesis of the nanocluster $[\mathbf{1}^-, \mathbf{2}^+]$ from the hydride reservoir **7** as example:

10 mg of cobalticenium hexafluorophosphate $[\text{CoCp}_2][\text{PF}_6]$ and dry THF (10 mL) were added into a Schlenk flask under N_2 at r.t., then 5 eq NaBH_4 was added, and the mixture was allowed to stir for 2 h. The solution progressively changed color from yellow to red indicating the formation of **7**. The solvent was removed *in vacuo* providing the crude product that was redissolved in pentane to eliminate the insoluble NaPF_6 salt by cannula filtration. Finally, pentane was removed *in vacuo*, and the product was redissolved again in dry THF (10 mL) for further use. 5 mg **1** was dissolved in 10 mL dry THF under nitrogen in a standard Schlenk flask and stirred at room temperature. Then a fresh **7** solution (1 equivalent was required) was quickly injected into the Schlenk flask after 5 min degassed, the color change of the solution from yellow brown to red brown (Figure S1) indicating the formation of the

composite $[1^-, 2^+]$ from **1**. The THF solvent was removed in *vacuo* and the products were extracted by toluene and then filtered, and the toluene solution was dried in *vacuo* at 30 °C to get the pure nanocluster composite $[1^-, 2^+]$. Similarly the nanocluster composites $[1^-, 3^+]$ and $[1^-, 4^+]$ were synthesized from the other organometallic hydride complexes (**8** was synthesized from $[\text{CpFe}(\eta^6\text{-C}_6\text{Me}_6)][\text{PF}_6]$ as starting material at 50 °C, and **9** was synthesized from $[\text{CoCp}^*]_2[\text{PF}_6]$ as starting material at 50 °C overnight. See the characterizations of **9** below.

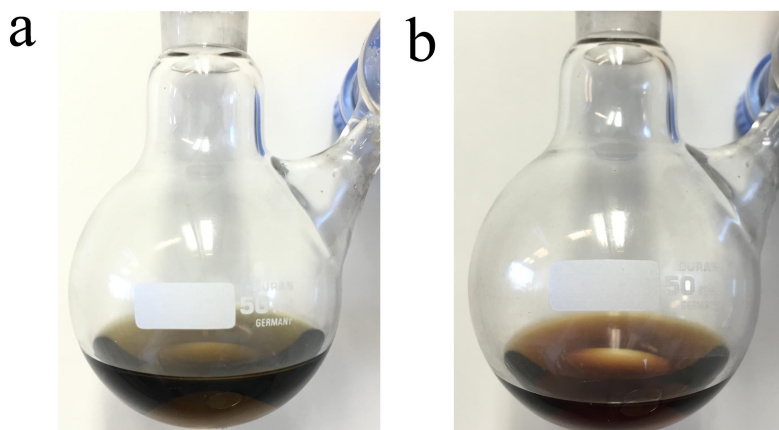


Figure 6. Photographs of the: a, $[\text{Au}_{25}(\text{SR})_{18}]^0$ and b, $[\text{Au}_{25}(\text{SR})_{18}]^-$ [metalloceniums] $^+$.

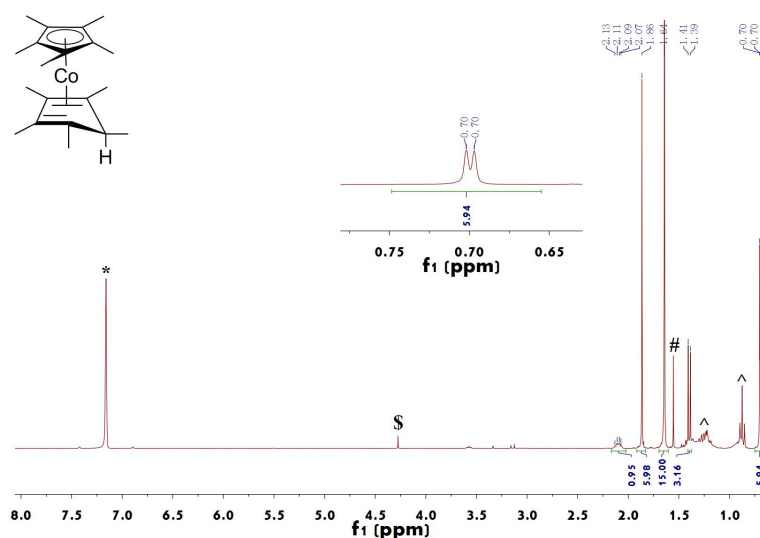


Figure 7. ^1H NMR of the $[\text{CoCp}^*(\eta^4\text{-C}_5\text{Me}_5\text{H})]$ **9**: ^1H NMR (300 MHz, C_6D_6 *) δ 2.10 (dd, $J = 12.3, 5.7$ Hz, 1H), 1.86 (s, 6H), 1.64 (s, 15H), 1.40 (d, $J = 6.6$ Hz, 3H), 0.70 (d, $J = 1.5$ Hz, 6H). \$, # and ^ are the solvents.

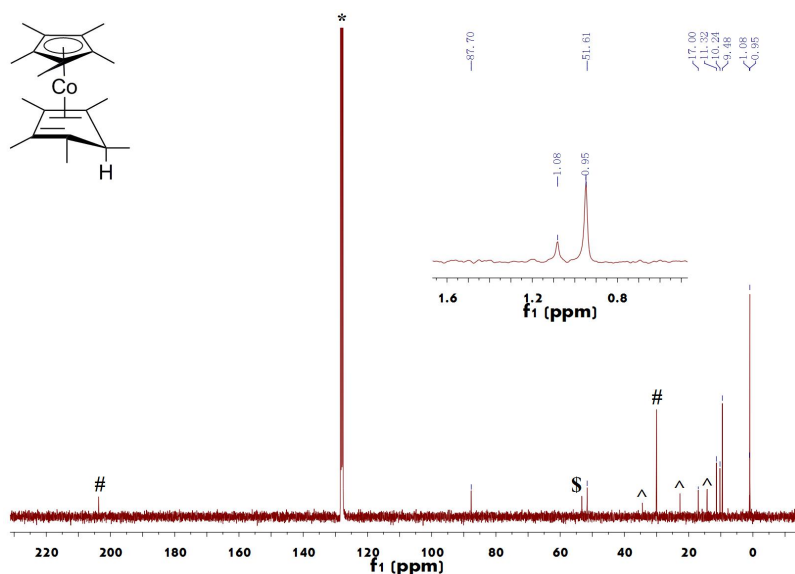


Figure 8. ^{13}C NMR of the $[\text{CoCp}^*(\eta^4\text{-C}_5\text{Me}_5\text{H})]$ **9**: ^{13}C NMR (300 MHz, C_6D_6 *) δ 87.70, 51.61, 17.00, 11.32, 10.24, 9.48, 1.08, 0.95. \$, # and ^ are the solvents.

2. Details for the synthesis of $\text{Au}_{25}(\text{SR})_{18}^- \text{Na}^+$ nanocluster

A Schlenk flask was charged with 5 mg $\text{Au}_{25}(\text{SR})_{18}$ and 10 mL dry THF under N_2 at r.t., then 2 equivalent NaBH_4 dissolved in 1 mL ethanol was added immediately after 5 min degassed and the color change of the solution from yellow brown to red brown. The solvent was removed *in vacuo* and the products were extracted by toluene and then filtered under N_2 by cannula to remove the excess NaBH_4 . The toluene solution was dried *in vacuo* at 30 °C to get the pure nanocluster composite $[\text{Au}_{25}(\text{SR})_{18}]^- \text{Na}^+$.

Characterization of the nanocluster composites $\text{Au}_{25}(\text{SR})_{18}^- \text{metallocenium}^+$.

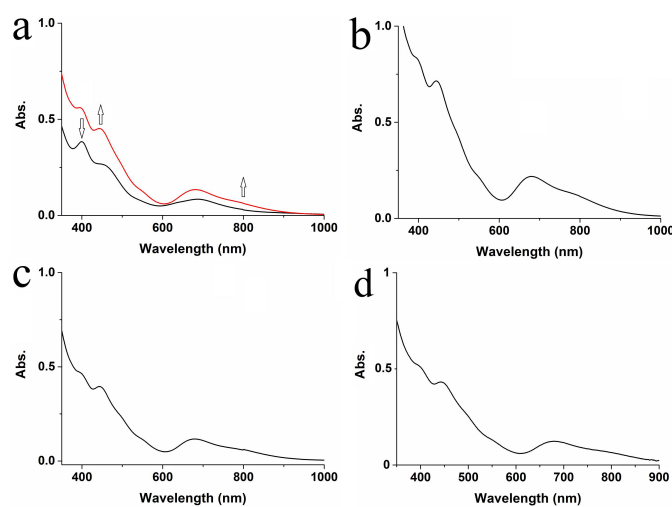


Figure 9. UV-vis. spectra of the: a, **1** (black), $[\mathbf{1}^-, \mathbf{2}^+]$ (red); b, $[\mathbf{1}^-, \mathbf{3}^+]$; c, $[\mathbf{1}^-, \mathbf{4}^+]$ and d, $[\mathbf{1}^-, \mathbf{5}^+]$.

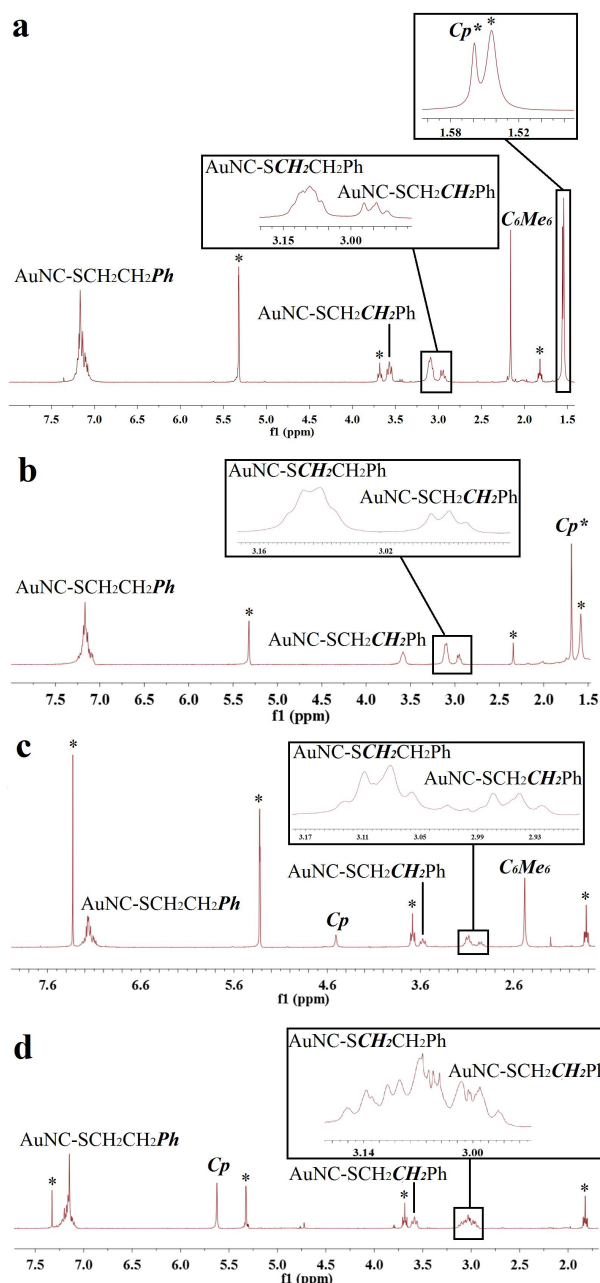


Figure 10. ^1H NMR (in CD_2Cl_2) of the nanocluster composites a, $[\mathbf{1}^-, \mathbf{5}^+]$; b, $[\mathbf{1}^-, \mathbf{4}^+]$ c, $[\mathbf{1}^-, \mathbf{3}^+]$ and $[\mathbf{1}^-, \mathbf{2}^+]$. * indicates the organic solvent and water. For instance, in $[\mathbf{1}^-, \mathbf{5}^+]$ (Figure S2a), the peaks at 7.04-7.22 ppm are attributed to the phenyl groups ($\text{AuNC-SCH}_2\text{CH}_2\text{Ph}$); the $\beta\text{-CH}_2$ ($\text{AuNC-SCH}_2\text{CH}_2\text{Ph}$) triplet at 3.57 and 2.95 ppm are distinct because of the different ligand sites and configurations. The $\alpha\text{-CH}_2$ ($\text{AuNC-SCH}_2\text{CH}_2\text{Ph}$) of the 18 thiolate ligands are located at 3.09 ppm as a broad multiplet. The single peak at 2.16 ppm is assigned to -CH_3 on the benzene ring of $\mathbf{5}^+$ and another single peak at 1.56 ppm is contributed to -CH_3 on the Cp^* ring of $\mathbf{5}^+$. In addition $[\mathbf{1}^-, \mathbf{2}^+]$, $[\mathbf{1}^-, \mathbf{3}^+]$ and $[\mathbf{1}^-, \mathbf{4}^+]$ show analogous ^1H NMR spectra; however the Cp signals of $\mathbf{2}^+$ and $\mathbf{3}^+$ are located at 5.62 and 4.50 ppm, respectively, and the -CH_3 signal of $\mathbf{3}^+$ is located at 2.47 ppm and the -CH_3 on the Cp^* ring of $\mathbf{4}^+$ is located at 1.69 ppm.

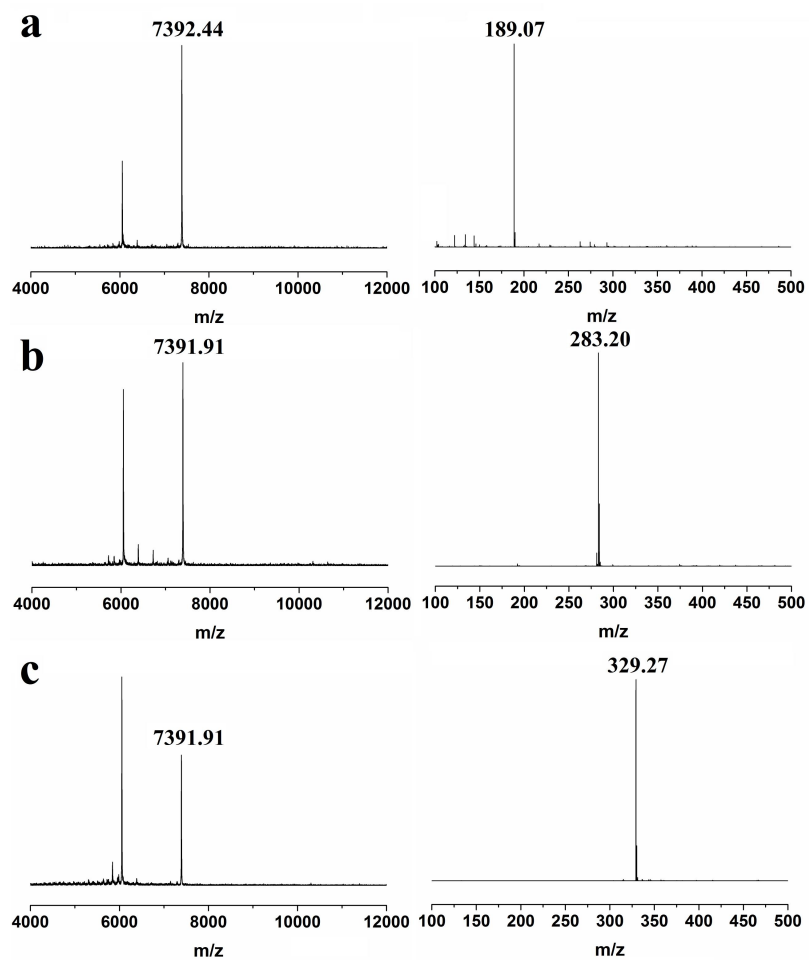


Figure 11. MALDI-MS (left) and ESI-MS (right) analysis of the: a, $[1^-, 2^+]$; b, $[1^-, 3^+]$ and c, $[1^-, 4^+]$

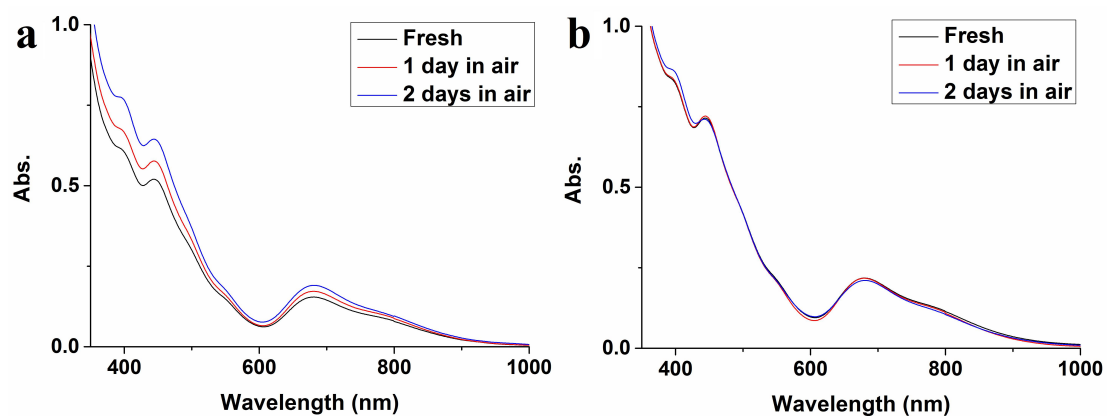


Figure 12. UV-vis. spectra tracked the $[1^-, 2^+]$ (a) and $[1^-, 3^+]$ (b) nanoclusters exposed to air in THF solution.

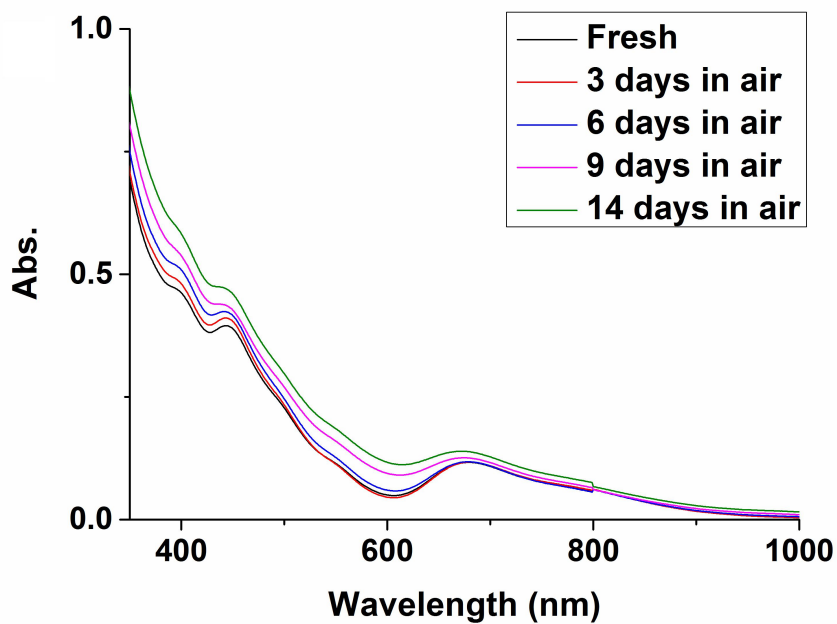


Figure 13. UV-*vis.* spectra tracked the nanocluster composite [1⁻, 4⁺] exposed to air in THF solution.

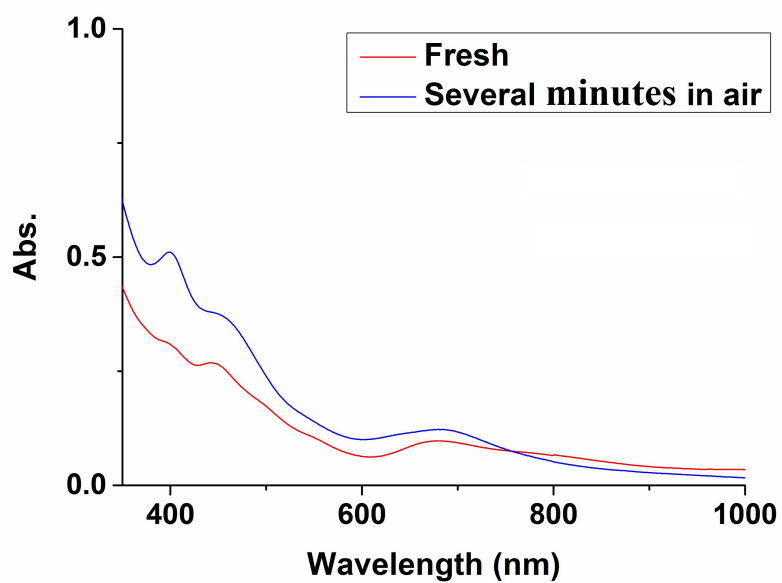


Figure 14. UV-*vis.* spectra showing the oxidation of [Au₂₅(SR)₁₈]⁻ Na⁺ to [Au₂₅(SR)₁₈]⁰ in air in THF solution within several minutes.

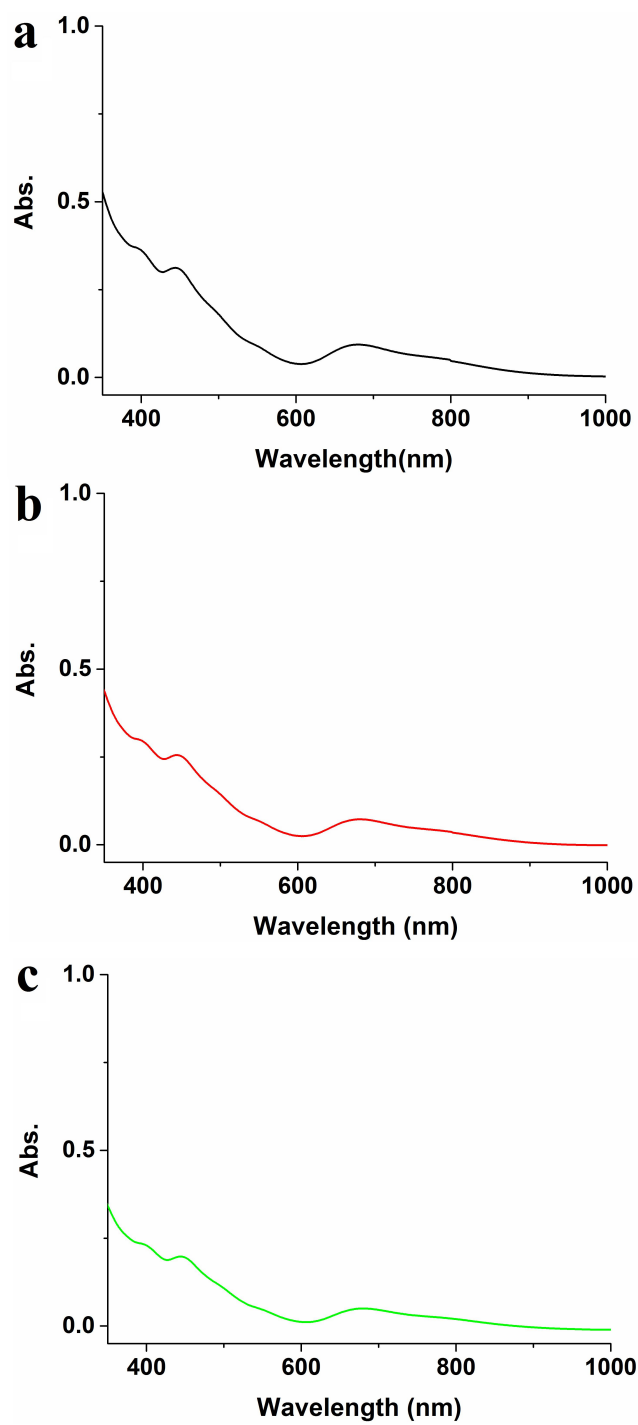


Figure 15. UV-*vis.* spectra of: a, $[1^-, 2^+]$; b, $[1^-, 3^+]$ and c, $[1^-, 4^+]$ obtained from 3 hydride-reservoir sandwich complexes.

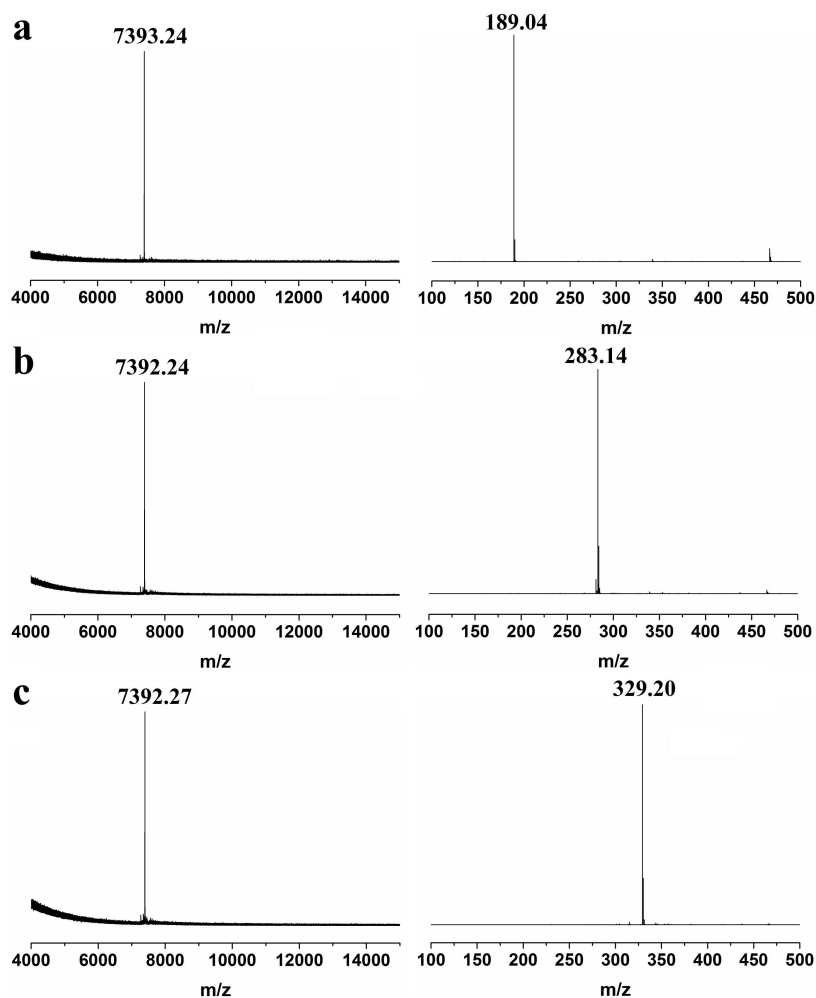


Figure 16. ESI-MS analysis of: a, $[1^-, 2^+]$; b, $[1^-, 3^+]$ and c, $[1^-, 4^+]$ obtained from 3 hydride-reservoir sandwich complexes.

References

- 1 a) R. Jin, *Nanoscale*, **2010**, 2, 343-362; b) H. Hakkinen, *Nat. Chem.*, **2012**, 4, 443-455; c) R. Jin, C. J. Zeng, M. Zhou and Y. X. Chen, *Chem. Rev.*, **2016**, 116, 10346-10413; d) J. Fang, B. Zhang, Q. F. Yao, Y. Yang, J. P. Xie and N. Yan, *Coord. Chem. Rev.*, **2016**, 322, 1-29; e) I. Chakraborty and T. Pradeep, *Chem. Rev.*, **2017**, 117, 8208-8271; f) Q. Yao, T. Chen and X. Yuan, *Acc. Chem. Res.*, **2018**, 51, 1338-1348; g) A. W. Cook and T. W. Hayton, *Acc. Chem. Res.*, **2018**, 51, 2456-2464; h) S. Sharma, K. K. Chakrahari, J.-Y. Saillard and C. W. Liu, *Acc. Chem. Res.*, **2018**, 51, 2475-2483; i) T. Higaki, Q. Li, M. Zhou, S. Zhao, Y. Li, S. Li and R. Jin, *Acc. Chem. Res.*, **2018**, 51, 2764-2773; j) M. Zhou, T. Higaki, G. Hu, M. Y. Sfeir, Y. Chen, D.-e. Jiang and R. Jin, *Science*, **2019**, 364, 279-282; k) Y. Du, H. Sheng, D. Astruc and M. Zhu, *Chem. Rev.*, **2019**, DOI: 10.1021/acs.chemrev.8b00726.

- 2 a) M. W. Heaven, A. Dass, P. S. White, K. M. Holt and R. W. Murray, *J. Am. Chem. Soc.*, **2008**, 130, 3754-3755; b) M. Zhu, C. M. Aikens, F. J. Hollander, G. C. Schatz and R. Jin, *J. Am. Chem. Soc.*, **2008**, 130, 5883-5885.
- 3 a) J. F. Parker, J.-P. Choi, W. Wang and R. W. Murray, *J. Phys. Chem. C*, **2008**, 112, 13976-13981; b) M. Zhu, M. W. T. Eckenhoff, T. Pintauer and R. Jin, *J. Phys. Chem. C*, **2008**, 112, 14221 -14224; c) Z. Liu, Xu, S. Jin, S. Wang, G. Xu and M. Zhu, *Int. J. Hydrogen Energy*, **2013**, 38, 16722-16726; d) S. Antonello, G. Arrigoni, T. Dainese, M. D. Nardi, G. Parisio, L. Perotti, A. Rene, A. Venzo and F. Maran, *ACS Nano*, **2014**, 8, 2788-2795.
- 4 a) Z. Liu, M. Zhu, X. Meng, G. Xu and R. Jin, *J. Phys. Chem. Lett.*, **2011**, 2, 2104-2109; b) K. Kwak, Q. Tang, M. Kim, D.-e. Jiang and D. Lee., *J. Am. Chem. Soc.*, **2015**, 137, 10833-10840.
- 5 D. Astruc, *Angew. Chem., Int. Ed. Engl.*, **1988**, 100, 662-680.
- 6 H. Chong, P. Li, S. Wang, F. Fu, J. Xiang, M. Zhou and Y. Li, *Sci. Rep.*, **2013**, 3, 3214.
- 7 a) A. M. Madonik and D. Astruc, *J. Am. Chem. Soc.*, **1984**, 106, 2437-2439; b) M.-H. Desbois, D. Astruc, J. Guillin, F. Varret, A. X. Trautwein and G. Villeneuve, *J. Am. Chem. Soc.*, **1989**, 111, 5800-5809.
- 8 a) J.-R. Hamon, D. Astruc and P. Michaud, *J. Am. Chem. Soc.*, **1981**, 103, 758-766; b) J. Green, M. R. Kelly, M. P. Payne, A. Seddon, D. Astruc, J.-R. Hamon and P. Michaud, *Organometallics*, **1983**, 2, 211-218; c) D. Astruc, *Acc. Chem. Res.*, **1986**, 19, 377-383;
- 9 a) U. Koelle and F. Khouzoumi, *Angew. Chem. Int. Ed.*, **1980**, 19, 640-641; b) B. Gloaguen and D. Astruc, *J. Am. Chem. Soc.*, 1991, 112, 4607-4609.
- 10 D. Astruc, *Electron-transfer and Radical Processes in Transition-Metal Chemistry*. VCH, New-York, **1995**, Chap. 1.
11. F. Fu, R. Ciganda, Q. Wang, A. Tabey, C. Wang, A. Escobar, A. M. Martinez-Villacorta, R. Hernández, S. Moya, E. Fouquet, J. Ruiz and D. Astruc, *ACS Catal.*, **2018**, 8, 8100-8106.
- 12 a) J. Ruiz and D. Astruc, *C. R. Acad. Sci.*, t. 1, sér. II, **1998**, 21-27; b) I. Noviandri, K. N. Brown, D. S. Fleming, P. T. Gulyas, P. A. Lay, A. F. Masters and L. Phillips, *J. Phys. Chem. B*, **1999**, 103, 6713-6722; c) J. Ruiz, M.-C. Daniel and D. Astruc, *Can. J. Chem.*, **2006**, 84, 288-299.
- 13 R. Marcus and N. Sutin, *Biochem. Biophys. Acta*, **1985**, 811, 265-322.
- 14 D. Rehm and A. H. Weller, *Isr. J. Chem.* **1970**, 8, 259-271.
- 15 a) M. L. H. Green, L. Pratt and G. Wilkinson, *J. Chem. Soc.*, **1959**, 3753-3767; b) I. U. Khand, P. L. Pauson and W. E. Watts, *J. Chem. Soc. C*, **1968**, 2257-2259; c) F. Fu, R. Ciganda, A. M. Martinez-Villacorta, S. Moya, E. Fouquet, J. Ruiz and D. Astruc, *Chem. Eur. J.* **2018**, 24, 6645-6653.

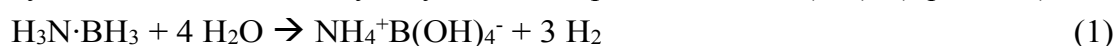
16. P. Michaud, D. Astruc and J. Ammeter, *J. Am. Chem. Soc.*, **1982**, 104, 3755-3757.
17. Manzhou Zhu, Eric Lanni, Niti Garg, Mark E. Bier, and Rongchao Jin. Kinetically Controlled, High-Yield Synthesis of Au₂₅ Clusters. *J. Am. Chem. Soc.* **2008**, 130, 1138-113.

Part III: Metal-organic frameworks (MOFs) supported heterogeneous catalyst.

**Chapter 6. Highly Selective and Sharp Volcano-type Synergistic
Ni₂Pt@ZIF-8- Catalyzed Hydrogen Evolution from Ammonia Borane
Hydrolysis.**

Introduction

One of the critical issues involving the increasing worldwide demand for clean energy sources is the development of new hydrogen-storage materials that would be used in automotive applications.¹ Ammonia borane (NH_3BH_3 , AB in short), with a high hydrogen content of ca. 19.6 wt%, is highly stable in the solid state and solution under ambient conditions, nontoxic, and highly water-soluble. AB is a promising hydrogen storage material attracting tremendous research efforts.² The hydrolysis of AB was initially shown to produce ammonium borate $\text{NH}_4^+\text{BO}_2^-$, but the borate appears to be hydrated; i.e., the overall hydrolysis reaction produces $\text{NH}_4^+\text{B}(\text{OH})_4^-$ (equation 1).³



In the past decade, intensive efforts have been achieved to investigate the hydrolytic dehydrogenation of AB generating 3 mol of H_2 per mole of AB using efficient, economical, and durable catalysts. In this regard, single-metal⁴ and bimetallic nanoparticles (NPs),⁵ metal NPs deposited on supports,⁶ transition-metal complexes,⁷ metal phosphide NPs,⁸ and organic molecules⁹ have been used in catalyzed AB hydrolysis. Many efforts have recently been devoted to the design of high-performance noble metal-free nanocatalysts.¹⁰ H_2 release was recently obtained from AB hydrolysis by Ni NPs supported on ZIF-8 metal-organic-frameworks (MOFs) reaching a turnover frequency (TOF) of $85.7 \text{ mol H}_2 \text{ mol mol}_{\text{H}_2}^{-1} \cdot \text{mol}_{\text{catal.}}^{-1} \cdot \text{min}^{-1}$ at ambient temperature. Hou *et al* synthesized bimetallic Ni-Co-P NPs on graphene oxide (GO) for hydrolysis of AB reaching a high initial turnover frequency (TOF) of up to $154 \text{ mol}_{\text{H}_2} \cdot \text{mol}_{\text{catal.}}^{-1} \cdot \text{min}^{-1}$ at ambient temperature,^{8b} which is an unprecedented value for first-row transition metal NP catalysts.

Earlier results involved molecular catalysts with sophisticated ligands for AB hydrolysis, but supported metal NPs appeared much more practical, efficient and ligandless catalysts. The NP support seems to play a key role, however, and therefore metal-organic frameworks (MOFs) are an intriguing and important class of inorganic-organic hybrids with intrinsic porous structures that are used as versatile precursors or sacrificial templates for the preparation of numerous functional nanomaterials.¹⁰ Indeed abundant works employing MOFs as precursors to access metal/MOF nanostructures have been reported.^{6a,6f,11} MOFs have permanent porosities (large Langmuir surface areas) and tunable pore sizes ensuring good NP dispersion. This allows exposing active sites and facilitates the accessibility of substrates to the active NP surface by reducing diffusion resistance.¹² Attention has in particular been attracted to the ZIF family due to their ease of synthesis and extraordinary high thermal stability and remarkable chemical resistance to boiling water and organic solvents.¹³

Pt, Ru, and Rh-based noble metals NPs are ideal catalysts for fast hydrogen evolution

from AB, but the high prices and global reserve scarcities of these precious metals limit their extensive usage. Developing robust and noble-metal-free catalysts with high and controllable activities is expected.^{6f, 8b, 14} It has not been possible, however, to obtain really high TOF values under ambient conditions with noble-metal-free catalysts. The two disadvantages might be escaped by the use of bimetallic NPs between a precious metal and an earth-abundant metal that activate substrates with a highly positive synergy between the two metals, especially if the content of the earth-abundant metal is large.¹⁵ The bimetallic NPs ranging from core-shell structures to alloys often have excellent physical and chemical properties because of their structures and electronic properties caused by the introduction of the foreign metal.¹⁶ Therefore the bimetallic NPs may disclose unusual functionality utilizing the synergistic effects between two different metals.

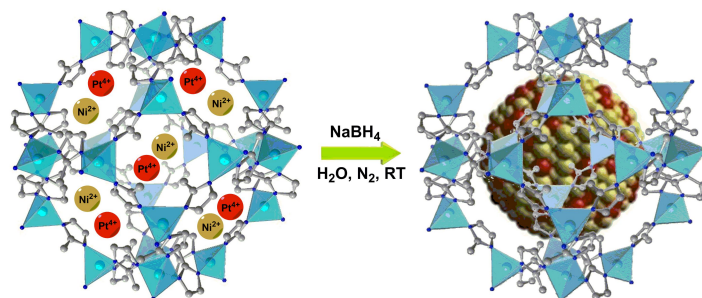
In this work the coreduction method is used to synthesize a series of nearly-monodispersed NiPt NPs with tunable compositions using ZIF-8 as NP support. These new nanostructures are characterized by high resolution transmission electron microscopy (HRTEM), transmission electron microscopy (TEM), high-angle annular dark-field scanning transmission electron microscopy (HAADF-STEM), energy-dispersive X-ray spectroscopy (EDS), X-ray photoelectron spectra (XPS), X-ray powder diffraction (XRD), Brunauer-Emmett-Teller (BET) and inductively coupled plasma atomic emission spectrometer (ICP-AES). These NiPt@ZIF-8 nanoalloy catalysts are shown to be highly active and selective as catalysts for AB hydrolysis, and scrutiny of the optimized composition will prove highly beneficial. In addition Kinetic isotope effects (KIEs) are used for the mechanistic study of this reaction, allowing the proposition of a viable reaction mechanism. The efficiency of the best catalyst will finally also be probed for several regioselective tandem hydrogenation reactions.

Results and discussion

Synthesis and Characterizations of the Nanocatalysts. The synthesis of ZIF-8 was efficiently conducted as described in a previous report.^{6f} The STEM and TEM figures (Figure 12, Experimental Section) show that the ZIF-8 NPs are polyhedron nanocrystals, and that their average size is 56.7 nm. ZIF-8 is very easy synthesized in water, and it is stable even in refluxing in either methanol or water during 1 day without change of the framework structure.^{6f} As shown by the X-ray powder diffraction (XRD) patterns in Figure 3, the sample discloses the typical crystal pattern of ZIF-8.

A series of NiPt@ZIF-8 NP catalysts with tunable compositions were successfully prepared by the deposition-precipitation (DP) method. First the mixture of metal cations was incorporated in ZIF-8 by mixing an aqueous solution of NiCl₂ and PtCl₄

in predetermined proportions with an aqueous ZIF-8 suspension under ambient conditions for 2h. Then fast coreduction by NaBH₄ in water was conducted under N₂, and the nanomaterial was collected by centrifugation, washed with water, and dried at 60°C *in vacuo* overnight (Scheme 1 and Experimental Section).



Scheme 1. Synthesis of the NiPt@ZIF-8 NPs.

The compositions of the catalysts NiPt@ZIF-8 NPs were adjusted by varying the molar ratios of the precursors. Nearly-monodispersed NPs were obtained under our experimental conditions as further indicated by the physical characterization. HAADF-STEM (Figure 1a) and TEM (Figure 1b) show that the as-prepared Ni₂Pt NPs are packed in the ZIF-8 framework with an average size of 2.0 nm (see the size distribution in Figure 13, Experimental Section). Clear lattice fringes are observed by HRTEM (Figure 1b insert), which indicates that a good crystallinity is achieved. The lattice spacing is about 2.2 Å, assuming that the crystallographic plane of the Ni₂Pt nanoalloy is {111}. EDS of the single Ni₂Pt NPs shows that the Pt, Ni and Zn elements are present in both 010 and 011 areas (Figure 2), which leads to conclude that the Ni₂Pt NPs have an alloy structure in ZIF-8 and not a core-shell structure. Even though the percentages of Ni and Pt in 010 and 011 are about 26:74 and 30:70 respectively, the ICP-AES result is 2.7:1, which justifies the Ni₂Pt composition.

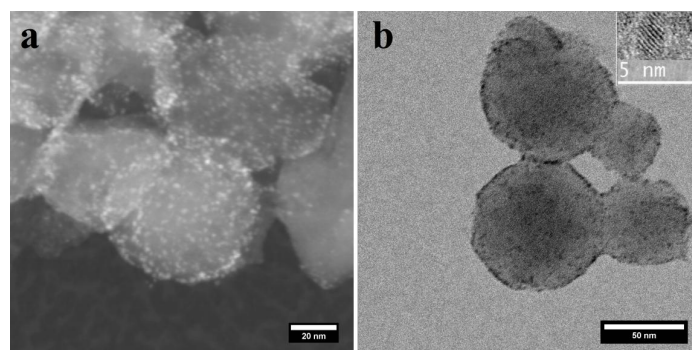


Figure 1. (a) HAADF-STEM and (b) TEM (insert is the HRTEM) images of Ni₂Pt@ZIF-8.

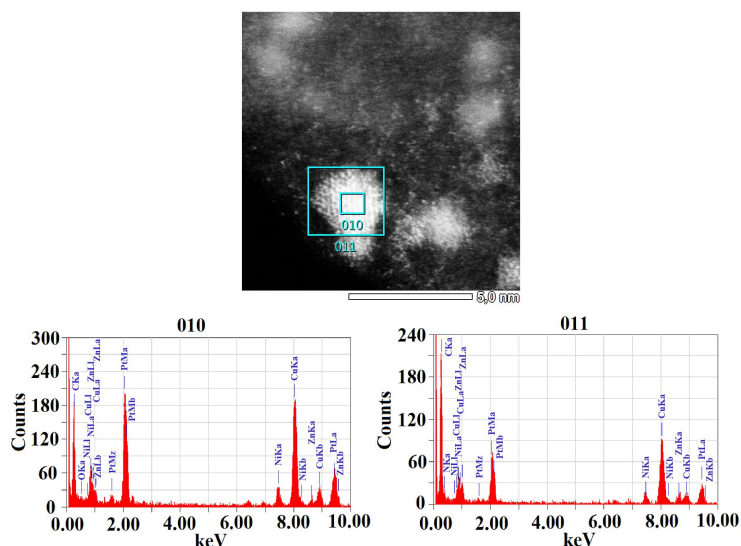


Figure 2. EDS of single Ni₂Pt NP in ZIF-8, showing that Pt, Ni and Zn are present in both the 010 and 011 areas.

The metal oxidation states are identified by XPS (Figure 14, Experimental Section). Binding energies of 71.3 and 74.7 eV are observed for Pt(0) 4f_{7/2} and Pt(0) 4f_{5/2} (Figure 14a, Experimental Section). Moreover the binding energy value detected at 852.9 eV shows that metallic Ni(0) is present in the Ni₂Pt@ZIF-8 NPs (Figure 14b, Experimental Section). TEM images and histograms of the other NiPt@ZIF-8 NPs are shown in Figures 15-19 (Experimental Section) and the average particle sizes are smaller than 3 nm except Pt@ZIF-8 (3.4 nm).

No diffractions were detected for the NiPt alloys or NiNPs in ZIF-8 from PXRD patterns after reduction (Figure 3), which indicates that the metal loadings in ZIF-8 are too low or that the NPs are too small, a feature that has precedents in the literature.¹⁶ The formation of Pt NPs in Pt@ZIF-8 is shown in the PXRD patterns, the diffraction peaks being composed of the standard Pt peak (JCPDS 04-0802, Figure 20, Experimental Section). This is due to the fact that the Pt loading is high (14.8 wt%, Table 2, Experimental Section) in ZIF-8, and the Pt NPs are larger than in the other cases. Importantly, the exact atomic ratios in the NiPt@ZIF-8 NPs were further determined by ICP-AES (Table 2, Experimental Section), and they confirm that the exact Pt/Ni ratios in the nanoalloys in ZIF-8 follow the trend of the designed compositions. The ZIF-8 NPs show a type I isotherm in the N₂ adsorption measurement, and the BET surface area of ZIF-8 is 1663.3 m² g⁻¹.^{6f} The BET surface area decreases as a consequence of the presence of the packing of the NPs. Indeed the BET surface area of Ni₂Pt@ZIF-8, that is the best catalyst in AB hydrolysis, is 938.4 m² g⁻¹ (Table 1, Experimental Section).

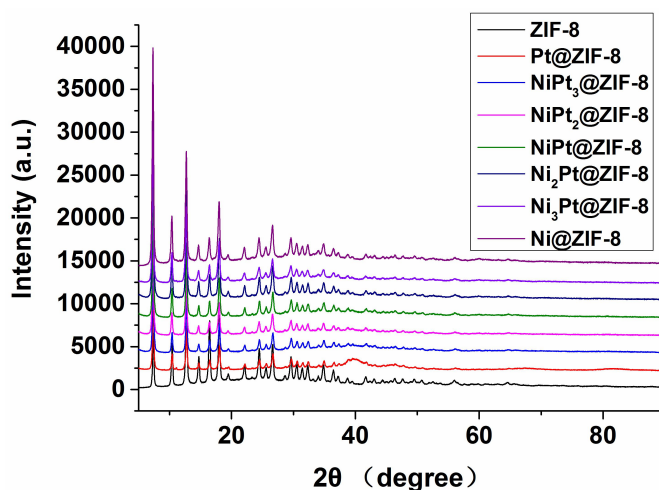


Figure 3. PXRD patterns of the prepared nanocatalysts.

Sharp Volcano-type Synergistic and Highly Selective Catalysis of Very Efficient H₂ Evolution From Ammonia Borane. The Pt@ZIF-8, Ni@ZIF-8 and NiPt@ZIF-8 described above were used for catalytically releasing H₂ from AB in water with 1 mol% of the various late transition-metal nanocatalysts (measured by ICP-AES). The oxidation of Pt(0) and Ni(0) in the NPs were avoided upon carrying out the reactions without exposure to air. The reaction rate and TOF curve in the presence of the nanocatalysts NiPt@ZIF-8 are shown in Figure 4 and Table 2 (Experimental Section). The volumes of gas collected represent nearly 3 equiv. of H₂ per AB with no detectable NH₃ (Experimental Section).⁴ It is known that Pt is an efficient metal for this reaction, but Pt@ZIF-8 only leads to a TOF value of 16.6 mol_{H₂} · mol_{catal.}⁻¹ · min⁻¹ to attain 61.1% H₂. On the other hand there is a dramatic rise in the TOF value from 16.6 to 361.4 (Ni₂Pt@ZIF-8) upon increasing the Ni proportion in the NiPt alloy. Indeed the TOF value related to the NP surface atoms of Ni₂Pt@ZIF-8 reaches 669.3 mol_{H₂} · mol_{catal.}⁻¹ · min⁻¹ (Experimental Section). The catalyst Ni₂Pt@ZIF-8 appears to be the best catalyst among this NP series, and when the Ni proportion in the NiPt alloy is higher than 2/3 the TOF value decreases. For instance in the alloy Ni₃Pt@ZIF-8 the TOF value only is 256.4 mol_{H₂} · mol_{catal.}⁻¹ · min⁻¹ for this reaction. All the alloyed NPs give better results than the pure Pt@ZIF-8 or Ni@ZIF-8 catalysts. These results show that the NiPt@ZIF-8 NPs present excellent synergistic effects between these two metals.

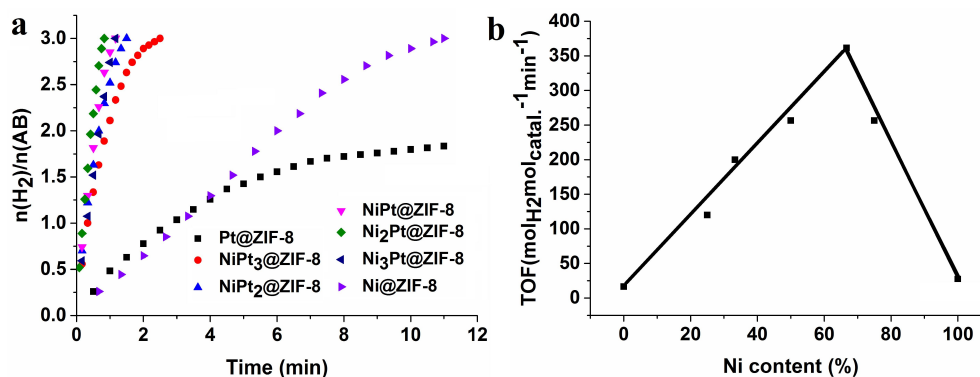


Figure 4. (a) Kinetics of the AB hydrolysis reaction catalyzed by various NiPt@ZIF-8 at 20 ± 0.5 °C with 1 mol% nanocatalysts; (b) Variation of the TOF obtained from various NiPt nanocatalysts in ZIF-8 as a function of Ni content (%) in the NiPt alloys.

High Selectivity of Ni₂Pt@ZIF-8 in ZIF-8 Compared to Other Supports.

Ni₂Pt@GO, Ni₂Pt@C and Ni₂Pt@SBA-15 were synthesized using the same method as that used for the synthesis of Ni₂Pt@ZIF-8 (Experimental Section) in order to understand if this obvious synergistic effect between Ni and Pt also exists with other common supports (GO, C and SBA-15). Figure 5 shows the comparison between various supports concerning the synergy effect between Ni and Pt in Ni₂Pt NPs. This comparison demonstrates that the best synergistic activity measured by the TOF values in the supported NiPt nanocatalysts is by far obtained with Ni₂Pt@ZIF-8. In addition various supports were examined and compared for this catalyst. Figures 29-31 (Experimental Section) show the compared AB hydrolysis reactions catalyzed by Ni₂Pt NPs, Ni NPs and Pt NPs on GO, C and SBA-15 respectively. Ni₂Pt NPs presents the largest synergistic effects in the ZIF-8. The TOF ratio (Ni₂Pt/noble metal Pt) on ZIF-8 is 21.8, which is much higher than the TOF ratio on other supports. This shows that ZIF-8 exhibits high selectivity for Ni₂Pt NPs among all supports for the AB hydrolysis reaction. Thus in sum there is a highly selective triple synergy between Ni, Pt and the ZIF-8 nanomaterials in the catalytic activation of the substrates.

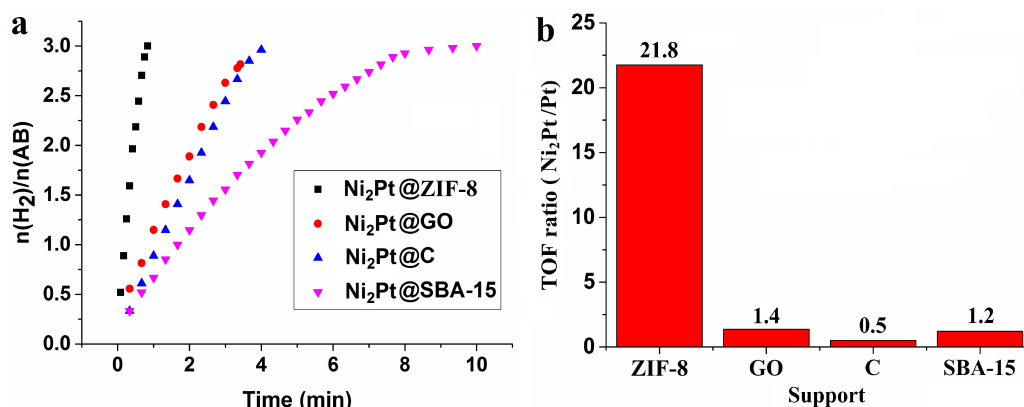


Figure 5. (a) Hydrolysis of AB catalyzed by Ni₂Pt on various supports at 20 ± 0.5 °C with 1 mol% nanocatalysts; (b) TOF ratio (Ni₂Pt/Pt) on various supports.

High Selectivity of Ni₂Pt@ZIF-8 Compared to Other Bimetallic NPs in ZIF-8. A series of bimetallic late-transition-metal NPs, Co₂Pt@ZIF-8, Cu₂Pt@ZIF-8, Ni₂Rh@ZIF-8 and Ni₂Ru@ZIF-8 have been synthesized by the same method as that used for the synthesis of Ni₂Pt@ZIF-8 (Experimental Section). The ICP-AES analysis indicates that the metal loadings are 8.6 , 5.9 , 6.1 and 4.6 wt% and the atomic ratios are 3:1, 2.1:1, 1.1:1 and 1.5:1 respectively. The comparison shows that Ni₂Pt@ZIF-8 exhibits the best efficiency among these five catalysts, followed by the Ni₂Rh@ZIF-8 and Ni₂Ru@ZIF-8. Only 55.6% and 19.1% H₂ are captured by 1 mol% Co₂Pt@ZIF-8 and Cu₂Pt@ZIF-8 respectively in 6 min at 20 ± 0.5 °C, however. Figures 32 and 33 (Experimental Section) illustrate AB hydrolysis catalyzed by pure Rh@ZIF-8 and Ru@ZIF-8 NPs respectively. Among all the bimetallic NPs, again Ni₂Pt shows the strongest synergistic effects in the ZIF-8 according to the TOF ratio (bimetal/noble metal) (Figure 6b). Since ZIF-8 exhibits a high selectivity of Ni₂Pt NPs among various bimetallic nanoparticles, support, and Ni/Pt ratio for AB hydrolysis, this catalytic system was chosen for further studies.

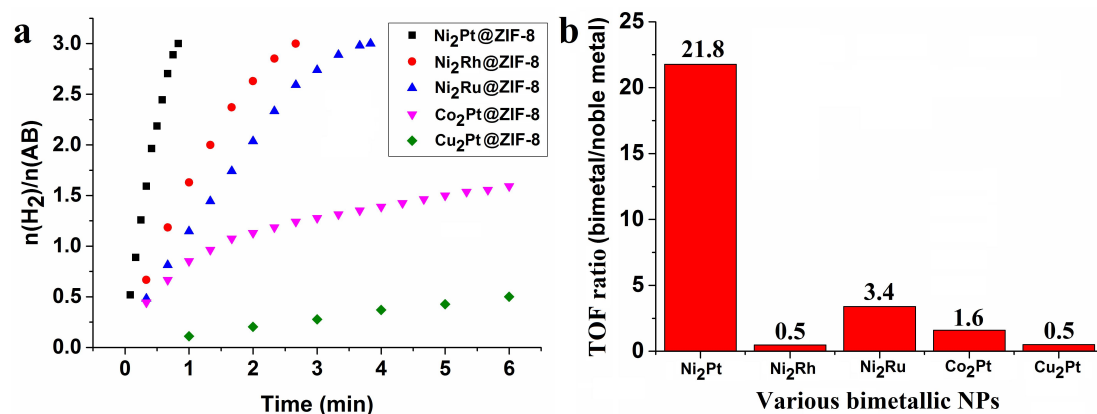


Figure 6. (a) Hydrolysis of AB catalyzed by various bimetallic NPs in ZIF-8 at 20 ± 0.5 °C with 1 mol% nanocatalysts; (b) TOF ratio (bimetal/noble metal) in ZIF-8.

Mechanistic Studies for AB Hydrolysis Catalyzed by Ni₂Pt@ZIF-8. Figure 7a shows the time plots of H₂ evolution vs. various concentration of AB with 1 mol% Ni₂Pt@ZIF-8 NPs. Interestingly the reaction time is exactly the same (50 s), and the logarithmic plot of H₂ generation rate vs. concentration AB is shown in Figure 7b, with a nearly horizontal line (slope is 0.06) indicating that hydrolysis of AB catalyzed by Ni₂Pt@ZIF-8 is zero-order in AB. This rules out AB activation alone in the rate-determining step (*vide infra*). The slope of the logarithmic plot of H₂ generation vs. concentration of Ni₂Pt@ZIF-8 NPs is 0.82 (Figure 7c and 7d), leading to the result of a first-order reaction in catalyst concentration. The measure of the time dependence of H₂ generation at various temperatures indicates that the activation energy (E_a) of AB hydrolysis is low (approximately 23.3 kJ/ mol) with the catalyst Ni₂Pt@ZIF-8

(Figure 7e and 7f and calculation) showing the strong implication of the catalyst in the transition state.

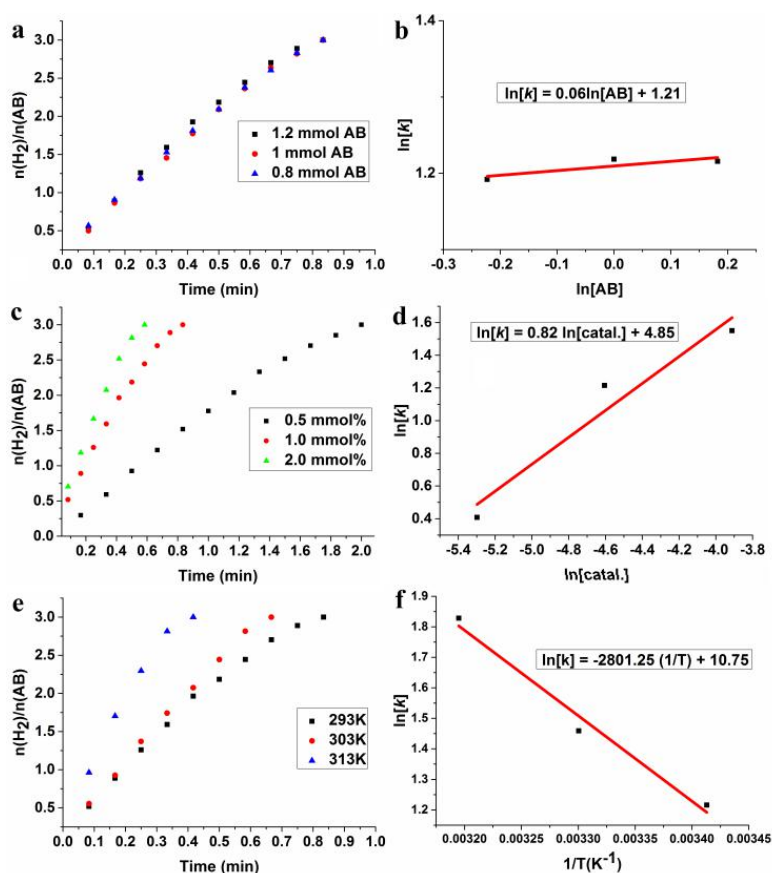


Figure 7. Kinetic studies: (a) time plots of the catalytic dehydrogenation of AB by 1 mol % Ni₂Pt@ZIF-8 with various AB concentrations; (b) plot of H₂ generation rate vs. the concentration of AB both in natural logarithmic scale; (c) time plots of the catalytic dehydrogenation of AB with various catalytic amounts; (d) plot of H₂ generation rate vs. the concentration of catalyst both in natural logarithmic scale; (e) time plots of the catalytic dehydrogenation of AB at various temperatures; (f) Arrhenius plots obtained from the kinetic data.

Kinetic studies were conducted using an isotopic experiment with D₂O instead of H₂O. The kinetic isotope effect (KIE) gives an indication concerning the role of H₂O in the rate-determining step of this reaction.^{3,6f,14e,f} The results with Ni₂Pt@ZIF-8-catalyzed AB hydrolysis are shown in Figure 8a. A large KIE¹⁷ of 4.95 is observed, strongly indicating cleavage of a water O-H bond in the rate-determining step.

Another series of experiments has been conducted with various amounts of NaOH in order to investigate the role of OH⁻ on the AB hydrolysis rate in the presence of the catalyst^{6f, 19} that is eventually beneficial.^{8b,14e,f,18} NaOH appears to be the best candidate among various bases. The catalytic performance of the Ni₂Pt@ZIF-8 NPs toward AB hydrolysis in the presence of various amounts of NaOH (0.1-0.4 M) has

been tested, and the results are shown in Figure 8b. The H₂ evolution rates are improved compared to those found in the absence of NaOH. The H₂ generation rate increases with the increased NaOH concentrations to the optimum level of 0.3 M, and the best result is obtained with 1 mol% Ni₂Pt@ZIF-8 reaching a TOF value of 600 mol_{H₂}/mol_{catal.}/min and 2222 mol_{H₂}/mol_{Pt}/min, which surpasses that of the Pt-base NPs systems at 20 ± 1°C (Table 3, Experimental Section). The results then decrease with higher NaOH concentration (0.4 M). No H₂ release are observed for AB hydrolysis in the NaOH (0.3 M) solution in the absence of the Ni₂Pt@ZIF-8 NPs, indicating that NaOH acts as a catalyst promoter, not as a catalyst for the hydrolytic dehydrogenation of AB. The favorable OH⁻ effect is consistent with coordination of OH⁻ to the NP surface, making the NP more electron-rich, which favors the rate-limiting oxidative addition of water. NaOH has a negative effect on Pt@ZIF-8 NP-catalyzed H₂ evolution upon AB hydrolysis, however. With Pt@ZIF-8 NPs that are the most electron-rich NP surfaces, the hydrogen bonding between AB and H₂O appears to be sufficient to favor O-H oxidative addition by the Pt NP surface without the need to further enriching the Pt NPs by OH⁻ coordination. Coordination of OH⁻ to the Pt NP surface possibly partly inhibits the oxidative addition of the water O-H bond by occupying the surface active sites, explaining why Pt@ZIF-8 shows negative effect with 0.3 M NaOH (Figure 9). Indeed the TOF decreases from 16.6 to 6.9 mol_{H₂} · mol_{catal.}⁻¹ · min⁻¹ after adding 0.3 M NaOH. It is interesting to see that the synergistic effect between Pt and Ni in the NiPt alloy in ZIF-8 is more marked in the presence of 0.3 M NaOH, whereas the opposite is found with Pt@ZIF-8 alone (Figure 34, Experimental Section). Figure 9 shows the comparison of the TOF variation obtained for various catalysts NiPt@ZIF-8 with and without 0.3 M NaOH. This comparison indicates that the catalyst presents an enhanced synergistic effect between Ni and Pt in the NiPt alloy in the presence of NaOH. Very remarkably the TOF obtained with Ni₂Pt@ZIF-8 is around 87 times higher than that of the noble metal catalyst Pt@ZIF-8 in the presence of 0.3 M NaOH.

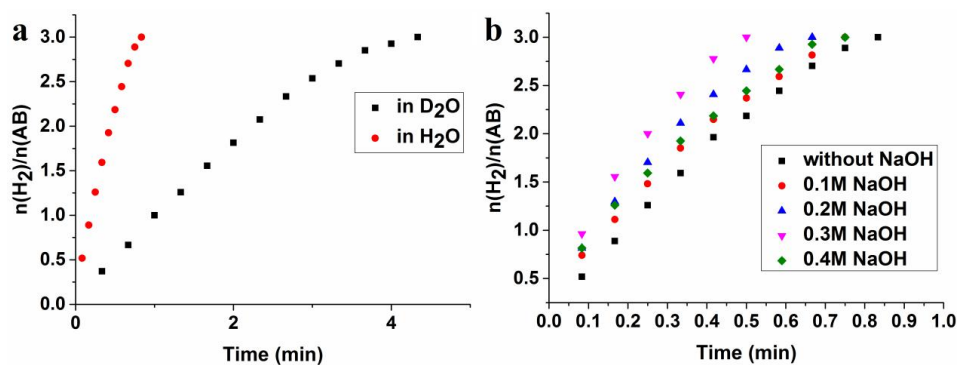


Figure 8. Hydrolysis of AB catalyzed by Ni₂Pt@ZIF-8 (a) in H₂O (red) or D₂O (black), (b) in the presence of 0.1-0.4M NaOH in water, at (20 ± 0.5 °C) with 1 mol% nanocatalyst.

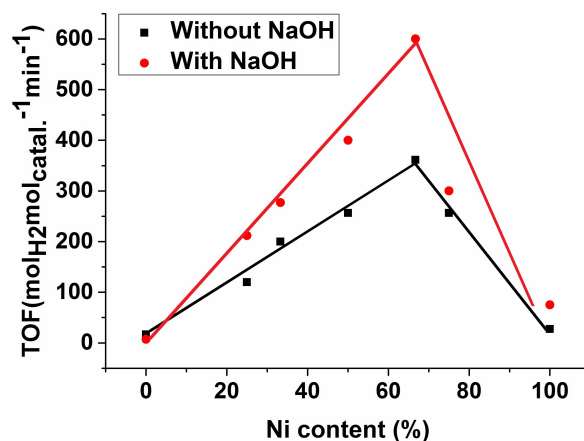
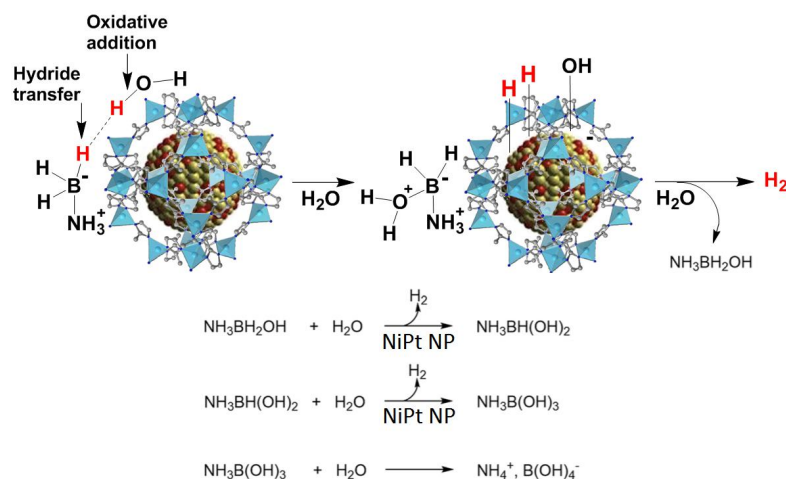


Figure 9. Comparison of the TOF variation obtained for various NiPt@ZIF-8 catalysts activities with and without 0.3 M NaOH.

Several mechanisms have been proposed for hydrolysis of AB catalyzed by late transition-metal NPs.^{2b, 2c, 6e} The intermediate $\text{BH}_3\text{OH}\cdot\text{NH}_4^+$ was proposed by Fu who also suggested its attack by H_2O for H_2 production.^{8a} Reaction of H_2O on the activated complex was suggested by Xu who proposed cleavage of the B-N bond, then NH_3 hydrolysis to yield H_2 .²⁰ Attack of H_2O on a transient M-H bond to produce H_2 by analogy with BH_4^- hydrolysis was suggested by Jagirdar²¹ and also by Ma.²² Cleavage of a water O-H bond in the rate-determining step was proposed by Chen's group²³ and Wang et al.^{6f} A mechanistic proposal based on the present results is shown in Scheme 2. Here it is likely that H_2O forms a hydrogen bond $[\text{H}_3\text{NBH}_2\text{H}]\dots\text{H}\text{-OH}$, because the B-H bond presents a hydridic character. The very large KIE obtained with D_2O shows that oxidative addition of the O-H bond of water occurs in the rate-determining step. This step appears to be water oxidative addition of an O-H bond. The rate increase provoked by 0.3 M OH^- is taken into account by a bond of OH^- to the NP surface. This effect increases the electron density on the NP surface, which favors oxidative addition of water that is proposed to be the rate-limiting step. Pt@ZIF-8 is the most electron-rich NP surface, which explains that the NP surface already is sufficiently electron rich to induce OH oxidative addition on the NP surface in the hydrogen bonded species $[\text{H}_3\text{NBH}_2\text{H}]\dots\text{H}\text{-OH}$. In this case only of Pt@ZIF-8 it does not need OH^- coordination, and on the contrary it is probable that the occupation of surface coordination site by OH^- inhibits further surface activity.



Scheme 2. Proposed mechanism for the hydrolysis of AB catalyzed by NiPt@ZIF-8.

Tandem Reactions for Hydrogenation with H₂ Generated from AB. The H₂ produced from AB catalyzed by Ni₂Pt@ZIF-8 was used for the hydrogenation²⁴ of 4-nitrophenol, styrene and benzonitrile with the same catalyst whose optimization was shown above and conducted in a sealed two-chamber system (Figure 10, detail in Experimental Section). Following H₂ evolution, the reaction was performed using this nanocatalyst at 30 °C, and the yellow color of 4-nitrophenol disappeared after 2 h. The isolated yield is 99%. The hydrogenation of styrene with the generated H₂ also occurred successfully and was complete (quantitative) after 12 h at 50 °C. Moreover, even the more difficult complete hydrogenation the C-N bond of benzonitrile was selectively achieved in 90% isolated yield at 50 °C for 24h. This means that H₂ produced from AB is conveniently used for hydrogenation reactions and that the catalyst Ni₂Pt@ZIF-8 is an efficient and versatile catalyst for these and presumably many other organic reactions.

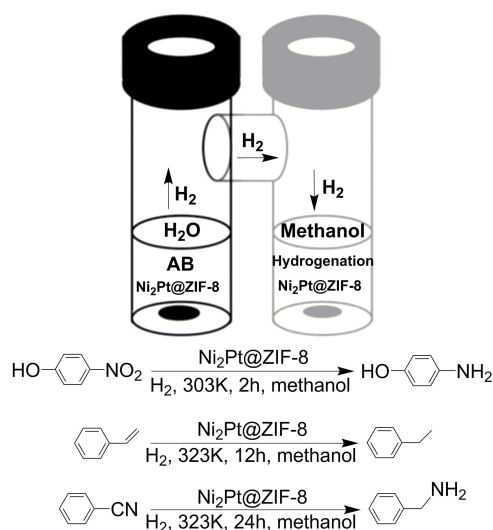


Figure 10. Tandem reaction for hydrogenation with H₂ generated from AB catalyzed by Ni₂Pt@ZIF-8.

Conclusion

A coreduction method has been established here for the synthesis of ligand-free nearly-monodispersed NiPt alloy NPs with tunable compositions using the ZIF-8 MOF as template. These new catalysts provoke the evolution of 3 mol H₂ upon AB hydrolysis, and the reaction is zero order in AB and first order in NP catalyst.

Upon scrutinizing the optimal amount of each metal proportion in the bimetallic catalyst, a very remarkable sharp volcano-type positive synergistic effect is disclosed for Ni₂Pt. This catalyst gives much better results than other compositions and other transition metal bimetallic catalysts.

The ZIF-8 support also appears extremely selective for this catalyst compared to the supports GO, C, SBA-15. The highest catalytic activity for H₂ evolution is shown to be that of Ni₂Pt@ZIF-8 with a TOF value of 600 mol_{H₂} · mol_{catal.}⁻¹ · min⁻¹ and 2222.2 mol_{H₂} · mol_{Pt}⁻¹ · min⁻¹ at 20 ± 1°C. This value is around 87 times higher than the TOF of the noble metal catalyst Pt@ZIF-8.

It is also found that NaOH much enhances the reaction rate with the catalyst Ni₂Pt@ZIF-8, whereas on the contrary it decreases that of the reaction catalyzed by Pt@ZIF-8. These results are taken into account by OH⁻ anion coordination to the NP surface enriching its electron density, thereby facilitating the crucial oxidative addition of a water O-H bond. With Pt@ZIF-8 the electron-rich Pt NP seems not to need additional electron density, and OH⁻ coordination is proposed to inhibit further substrate activation, causing a decrease of catalyst activity.

A large kinetic isotope effect of 4.95 upon replacing H₂O by D₂O indicates that cleavage of the O-H bond of water appears to be the rate-determining step. In this mechanism water is part of the source of dihydrogen production. The high proportion of Ni in the catalysts shows excellent results obtained using such a “green” approach, yet benefitting from unprecedented synergistic activation boosting efficiency and selectivity.

Tandem reactions were successfully conducted for hydrogenation with H₂ generated from AB with the catalyst Ni₂Pt@ZIF-8 showing that it is also a very efficient and versatile general catalyst. These remarkable performances and results not only enrich the family of highly efficient catalysts for hydrolysis of AB, but also provide significant and promising insights into the optimization of the electronic structure design of the alloy surface involving heteroatom bonding. The principles shown here might be applicable to progress in catalyst design in general including for suitable and convenient H₂ generation systems in the future.

Experimental Section

General data.

All the chemicals and reagents are commercially available and were used as received. Milli-Q water (18.2 M Ω) was used for all the nanoparticle preparations. Prior to the synthesis, all the flasks were washed with a solution of aqua regia (HCl/HNO₃ = 3:1 v/v) to remove any traces of metal residue. Nitrogen physisorption isotherms were measured at 77 K on an automatic volumetric adsorption apparatus (Micromeritics ASAP 2420). The samples were filled into glass ampoules and outgassed in high vacuum at 473 K for 24 h before the start of the sorption measurements. Brunauer-Emmett-Teller (BET) areas were recorded with a 30% v/v N₂/He flow using pure N₂ (99.9%) as internal standard. At least 2 cycles of N₂ adsorption-desorption in the flow mode were employed to determine the total surface area using the standard single point method. Transmission Electron Microscopy (TEM), High-resolution TEM (HRTEM), High-angle Annular Dark-field Scanning Transmission Electron Microscopy (HAADF-STEM) images were recorded using a TEM JEOL JEM-2100F. Energy-dispersive X-ray Spectroscopy (EDS) images were recorded by JEM-ARM200F (URP) ED. X-ray photoelectron spectra (XPS): System: SPECS SAGE HR, X-Ray source: Mg K α non-monochromatic, operated at 12.5 kV and 250 W. Take-off angle 90°, at $\sim 10^{-8}$ Torr. Pass energy for survey spectra 30 eV, 15 eV for narrow scans. Analysis: spectra were calibrated to CC carbon 285 eV. Analysis consisted of Shirley background subtraction. Peaks were fitted with symmetrical Gaussian-Lorentzian (GL) line shapes. The sample was dispersed on a silica substrate and evaporated prior to measurement. X-ray powder diffraction (XRD) data of samples were determined using a Rigaku RU-200b X-ray powder diffractometer with Cu K α radiation ($\lambda = 1.5406$ Å). Elemental analysis in the solid samples was detected by an Optima 7300 DV inductively coupled plasma atomic emission spectrometer (ICP-AES). NMR spectra were recorded at 25 °C with a Bruker AC 300 (300 MHz). All the chemical shifts were reported in parts per million (δ , ppm) with reference to Me₄Si for the ¹H NMR spectra. The GC-MS analysis was performed by the CESAMO on a Thermo Trace GC ultra gas chromatograph coupled to a Thermo ISQ mass detector.

Details of the synthesis

Synthesis of the ZIF-8 NPs: The method used was that published previously.^{6f} In a typical synthesis, 2-methylimidazole (0.28 mol, 22.95 g) was dissolved in 80 mL water and stirred at 35°C to form a homogeneous solution. Then an aqueous solution of Zn(NO₃)₂•6H₂O (1.19 g, 4.0×10^{-3} mol) dissolved in 9 mL water was rapidly injected into the above aqueous solution. The mixture was stirred for 1 h, and the product was collected by centrifugation and washed with water and ethanol several times. The ZIF-8 NPs were then dried at 60°C *in vacuo* overnight, and the white solids were collected for further use.

Synthesis of the Nanocatalysts (Ni₂Pt@ZIF-8 as Example): A Schlenk flask was charged with 100 mg ZIF-8 NPs under N₂. Then 5 mL water was injected, and the mixture was sonicated for 5 min and allowed to stir for 30 min under N₂. The precursors NiCl₂ (9 mg) and PtCl₄ (6.4 mg) (the molar ratio of the Pt: Ni precursor were 1:2, totally 5.68×10^{-5} mol) dissolved in 2 mL water were injected. This mixture was stirred continuously at room temperature for 2 h. Then 1 mL aqueous solution of fresh prepared NaBH₄ (21 mg, 5.5×10^{-4} mol) was quickly added after degassing with N₂ for 5 min. The mixture was allowed to further stir for another 30 min, and the resulting nanocatalyst was collected by centrifugation, washed with water and dried at 60°C *in vacuo* overnight. The metal content was quantified by inductively coupled plasma atomic emission spectroscopy (ICP-AES). A similar synthetic process was used for various other Ni/Pt ratios, other bimetallic nanoparticles and supports (C, GO and SBA-15).

Hydrolysis reactions of H₃N-BH₃:

The hydrolysis reactions of H₃N-BH₃ were conducted in water at the given experimental temperature. In a round bottom 50 mL flask, the nanocatalyst (the metal to AB ratio was fixed at 1%, which was measured by ICP-AES.) was dissolved in 9 mL water with continuous stirring. An aqueous solution of H₃N-BH₃ (37.5 mg, 1.215 mmol, in 1 mL H₂O) was injected in this round bottom flask, and timing started. The flask was fitted with a gas outlet, and a side arm was sealed with a tight-fitting septum cap. The flask was connected *via* the gas outlet to a water-filled gas burette. Gas evolution began immediately, and the amount of gas evolved was determined periodically by measuring the displacement of water in the burette. In our case, a quantitative conversion of H₃N-BH₃ produced 3.0 equivalents of H₂ at atmospheric pressure. Prior to the reactions, the volumes were measured at atmospheric pressure and corrected for water vapor pressure at room temperature.

Detection of NH₃ gas:

The gas generated from the hydrolysis was passed through a 25 mL standard HCl solution (0.01 M) at room temperature, by which the ammonia gas was captured. After gas generation was ceased, the resulted solution was titrated with standard NaOH solution (0.01 M) by using the acid-base indicator phenolphthalein. The quantity of the liberated ammonia gas was calculated from the difference between two HCl solutions before and after the reaction.

Hydrogenation with hydrogen generated from AB hydrolysis.

The tandem reaction was reacted in the sealed two-chamber system (Figure S1). The left tube was used for hydrogen generation, and the right one was used for hydrogenation. The generated hydrogen transports to the hydrogenation reaction through the connected glass tube.

Hydrogenation of 4-nitrophenol: 8 mg (0.5 mmol% per AB) Ni₂Pt@ZIF-8 was added

into the left tube. Meanwhile, 10 mg (1.5 mmol% per 4-nitrophenol) Ni₂Pt@ZIF-8 catalyst and 69.5 mg (0.5 mmol) 4-nitrophenol were added to the right tube. Air was removed *in vacuo*, and 2 mL methanol was injected into the right tube. Thereafter 37.5 mg (1.215 mmol) AB dissolved in 2 mL water was injected into the left tube. After 5 min, the system was reacted at 30°C for 2 h, filtered and methanol was removed *in vacuo* to provide 4-aminophenol (54.5 mg, 99%).

Hydrogenation of styrene: 8 mg (0.5 mmol% per AB) Ni₂Pt@ZIF-8 was added into the left tube. Meanwhile, 10 mg (1.5 mmol % per styrene) Ni₂Pt@ZIF-8 catalyst was added to the right tube. Air was removed *in vacuo*, and 2 mL methanol included 52 mg (0.5 mmol) styrene was injected into the right tube. Then 37.5 mg (1.215 mmol) AB dissolved in 2 mL water was injected into the left tube. After 5 min, the system was reacted at 50 °C for 12h. Then, the reaction solution was collected by centrifugation for GC-MS analysis without any work-up.

Hydrogenation of benzonitrile: 8 mg (0.5 mmol% per AB) Ni₂Pt@ZIF-8 was added into the left tube. Meanwhile, 20 mg (7.6 mmol% per benzonitrile) Ni₂Pt@ZIF-8 catalyst was added to the right tube. Air was removed *in vacuo*, and 2 mL methanol containing 20.6 mg (0.2 mmol) benzonitrile was injected into the right tube. Then 37.5 mg (1.215 mmol) AB dissolved in 2 mL water was injected into the left tube. After 5 min, the system was reacted at 50 °C for 24h, filtered and methanol was removed *in vacuo*. Purification by flash chromatography column was conducted with silica gel as the stationary phase and dichloromethane/methanol (9:1) as the mobile phase. Isolated yield: (19 mg, 90%).



Figure 11. The sealed two-chamber system for the tandem reaction.

Characterizations of the nanocatalysts.

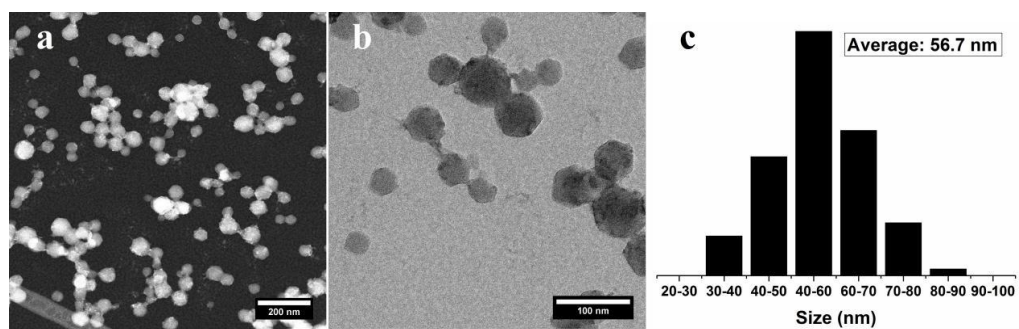


Figure 12. STEM (a), TEM (b) images and size distributions (c) of the as-synthesized ZIF-8 NPs.

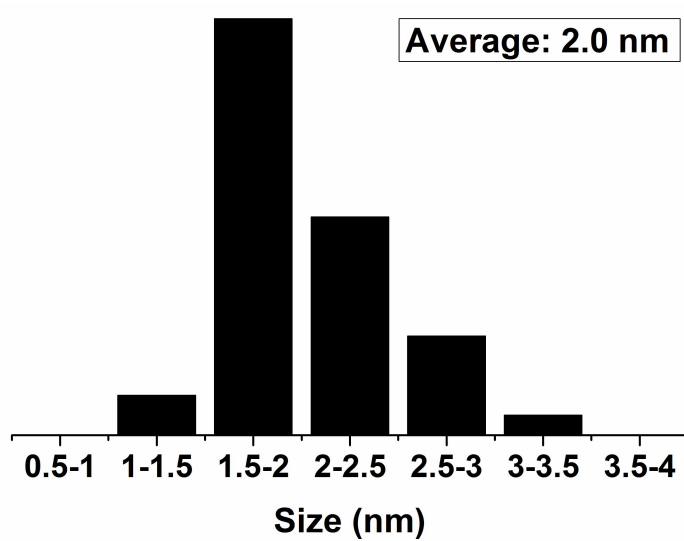


Figure 13. Size distributions of the as-synthesized Ni₂Pt@ZIF-8 NPs.

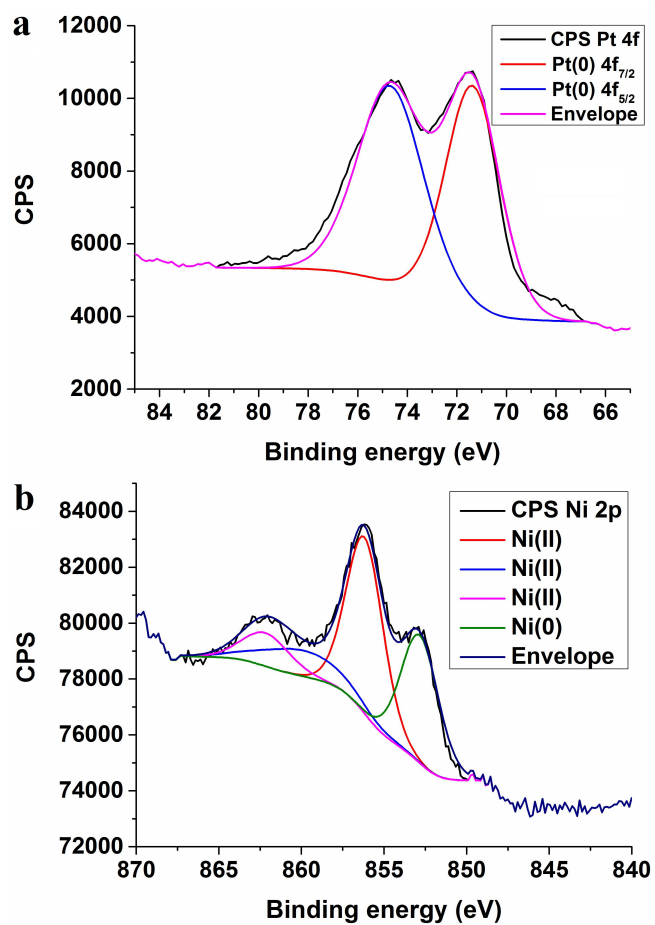


Figure 14. XPS spectra of the as-synthesized Ni₂Pt@ZIF-8 NPs: a: Pt 4f; b: Ni 2p.

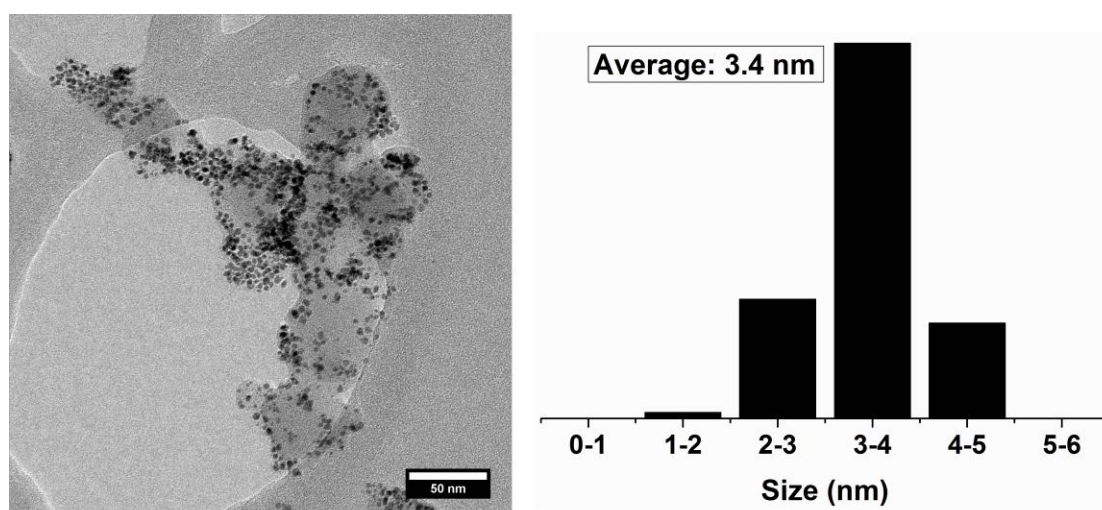


Figure 15. TEM images and size distributions of the as-synthesized Pt@ZIF-8 NPs.

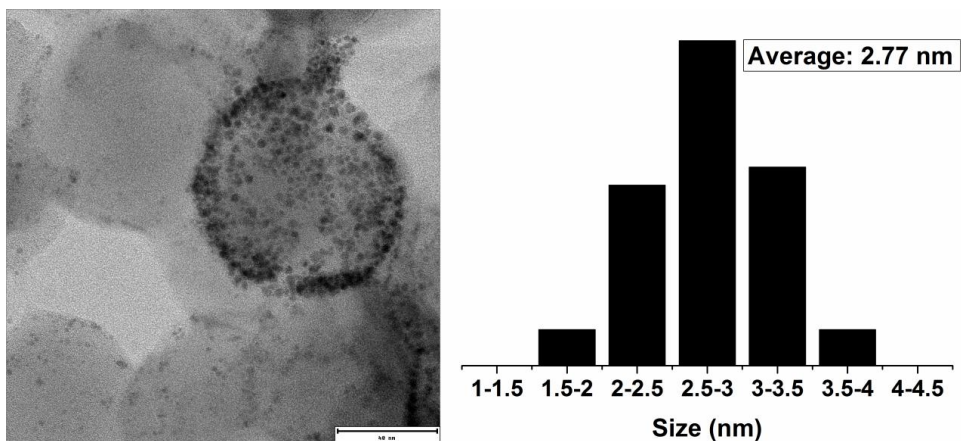


Figure 16. TEM image (scale bar: 40 nm) and size distributions of the as-synthesized NiPt₃@ZIF-8 NPs.

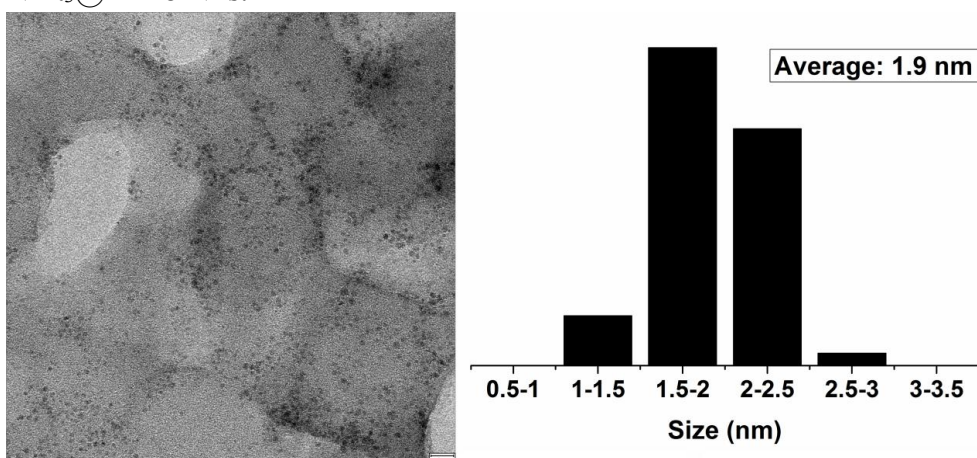


Figure 17. HRTEM image (scale bar: 9 nm) and size distributions of the as-synthesized NiPt₂@ZIF-8 NPs.

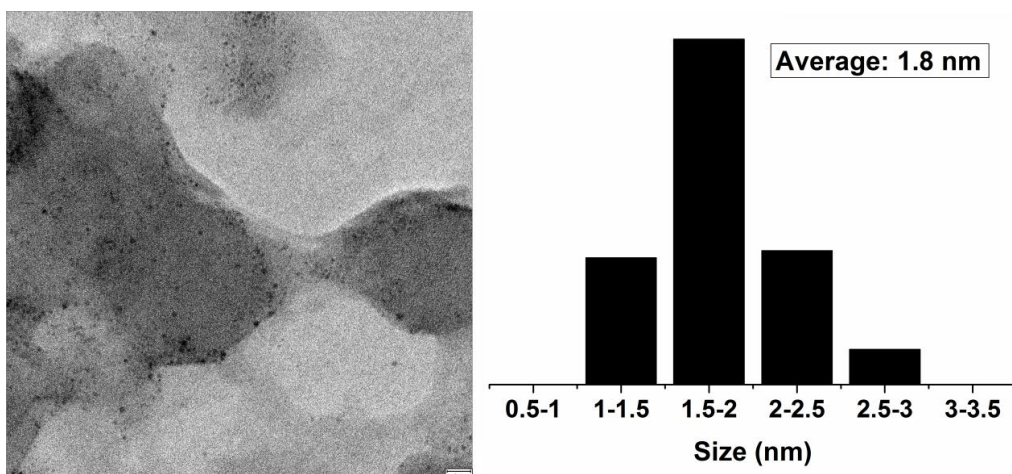


Figure 18. HRTEM image (scale bar: 9 nm) and size distributions of the as-synthesized NiPt@ZIF-8 NPs.

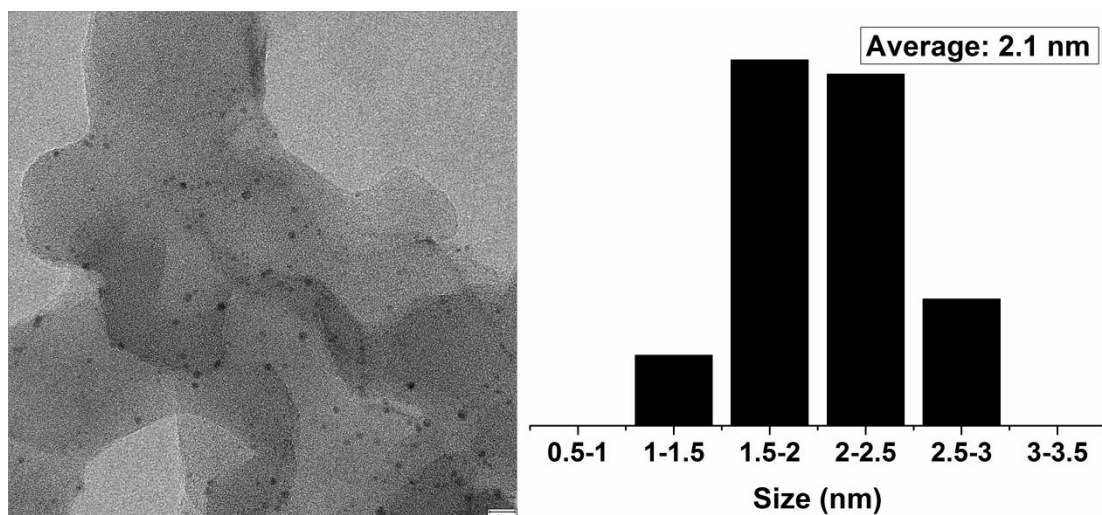


Figure 19. HRTEM image (scale bar: 9 nm) and size distributions of the as-synthesized Ni₃Pt@ZIF-8 NPs.

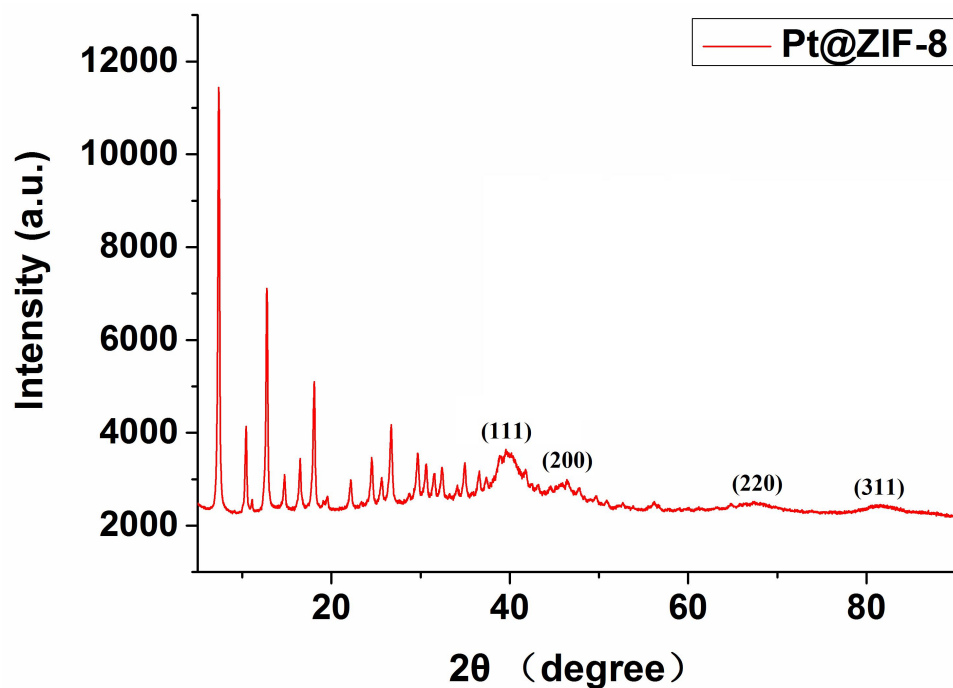


Figure 20. PXRD patterns of as-synthesized Pt@ZIF-8 NPs.

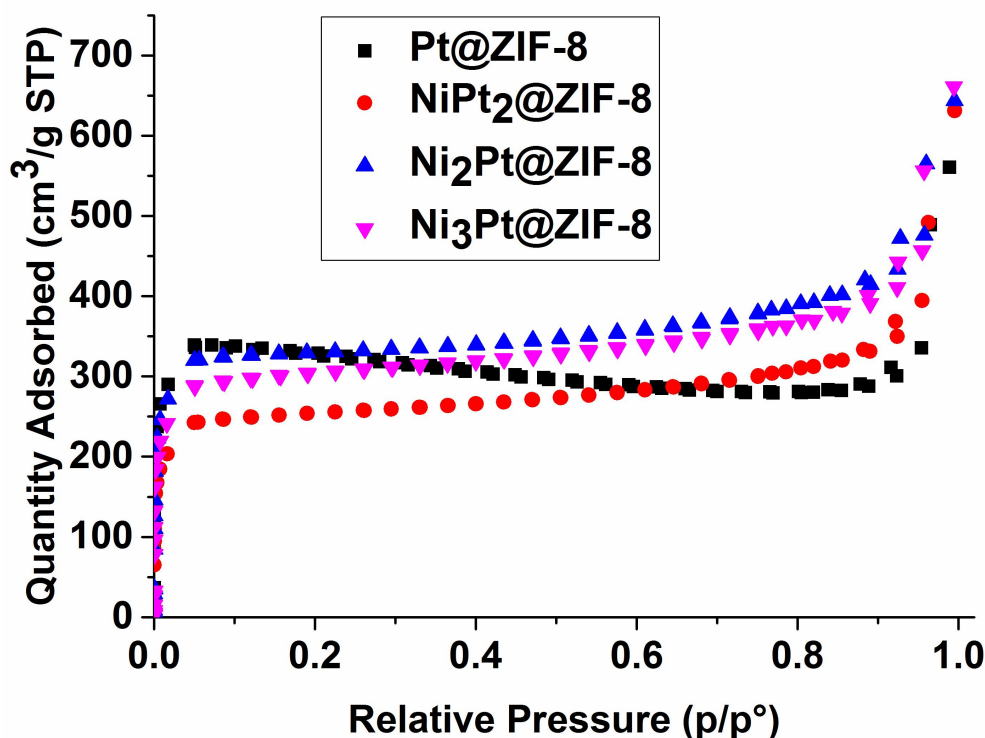


Figure 21. Nitrogen adsorption-desorption isotherms of nanocatalysts on ZIF-8

Table 1. Physical Properties of the Nanocatalysts on ZIF-8.

Sample	BET surface area ($\text{m}^2 \text{g}^{-1}$)	pore volume ($\text{cm}^3 \text{g}^{-1}$)
ZIF-8 ¹	1663.3	0.6614
Pt@ZIF-8	968.8	0.4769
NiPt ₂ @ZIF-8	781.2	0.2712
Ni ₂ Pt@ZIF-8	938.4	0.6232
Ni ₃ Pt@ZIF-8	1001.1	0.2726
Ni@ZIF-8 ¹	1324.3	0.4255

Calculation of the NP surface atoms number (Ns) and TOFs related to the Ns.

$$V_{\text{NP}} = N V_{\text{atom}} \quad (\text{eq. 1})$$

$$\frac{4}{3} \pi (R_{\text{NP}})^3 = N \frac{4}{3} \pi (R_{\text{atom}})^3 \quad (\text{eq. 2})$$

Where V is the atom volume of the NP, R is the atomic radius of the NP, and N is the total number of atoms within the NP. Rearranging, we obtain:

$$N = (R_{\text{NP}}/R_{\text{atom}})^3 \quad (\text{eq. 3})$$

Knowing the NP radius, we can also calculate the surface area (S) of a NP with the following equation:

$$S_{\text{NP}} = 4 \pi (R_{\text{NP}})^2 \quad (\text{eq. 4})$$

So, we may also calculate the number of surface atoms (N_s) directly by dividing the surface area of the NP by the cross section of an individual NP atom and then simplifying using the relationship in (eq. 3):

$$N_s = (4 \pi (R_{NP})^2) / (\pi (R_{atom})^2) = 4 N (R_{atom}/R_{NP}) \text{ (eq. 5)}$$

The ratio of the $N_s/N = 4 (R_{atom}/R_{NP})$

So $TOFs = TOF/(N_s/N)$

Where $TOF = \text{mol}_{H_2} \text{ released}/(\text{mol}_{catal.} \times \text{reaction time (min)})$

Table 2. Physical properties and comparison of the catalytic efficiency of the nanocatalysts.

Catalyst	Size (nm)	atomic ratios ^a	Metal loadings (wt%) ^a	R _{NP} (nm)	R _{atom} (nm)	N _s /N	Initial TOF ^b	Total TOF ^b	TOFs ^b
Pt@ZIF-8	3.4	-	14.8	1.7	0.135	0.32	48.1/9.3 ^c	16.6/6.9 ^c	51.9/21.6 ^c
NiPt ₃ @ZIF-8	2.8	1:2.4	8.4	1.4	0.135	0.39	300/488.8 ^c	120/211.8 ^c	307.7/543 ^c
NiPt ₂ @ZIF-8	1.9	1:1.3	7.3	0.95	0.135	0.57	366.7/555.5 ^c	200/276.9 ^c	350.8/485.8 ^c
NiPt@ZIF-8	1.8	1:0.7	6.1	0.9	0.135	0.60	388.9/733.3 ^c	256.4/400 ^c	427.3/666.7 ^c
Ni₂Pt@ZIF-8	2.0	2.7:1	7.3	1.0	0.135	0.54	533.3/933.3 ^c	361.4/600 ^c	669.3/1111 ^c
Ni ₃ Pt@ZIF-8	2.1	3.9:1	6.5	1.05	0.135	0.51	322.2/511.1 ^c	256.4/300 ^c	502.7/588.2 ^c
Ni@ZIF-8	2.7	-	2.2	1.35	0.135	0.40	33.3/127.8 ^c	27.3/75 ^c	68.3/187.5 ^c

^a Measured by ICP-AES; ^b Hydrolysis of AB in water at room temperature (20 ± 0.5 °C) with 1 mol% catalysts. $TOF = \text{mol}_{H_2} \text{ released}/(\text{mol}_{catal.} \times \text{reaction time (min)})$ ^c TOF is obtained in the presence of 0.3 M NaOH.

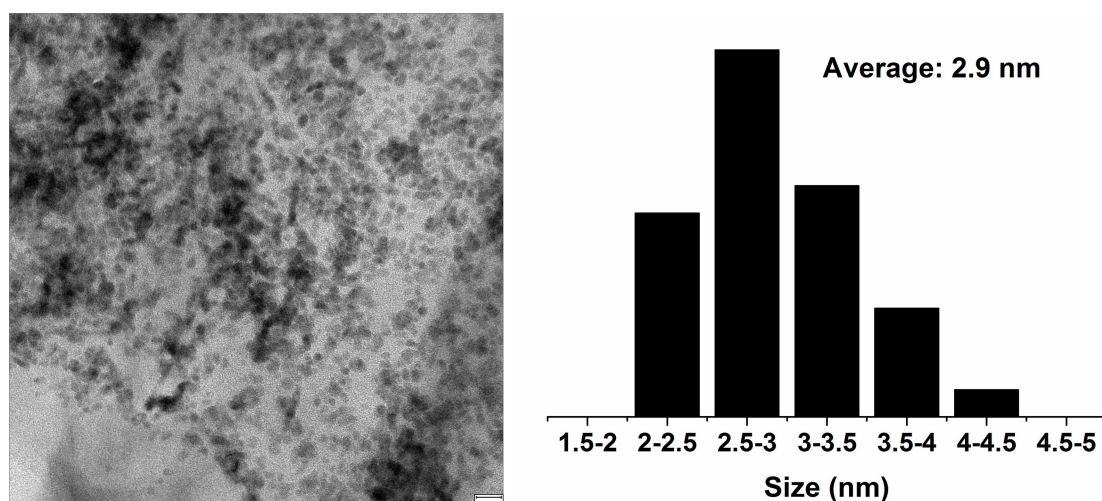


Figure 22. HRTEM image (scale bar: 9 nm) and size distribution of the as-synthesized Ni₂Pt@GO NPs.

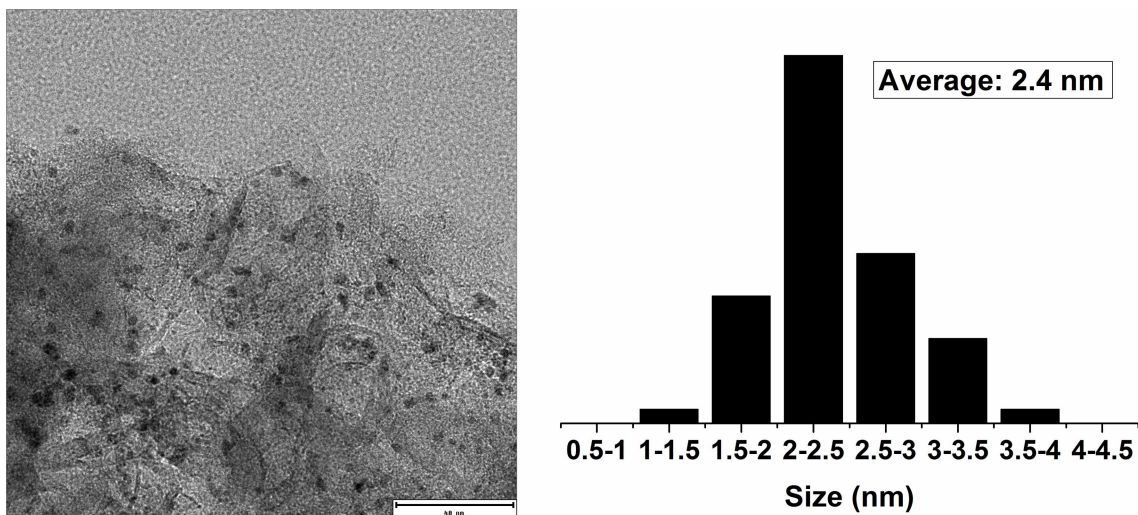


Figure 23. HRTEM image and size distribution of the as-synthesized Ni₂Pt@C NPs.

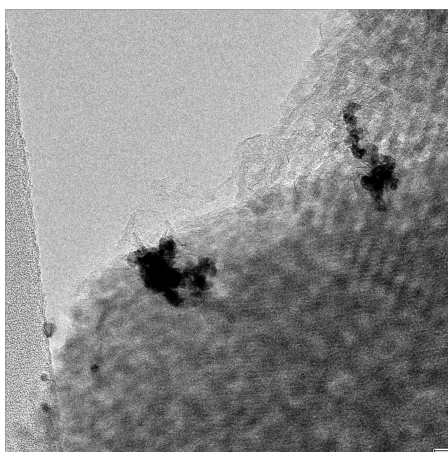


Figure 24. HRTEM image (scale bar: 10 nm) of the as-synthesized Ni₂Pt@SBA-15 NPs.

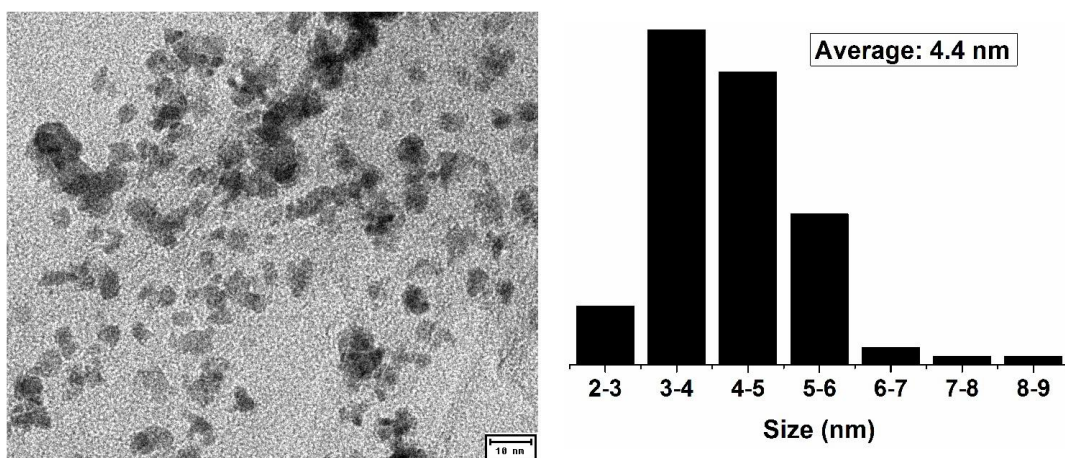


Figure 25. HRTEM image and size distribution (scale bar: 10 nm) of the as-synthesized Pt@GO NPs.

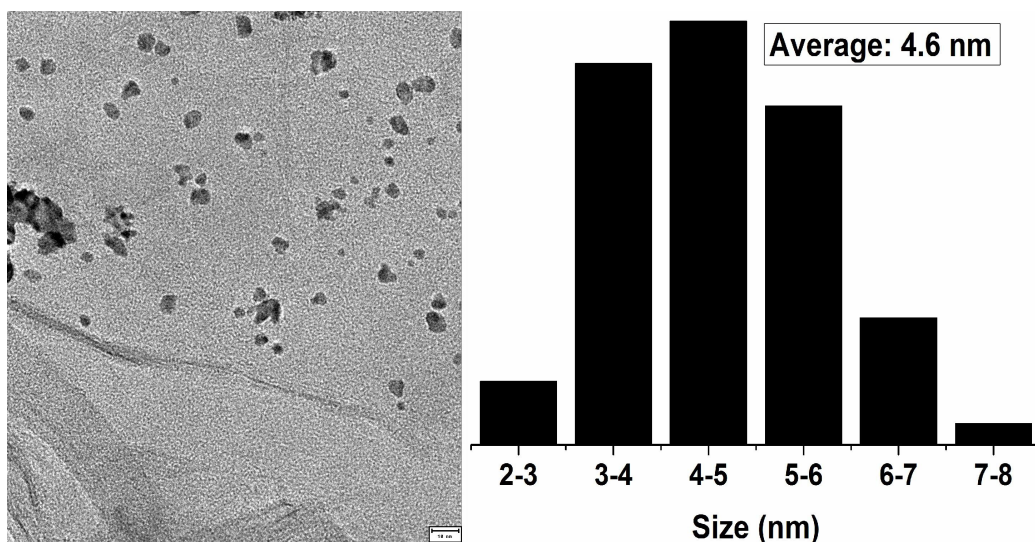


Figure 26. HRTEM image and size distribution (scale bar: 10 nm) of the as-synthesized Ni@GO NPs.

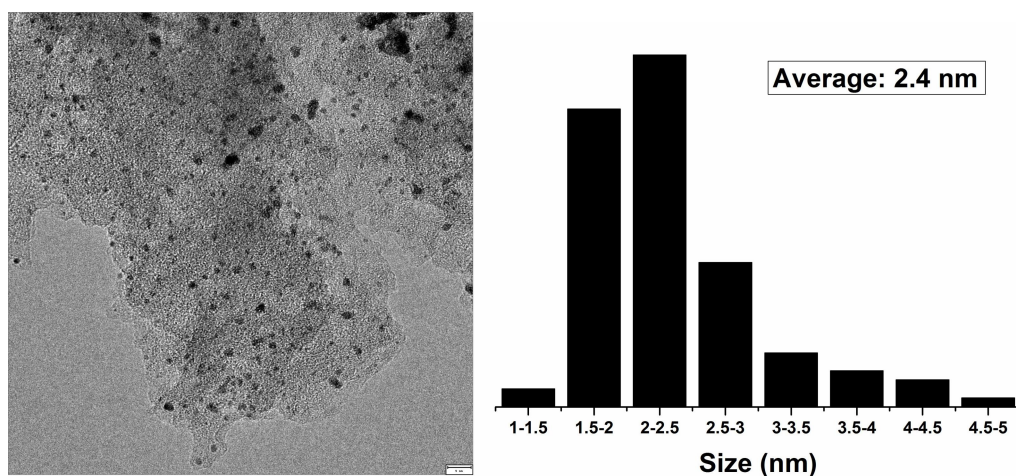


Figure 27. HRTEM image and size distribution (scale bar: 9 nm) of the as-synthesized Pt@C NPs.

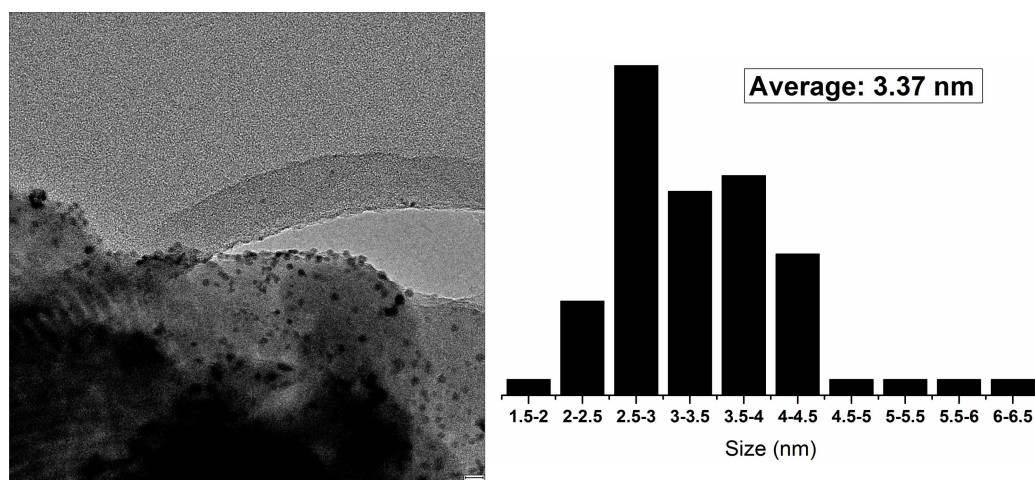


Figure 28. HRTEM image and size distribution (scale bar: 10 nm) of the as-synthesized Pt@SBA-15 NPs.

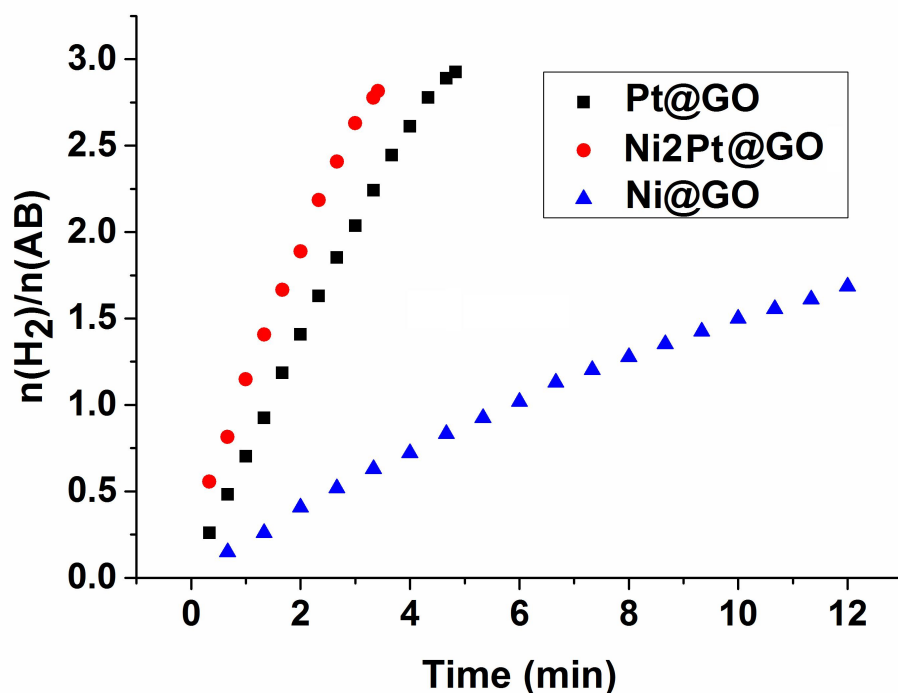


Figure 29. Hydrolysis of AB catalyzed by Pt@GO (13.2 wt%), Ni₂Pt@GO (12.8 wt%, atomic ratios: 1.4:1) and Ni@GO (4.5 wt%) at (20 ± 0.5 °C) with 1 mol% nanocatalyst.

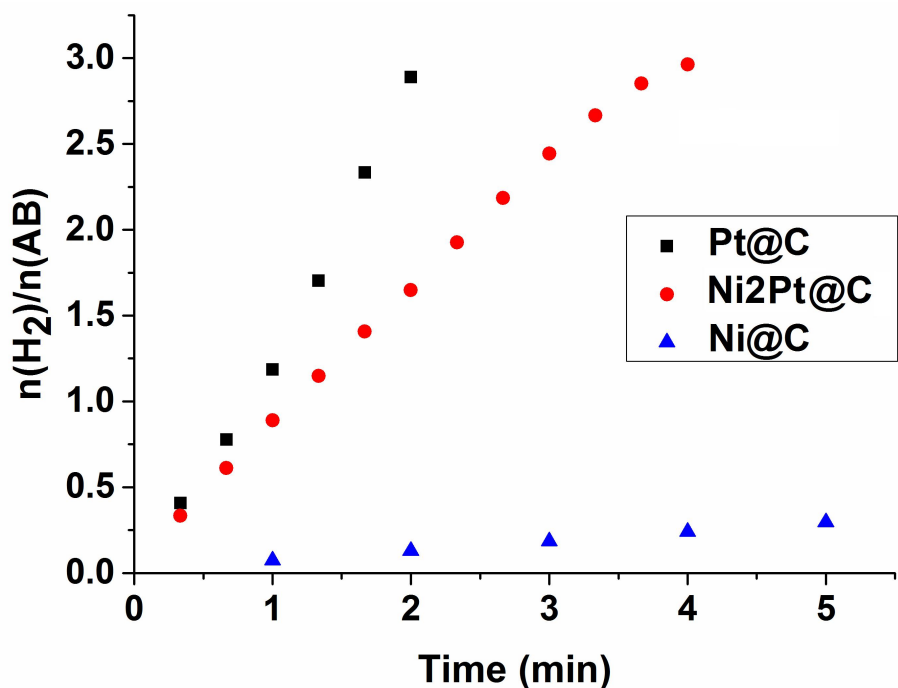


Figure 30. Hydrolysis of AB catalyzed by Pt@C (3.8 wt%), Ni₂Pt@C (3.2 wt%, atomic ratios: 3.9:1) and Ni@C (2.3 wt%) at (20 ± 0.5 °C) with 1 mol% nanocatalysts.

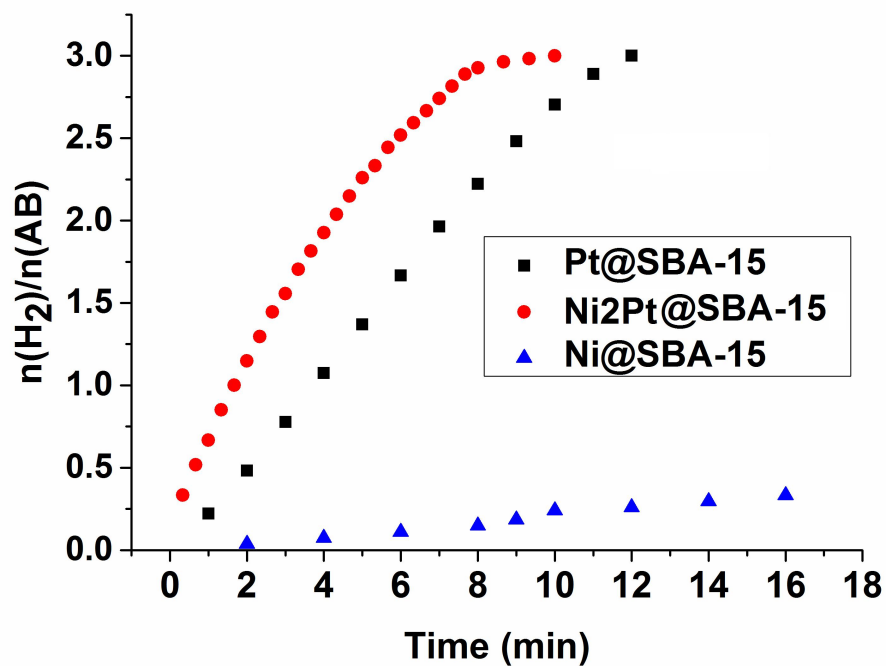


Figure 31. Hydrolysis of AB catalyzed by Pt@SBA-15 (2.3 wt%), Ni₂Pt@SBA-15 (2.0 wt%, atomic ratios: 3.9:1) and Ni@SBA-15 (1.4 wt%) at (20 ± 0.5 °C) with 1 mol% nanocatalysts.

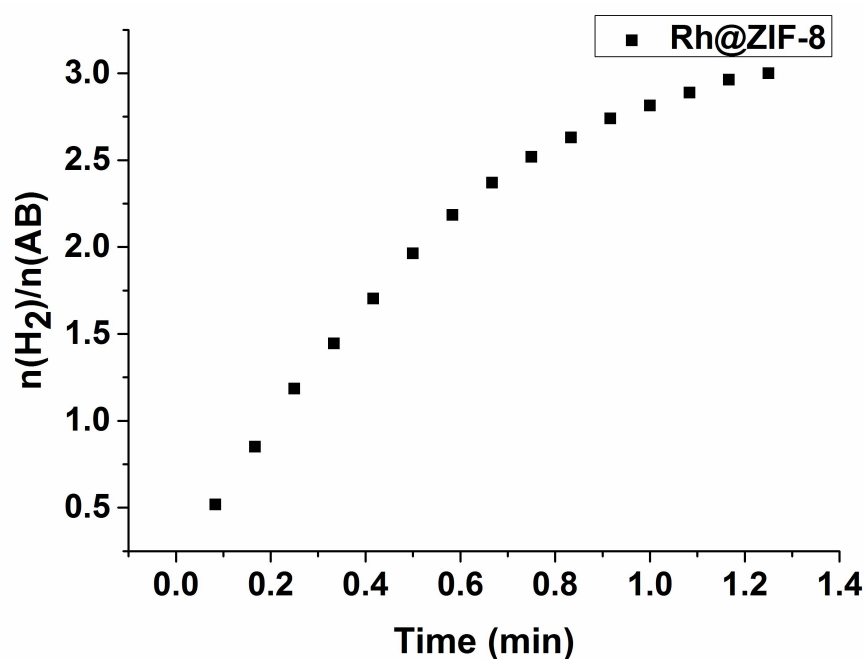


Figure 32. Hydrolysis of AB catalyzed by Rh@ZIF-8 at (20 ± 0.5 °C) with 1 mol% nanocatalysts.

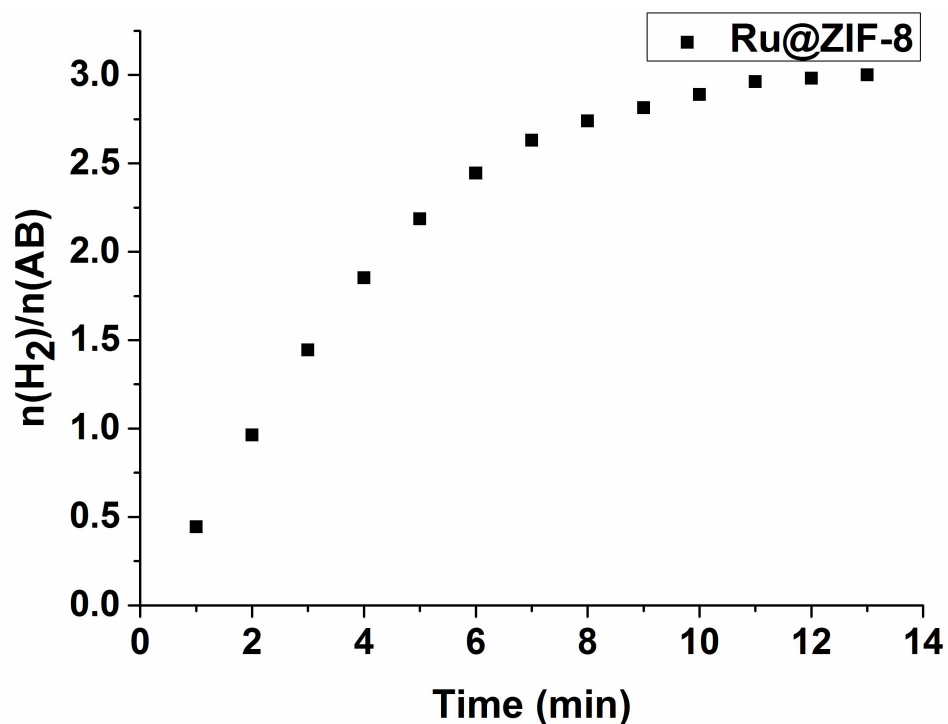


Figure 33. Hydrolysis of AB catalyzed by Ru@ZIF-8 at (20 ± 0.5 °C) with 1 mol% nanocatalyst.

Table 3. Comparison of recent literature results for various Pt-base catalysts concerning the hydrolysis of AB.

Catalyst	Temperature (°C)	Catalyst/AB (molar ratio)	TOF ($\text{mol}_{\text{H}_2} \cdot \text{mol}_{\text{catal.}}^{-1} \cdot \text{min}^{-1}$)	References
Ni₂Pt@ZIF-8	rt	0.01	600/ 2222.2 (based on Pt)	This work
PtCu	25	0.002 Pt	859 (based on Pt)	25
Pt _{0.08} Co _{0.92} / Ti ₃ C ₂ X ₂	25	-	727 (based on Pt)	26
Pt/CNT	30	0.0047	567	27
PtNi@PVP	rt	0.0078	511	28
PtAuNi	25	0.013	496	29
Pt/Ni SAA	rt	0.016 Pt	488/ 12000 (based on Pt)	30

Pt-Co@PG	rt	-	461.17 (based on Pt)	31
PtNi/NiO	30	0.0034	421.7/ 1240.3 (based on Pt)	32
Pt20/CNT	25	-	416.5	33
Pt@MIL-101	rt	0.0029	414	34
PtCo/PEI-GO	25	0.0027	377,83	35
PtRu@PVP	25	0.003	308	36
Pt-CoCu@SiO ₂	30	-	272.8 (based on Pt)	37
Pt/ γ -Al ₂ O ₃	30	0.018	261	38
Pt/CeO ₂	25	0.018	182	39
Pt@SiO ₂	25	0.0024	158.6	40
Pt@Co/mCN	35	8 mg	118.25	41
Pt/C	25	0.018	111	42
Ni _{0.33} @Pt _{0.67} /C	25	0.018	81	43
Co _{0.32} Pt _{0.68} /C	25	0.038	67	44
PtRu	25	0.001	59.6	45
40 wt % Pt/C	25	0.018	55.56	42
PtPd cNPs	25	0.002	50.02	46
Pt _{0.65} Ni _{0.35}	30	-	44.3	47
PtNi@SiO ₂	30	-	20.7	48
PtRu/C	25	0.03	8	49
PtNi@SiO ₂	30	0.036	5.54	50

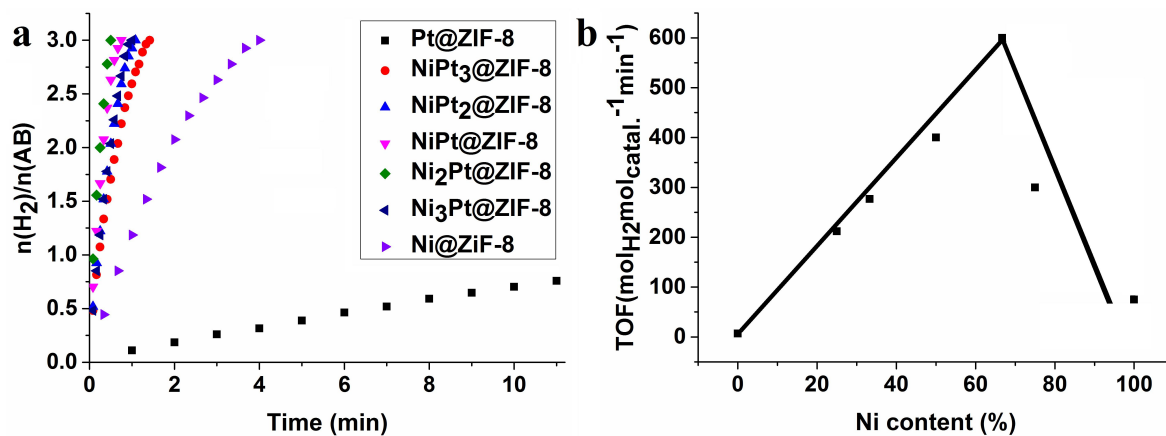


Figure 34. Hydrolysis of AB catalyzed by various NiPt@ZIF-8 in presence of 0.3 M NaOH at 20 ± 0.5 °C with 1 mol% nanocatalyst; (b) TOF variation obtained from various heterogeneous nanocatalysts in ZIF-8.

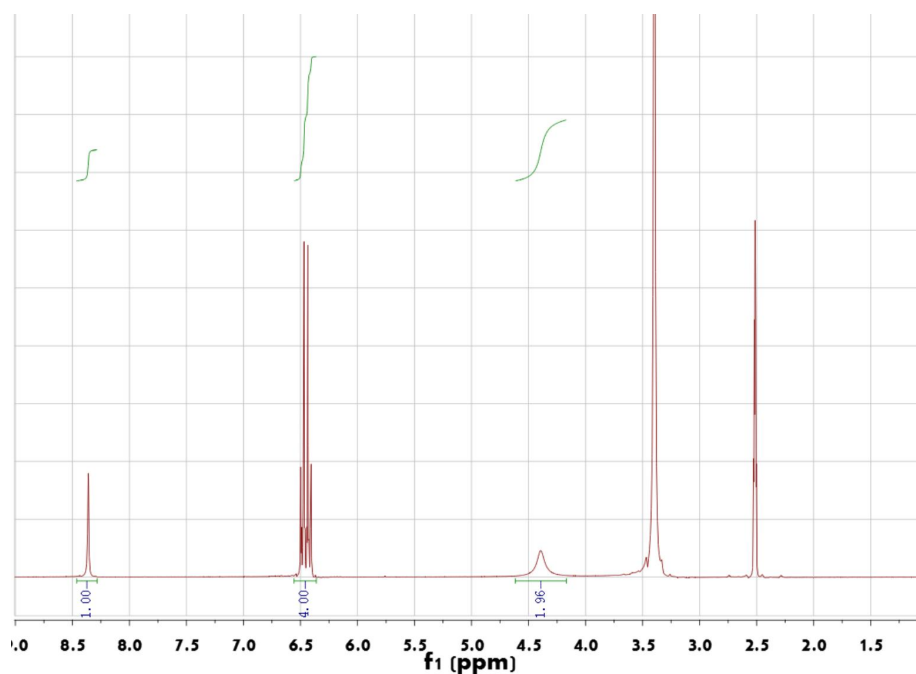


Figure 35. ¹H NMR spectrum of 4-aminophenol.

¹H NMR (300 MHz, DMSO) δ 8.36 (s, 1H), 6.56-6.36 (m, 4H), 4.39 (s, 2H).

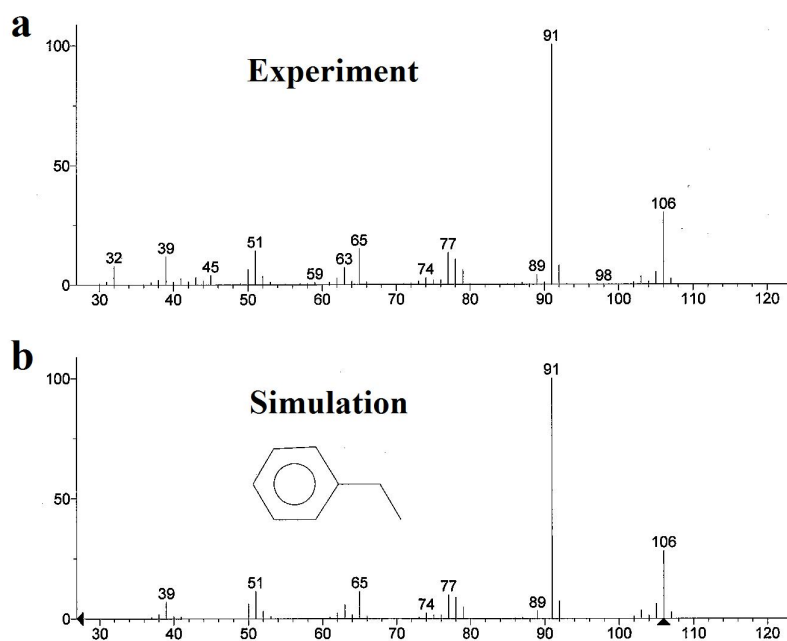


Figure 36. The GC-MS analysis of ethylbenzene.

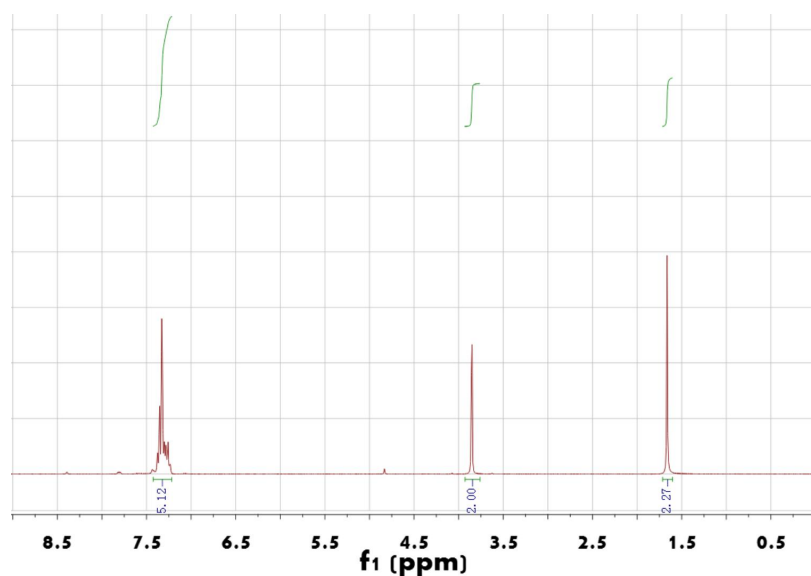


Figure 37. ^1H NMR spectrum of benzylamine.

^1H NMR (300 MHz, CDCl_3) δ 7.43-7.22 (m, 5H), 3.85 (s, 2H), 1.66 (s, 2H).

References

- (a) Schlapbach, L.; Zuttel, A. *Nature* **2001**, *414*, 353-358; (b) Grochala, W.; Edwards, P. P. *Chem. Rev.* **2004**, *104*, 1283-1315; (c) Marder, T. B. *Angew. Chem. Int. Ed.* **2007**, *46*, 8116-8118.
- (a) Stephens, F. H.; Pons, V.; Baker, R. T. *Dalton Trans.* **2007**, 2613-2626; (b) Hamilton, C. W.; Baker, R. T.; Staubitz, A.; Manners, I. *Chem. Soc. Rev.* **2009**, 38,

- 279-293; (c) Zhu, Q. L.; Xu, Q. *Energy Environ. Sci.* **2015**, *8*, 478-512.
- 3 Chen, W.; Li, D.; Wang, Z.; Qian, Q.; Sui, Z.; Duan, X.; Zhou, X.; Yeboah, I.; Chen, D. *AIChE J.* **2017**, *63*, 60-65.
- 4 Metin, Ö.; Mazumder, V.; Özkar, S.; Sun, S. *J. Am. Chem. Soc.* **2010**, *132*, 1468-1469.
- 5 (a) Yan, J. M.; Zhang, X. B.; Akita, T.; Haruta, M.; Xu, Q. *J. Am. Chem. Soc.* **2010**, *132*, 5326-5327; (b) Ge, Y.; Ye, W.; Shah, Z.H.; Lin, X.; Lu, R.; Zhang, S. *Acs Appl. Mater. Interfaces* **2017**, *9*, 3749-3756; (c) Fan, G.; Li, X.; Ma, Y.; Zhang, Y.; Wu, J.; Xu, B.; Sun, T.; Gao, D.; Bi, J. *New J. Chem.* **2017**, *41*, 2793-2799; (d) Cui, X.; Li, H.; Yu, G.; Yuan, M.; Yang, J.; Xu, D.; Hou, Y.; Dong, Z. *Int. J. Hydrogen Energy* **2017**, *42*, 27055-27065; (e) Karaca, T.; Sevim, M.; Metin, Ö. *ChemCatChem* **2017**, *9*, 4185-4190; (f) Zhan, W. -W.; Zhu, Q.-L.; Dang, S.; Liu, Z.; Kitta, M.; Suenaga, K.; Zheng, L. -S.; Xu, Q. *small* **2017**, *13*, 1603879; (g) Ke, D.; Wang, J.; Zhang, H.; Li, Y.; Zhang, L.; Zhao, X.; Han, S. *Int. J. Hydrogen Energy* **2017**, *42*, 26617-26625.
- 6 (a) Zhu, Q. L.; Li, J.; Xu, Q. *J. Am. Chem. Soc.* **2013**, *135*, 10210-10213; (b) Chen, W.; Ji, J.; Feng, X.; Duan, X.; Qian, G.; Li, P.; Zhou, X.; Chen D.; Yuan, K. *J. Am. Chem. Soc.* **2014**, *136*, 16736-16739; (c) Guo, L.-T.; Cai, Y.-Y.; Ge, J.-M.; Zhang, Y.-N.; Gong, L.-H.; Li, X.-H.; Wang, K.-X.; Ren, Q.-Z.; Su, J.; Chen, J. S. *ACS Catal.* **2015**, *5*, 388-392; (d) Chen, Y.-Z.; ; Yu, S.-H. Jiang, H.-L. *Small* **2015**, *11*, 71-76; (e) Zhan, W. -W.; Zhu, Q. -L.; Xu, Q. *ACS Catal.* **2016**, *6*, 6892-6905; (f) Wang, C.; Tuninetti, J.; Wang, Z.; Zhang, C.; Ciganda, R.; Salmon, L.; Moya, S.; Ruiz, J.; Astruc, D. *J. Am. Chem. Soc.* **2017**, *139*, 11610-11615; (g) Chen, W.; Ji, J.; Duan, X.; Qian, G.; Li, P.; Zhou, X.; Chen, D.; Yuan, W. *Chem. Commun.* **2014**, *50*, 2142-2144; (h) Du, C.; Ao, Q.; Cao, N.; Yang, L.; Lou, W.; Cheng, G. *Int. J. Hydrog. Energy* **2015**, *40*, 6180-6187; (i) Akbayrak, S.; Tonbul, Y.; Özkar, S.; *App. Catal. B* **2016**, *198*, 162-170;
- 7 (a) Johnson, H. C.; Weller, A. S. *Angew. Chem. Int. Ed.* **2015**, *54*, 10173-10177; (b) Wang, X. B.; Xie, L. H.; Huang, K.-W.; Lai, Z. P. *Chem. Commun.* **2015**, *51*, 7610-7613.
- 8 (a) Peng, C.-Y.; Kang, L.; Cao, S.; Chen, Y.; Lin, Z.-S; Fu, W.-F. *Angew. Chem. Int. Ed.* **2015**, *54*, 15725-15729. (b) Hou, C. -C.; Li, Q.; Wang, C. -J.; Peng, C. -Y.; Chen, Q. -Q.; Ye, H. -F.; Fu, W. -F.; Che, C. -M.; López, N.; Chen, Y. *Energy Environ. Sci.* **2017**, *10*, 1770-1776.
- 9 Lu, Z.; Schweighauser, L.; Hausmann, H.; Wegner, H. A. *Angew. Chem. Int. Ed.* **2015**, *54*, 15556-15559.
- 10 (a) Lee, J. Y.; Farha, O. K.; Roberts, J.; Scheidt, K. A.; Nguyen, S. T.; Hupp, J. T. *Chem. Soc. Rev.* **2009**, *38*, 1450-1459; (b) Farrusseng, D.; Aguado, S.; Pinel, C. *Angew. Chem. Int. Ed.* **2009**, *48*, 7502-7513; (c) Rakap, M.; Özkar, S. *Int. J.*

- Hydrog. Energy* **2010**, *35*, 3341-3346; (d) Dhakshinamoorthy, A.; Garcia, H. *Chem. Soc. Rev.* **2012**, *41*, 5262-5284; (e) Liu, J.; Chen, L.; Cui, H.; Zhang, J.; Zhang, L.; Su, C. -Y. *Chem. Soc. Rev.* **2014**, *43*, 6011-6061; (f) Chughtai, A. H.; Ahmad, N.; Younus, H. A.; Laypkov, A.; Verpoort, F. *Chem. Soc. Rev.* **2015**, *44*, 6804-6849; (g) Zeng, L.; Guo, X.; He, C.; Duan, C. *ACS Catal.* **2016**, *6*, 7935-7947.
- 11 (a) Aijaz, A.; Karkamkar, A.; Choi, Y. J.; Tsumori, N.; Rönnebro, E.; Autrey, T.; Shioyama, H.; Xu, Q. *J. Am. Chem. Soc.* **2012**, *134*, 13926-13929; (b) Lu, G.; Li, S.; Guo, Z.; Farha, O. K.; Hauser, B. G.; Qi, X.; Wang, Y.; Wang, X.; Han, S.; Liu, X. *Nat. Chem.* **2012**, *4*, 310-316; (c) Xia, B. Q.; Liu, C.; Wu, H.; Luo, W.; Cheng, G. Z. *Int. J. Hydrogen Energy* **2015**, *40*, 16391-16397; (d) Yin, P.; Yao, T.; Wu, Y.; Zheng, L.; Lin, Y.; Liu, W.; Ju, H.; Zhu, J.; Hong, X.; Deng, Z.; Zhou, G.; Wei, S.; Li, Y. *Angew. Chem. Int. Ed.* **2016**, *55*, 10800-10805; (e) Cao, X.; Tan, C.; Sindoro, M.; Zhang, H. *Chem. Soc. Rev.* **2017**, *46*, 2660-2677; (f) Wang, X.; Chen, W.; Zhang, L.; Yao, T.; Liu, W.; Lin, Y.; Ju, H.; Dong, J.; Zheng, L.; Yan, W.; Zheng, X.; Li, Z.; Wang, X.; Yang, J.; He, D.; Wang, Y.; Deng, Z.; Wu, Y.; Li, Y. *J. Am. Chem. Soc.* **2017**, *139*, 9419-9422.
- 12 (a) Lu, G.; Li, S.; Guo, Z.; Farha, O. K.; Hauser, B. G.; Qi, X.; Wang, Y.; Wang, X.; Han, S.; Liu, X.; DuChene, J. S.; Zhang, H.; Zhang, Q.; Chen, X.; Ma, J.; Loo, S. C. J.; Wei, W. D.; Yang, Y.; Hupp, J. T.; Huo, F. *Nat. Chem.* **2012**, *4*, 310-316; (b) Rungtaweivoranit, B.; Baek, J.; Araujo, J. R.; Archanjo, B. S.; Choi, K. M.; Yaghi, O. M.; Somorjai, G. A. *Nano Lett.* **2016**, *16*, 7645-7649; (c) Zhao, M.; Yuan, K.; Wang, Y.; Li, G.; Guo, J.; Gu, L.; Hu, W.; Zhao, H.; Tang, Z. *Nature* **2016**, *539*, 76-80; (d) Choi, K. M.; Kim, D.; Rungtaweivoranit, B.; Trickett, C. A.; Barmanbek, J. T. D.; Alshammari, A. S.; Yang, P.; Yaghi, O. M. *J. Am. Chem. Soc.* **2017**, *139*, 356-362.
- 13 Park, K. S.; Ni, Z.; Côté, A. P.; Choi, J. Y.; Huang, R.; Uribe-Romo, F. J.; Chae, H. K.; O’Keeffe, M.; Yaghi, O. M. *PNAS* **2006**, *13*, 10186-10191.
- 14 (a) Mahyari, M.; Shaabani, A. *J. Mater. Chem. A* **2014**, *2*, 16652-16659; (b) Bulut, A.; Yurderi, M.; Ertas, I. E.; Celebi, M.; Kaya, M.; Zahmakiran, M. *Appl. Catal., B* **2016**, *180*, 121-129; (c) Tang, C.; Xie, L.; Wang, K.; Du, G.; Asiri, A. M.; Luo, Y.; Sun, X. *J. Mater. Chem. A* **2016**, *4*, 12407-12410; (d) Feng, K.; Zhong, J.; Zhao, B.; Zhang, H.; Xu, L.; Sun, X.; Lee, S.-T. *Angew. Chem. Int. Ed.* **2016**, *55*, 11950-11954; (e) Li, Z.; He, T.; Liu, L.; Chen, W.; Zhang, M.; Wu, G.; Chen, P. *Chem. Sci.* **2017**, *8*, 781-788; (f) Yu, C.; Fu, J.; Muzzio, M.; Shen, T.; Su, D.; Zhu, J.; Sun, S. *Chem. Mater.* **2017**, *29*, 1413-1418; (g) Zhou, L.; Meng, J.; Li, P.; Tao, Z.; Mai, L.; Chen, J. *Mater. Horiz.* **2017**, *4*, 268-273; (h) Yin, H.; Kuwahara, Y.; Mori, K.; Cheng, H.; Wen, M.; Yamashita, H. *J. Mater. Chem. A* **2017**, *5*, 8946-8953; (i) Liu, P.; Gu, X.; Kang, K.; Zhang, H.; Cheng, J.; Su, H. *ACS Appl. Mater. Interfaces* **2017**, *9*, 10759-10767; (j) Zhang, H.; Gu, X.; Liu, P.; Song, J.;

- Cheng, J.; Su, H. *J. Mater. Chem. A* **2017**, *5*, 2288-2296. (k) Wang, D.; Astruc, D. *Chem. Soc. Rev.* **2017**, *46*, 816-854.
- 15 (a) Li, X.; Zeng, C.; Fan, G. *Int. J. Hydrogen Energy* **2015**, *40*, 9217-9224; (b) Li, X.; Zeng, C.; Fan, G. *Int. J. Hydrogen Energy* **2015**, *40*, 3883-3891; (c) Mori, K.; Miyawaki, K.; Yamashita, H. *ACS Catal.* **2016**, *6*, 3128-3135.
- 16 (a) Hansgen, D.A.; Vlachos, D. G.; Chen, J. G.; *Nat. Chem.* **2010**, *2*, 484-489; (b) Chen, W.; Yu, R.; Li, L.; Wang, A.; Peng, Q.; Li, Y. *Angew. Chem. Int. Ed.* **2010**, *49*, 2917-2921; (c) Snyder, J.; McCue, I.; Livi, K.; Erlebacher, J. *J. Am. Chem. Soc.* **2012**, *134*, 8633-8645; (d) Yu, W.; D Porosoff, M. G.; Chen, J. *Chem. Rev.* **2012**, *112*, 5780-5817; (e) Saleem, F.; Zhang, Z.; Xu, B; Xu, X.; He, P.; Wang, X. *J. Am. Chem. Soc.* **2013**, *135*, 18304-18307; (f) Yurderi, M.; Bulut, A.; Zahmakiran, M.; Gulcan, M.; Özkar, S. *Appl. Catal. B* **2014**, *160*, 534-541.
- 17 (a) Keaton, R. J.; Blacquiere, J. M.; Baker, R. T. *J. Am. Chem. Soc.* **2007**, *129*, 1844-1845; (b) Bhattacharya, P.; Krause, J. A.; Guan, H. *J. Am. Chem. Soc.* **2014**, *136*, 11153-11161; (c) Buss, J. A.; Edouard, G. A.; Cheng, C.; Shi, J.; Agapic, T.; *J. Am. Chem. Soc.* **2014**, *136*, 11272-11275.
- 18 Fu, Z. C.; Xu, Y.; Chan, S. L.; Wang, W. W.; Li, F.; Liang, F.; Chen, Y.; Lin, Z. S.; Fu, W. F.; Che, C. M. *Chem. Commun.* **2013**, *53*, 705-708;
- 19 Yao, Q.; Yang, K.; Hong, X.; Chen, X.; Lu, Z. H. *Catal. Sci. Technol.* **2018**, *8*, 870-877.
- 20 Xu, Q.; Chandra, M. *J. Power Sources.* **2006**, *163*, 364-370.
- 21 Kalidendi, S. B.; Sanyal, U.; Jagirdar, B. R. *Phys. Chem. Chem. Phys.* **2008**, *10*, 5870-5874.
- 22 Ma, H.; Na, C. *ACS Catal.* **2015**, *5*, 1726-1735.
- 23 (a) Li, Z.; He, T.; Liu, L.; Chen, W.; Zhang, M.; Wu, G.; Chen P. *Chem. Sci.* **2017**, *8*, 781-788; (b) Li, Z.; He, T.; Matsumura, D.; Miao, S.; Wu, A.; Liu, L.; Wu, G.; Chen, P. *ACS Catal.* **2017**, *7*, 6762-6769.
- 24 (a) Stanislaus, A.; Cooper, B. H. *Catal. Rev.-Sci. ENG.* **1994**, *36*, 75-123; (b) Ji, P.; Manna, K.; Lin, Z.; Feng, X.; Urban, A.; Song, Y.; Lin W. *J. Am. Chem. Soc.* **2017**, *139*, 7004-7011.
- 25 Karaca, T.; Sevim, M.; Metin, Ö. *ChemCatChem* **2017**, *9*, 4185-4190.
- 26 Fan, G.; Li, X.; Ma, Y.; Zhang, Y.; Wu, J.; Xu, B.; Sun, T.; Gao, D.; Bi, J. *New J. Chem.*, **2017**, *41*, 2793-2799.
- 27 Chen, W.; Ji, J.; Duan, X.; Qian, G.; Li, P.; Zhou, X.; Chen, D.; Yuan, W. *Chem. Commun.* **2014**, *50*, 2142-2144.
- 28 Wang, S.; Zhang, D.; Ma, Y.; Zhang, H.; Gao, J.; Nie, Y.; Sun, X. *ACS Appl. Mater. Interfaces* **2014**, *6*, 12429-12435.
- 29 Kang, J.-X.; Chen, T.-W.; Zhang, D.-F.; Guo, L. *Nano Energy* **2016**, *23*, 145-152.
- 30 Li, Z.; He, T.; Matsumura, D.; Miao, S. Wu, A.; Liu, L.; Wu, G.; Chen, P. *ACS*

- Catal.* **2017**, *7*, 6762-6769.
- 31 Ke, D.; Wang, J.; Zhang, H.; Li, Y.; Zhang, L.; Zhao, X.; Han, S. *Int. J. Hydrogen Energy* **2017**, *42*, 26617-26625.
- 32 Ge, Y.; Ye, W.; Shah, Z.H.; Lin, X.; Lu, R.; Zhang, S. *Acs Appl. Mater. Interfaces* **2017**, *9*, 3749-3756.
- 33 Zhang, J.; Chen, C.; Chen, S.; Hu, Q.; Gao, Z.; Li, Y.; Qin, Y. *Catal. Sci. Technol.* **2017**, *7*, 322-329
- 34 Aijaz, A.; Karkamkar, A.; Choi, Y. J.; Tsumori, N.; Roennebro, E.; Autrey, T.; Shioyama, H.; Xu, Q. *J. Am. Chem. Soc.* **2012**, *134*, 13926-13929.
- 35 Li, M.; Hu, J.; Chen, Z.; Lu, H. *RSC Adv.* **2014**, *4*, 41152-41158.
- 36 Rakap, M. *Appl. Catal., A* **2014**, *478*, 15-20.
- 37 Ge, Y.; Shah, Z. H.; Lin, X. -J.; Lu, R.; Liao, Z.; Zhang, S. *ACS Sustainable Chem. Eng.* **2017**, *5*, 1675-1684.
- 38 Chandra, M.; Xu, Q. *J. Power Sources*, **2007**, *168*, 135-142.
- 39 Wang, X.; Liu, D. P.; Song, S. Y.; Zhang, H. J. *Chem. Commun.*, **2012**, *48*, 10207-10209.
- 40 Hu, Y.; Wang, Y.; Lu, Z.-H.; Chen, X.; Xiong, L. *Appl. Surf. Sci.* **2015**, *341*, 185-189.
- 41 Cui, X.; Li, H.; Yu, G.; Yuan, M.; Yang, J.; Xu, D.; Hou, Y.; Dong, Z. *Int. J. Hydrogen Energy* **2017**, *42*, 27055-27065.
- 42 Xu, Q.; Chandra, M. *J. Alloys Compd.* **2007**, *446-447*, 729-732.
- 43 Yang, X. J.; Cheng, F. Y.; Liang, J. Z.; Tao, L.; Chen, J. *Int. J. Hydrogen Energy* **2011**, *36*, 1984-1990.
- 44 Yang, X. J.; Cheng, F. Y.; Tao, Z. L.; Chen, J. *J. Power Sources* **2011**, *196*, 2785-2789.
- 45 Zhou, Q.; Xu, C. *Chem. - Asian J.* **2016**, *11*, 705-712.
- 46 Amali, A. J.; Aranishi, K.; Uchida, T.; Xu, Q. *Part. Part. Syst. Charact.* **2013**, *30*, 888-892.
- 47 Yang, X.; Cheng, F.; Liang, J.; Tao, Z.; Chen, J. *Int. J. Hydrogen Energy* **2009**, *34*, 8785-8791.
- 48 Qi, X.; Li, X.; Chen, B.; Lu, H.; Wang, L.; He, G. *ACS Appl. Mater. Interfaces* **2016**, *8*, 1922-1928.
- 49 Yao, C. F.; Zhuang, L.; Cao, Y. L.; Ai, X. P.; Yang, H. X. *Int. J. Hydrogen Energy*, **2008**, *33*, 2462-2467.
- 50 Qi, X.; Li, X.; Chen, B.; Lu, H.; Wang, L.; He, G. *ACS Appl. Mater. Interfaces* **2016**, *8*, 1922-1928.

Conclusion and Perspectives

In this thesis, our investigations have concerned the design and catalytic applications of late transition-metal nanomaterials, specifically focusing on three aspects:

- (i) The synthesis, purification and catalytic application of TMNPs reduction by sodium-naphthalenide and their SBA-15 support heterogeneous catalysts.
- (ii) The design, synthesis and catalytic properties of metallocenium stabilized homogeneous TMNPs catalyst or nanoclusters.
- (iii) The synthesis, optimization and catalytic application of ZIF-8 supported heterogeneous alloy catalysts.

The investigation of a new PEG stabilized CuNP reduction by sodium-naphthalenide for “CuAAC” reactions indicates that the purified aqueous catalyst Cu(0)NP-PEG by simple salting-out process performs better than the crude catalyst Cu(0)NP-PEG-1. The first extraction helps purifying the inorganic salts in the water phase, and the second extraction removes the organic by-product in the organic phase on the CuNPs surface. This results in exposing more catalytic active sites for “click” substrates. A similar purification also improves the catalytic efficiencies for 4-NP reduction catalyzed by very small Au, Pd, Ag, Cu NPs and C-C coupling reactions with Pd and Cu catalysts. Furthermore, the fact air boosts the “CuAAC” reaction indicates that Cu(I) NP is the real “CuAAC” catalyst. Cu(0) and Cu(I) (the later being obtained by aerobic oxidation from Cu(0)) NPs both are active in the “CuAAC” reaction, but this study is more inclined to Cu(I) resulting from aerobic oxidation. The achieved Cu and Pd NPs are heterogenized on SBA-15 for efficient recycling without metal leaching. They are efficiently applied to the synthesis of some compounds of biomedical interest. The SBA-15 supported heterogeneous catalysts perform better than the homogeneous ones, since there is synergy between the NPs and SBA-15 support. These methods are also potentially extendable to other types of catalysis in the future. The investigation of PVP stabilized Au and Pd NPs reduction by several neutral electron- and hydride- rich late transition metal organometallics indicates that the nature of the reductant has more influence on the NP size in the case of AuNPs than on that of PdNPs. The hydride reservoir complexes are shown here to form AuNPs and PdNPs. Better catalytic results are obtained with hydride reservoirs than using the electron-reservoir complexes. A possible explanation is that hydride reservoirs transfer hydrides to transition metal cations followed by fast reductive elimination to metal (0), and further hydride transfer renders the NP surface very reactive. AuNPs and PdNPs obtained from [CoCp(η^4 -C₅H₆)] show the best catalytic activity for both 4-NP reduction and Suzuki reaction, but the bulky reductants give less satisfactory catalytic efficiencies because of steric problems around the NP core. The presence of the cationic sandwich complex that surrounds the NP cores is responsible for a higher catalytic efficiency than that of NPs protected by the PVP ligand only. Then organometallic sandwich complexes surrounding the NPs are not catalysts, but promoters.

To further study, commercial 19 electron-reservoir cobaltocene is used to reduce Cu and 3 different Ag salts to yield small and monodispersed Cu and Ag NPs without any

ligand or support. In this case the NPs are electrostatically protected by the cobalticinium salt network. The remarkable variation of the surface plasmon band wavelength and kinetics of the AgNP-catalyzed 4-nitrophenol reduction as a function of the nature of the counter anion of the precursor Ag(I) salt shows that the counter anions are weakly bonded to the NP surface, and the sandwich cations are not bound to the surface, which leaves the NP surface free for substrate activity. However, this stabilization is strong enough to prevent NP oxidation by air, which is corroborated by the zero-value-state in the CuNP XPS result. A variety of CuAAC reactions have been shown to proceed very efficiently with the water-soluble CuNP catalyst synthesized in this way including CuAAC synthesis of biologically relevant compounds. These results contribute to stimulate the design and optimization of transition metal NPs for given catalytic property with active particle surface.

In addition, even if the sterically bulky sandwich complexes prevents optimized catalytic efficiency of the NPs, they are advantageous to protect the normally unstable gold nanoclusters. In this investigation, we find that the $\text{Au}_{25}(\text{SR})_{18}^-$ nanocluster with 18-electron sandwich complexes as counter cations are more stable than the well-known $\text{Au}_{25}(\text{SR})_{18}\text{-TOA}^+$ salt. The aerobic stability studies show that the best protection against the kinetic instability in air is achieved by permethylated Cp* rings near the nanocluster surface. The chemistry described here is a significant step forward in order to design nano-composites for applications.

Finally, the systematic introduction of a co-reduction method was used to synthesize a series of ligand-free ZIF-8 supported bimetallic NiPt alloy NPs with tunable compositions and full characterizations. These catalysts are able to completely release 3 equivalent H_2 from ammonia borane hydrolysis. Concerning the compositions of the alloy catalysts, $\text{Ni}_2\text{Pt@ZIF-8}$ shows the best catalytic efficiency among the alloys and the alloy NPs are much more active than the Pt and Ni NPs @ZIF-8 alone. There is a very remarkable sharp volcano-type positive synergistic effect between Pt and Ni metals. $\text{Ni}_2\text{Pt@ZIF-8}$ give much better performances compared to the other bimetallic NPs such as $\text{Ni}_2\text{Rh@ZIF-8}$, $\text{Ni}_2\text{Ru@ZIF-8}$, $\text{Co}_2\text{Pt@ZIF-8}$, $\text{Cu}_2\text{Pt@ZIF-8}$. This indicates that there is a high selectivity in Ni_2Pt alloy on ZIF-8 support. The ZIF-8 support also appears selective for the Ni_2Pt alloy compared to the other common supports such as GO, C, SBA-15. Kinetic studies show that the ammonia borane hydrolysis reaction is zero order in ammonia borane and first order in NP catalyst, and a large kinetic isotope effect of 4.95 upon replacing H_2O by D_2O indicates that cleavage of the O-H bond of water appears to be the rate-determining step. NaOH promotes the catalytic rate with the alloy catalyst, but it decreases that of the reaction catalyzed by Pt@ZIF-8 that is already an electron rich metal. We propose that the OH^- anion coordinates to the NP surface and enriches the surface electron density, which is in favor of the crucial oxidative addition of a water O-H bond. However, the electron density of the Pt NP surface is rich enough, so that the coordination of the OH^- anion inhibits further substrate activation, causing a decrease of catalyst activity. At last, 3 tandem hydrogenation reactions are conducted with H_2 generated from AB with the catalyst $\text{Ni}_2\text{Pt@ZIF-8}$ using the same catalyst $\text{Ni}_2\text{Pt@ZIF-8}$ in order to show that this

catalyst is very efficient with multiple applications. This strategy might be used for other catalyst designs towards green energy processes.

In summary, our thesis work has led to advances in the development of current knowledge of catalytic applications of late transition-metal nanomaterials. The stabilization of homogeneous transition metal NPs by metallocenium cations provided by (19e) organometallic electron reservoirs or hydride reservoirs is a new concept that appears very efficient in a variety of catalytic reactions. Through the PhD research we have reached a good understanding of the parameters that guide the stabilization of NPs and their catalytic efficiency (and the balance between their conflicting effects) Nanocatalysis is a rapidly expanding science.¹ Its development involves challenges of the 21st century related to health (nanomedicine), energy (hydrogen, the molecule of the century) and nanomaterials towards light storage and conversion. New catalysts should emerge from the synergy between molecular science with new ligands² and well-defined solids such as MOFs^{3,4} and COFs⁵. MOF materials should have a bright future in the catalytic synthesis of some important and valuable organic molecules because on one hand, they can be pre-designed on a rational basis according to a specific requirement of catalytic reaction, or deliberately tailored and modified to suit a specific catalytic purpose; on the other hand, the well-defined crystal structure of MOFs on the atomic level allows the explicit assessment of structure-activity relationships and application of the catalytic mechanism to a demanding reaction, most importantly, the uniform catalytic sites arrangement and their isolation in three dimensionality make them readily accessible by the substrates, which offers great advantages in light of the catalytic efficiency and economy in contrast to the bulky heterogeneous catalysts of which only the active sites on the solid surface are useful in catalytic reactions.

With the in-depth study of single atom catalysts (SACs).⁶ these catalysts have arguably become the most active new frontier in heterogeneous catalysis. SACs have well-defined active centers, such that unique opportunities exist for the rational design of new catalysts with high activities, selectivities and stabilities. Metal-organic frameworks (MOFs) have demonstrated their great potential for creating SACs in the last 2 years. The SACs can be prepared by converting atomically dispersed metal nodes in situ from MOFs,⁷ and pyrolysis strategy from MOFs packing metal ions.⁸ Besides, SACs can be directly transformed from bulk metals using MOFs as templates.⁹

Nanoclusters (NCs) catalysts are the bridge to understand the relationship between catalytic structure and property at atomic and molecular level, because of the precise atomic structure of the NCs.¹⁰ However the synthesis of MOF supported NC catalysts are still a challenge and are rare in the literature.^{11,12} It would be of interest to synthesize and compare the properties of NCs catalysts inside and outside the MOFs. As a promising heterogeneous catalyst, Au atom surface is essential for reactants in Au NCs catalysis, which requires the removal of the thiolate ligands to expose more active sites and reduce steric hindrance. Thus pyrolysis of MOF encapsulated Au NCs is a facile strategy to remove the thiolate ligand without size increase, and the nitrogen-doped carbon (NC) materials derived from MOFs has attracted particular

research interest. A variety of heteroatom-doped carbon based composites have been reported to date.¹³ Because a heteroatom is more electronegative than a carbon atom, for example the NC materials can generate defect sites and enhance the electrical conductivity. Interestingly, more and more trends indicate that small NCs catalysis perform better than either NPs or SACs.¹⁴ Relative to atomically precise NCs, the unknown surface of NP catalysts is detrimental to study the catalytic mechanism and there can be no bimetallic synergistic effect in the SACs. Hence, NCs catalysts without ligands might be prevalent candidates for industrial catalysis.

The development of multifunctional MOFs for synergistic catalytic application is one of the fastest growing research fields today,⁴ including water-splitting, CO₂ reduction, and organic synthesis and/or degradation. However, MOF systems require sacrificial agents and/or noble metals such as Pt and Rh, making them expensive and environmentally unfriendly. Developing cheap materials such as earth-abundant metal, Fe, Co, Ni, Cu, to avoid the use of noble metals is one way to address this problem. Significantly, stability is a very important issue in heterogeneous catalysis; it is related to the catalyst lifetime and recyclability. Compared with inorganic porous materials, MOFs have relatively low thermal and chemical stability. However, this limitation could be overcome by developing more robust MOFs, such as Zr-based MOFs. The transformation of MOFs to porous stable carbons and/or other related nanostructured functional materials for catalysis is one possible strategy for circumventing this problem.

References

- 1 Thematic *Chem. Rev.* issue “Nanoparticles and Catalysis”, Guest Ed. D. Astruc, January **2020** (see articles already online).
- 2 Liu, X.; Manzur, C.; Novoa, N.; Seledon, S.; Carrillo, D.; Hamon, J.-R.; Multidentate unsymmetrically-substituted Schiff bases and their metal complexes: Synthesis, functional materials properties, and applications to catalysis. *Coord. Chem. Rev.* **2018**, *357*, 144-172.
- 3 Jagadeesh, R. V.; Murugesan, K.; Alshammari, A. S.; Neumann, H.; Pohl, M.-M.; Radnik, J.; Beller, M. MOF-derived cobalt nanoparticles catalyze a general synthesis of amines. *Science* **2017**, *358*, 326-332.
- 4 Wang, Q.; Astruc, D. State of the Art and Prospects in Metal-Organic Framework (MOF)-Based and MOF-Derived Nanocatalysis. *Chem. Rev.* DOI: 10.1021/acs.chemrev.9b00223.
- 5 Diercks, C. S.; Liu, Y.; Cordova, K. E.; Yaghi, O. M. The role of reticular chemistry in the design of CO₂ reduction catalysts. *Nat. Mater.* **2018**, *17*, 301-307.
- 6 Chen, Y.; Ji, S.; Chen, C.; Peng, Q.; Wang, D.; Li, Y. Single-Atom Catalysts: Synthetic Strategies and Electrochemical Applications. *Joule* **2018**, *2*, 1242-1264.
- 7 Yin, P.; Yao, T.; Wu, Y.; Zheng, L.; Lin, Y.; Liu, W.; Ju, H.; Zhu, J.; Hong, X.; Deng, Z.; Zhou, G.; Wei, S.; Li, Y. Single Cobalt Atoms with Precise N-Coordination as Superior Oxygen Reduction Reaction Catalysts. *Angew. Chem., Int. Ed.* **2016**, *55*, 10800-108005.

- 8 Wang, X.; Chen, W.; Zhang, L.; Yao, T.; Liu, W.; Lin, Y.; Ju, H.; Dong, J.; Zheng, L.; Yan, W.; Zheng, X.; Li, Z.; Wang, X.; Yang, J.; He, D.; Wang, Y.; Deng, Z.; Wu, Y.; Li, Y. Uncoordinated Amine Groups of Metal–Organic Frameworks to Anchor Single Ru Sites as Chemoselective Catalysts toward the Hydrogenation of Quinoline. *J. Am. Chem. Soc.* **2017**, *139*, 9419-9422
- 9 Qu, Y.; Li, Z.; Chen, W.; Lin, Y.; Yuan, T.; Yang, Z.; Zhao, C.; Wang, J.; Zhao, C.; Wang, X.; Zhou, F.; Zhuang, Z.; Wu, Y. Direct transformation of bulk copper into copper single sites via emitting and trapping of atoms. *Nature Catalysis* **2018**, *1*, 781-786.
- 10 Liu, L.; Song, Y.; Chong, H.; Yang, S.; Xiang, J.; Jin, S.; Kang, X.; Zhang, J.; Yu, H.; Zhu, M. Size-confined growth of atom-precise nanoclusters in metal-organic frameworks and their catalytic applications. *Nanoscale* **2016**, *8*, 1407-1412.
- 11 Du, Y.; Sheng, H.; Astruc, D.; Zhu, M. Atomically Precise Noble Metal Nanoclusters as Efficient Catalysts: A Bridge between Structure and Properties. *Chem. Rev.* DOI: 10.1021/acs.chemrev.8b00726.
- 12 Sun, L.; Yun, Y.; Sheng, H.; Du, Y.; Ding, Y.; Wu, P.; Li, P.; Zhu, M. Rational encapsulation of atomically precise nanoclusters into metal–organic frameworks by electrostatic attraction for CO₂ conversion. *J. Mater. Chem. A*, **2018**, *6*, 15371-15376.
- 13 Ren, Q.; Wang, H.; Lu, X. -F.; Tong, Y. -X.; Li, G. -R. Recent Progress on MOF-Derived Heteroatom-Doped Carbon-Based Electrocatalysts for Oxygen Reduction Reaction. *Adv. Sci.* **2018**, *5*, 1700515.
- 14 Ji, S.; Chen, Y.; Fu, Q.; Chen, Y.; Dong, J.; Chen, W.; Li, Z.; Wang, Y.; Gu, L.; He, W.; Chen, C.; Peng, Q.; Huang, Y.; Duan, X.; Wang, D.; Draxl, C.; Li, Y. Confined Pyrolysis within Metal-Organic Frameworks To Form Uniform Ru₃ Clusters for Efficient Oxidation of Alcohols. *J. Am. Chem. Soc.* **2017**, *139*, 9795-9798.

Publications

- [1] **Fangyu Fu**, Anthony Dedieu, Wenjuan Wang, Tao Chen, Yongbo Song, Eric Fouquet, Jean-René Hamon, Manzhou Zhu,* and Didier Astruc*. Stabilization of a New Nanocomposite Family by Reduction of Gold Nanoclusters with Electron-reservoir Complexes. *Chem. Commun.*, **2019**, 55, 10277-10280. (IF: 6.164)
- [2] **Fangyu Fu**, Changlong Wang, Qi Wang, Angel M. Martinez-Villacorta, Ane Escobar, Hanbao Chong, Xin Wang, Sergio Moya, Lionel Salmon, Eric Fouquet, Jaime Ruiz and Didier Astruc*. Highly Selective and Sharp Volcano-type Synergistic Ni₂Pt@ZIF-8- Catalyzed Hydrogen Evolution from Ammonia Borane Hydrolysis. *J. Am. Chem. Soc.*, **2018**, 140, 10034-10042. (IF: 14.357)
- [3] **Fangyu Fu**, Roberto Ciganda*, Qi Wang, Alexis Tabey, Changlong Wang, Ane Escobar, Angel M. Martinez-Villacorta, Ricardo Hernández, Sergio Moya, Eric Fouquet, Jaime Ruiz and Didier Astruc*. Cobaltocene Reduction of Cu and Ag Salts and Catalytic Behavior of the Nanoparticles Formed. *ACS Catal.*, **2018**, 8, 8100-8106. (IF: 11.384)
- [4] **Fangyu Fu**, Qi Wang, Roberto. Ciganda, Angel M. Martinez-Villacorta, Ane Escobar, Sergio Moya, Eric Fouquet, Jaime Ruiz and Didier Astruc*. Electron- and Hydride- Reservoir Organometallics as Precursors of Catalytically Efficient Transition Metal Nanoparticles in Water. *Chem. Eur. J.*, **2018**, 24, 6645-6653. (IF: 5.16)
- [5] **Fangyu Fu**, Angel Martinez, Changlong Wang, Roberto Ciganda, Luis Yate, Ane Escobar, Sergio Moya, Eric Fouquet, Jaime Ruiz and Didier Astruc*. Exposure to air boosts CuAAC reactions catalyzed by PEG-stabilized Cu nanoparticles. *Chem. Commun.*, **2017**, 53, 5384-5387. (IF: 6.29)
- [6] **Fangyu Fu**, Angel M. Martinez-Villacorta, Ane Escobar, Joseba Irigoyen, Sergio Moya, Eric Fouquet, Jaime Ruiz and Didier Astruc*. Synthesis of late transition-metal nanoparticles by Na naphthalenide reduction of salts and their catalytic efficiency. *Inorg. Chem. Front.*, **2017**, 4, 2037-2044. (IF: 5.106)
- [7] Qi Wang, **Fangyu Fu**, Sha Yang, Marta Martinez Moro, Maria de los Angeles Ramirez, Sergio Moya, Lionel Salmon, Jaime Ruiz, and Didier Astruc*. Dramatic Synergy in CoPt Nanocatalysts Stabilized by “Click” Dendrimers for Evolution of Hydrogen from Hydrolysis of Ammonia Borane. *ACS Catal.* **2019**, 9, 1110-1119. (IF: 11.384)
- [8] Naixin Kang, Rodrigue Djeda, Qi Wang, **Fangyu Fu**, Jaime Ruiz, Jean - Luc Pozzo, Didier Astruc*. Efficient “Click” - Dendrimer - Supported Synergistic

Bimetallic Nanocatalysis for Hydrogen Evolution by Sodium Borohydride Hydrolysis. *ChemCatChem*, **2019**, *11*, 2341-2349. (IF: 4.674)

[9] Chun Luo, **Fangyu Fu**, Xiaojiao Yang, Jianyu Wei, Changlong Wang, Jing Zhu, Deshun Huang, Didier Astruc,* and Pengxiang Zhao*. Highly Efficient and Selective Co@ZIF-8 Nanocatalyst for Hydrogen Release from Sodium Borohydride Hydrolysis. *ChemCatChem*, **2019**, *11*, 1643-1649. (IF: 4.674)

[10] Qi Wang, **Fangyu Fu**, Ane Escobar, Sergio Moya, Jaime Ruiz and Didier Astruc*. "Click" Dendrimer - Stabilized Nanocatalysts for Efficient Hydrogen Release upon Ammonia - Borane Hydrolysis. *ChemCatChem*, **2018**, *10*, 2673-2680. (IF: 4.674)

[11] Qi Wang, **Fangyu Fu**, Angel M. Martinez-Villacorta, Sergio Moya, Lionel Salmon, Amelie Vax, Julien Hunel, Jaime Ruiz and Didier Astruc*. Electron Flow in Large Metallomacromolecules and Electronic Switching of Nanoparticle Stabilization: Click Ferrocenyl Dendromers that Reduce Au^{III} to Au Nanoparticles. *Chem. Eur. J.*, **2018**, *24*, 1-10. (IF: 5.16)

Synthèses et Applications Catalytiques de Nanoparticules d'Éléments de Transition

Résumé:

La catalyse constitue un élément clé en synthèse chimique et la recherche actuelle tend à rendre les procédés catalytiques plus propres dans le contexte de la chimie verte. Dans cet esprit, cette thèse a impliqué la recherche de catalyseurs nanoparticulaires utilisés en milieu aqueux, sans ligand toxique et en très faible quantité. La synthèse des nanoparticules (NPs) catalytiques a utilisé des ions des éléments de transition de la droite du tableau périodique et des réducteurs capables de réduire rapidement ces cations en atomes de degré d'oxydation nul s'agréant en petites NPs métalliques très actives en catalyse. Les réducteurs choisis ont été des composés réservoirs d'électron organique (naphthyl sodium) ou organométalliques (complexes sandwichs à 19 électrons de valence du fer tel que $[\text{Fe}(\text{I})\text{Cp}^*(\eta^6\text{-C}_6\text{Me}_6)]$ ou du cobalt tel que $[\text{Co}(\text{II})\text{Cp}^*_2]$, ($\text{Cp}^* = \eta^5\text{-C}_5\text{Me}_5$). Les supports limitant l'agrégation des NPs métalliques ont été le solvant (polyéthylène glycol, 1ère partie de la thèse), les cations des réservoirs d'électron organométalliques (2ème partie de la thèse) ou un réseau zéolitique imidazolate (MOF de type ZIF-8, 3ème partie de la thèse). Au lieu d'un cation métallique, il a aussi été possible d'utiliser un cluster tel que $[\text{Au}_{25}(\text{SR})_{18}]$ ($\text{R} = \text{CH}_2\text{CH}_2\text{Ph}$) comme précurseur, auquel cas la réduction peut se limiter à un simple transfert d'électron produisant un cluster anionique stabilisé par le contre-cation sandwich encombré du réservoir d'électron. Les petites NPs ainsi stabilisées se sont avérées d'excellents catalyseurs "verts" de plusieurs réactions de couplage C-C ou C-N et de production d'hydrogène par hydrolyse d'hydrures métalliques en milieu aqueux dans des conditions très douces. Cette dernière réaction a été efficacement catalysée par des NPs bimétalliques $\text{Ni}_2\text{Pt}@\text{ZIF-8}$ avec une synergie spectaculaire entre les deux métaux.

Mots Clés: Réservoir à Electrons, Métal de Transition, Nanoparticules, Organométalliques, Catalyseur Homogène, Catalyseur Hétérogène.

Synthesis and Catalytic Applications of the Transition Elements Nanoparticles

Abstract:

Catalysis is a key element in chemical synthesis, and current research is focusing on making catalytic processes cleaner in the context of green chemistry. In this spirit, this thesis involves the research of nanoparticle (NP) catalysts used in aqueous medium, without toxic ligand and in very small quantities toward a variety of useful processes. The synthesis of the catalytic NPs used cations of the transition elements of the right of the periodic table and of reducing agents capable of rapidly reducing these cations to atoms of zero oxidation state aggregating into small catalytically active metal NPs. The chosen reducing agents were organic (naphthyl sodium) or organometallic (19-electron) sandwich complexes of iron such as $[\text{Fe}(\text{I})\text{Cp}^*(\eta^6\text{-C}_6\text{Me}_6)]$ or cobalt such as $[\text{Co}(\text{II})\text{Cp}^*_2]$, ($\text{Cp}^* = \eta^5\text{-C}_5\text{Me}_5$) used as electron reservoirs. The supports limiting the aggregation of the metal NPs were the solvent (polyethylene glycol, first part of the thesis), the cations of the organometallic electron reservoirs (2nd part of the thesis) or a zeolitic imidazolate framework (MOF of ZIF-8 type, 3rd part of the thesis). Instead of a metal cation, it has also been possible to use a cluster such as $[\text{Au}_{25}(\text{SR})_{18}]$ ($\text{R} = \text{CH}_2\text{CH}_2\text{Ph}$) as a precursor, in which case the reduction was limited to a simple electron transfer producing an anionic cluster stabilized by the congested sandwich counter cation of the electron reservoir. The small NPs thus stabilized proved to be excellent "green" catalysts for several C-C or C-N reactions and hydrogen production by hydrolysis of metal hydrides in an aqueous medium under very mild conditions. This latter reaction was efficiently catalyzed by $\text{Ni}_2\text{Pt}@\text{ZIF-8}$ bimetallic NPs with a spectacular synergy between the two metals.

key words: Electron Reservoir, Transition Metal, Nanoparticles, Organometallics, Homogeneous Catalyst, Heterogeneous Catalyst.

Institut des Sciences Moléculaires (ISM, UMR CNRS 5255), Université de Bordeaux,
351 Cours de la Libération, 33405 Talence Cedex